



Theses and Dissertations

2019-11-01

An Experimental and Theoretical Investigation of Internal Wave Kinetic Energy Density in Variable Stratifications

Allison Marie Lee
Brigham Young University

Follow this and additional works at: <https://scholarsarchive.byu.edu/etd>



Part of the [Engineering Commons](#)

BYU ScholarsArchive Citation

Lee, Allison Marie, "An Experimental and Theoretical Investigation of Internal Wave Kinetic Energy Density in Variable Stratifications" (2019). *Theses and Dissertations*. 7737.
<https://scholarsarchive.byu.edu/etd/7737>

This Dissertation is brought to you for free and open access by BYU ScholarsArchive. It has been accepted for inclusion in Theses and Dissertations by an authorized administrator of BYU ScholarsArchive. For more information, please contact scholarsarchive@byu.edu, ellen_amatangelo@byu.edu.

An Experimental and Theoretical Investigation of Internal Wave
Kinetic Energy Density in Variable Stratifications

Allison Marie Lee

A dissertation submitted to the faculty of
Brigham Young University
in partial fulfillment of the requirements for the degree of
Doctor of Philosophy

Julie Crockett, Chair
R. Daniel Maynes
Steven E. Gorrell
Scott L. Thomson

Department of Mechanical Engineering
Brigham Young University

Copyright © 2019 Allison Marie Lee
All Rights Reserved

ABSTRACT

An Experimental and Theoretical Investigation of Internal Wave Kinetic Energy Density in Variable Stratifications

Allison Marie Lee

Department of Mechanical Engineering, BYU

Doctor of Philosophy

Internal waves are generated in a fluid if the density increases continuously with depth. The variation in density with depth, or stratification, defines the natural frequency of the fluid N . Two common examples of stratified fluids are the ocean and atmosphere; internal waves are generated continuously in both mediums. Although there are many internal wave generation mechanisms, one common and frequently studied method is tidal flow over oceanic bathymetry. If the local natural frequency of the water near the topography is greater than the tidal frequency ω , internal waves will be generated by the tidal flow over the topography. If $N < \omega$, only evanescent waves will be formed. Unlike internal waves, evanescent waves decay rapidly as they move vertically away from their generation site. As evanescent waves pass from an evanescent region ($N < \omega$), through a turning depth ($N = \omega$) and into a propagating region ($N > \omega$), they become propagating internal waves. Because internal waves can propagate energy across large distances, they play an important role in oceanic mixing and the overall energy budget of the ocean. Knowing where these waves are formed from evanescent waves and their corresponding energy improves understanding of the impact on their surrounding area.

Kinetic energy density of evanescent and internal waves formed from oscillatory flow over topography in evanescent regions is first estimated using synthetic schlieren experiments and a novel linear theory model. Experiments were performed with two Gaussian topographies in an exponential density profile. The linear theory model, which uses a set of equations that links the evanescent and propagating regions with the Airy function to overcome the discontinuity inherent with a turning depth, was compared to the experiments. Both methods showed that increasing \overline{Fr}_1 , the strength of the evanescent region relative to the excitation frequency, causes the propagating kinetic energy to decrease. In addition, kinetic energy decreased with increasing distance between the topography and the turning depth. Because the model does not account for nonlinearities such as turbulence generation, it regularly overestimates propagating kinetic energy relative to the experiments. After comparing the model with synthetic schlieren experiments, it was used to estimate that 25% of the evanescent wave energy generated by an oceanic topography located at 15°N, 130°E can become propagating wave energy.

The influence of topography shape and fluid density profile on kinetic energy density was also explored through a combination of experiments, a linear theory model, and numerical simulations. From numerical simulations, kinetic energy can be directly calculated with the velocity profile and indirectly with the density perturbation field, in the same manner as the synthetic schlieren experiments. Average propagating internal wave kinetic energy (\overline{KE}_2^*) as a function of $\overline{Fr}_1 D/H$, which combines \overline{Fr}_1 with the relative distance between the topography and the turning depth D/H , was compared for all methods. \overline{KE}_2^* decreases with increasing $\overline{Fr}_1 D/H$ for all methods. Also, far from the turning depth, the direct and indirect simulations indicate similar kinetic energy when

in the propagating region, where a distance from the turning depth can be quantified based on N and ω . This work was expanded to include a medium Gaussian, steep Gaussian, sinusoidal, and complex topography with two layer linear, parabolic, cubic, and exponential density profiles to investigate the validity of assuming an average natural frequency in the evanescent region and the impact of the topographic slope on \overline{KE}_2^* . A comparison of the density profiles indicated that using a two layer linear density profile has similar results compared to the other density profiles for estimating \overline{KE}_2^* as a function of $\overline{Fr}_1 D/H$. Also, \overline{KE}_2^* is non-negligible for $\overline{Fr}_1 D/H < 4$. Increasing the maximum slope of a topography shape decreases the kinetic energy of the generated internal waves, though it was found that the energy is dependent upon the actual shape of the topography as well.

Particle image velocimetry (PIV) experiments were performed and compared to synthetic schlieren (SS). While SS experiments generally resulted in an overestimate of kinetic energy relative to the PIV results, the trends from each experimental method matched well. It is recommended that SS be used in regions away from turning depths, but that either are valid in the evanescent and propagating regions. PIV methods should be used when results near the turning depth or the topography are desired.

Keywords: stratified flow, internal waves, variable stratifications, oceanic bathymetry

ACKNOWLEDGMENTS

This work has been supported by the Utah NASA Space Grant Consortium and by NSF Grant CBET-1606040.

I would like to first express appreciation to all the members of my committee for their help and willingness to work with me in providing comments and suggestions on this work. In addition, I am grateful for the collaboration work done with Michael Allshouse and Yuxuan Liu at Northeastern University. They performed all of the numerical simulations and were very helpful in the writing and editing of those sections.

Numerous undergraduate students have worked in the Stratified Flow lab with me during my graduate career. They have all helped improve lab equipment, run tests and create new experimental setups. Katie Pusey and Kyle Hakes worked in the lab for multiple semesters and made significant contributions to how experiments are performed in the Stratified Flow Lab.

My time as a graduate student has been enhanced by the numerous friendships I have made as I learned to find a balance between school and life. I am especially grateful for the support of Melody Palmer, whose kindness knows no bounds, and Kimberley Stevens, who is a great example of dedication and perseverance. Jessica Morgan gifted me with trust and friendship during a difficult time. Michael Goodrich taught me about true hope and the importance of striving. These people, along with many others, helped me overcome personal, educational, and emotional challenges, and I am thankful for each of them.

I am grateful for the support of my parents, Michael and Suzanne, who encouraged me both in my undergraduate and graduate studies. They have listened to practice presentations, guided me through trials, and have been a constant source of strength through all of my schooling. My brothers, Jonathan and William, have been similarly loving and supportive. They both provided numerous opportunities to take a break from school to enjoy beautiful musical performances in Arizona and Utah.

My advisor, Julie Crockett, deserves more acknowledgment and gratitude than is possible to express here. She saw my potential and so encouraged me through “fun” math, edited with exactness and kindness, and guided me to be the researcher I am today. Aware of my long term goal of teaching, she encouraged me to accept three teaching opportunities. She was patient while I struggled through emotional turmoil that affected my research and was supportive as I found a work-life balance. She is a remarkable mentor and will always be my friend.

If there could be one theme for my graduate career, it would be that my loving Heavenly Father knows exactly who to put into my life and when they are most needed. His inspiration started my graduate school path and His continual faith in me sustained me when I otherwise would have turned away. I am eternally blessed to have His hand in my life.

TABLE OF CONTENTS

LIST OF TABLES	ix
LIST OF FIGURES	x
Chapter 1 Introduction	1
1.1 Internal waves	1
1.2 Motivation	3
1.2.1 Atmospheric waves	3
1.2.2 Oceanic waves	4
1.3 Internal waves and evanescent waves	5
1.4 Wave generation mechanisms	7
1.5 Investigative methods for internal waves	8
1.5.1 Observations	9
1.5.2 Experimental techniques	10
1.5.3 Simulations	15
1.5.4 Theory	16
1.6 Current research	16
1.6.1 Varying stratifications	17
1.6.2 Evanescent waves and turning depths	18
1.6.3 Topography shape	19
1.7 Current research needs	20
Chapter 2 Methodology	22
2.1 Navier-Stokes equations	22
2.2 Analytical model	24
2.2.1 Evanescent region	26
2.2.2 Propagating region	27
2.2.3 Airy integral matching	27
2.2.4 Accuracy of analytical model	29
2.3 Experimental processes	31
2.3.1 Tank preparation	31
2.3.2 Synthetic schlieren and Digiflow	33
2.3.3 Particle image velocimetry	38
2.4 Numerical Simulations	39
Chapter 3 Turning depths: evanescent to propagating wave kinetic energy density	42
3.1 Contributing authors and affiliations	42
3.2 Abstract	42
3.3 Introduction	43
3.4 Methodology	47
3.4.1 Experimental procedures	47
3.4.2 Theory	53

3.5	Results	58
3.6	Ocean case study	69
3.7	Conclusion	72
Chapter 4	Evanescent to propagating internal waves in simulations, experiments, and linear theory	75
4.1	Contributing authors and affiliations	75
4.2	Abstract	75
4.3	Introduction	76
4.4	Methodology	79
4.4.1	Theory	82
4.4.2	Experimental procedure	86
4.4.3	Numerical simulations	88
4.5	Results	89
4.5.1	Qualitative comparison	89
4.5.2	Kinetic energy variation with depth	94
4.5.3	Average kinetic energy	102
4.6	Summary of methodologies	106
4.7	Conclusion	108
Chapter 5	Effects of stratification and topography shape on kinetic energy density of evanescent and internal waves	110
5.1	Contributing authors and affiliations	110
5.2	Abstract	110
5.3	Introduction	111
5.4	Methods	113
5.4.1	Experiments	116
5.4.2	Linear theory	117
5.4.3	Numerical simulations	119
5.4.4	Average kinetic energy	120
5.5	Results	122
5.6	Conclusion	137
Chapter 6	Synthetic schlieren and particle image velocimetry: an investigation of two experimental techniques for internal wave kinetic energy density . . .	139
6.1	Contributing authors and affiliations	139
6.2	Abstract	139
6.3	Introduction	140
6.4	Methods	142
6.4.1	Average kinetic energy	146
6.4.2	Synthetic schlieren	147
6.4.3	Particle image velocimetry	148
6.5	Results	149
6.6	Discussion	163

Chapter 7	Conclusion	165
REFERENCES		169
Appendix A	Supplemental experimental details	177
A.1	Cases of Chapter 5	177
A.2	Filling the tank	179
A.3	Density measurements and finding N	181
A.4	Taking SS images	182
A.5	Running the stepper motor	184
A.6	Processing the images with Digiflow	185
Appendix B	Computer code	189
B.1	MATLAB	189
B.1.1	Generating natural frequency profile and output voltages	189
B.1.2	Measuring the density profile	194
B.1.3	MATLAB setup from Digiflow DATs	198
B.1.4	Supercomputer MATLAB file to calculate kinetic energy	203
B.1.5	PIV calculations	207
B.1.6	Linear theory calculations	222
B.2	Arduino	229
B.3	Supercomputer files	230
B.3.1	Setup data for SS kinetic energy processing	230
B.3.2	Create experimental energy	230
Appendix C	Uncertainty analysis	231
C.1	Density perturbation	231
C.2	Kinetic energy	233

LIST OF TABLES

3.1	A summary of experiments and experimental parameters. Cases 1-14 used the medium topography ($W/H = 1.8$), while cases 15-24 used the steep topography ($W/H = 0.45$). Water height, z_{td} , and L are given in centimeters.	50
4.1	A summary of the parameters of each case.	81
4.2	N/ω shown for each case indicates where in the propagating region the difference between the direct and indirect methods is less than 5%.	100
4.3	Constants and goodness of fit values for Eq. (4.38).	103
5.1	Names, equations and images of the four topography profiles. All units are in meters.	113
5.2	Density Profile Equations	114
5.3	Summarized details of all cases including the topography shape and density profile listed in Tab. 5.2 and the range of values for ω , D/H , \overline{Fr}_1 , and $\overline{Fr}_1 D/H$	115
5.4	Slopes of the trendlines based on the theoretical data points in Figs. 5.3-5.6 for each topography and each density profile using Eq. 5.23.	128
5.5	Coefficients corresponding to Eq. (5.23) for the trendlines associated with each topography.	135
6.1	Equations for each of the density profiles.	143
6.2	Names, equations and images of the four topography profiles. All units are in meters.	144
6.3	Experimental details for each case. The medium topography was used for cases 1-12, steep for case 13, sinusoidal for cases 14 and 15, and complex for case 16. All lengths are in meters. The units of a , b , c , and d are defined by the appropriate density profile in Tab. 6.1.	145
A.1	Case details for the medium topography. All heights are given in centimeters and a , b , c , and d correspond to the density profile listed in the second column and detailed in Tab. 5.2. Simulations were performed on cases with an asterisk.	177
A.2	Case details for the steep topography.	178
A.3	Case details for the sinusoidal topography.	178
A.4	Case details for the complex topography.	179
C.1	Inputs and output of Eq. C.1 with a sequential perturbation analysis. The labels on the right half of the table indicate which variable was perturbed. $\partial\rho'/\partial z$ for each scenario, along with the uncertainty (based on the perturbed solution) are listed in the bottom row. All inputs have units of meters, with $\partial\rho'/\partial z$ in units of kg/m^4	232
C.2	Uncertainty analysis of KE_1 based on Eq. (C.3).	234
C.3	Uncertainty analysis of KE_2 based on Eq. (C.4).	235

LIST OF FIGURES

1.1	A ship generates an interfacial wave between fresh (light blue) and salty (dark blue) water.	1
1.2	(a) Continuously varying density profile and (b) internal waves generated from an oscillatory flow.	2
1.3	Examples of (a) internal waves, (b) evanescent waves, and (c) internal waves formed from evanescent waves shown with isopycnals.	6
1.4	Mooring, measurement, and ship locations of the R/V Revelle as part of the IWAP experiment [16].	10
1.5	Using parallel light rays and an array of lenses, density fluctuating flows can be visualized as the variations in density caused variation in the index of refraction. The knife edge on the right side of the figure would prevent lights rays which were bent below the edge to be seen, thus causing dark spots to be seen on the imaging lens. (Figure created by Jonathan Stoddard)	12
1.6	A top down view of the experimental arrangement for a synthetic schlieren image set up. The important lengths noted here are necessary to find the change in the index of refraction and are used in Equations (1.4) and (1.5). Notice that the y-coordinate follows the camera line of sight while the x direction is parallel to the length of the tank. The z-direction is not shown here, but follows the height of the tank.	12
1.7	Digiflow images of the (a) undisturbed water, (b) experiment in progress, and (c) processed data of $\partial\rho'/\partial z$	14
1.8	An example of internal waves tunneling through and reflecting off of an evanescent region.	18
2.1	An example of the natural frequency profile in the tank (a) shown relative to the experimental setup (b).	25
2.2	The kinetic energy as a function of height is shown for the scenarios of including or excluding dq/dz and dm/dz when calculating the horizontal velocity. The turning depth is shown by the dashed horizontal line and the dash-dot line indicates the height of a 10% increase in N from the turning depth.	30
2.3	An example of a topography attached to the track in the experimental tank. The two buckets used to fill the tank are on the left side, while the lightbox and mask are behind the tank.	32
2.4	Experimental setup of (a) SS and (b) PIV experiments	34
2.5	Fourier amplitudes of ΔN^2 in the evanescent region (a) and propagating region (b) are shown in contours increasing by 0.0025 for each line. Both figures use the same scaling. The highest value for the contour lines for (a) is 0.01 s^{-2} and for (b) is 0.0125 s^{-2}	37
3.1	A propagating internal wave is shown in (a) and the vertically decaying evanescent wave is seen in (b). In (c), the a turning depth indicates the boundary between the evanescent and propagating regions, with the evanescent wave becoming an internal wave as it pass through the turning depth.	44
3.2	The measured density is shown in red points and the exponential curve fit is the black line.	48

3.3	Experimental tank and visualization system schematic. In (a), the front view of tank is shown with internal wave regions and turning depth as labeled. In (b), the side view of the setup with camera for synthetic schlieren imaging is shown.	49
3.4	Fourier amplitudes of ΔN^2 in the evanescent region (a) and propagating region (b) are shown in contours increasing by 0.0025 for each line. Both figures uses the same scaling. The highest value for the contour lines for (a) is 0.01 s^{-2} and for (b) is 0.0125 s^{-2}	54
3.5	The kinetic energy as a function of height is shown for the scenarios of including or excluding dq/dz and dm/dz when calculating the horizontal velocity. The turning depth is shown by the dashed horizontal line and the dash-dot line indicates the height of a 10% increase in N from the turning depth.	59
3.6	Normalized kinetic energy is shown as a function of height for two cases. The solid lines are experimentally calculated KE^* while the dotted represent model results. Data from (a) and (b) come from Cases 1 and 8 which used the medium topography, while (c) and (d) are Cases 18 and 20 and used the steep topography. The turning depth location, z_{td} is marked with a dashed line. The black x markers indicate the distance over which kinetic energy is averaged in the propagating region.	60
3.7	Contours of $\Delta \tilde{N}^2$ for Case 15 as a function of ω^* and k^* in the evanescent (a) and propagating (b) regions. $\Delta \tilde{N}^2$ values have been scaled by a factor of 10^3	63
3.8	The average, normalized, kinetic energy in the propagating region as a function of H/D for both the medium and steep topographies with experimental and model values. Red circles represent the medium topography, with closed filled circles representing experimental data and open for the model. Steep topography data is represented with black triangles, again with the filled triangles representing experimental data and open for the model. The inset contains five steep topography model points with normalized kinetic energy values less than 10^{-5}	64
3.9	\overline{KE}_2^* is shown as a function of \overline{Fr}_1 . The symbols and lines follow the same legend as shown in Fig. 3.8.	65
3.10	\overline{KE}_2^* as a function of H/D and \overline{Fr}_1 for the analytical model. The solid red line indicates the medium topography, while the dashed black line is the steep topography. Markers for H/D as shown.	67
3.11	\overline{KE}_2^* is shown as a function of W/H , a/ρ_0 , and bH , showing the effects of topographic shape (a) and an exponential density profile in (b) and (c). In (a), the square and circle indicate $W/H = 0.45$ and 1.8 , or the steep and medium topographies, respectively.	69
3.12	Data from the GEBCO worldwide bathymetry map is indicated by the shaded portion, with a Gaussian curve fit through topographical feature analyzed in this work.	71
3.13	WOCE data is used to calculate N^2 indicated by the red dashed line in (a), while the black line is the curve fit of the data used for the model analysis. The normalized kinetic energy calculated from the model is shown in (b) as a function of depth.	72
4.1	An example of the natural frequency profile in the tank (a) shown relative to the experimental setup (b)	80
4.2	Snapshots in time of experimental ΔN^2 data (a), full amplitude ΔN^2 simulation data (b,c), full amplitude simulation velocity field (d), 1/10 amplitude ΔN^2 simulation data (e), and 1/10 amplitude simulation velocity field (f) for case 1. The topography location is masked in grey	90

4.3	Contour plots of the experiments (a-c), full amplitude simulation (d-f) and 1/10 amplitude simulation (g-i) for case 1. A sketch of the relative height of each scenario is shown on the left. Each column of figures is at the same location, meaning figures (a), (d), and (g) are at the tip of the topography	92
4.4	Kinetic energy of the experiments (red line with diamond marker), indirect simulations (black line), and direct simulations (black dashed line) are compared for each of the five cases. Case 1 corresponds to (a), case 2 to (b), etc.	95
4.5	Normalizing values for the kinetic energy density for each of the methods as a function of $\overline{Fr}_1 D/H$	97
4.6	Normalized kinetic energy for each of the four methods for case 1 (a) and case 4 (b)	98
4.7	Average, normalized kinetic energy in the propagating region as a function of $\overline{Fr}_1 D/H$, with curve fits for the theory, direct simulations, and 1/10 amplitude direct simulations	103
4.8	A ratio of the full amplitude simulation and theory kinetic energies as a function of $\overline{Fr}_1 D/H$	106
5.1	Normalized kinetic energy for the steep topography with (a) two layer, (b) parabolic, (c) cubic, and (d) exponential density profiles. Each method of estimating kinetic energy is indicated in the legend and the location of the turning depth is the horizontal dotted line.	123
5.2	Normalized Kinetic energy of cubic density profiles corresponding to the (a) medium, (b) steep, (c) sinusoidal, and (d) complex topographies. Data for (b) is the same as Fig. 5.4(c).	125
5.3	\overline{KE}_2^* as a function of $\overline{Fr}_1 D/H$ for the medium topography for cases with (a) two layer, (b) parabolic, (c) cubic, and (d) exponential density profiles.	126
5.4	\overline{KE}_2^* as a function of $\overline{Fr}_1 D/H$ for the steep topography for cases with (a) two layer, (b) parabolic, (c) cubic, and (d) exponential density profiles.	129
5.5	\overline{KE}_2^* as a function of $\overline{Fr}_1 D/H$ for the sinusoidal topography for cases with (a) two layer, (b) parabolic, (c) cubic, and (d) exponential density profiles.	130
5.6	\overline{KE}_2^* as a function of $\overline{Fr}_1 D/H$ for the complex topography for cases with (a) two layer, (b) parabolic, (c) cubic, and (d) exponential density profiles.	131
5.7	\overline{KE}_2^* as a function of (a) \overline{Fr}_1 , (b) D/H , and (c) $\overline{Fr}_1 D/H$ for all density profiles.	133
5.8	\overline{KE}_2^* as a function of $\overline{Fr}_1 D/H$ for the (a) steep, (b) sinusoidal, and (c) complex topographies.	134
5.9	Trendlines for each topography matching those from Fig. Figs. 5.7(c) and 5.8.	136
6.1	Experimental setup of (a) SS and (b) PIV experiments	143
6.2	ΔN^2 data from case 14 for SS tests in (a) and (b), u data from PIV tests in (c)-(f). Unfiltered data is shown in the left column, while the right column shows data that has been filtered.	149
6.3	Images from case 16 with the same setup as Fig. 6.2, including both SS and PIV data.	150
6.4	Contours of Fourier amplitudes of velocity in the left column and ΔN^2 in the right for case 14 in the evanescent region (a,b) and propagating region (c,d).	152
6.5	Fourier amplitudes of velocity and ΔN^2 as in Fig. 6.4 for the complex topography (case 16).	153

6.6	Kinetic energy density for case (a) 1, (b) 2, (c) 3, and (d) 4 each with one layer density profiles. Cases 1-3 are full propagating regions while case 4 is an evanescent region. . .	154
6.7	Kinetic energy as a function of height for the (a) sinusoidal, (b) complex, (c) steep, and (d) medium topographies in an exponential density profile.	156
6.8	Kinetic energy as a function of height for the medium topography with (a) one layer, (b) two layer, (c) quadratic, and (d) cubic density profiles.	158
6.9	Average kinetic energy in the propagating region for all topographies. Symbols follow the legend shown, with the specific shapes for each topography. All SS points are in open blue symbols and PIV points are filled red symbols.	160
6.10	Average kinetic energy in the propagating region for the medium topography SS and PIV data with three density profiles.	162

CHAPTER 1. INTRODUCTION

1.1 Internal waves

When the density of a fluid varies with height, it is termed a stratified fluid. One simple stratification is a discrete two layer system with either two fluids or one fluid with two different densities, such as fresh water on top of salt water. A disturbance in one layer, such as a ship, generates surface waves, but also a wave at the interface, known as an interfacial wave [1] as seen in Fig. 1.1. If the density of a fluid continuously varies, as shown in Fig. 1.2(a), then instead of one interface, there are an infinite number of interfaces. A disturbance to this continuous stratification under the right conditions, such as an oscillatory flow over a topography, will generate internal waves as seen in Fig. 1.2(b).

Internal waves were recognized by Pettersson in 1908 and have been a topic of much investigation since then because they play a critical role in understanding atmospheric and oceanic dynamics [2–4]. Both the atmosphere and ocean are stratified fluids. In the atmosphere, the decreasing temperature with increasing altitude causes a variation in the density [5]. In the ocean, the decreasing temperature and increasing salinity cause combined effect of increasing the den-

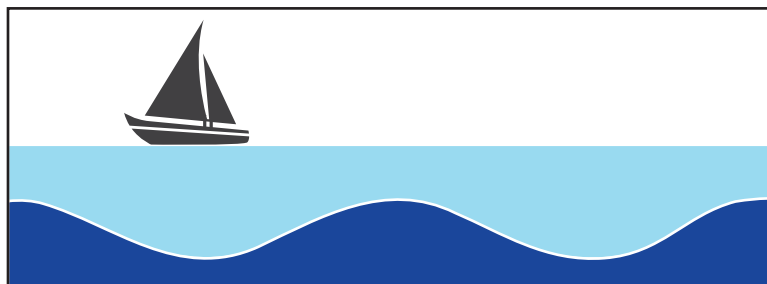


Figure 1.1: A ship generates an interfacial wave between fresh (light blue) and salty (dark blue) water.

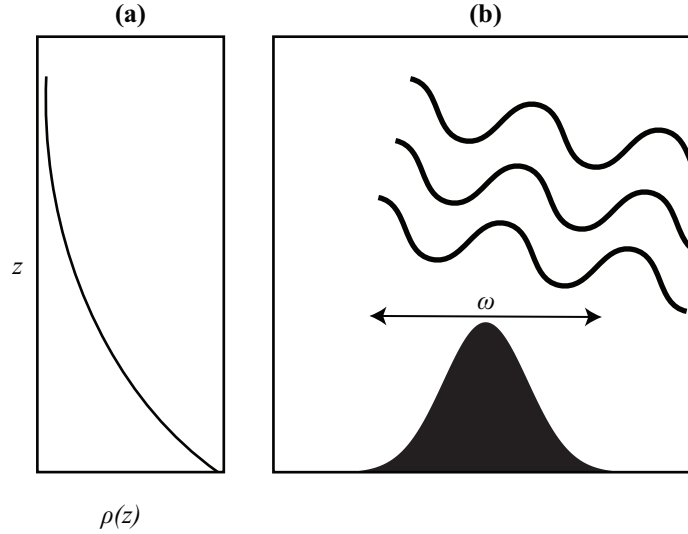


Figure 1.2: (a) Continuously varying density profile and (b) internal waves generated from an oscillatory flow.

sity with increased depth [4]. To define the strength of a stratification, the natural frequency is calculated with

$$N^2 = \frac{-g}{\rho_0} \frac{\partial \rho}{\partial z} \quad (1.1)$$

where g is the gravitational constant, ρ_0 is a reference density (1000 kg/m³ for water), and $\partial \rho / \partial z$ is the variation of density with respect to height. The natural frequency is also known as the buoyancy frequency or the Brunt-Väisälä frequency. Internal waves are generated in a stratified fluid when the disturbance frequency, or excitation frequency, ω , is less than the natural frequency of the fluid. As internal waves propagate away from their generation site, they suffer little to no viscous dissipation [5] and are important factors in both the atmosphere [6] and ocean [7]. If $N < \omega$, evanescent waves are formed and the amplitudes of these waves decay at an exponential rate as they move vertically away from their generation site [5]. If an evanescent wave travels through a turning depth, where $N = \omega$, then they become propagating internal waves which no longer decay.

This chapter will introduce internal and evanescent waves, provide motivation for their study, outline several investigative techniques, give background on past research, and define the specific research topics that will be discussed in the remainder of this work.

1.2 Motivation

Internal waves are generated almost continuously in both the ocean and atmosphere because both mediums are stratified. Although internal waves in the atmosphere can be relatively small compared to other atmospheric phenomena, they have an important impact on the thermal structure of the atmosphere [4]. In the ocean, internal waves transport energy and their eventual breaking directly influences oceanic mixing [4]. To provide motivation for the study of internal waves, this section will detail the overall influence of these waves on both mediums. Because oceanic waves are the main topic for this dissertation, atmospheric internal waves will be introduced here, but oceanic internal waves will be focused on throughout the remainder of this chapter.

1.2.1 Atmospheric waves

Internal waves in the atmosphere are relatively small compared to the many other phenomena occurring in the atmosphere, such as the jet stream, but they have a non-negligible effect on climate, weather, and the overall thermal structure of the atmosphere [4, 5]. In general, atmospheric scientists and researchers investigate internal waves because of the vertical momentum transport facilitated by internal waves [8] and if weather and climate models do not account for the generation and breaking (overturning) of internal waves, they incorrectly predict wind speeds and temperature of the atmosphere [4].

When internal waves approach a region of varying stratification, the angle of propagation can steepen to the point where the wave overturns and breaks, similar to how a surface wave on the ocean will break. Internal waves breaking in the atmosphere causes vertical mixing and is a method wherein energy is dissipated into smaller scales in the atmosphere [8]. In addition researchers have found that internal waves generated near or from mountain topographies generated Clear Air

Turbulence (CAT) [9]. While all air turbulence can be dangerous for aircraft, CAT is particularly hazardous because it is not visible and may come up unexpectedly. Research on internal waves is improving forecast predictions of CAT to improve the safety of aircraft [9].

1.2.2 Oceanic waves

Other than in the first 100 m of the ocean where the fluid is well mixed, internal waves can be formed. They can be generated in many ways, including through horizontal shear caused by winds on the ocean surface and tidal motions over topography [10]. Oceanographers are interested in internal waves because they transport energy across oceans and from the deep ocean upward and induce oceanic mixing [8, 11]. Off-shore drilling companies study internal waves to understand and prevent the often negative impact of the motions caused by these waves on both drilling rigs and oil pipelines [12], marine biologists use internal waves to help predict the influx of nutrients near the coasts [13], and the U.S. Navy has investigated the effect of internal waves on submarines and associated equipment, along with the generation of these waves by submarines [14]. Although many aspects of internal waves impact the ocean, this dissertation is focused mainly on internal wave generation and propagation, where the potential impact on the ocean is known to be important.

As the diurnal and semidiurnal tides oscillate over topography in the ocean, satellite data indicates that approximately 1 TW is converted from barotropic tides into internal waves in the deep ocean [11]. When internal waves are initially formed from the tides, some tidal energy is dissipated and creates local turbulent mixing [11]. As internal waves propagate away from their generation site, they convert energy from the horizontal plane of the tides to a more vertical motion, moving energy throughout the ocean and interacting with other internal waves, oceanic topographies, or oceanic currents [11]. Observations of oceanic internal waves have recorded varying sizes depending on where and how the internal waves are generated. For example, wave packets near the Hudson Canyon, near the continental shelf of New York, have wavelengths of about 500 m and peak to trough amplitudes of close to 15 m, while internal waves packets in the Andaman Sea have wavelengths of about 15 km [15]. For internal waves generated by

the semidiurnal tide, Alford and Zhao reported group velocities, or the velocity associated with internal wave energy, between 1 and 2 m/s [16].

Similar to atmospheric internal waves, oceanic internal waves can steepen, overturn, and break. Breaking internal waves impact oceanic circulation and climate simulations [17] and models that do not include internal waves do not accurately capture the turbulent diffusivity seen in the ocean [4]. Turbulent mixing is important to oceanic circulation, such as meridional overturning circulation, or the circulation of warm water near the surface of the water and cold water in the deep ocean [10, 11]. Thus both internal waves and the motions caused by internal waves have far reaching effects throughout the ocean.

1.3 Internal waves and evanescent waves

Because the focus of this dissertation is internal waves generated from flow over topography in oceanic scenarios, an example of tidal flow over oceanic topography will be used to illustrate the similarities and differences between internal and evanescent waves.

The most well known oceanic tide is the M2 semidiurnal tide, which regularly oscillates on a 12.1 hour period within the ocean [18]. In the ocean, the density increases with depth due to increasing salinity and decreasing temperature, and thus the natural frequency, N , of the ocean varies also with depth [19]. For an oceanic topography, internal waves are generated when the stratification is larger than the tidal oscillation frequency such that $N(z) > \omega_{M2}$. In this scenario, internal waves will be generated and the angle of propagation of the waves is defined by the general equation

$$\omega = N \cos(\theta) \tag{1.2}$$

where θ is defined from the vertical axis. This is called the dispersion relation and can also be written as

$$\omega^2 = \frac{N^2(k^2 + l^2)}{k^2 + l^2 + m^2} \tag{1.3}$$

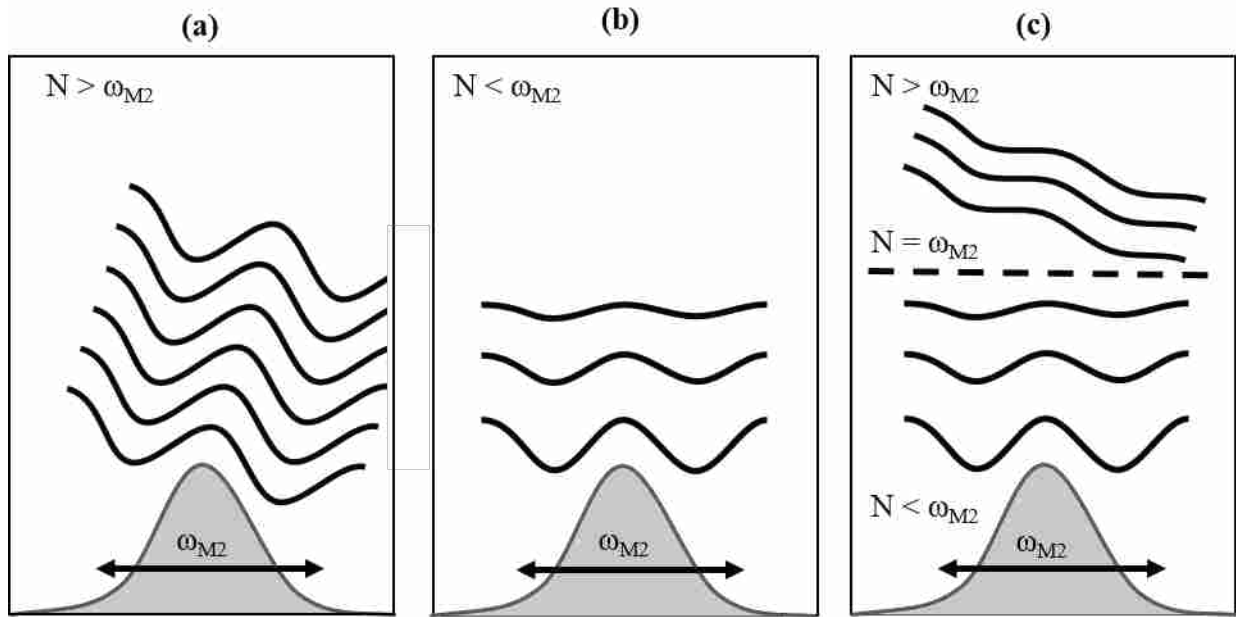


Figure 1.3: Examples of (a) internal waves, (b) evanescent waves, and (c) internal waves formed from evanescent waves shown with isopycnals.

where k , l , and m are wavenumbers corresponding to the x , y , and z directions, and corresponding wavelengths are $\lambda_x = 2\pi/k$, etc. From Eq. (1.2), we see that as N approaches ω , the waves become more vertical. Thus, as the M2 tides oscillate over an oceanic topography where $N > \omega_{M2}$, as is shown in Fig. 1.3 (a), internal waves will form. In Fig. 1.3, the lines indicate isopycnals, or lines of constant density, and depict how the density layers are disturbed by the tidal motions over topography.

Due to the three dimensional nature of the internal waves, the group velocity of the waves, which defines the direction and speed of the energy, will always be perpendicular to the phase speed, or the movement of the crest and troughs of the wave. Thus, the energy of the internal waves in Fig. 1.3(a) is moving up and to the right while the crests and troughs move down and to the right.

Figure 1.3(b) illustrates an example of evanescent waves, or the disturbances created when the tides pass over topography in a region where $N < \omega_{M2}$, which occurs in many regions of the deep ocean [19]. Because the excitation frequency is greater than the natural frequency, the fluid is

pushed vertically upwards, but this amplitude of this motion decays exponentially with increasing height [5].

A turning depth is the location where $N = \omega$ as shown by the horizontal dashed line in Fig. 1.3(c). Below this line, near the topography is an evanescent region, where only evanescent waves will be formed as the M2 tide oscillates over the topography. As the evanescent waves move vertically, they decay until they reach the turning depth. As they pass through it, they move into a propagating region and become propagating internal waves. This scenario has been proven through linear theory, experiments, and simulations [5, 18]. As indicated by sketch of the waves in Fig. 1.3, the internal waves generated from the evanescent region have smaller amplitudes than those of the waves generated directly from the topography, which is indicative of the decrease in kinetic energy of the evanescent waves as they move through an evanescent region.

1.4 Wave generation mechanisms

Because internal waves are generated when a stratified fluid is disturbed, they are generated almost continuously throughout the ocean. The exception to this is the mixed region at the top of the ocean, about 100 m in depth [4]. Here, a few generation mechanisms for oceanic internal waves are highlighted.

Immediately below the mixed region in the ocean is the pycnocline, a region of rapid density increase [20]. Internal waves can be formed in this region from tidal flow over topography within this region [15] or by wave coming up from below the pycnocline and impinging on the region [21]. In addition, they can be formed by strong surface winds which results in a shear stress moving through the mixed region and moving the pycnocline, and nonlinear interactions with surface waves [10].

Turbulence in or near stratified fluids is also a common generator of internal waves [22]. Turbulence generated waves can be formed when the turbulence occurs in a stratified fluid [23], or if a mixed region is next to a stratified region. Dohan and Sutherland [24] found experimentally that internal waves generated from a turbulent region propagated at angles of 42-55° regardless of the

strength of the stratification. These results were later confirmed using numerical simulations [25]. Turbulence generated internal waves have been studied in many situations including turbulence near boundaries [23], turbulent wakes [26], sheared turbulence [27], and turbulence generated by oscillatory flow over rough topography [28], among others.

One of the most common generation mechanisms of oceanic internal waves is tidal flow over oceanic topography [7]. These waves are an important mechanism for transferring horizontal tidal motions into vertically propagating waves needed to transfer energy throughout the depth of the ocean [29]. Significant research on this topic has occurred for a variety of scenarios including deep ocean topography [3], mid-ocean topography [30], and waves generated from the continental shelf [31]. Laboratory experiments [28, 32–34], numerical simulations [35–38], and linear theory [39, 40] have all been employed to study topographically generated internal waves.

Within the ocean, internal waves can transfer energy through resonant and non-resonant wave-wave interactions. In resonant interactions, two waves collide and form a third wave that is a combination of the total wavenumbers (\mathbf{k}) and frequencies (ω) of the other two waves such that $\mathbf{k}_1 \pm \mathbf{k}_2 = \mathbf{k}_3$ and $\omega_1 \pm \omega_2 = \omega_3$ [7, 41, 42]. Stemming from resonant interactions is the idea of parametric subharmonic instability (PSI) wherein a single, or primary, wave is disturbed and emits two waves whose frequencies and wavenumbers are half those of the primary waves [43]. Non-resonant wave interactions can also produce other waves that are harmonics of the primary waves [44–46].

1.5 Investigative methods for internal waves

The four main methods of studying internal waves are through observations, experiments, numerical simulations, and analytical theory. In this work, all of these methods except observations are used. A description of all standard methods is provided here, with further details for the exact setups used in this research provided in Chapter 2.

1.5.1 Observations

Internal waves have been an area of study since they were first observed in the Baltic Sea by Pettersson [2]. Oceanic observations are an important method of internal wave investigations because they provide information about actual oceanic conditions needed to validate theories on internal waves. Data can be collected from a variety of sources such as current, temperature, and depth (CTD) devices [47], sonar survey equipment [48], and satellite images [49]. Recent large scale efforts by teams of university researchers to observe internal waves and other stratified phenomena include the World Ocean Circulation Experiment (WOCE) [50], the Hawaiian Ocean Mixing Experiment (HOME) [51], and Internal Waves Across the Pacific (IWAP) [16]. These experiments ranged from 2 months of observations with 2 cruises on a single ship (IWAP), to multi-year, multi-ship excursions (WOCE and HOME). These cruises have specific goals in mind and significant preparation goes into selecting cruise locations and designing and building observational equipment that will travel between hundreds and thousands of meters below the surface of the water. To provide a basic idea of the data collected on an observational experiment, details of the IWAP cruise are given here.

During the IWAP experiment, the research vessel R/V Reville placed 6 moorings at varying intervals from 25-37°N near the French Frigate Shoals, Hawaii as shown in Fig. 1.4. Along these moorings, CTD data was collected every 1.5 hrs at depths from 80-1400m, velocity data was collected at a rate of 300 KHz every few minutes from 5-40m, and temperature data was collected at 3000 m. After placing the moorings, the ship traveled thousands of kilometers back and forth along the same line of 25-37°N collecting velocity and shear data using a Hydrographic Sonar System. One of the main purposes of this experiment was to investigate the prevalence of parametric subharmonic instability (PSI), or the breakdown of a primary wave into two daughter waves, which had been seen previously in experiments and simulations occurring in locations where the rotational rate of the earth, f , is equal to ω_{M2} . Among other results, the observation data indicated that PSI does not substantially affect tidally propagating waves in those locations,

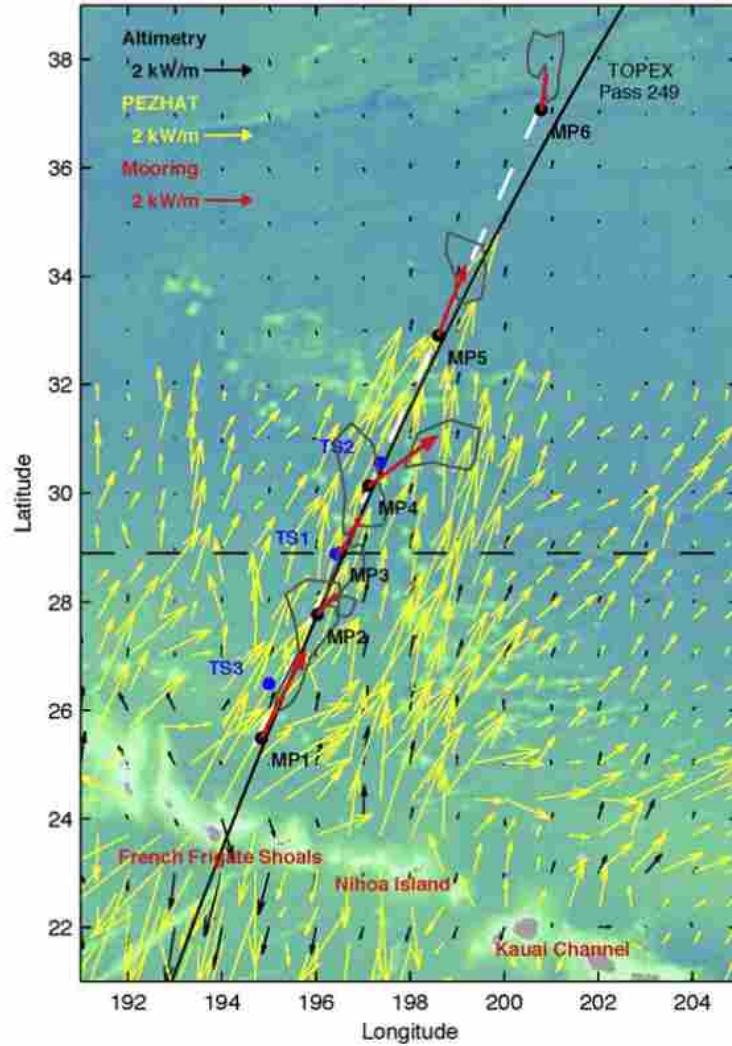


Figure 1.4: Mooring, measurement, and ship locations of the R/V Revelle as part of the IWAP experiment [16].

contrary to what the researchers had originally hypothesized from idealized theoretical models and simulations.

1.5.2 Experimental techniques

This section will detail three experimental techniques: schlieren, synthetic schlieren, and particle image velocimetry. Although each of these methods has been used for a wide variety of research topics including visualization of hot supersonic jets [52], the temperature of a natural gas

flame [53], and turbomachinery [54], this work will focus on how these methods have been used previously to investigate internal waves.

Schlieren Imaging

While the first experiments on internal waves were performed by Görtler in 1943 [55], the most well known experiments were performed by Mowbray and Rarity using a schlieren system [56]. Schlieren imaging capitalizes on the fact that variations in the density of a fluid are directly related to variations in the index of refraction. An example of a classical schlieren setup is shown in Fig. 1.5. Original schlieren imaging focused parallel light sources with either parabolic mirrors or lenses through an experimental field and then on to a knife edge. The variations in density and index of refraction would bend certain light rays below the knife edge, and thus a dark spot would be seen on the final image plane. If the density fluctuated in the opposite direction, the light rays would still pass through and could be seen in the final image [57]. This created an excellent qualitative way to view fluctuating density flows. Mowbray and Rairty used a schlieren system to visualize the internal waves generated by an oscillating cylinder in a constant N fluid which creates internal waves that propagate in four directions creating what is known as St. Andrew's Cross. By varying the oscillation frequency, the angle of the wave beams varied. Their experiments are well known for matching the linear theory of internal waves in predicting the 90° angle of separation between the group velocity and phase speed.

Synthetic schlieren

In an effort to improve the quantitative results of standard schlieren imaging, a novel technique known as synthetic schlieren was created [58]. The term synthetic schlieren is most commonly used in the internal waves community, but a similar technique known as Background Oriented Schlieren (BOS) [59] is frequently used in other fields that focus on varying densities in flows such as jets [59], supersonic air jets [60], and wildfires [61]. Both methods follow the same

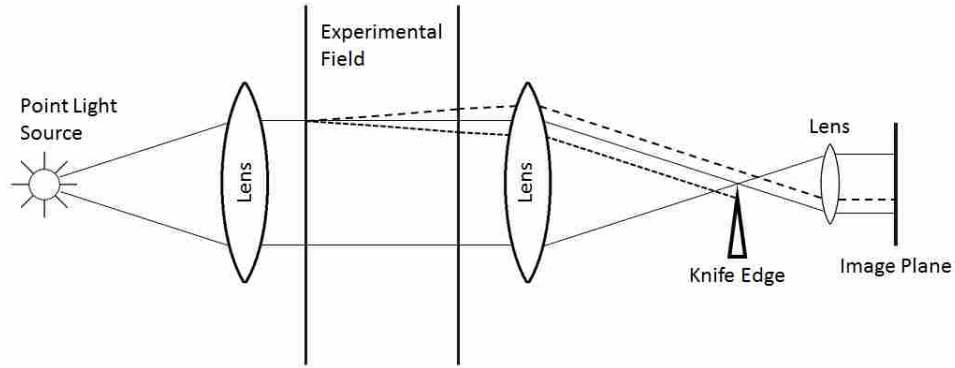


Figure 1.5: Using parallel light rays and an array of lenses, density fluctuating flows can be visualized as the variations in density caused variation in the index of refraction. The knife edge on the right side of the figure would prevent lights rays which were bent below the edge to be seen, thus causing dark spots to be seen on the imaging lens. (Figure created by Jonathan Stoddard)

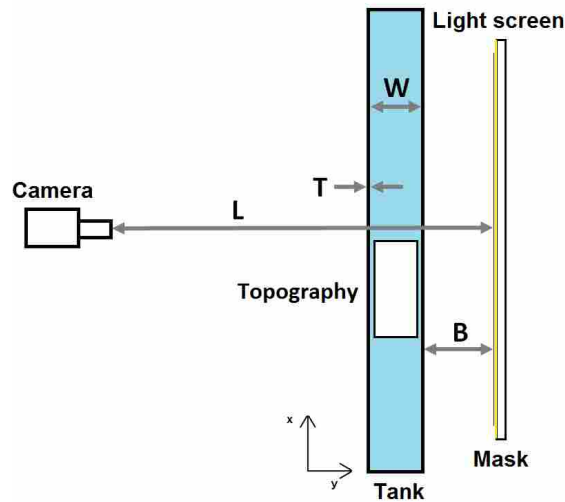


Figure 1.6: A top down view of the experimental arrangement for a synthetic schlieren image set up. The important lengths noted here are necessary to find the change in the index of refraction and are used in Equations (1.4) and (1.5). Notice that the y-coordinate follows the camera line of sight while the x direction is parallel to the length of the tank. The z-direction is not shown here, but follows the height of the tank.

principle as schlieren imaging, using the relationship between a varying index of refraction and the corresponding variation in density.

Synthetic schlieren uses a simple experimental setup shown in Fig. 1.6 to find excellent quantitative and qualitative data for two-dimensional flows. A camera is placed in front of the

experiment and is focused on a lighted mask behind the experiment. The mask may consist of horizontal lines or a random dot pattern as seen in Fig. 1.7(a). By comparing the original, undisturbed image to those taken during the experiment (Fig. 1.7(b)), an apparent shift of the dots (or lines) is recorded by the camera, although this variation is not visible to the naked eye. By calculating this shift, it is possible to calculate the change in the index of refraction, which is proportional to the change in the density. Dalziel et. al [58] found that the movement of the light rays could be described by Eqs. (1.4) and (1.5), which relate the distance of each medium and their respective index of refraction through which the dots are being viewed to the apparent mask displacement in the x (Δx) and z (Δz) directions.

$$\Delta x = -\frac{1}{2} \left[\frac{L - B - \left(1 - \frac{n_{\text{air}}}{2n_0}\right)W - 2\left(1 - \frac{n_{\text{air}}}{2n_{\text{wall}}}\right)T}{L - \left(1 - \frac{n_{\text{air}}}{n_0}\right)W - 2\left(1 - \frac{n_{\text{air}}}{n_{\text{wall}}}\right)T} \right] W \left(W + 2\frac{n_0}{n_{\text{air}}}B + 2\frac{n_0}{n_{\text{wall}}}T \right) \frac{\beta}{\rho_0} \frac{\partial \rho'}{\partial x} \quad (1.4)$$

$$\Delta z = -\frac{1}{2} \left[\frac{L - B - \left(1 - \frac{n_{\text{air}}}{2n_0}\right)W - 2\left(1 - \frac{n_{\text{air}}}{2n_{\text{wall}}}\right)T}{L - \left(1 - \frac{n_{\text{air}}}{n_0}\right)W - 2\left(1 - \frac{n_{\text{air}}}{n_{\text{wall}}}\right)T} \right] W \left(W + 2\frac{n_0}{n_{\text{air}}}B + 2\frac{n_0}{n_{\text{wall}}}T \right) \frac{\beta}{\rho_0} \frac{\partial \rho'}{\partial z} \quad (1.5)$$

In these equations, L is the distance between the camera and the light mask, T is the thickness of one side of the tank, B is the distance from the outside of the tank to the light mask, and W is the interior width of the tank as shown in Fig. 1.6. Here, density has been defined as $\rho = \rho_0 + \bar{\rho} + \rho'$, where ρ_0 is the background or reference density of the fluid, $\bar{\rho}$ is the stratification profile, and ρ' is the perturbation density, or the small variations in the density caused by a disturbance in the flow. The index of refraction for air and the wall of the experimental tank are represented with η_{air} and η_{wall} , respectively, and are assumed to be constants. η_0 is the reference index of refraction for the experimental fluid and is also needed for the definition of β , where $\beta = (\rho_0/n_0)(\partial n/\partial \rho)$. Although the index of refraction of the fluid will vary with the density, the actual derivative of $\partial n/\partial \rho$ can be considered constant for water. Thus, with $\rho_0 = 1000 \text{ kg/m}^3$ as the reference density for water, $\beta \approx 0.184$. These two equations assume that the experiment is two dimensional so the variation in the y direction is negligible. Each equation represents the distance the mask has shifted between images and can be used to solve for the rate of density change in the x and z directions,

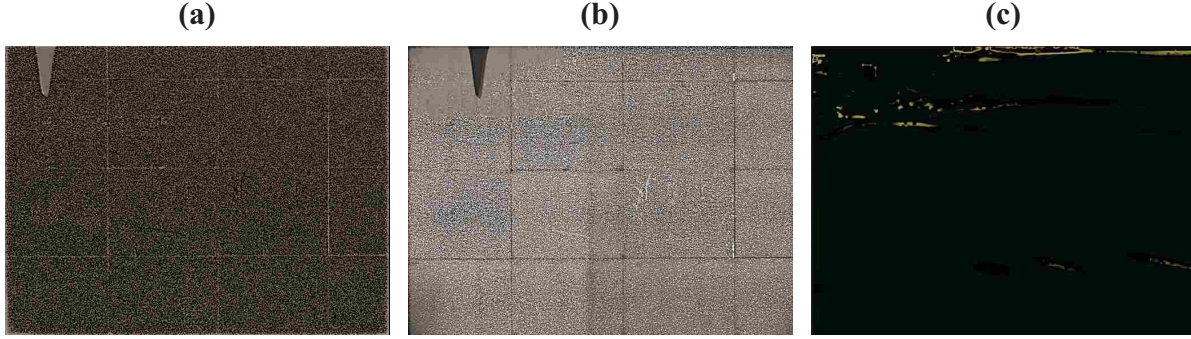


Figure 1.7: Digiflow images of the (a) undisturbed water, (b) experiment in progress, and (c) processed data of $\partial\rho'/\partial z$.

represented by $\partial\rho'/\partial x$ and $\partial\rho'/\partial z$ respectively. Full details on this derivation are given by Dalziel et al. [58].

Results from the comparison of Figs. 1.7(a) and (b) using Eqs. (1.4) and (1.5), is shown in Fig. 1.7(c). Colors in the image correspond to $\partial\rho'/\partial z$ and thus crest and troughs of the waves are represented by changing colors. Note here the waves are generated at the topography and then propagate down and to the right. Vertical and horizontal wavelengths can be seen as the thickness of the changing color beam. Wave packet size is the entire region (changing color) with waves.

PIV

Particle Image Velocimetry (PIV) is an experimental technique used to study a variety of fluid flows [62], including internal waves [63]. With PIV, neutrally buoyant particles are seeded into a fluid flow and tracked to estimate the velocity field in the fluid [62]. PIV can be used to study both internal and evanescent waves [64]. To characterize the decay of evanescent waves, Paoletti and Swinney [64] used PIV to validate numerical simulations of internal waves entering an evanescent region. Looking at both evanescent and propagating internal waves, Paoletti et al. [18] used PIV to estimate radiated power of internal waves formed from an evanescent region and their results match very well with their numerical simulations.

Inherent to all stratified flow experiments is that the index of refraction of the fluid being studied will vary as waves move through the fluid. While SS uses this in order to define variations

in N^2 , a varying index of refraction could cause inaccurate particle tracking in PIV. To address this problem, Dalziel et al. [63] used simultaneous SS and PIV experiments in a stratified flow. SS data was used to define the density field while PIV defined the velocity field. Corrections were made to the velocity field based on the SS data, and they found that particle movement caused by the changing index of refraction is small, but not completely negligible. Using SS density field data is important to correct PIV data when there are significant variations in the density field [63].

1.5.3 Simulations

Along with experiments, numerical simulations, which can be used to solve the full equations of wave motion, are often used to study internal waves [11]. Simulations can be performed in two or three dimensions [25, 65] and allow for solving complex flows without some of the restrictive assumptions needed to solve analytical equations. Although considerable effort has been made to model internal waves in a variety of applications [11], since this work focuses on two-dimensional waves in varying stratification conditions, prior work in this area is reviewed only.

Using simulations, Sutherland found that internal gravity wave packets, as opposed to internal wave beams, can transmit energy through an evanescent level through the wave-induced mean flow associated with the start and end of waves [66]. Effects of finite amplitude on internal wave propagation in an abruptly changing N profile is explored numerically in the Boussinesq approximation, which assumes that a density perturbation is important when multiplied by gravity [4, 67]. Another extreme change in N occurs in the ocean at the pycnocline, where the generation of harmonics from approaching internal wave beams was shown to be a strong function of pycnocline thickness using fully nonlinear direct numerical simulations [68]. Turning depths in exponential N stratified Boussinesq flows have been analyzed numerically and showed relatively good agreement with nonlinear theory [64]. Paoletti et al. [18] used 2-D numerical simulations in the Boussinesq approximation to study wave generation by tidal flow over primarily Gaussian topographies in exponential N profiles and found that internal waves formed directly from tidal flow over topography had greater radiated power than internal waves formed from evanescent waves.

1.5.4 Theory

Theoretical methods to analyze internal wave generation and propagation must use a variety of assumptions if an exact solution is to be found. These assumptions may include that the flow is inviscid, that waves have small amplitudes, that the wave amplitudes, wavenumber, frequency, or N may slowly vary with wavelength, or that there are no wave packets (infinite waves). The Boussinesq approximation, which assumes that the vertical variation in density is small relative to the background density [4], is also frequently used. Many, or all, of these may be used to more quickly analyze wave propagation. Ray theory, a linear method, represents one of the simplest mathematical methods which results in tracing the path of wave energy. It has been used throughout the ocean and atmosphere for waves propagating through varying velocity and N profiles with great success [69–73]. Part of ray theory includes the Wentzel–Kramers–Brillouin (WKB) approximation, wherein N and the amplitudes of wave velocity are allowed to vary slowly only in the vertical direction [4, 5, 74]. Other analytical methods have been used for a plethora of internal wave dynamics analysis: linear theory of wave generation over weak two-dimensional topography [75]; Green’s function methods for wave generation by a moving point mass source [76]; small-amplitude, inviscid flow analysis in the Boussinesq approximation for wave propagation through a sharp N profile [77]; linear theory for a two-dimensional plane wave at an N interface [78]; and linear theory for two dimensional, small amplitude wave beam transmission and reflection [79]; to name a few. In addition, although significant assumptions must be made for these exact solutions, each result has contributed to our understanding of internal wave generation and propagation in variable stratifications and flow situations.

1.6 Current research

As previously described, internal wave research covers many areas from the generation of internal waves to their propagation and interactions, to their ultimate breaking and dissipation affecting oceanic mixing and circulation. Given the wide variety of research possibilities, this section will cover the current research directly applicable to the work presented in the upcoming chapters.

These topics include the effect of varying stratifications on wave propagation, the influence of topography shape on wave generation, and the influence of evanescent waves and turning depths on wave energy.

1.6.1 Varying stratifications

Significant research has been accomplished in both varying stratifications and internal waves approaching evanescent regions. Pedlosky [74] used linear theory and the WKB approximation to account for wave propagation in non-uniform stratifications in propagating regions. For multi-layered stratification profiles, internal waves have been shown to tunnel through an evanescent region of fluid as is shown in Fig. 1.8, and the transmission coefficient of incident internal wave energy across the evanescent region can be calculated with linear theory [80]. Further work on tunneling includes smooth changes in natural frequency and the inclusion of a shear flow [77, 81]. Gregory and Sutherland [79] found that the transmission coefficient was larger for internal waves that tunneled through a weakly stratified region instead of a well-mixed region. Mathur and Peacock [78] extended this work for transmission and reflection of internal waves and varied the scale of the transitional region. They found that a wave beam will adjust to a varying stratification and be either amplified or diminished based on the characteristics of the stratification, as long as the changes in the stratification occurred over a sufficiently large distance. Rapid changes in stratification led to wave scattering. Sutherland [82] found an analytical solution for the transmission coefficient for an arbitrary number of density staircases that are all equal in size, and also used simulations to calculate the transmission coefficient for uneven length staircases. Sutherland found, similar to the results of Ghaemsaidi et al. [83], that density staircases can act as a filter allowing only internal waves with long horizontal wavelengths and high frequencies to completely pass through. Paoletti and Swinney [64] used exponential density profiles and stratifications to investigate internal wave reflection and transmission from a turning depth. Their results compared well with the viscous theory of Kistovich and Chashechkin [84] which allowed for arbitrary stratifications. Each of these cases assumed that internal waves were formed in a propagating region

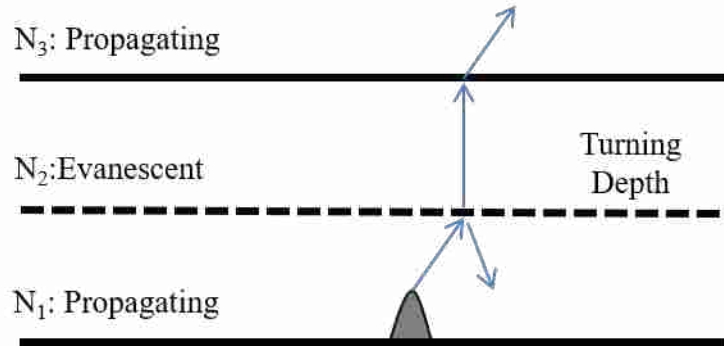


Figure 1.8: An example of internal waves tunneling through and reflecting off of an evanescent region.

and then pass into an evanescent region, but did not investigate waves formed in an evanescent region passing into a propagating region.

1.6.2 Evanescent waves and turning depths

Although linear theory indicates that evanescent waves can become propagating internal waves [5], this has not been a topic of significant research. This is because it was not known if there were locations in the ocean that would generate these types of internal waves or if they would be important because of the exponential decay of evanescent waves. This changed because of the data collected in the World Ocean Circulation Experiment (WOCE) which conducted surveys of hundreds of oceanic locations and collected thousands of casts to collect oceanic data from 1990-1998 [50]. Using data from WOCE, King et al. [19] calculated the natural frequency in the ocean for over 18,000 casts from all of the WOCE data in an effort to find oceanic turning depths. They found that while turning depths were not prevalent throughout the entire ocean, they are often found in locations where the depth of the water is greater than 5 km. Based on the work of King et al., Paoletti et al. [18] used experiments and simulations to investigate the radiated power of internal waves generated from evanescent waves formed over topography. Based on an iterative averaging scheme, they found that they could match their results with those of the analytical theory of Kistovich and Chashechkin [84]. Paoletti et al. found that that radiated power of the evanescent to propagating waves was much weaker than the internal wave power.

1.6.3 Topography shape

When investigating topographically generated internal waves, topographies are frequently divided into different categories based on criticality. Criticality is defined as

$$\varepsilon = S_{\text{top,m}}/S_{\text{wave}} \quad (1.6)$$

where $S_{\text{top,m}}$ is the maximum topographical slope and $S_{\text{wave}} = \sqrt{\omega^2/(N^2 - \omega^2)}$ is the slope of the generated waves (assuming no rotation). Topographies in propagating regions are considered subcritical ($\varepsilon < 1$), critical ($\varepsilon = 1$), or supercritical ($\varepsilon > 1$). Energy of internal waves generated from subcritical topography increase with increasing ε , until $\varepsilon = 1$, where linear theory is no longer applicable and wave beams overturn [39]. $\varepsilon > 1$ causes internal wave scattering [40]. Internal wave energy has been estimated for subcritical topography for constant stratifications [29], depth varying stratifications, and a finite depth ocean [75, 85]. Work has also been done for supercritical topographies both experimentally and with a viscous linear theory model [86, 87]. However, for evanescent waves, ε is undefined because S_{wave} is imaginary in an evanescent region. Paoletti et al. [18] used a novel technique to define an effective height of the topography, based on both the slope of the topography and the stratification profile. Using this, they could estimate radiated power for internal waves generated from evanescent waves formed from topography. They found that internal wave power is significantly decreased in the presence of a turning depth. Their results compared well with previous research on topographically generated internal waves and varying stratifications.

Along with investigations of topographical slope, researchers have investigated the influence of topography shape. Paoletti et al. [18] included a knife-edge topography, four types of Gaussian topographies, and a complex topography (multiple peaks and varying slopes) in their investigations of radiated internal wave power and found that increasing the maximum slope of the topography decreased in the radiated power. Although these topographies were all two-dimensional, three-dimensional topographies have also been used to investigate topographies that more realisti-

cally represent oceanic topographies [88,89]. Another aspect of topography shape is the number of peaks and the influence of the distance between peaks. Zhang and Swinney [90] found that successive peaks close to one another created a “virtual seafloor”, such that the internal waves generated had less power than would have been expected based on the size of the topographies due to mixing pockets between the peaks decreasing the effective amplitude of the topography.

1.7 Current research needs

While significant work has been accomplished on internal waves, there are still many new research areas to be studied as new knowledge of realistic oceanic scenarios are uncovered. Specifically, new interest in propagating energy from internal waves generated from common evanescent regions will be explored. The influence of topography shape and location, the effects of variable stratification, and multiple methods will be used to study evanescent to propagating internal waves.

Although the influence of topography shape has been well documented for topographically generated internal waves, the same is not true for evanescent waves. Here, I will investigate the influence of topography slope, height, shape, and relative location to the turning depth on the kinetic energy of both evanescent and internal waves.

King et al. [19] found that many locations in the ocean can be described with exponential density profiles, but it is common for researchers to average the density variation, and therefore the natural frequency, when studying internal waves. Whether or not this averaging will produce accurate results when applied to an evanescent region has not been discussed previously and will be part of my investigations. This will be explored by using a variety of density profiles which create varying stratifications.

Finally, there are many methods for studying internal waves, and each has different advantages and disadvantages. To understand which method would be appropriate for various situations, this work will present results from linear theory, two experimental methods, and numerical simulations to study evanescent and propagating internal waves, and provide guidelines on when each

method is best used. In addition, a direct comparison of kinetic energy for evanescent and internal waves based on two experimental methods, PIV and synthetic schlieren, will be made.

Details and background on the various methods used to study evanescent and internal waves in this work is given in Chapter 2. Chapter 3 is work previously published in the journal *Physical Review Fluids* and compares a linear theory model to synthetic schlieren (SS) experiments. Kinetic energy predicted by the model and estimated by the SS experiments are further compared to numerical simulations that were performed at Northeastern University in Chapter 4. Chapter 4 has been submitted to the journal *Experiments in Fluids*. In Chapter 5, the effects of topography shape and density profile on kinetic energy density investigated. Chapter 6 introduces particle image velocimetry (PIV) experiments and explores under what circumstances PIV and SS can be used to accurately describe the kinetic energy density of evanescent and internal waves. A summary of the work presented throughout this dissertation is provided in Chapter 7.

CHAPTER 2. METHODOLOGY

To investigate the kinetic energy density of evanescent and internal waves, three methods are used: a linear theory model, two types of experiments (synthetic schlieren and PIV), and numerical simulations. For all of these methods except PIV, the Navier-Stokes equations must be solved to calculate the velocity field of the generated waves. A general description of these equations will be given here, with more complete details in each section of this chapter. In addition, the domain of the experiments and theory is a that of a flipped ocean, meaning the topography is oscillated at the top of the domain, creating waves moving vertically downward. For the stratifications described throughout this work, there is no difference between a wave propagating up (from a topography at the bottom of the domain) or down [28].

2.1 Navier-Stokes equations

There are many forms of the Navier-Stokes (NS) equations, based on the underlying assumptions of the fluid flow. For internal waves, it is assumed that the flow is inviscid and incompressible, and that the density perturbation is only important when multiplied by gravity. In addition, the Boussinesq approximation, which assumes that the vertical variation in density is small relative to the background density [4], will be used here. Density is broken down into three parts with the reference density of the fluid (ρ_0), the stratification profile ($\bar{\rho}$), and the wave perturbation density (ρ'). Combining these terms defines the total density

$$\rho = \rho_0 + \bar{\rho}(z) + \rho'(x, y, z) \quad (2.1)$$

The Boussinesq approximation is valid when $\rho/\rho_0 \sim 1$, which is true for all cases presented in this work. With the given assumptions, the x , y , and z momentum NS equations, along with incompressibility and continuity can be written as

$$\rho \frac{Du}{Dt} = \frac{-dP}{dx} \quad (2.2)$$

$$\rho \frac{Dv}{Dt} = \frac{-dP}{dy} \quad (2.3)$$

$$\rho \frac{Dw}{Dt} = \frac{-dP}{dz} - \rho g \quad (2.4)$$

$$\frac{D\rho}{Dt} = 0 \quad (2.5)$$

$$\nabla \cdot \vec{V} = 0 \quad (2.6)$$

By assuming that u , v , and w are small, and defining the pressure as $P = \bar{P} + P'$, the above equations can be simplified and put into linear form such that

$$\frac{\partial u}{\partial t} = \frac{-1}{\rho_0} \frac{\partial P'}{\partial x} \quad (2.7)$$

$$\frac{\partial v}{\partial t} = \frac{-1}{\rho_0} \frac{\partial P'}{\partial y} \quad (2.8)$$

$$\frac{\partial w}{\partial t} = \frac{-1}{\rho_0} \frac{\partial P'}{\partial z} - \frac{\rho' g}{\rho_0} \quad (2.9)$$

$$\frac{\partial \rho'}{\partial t} + w \frac{\partial \bar{\rho}}{\partial z} = 0 \quad (2.10)$$

$$\frac{\partial u}{\partial x} + \frac{\partial v}{\partial y} + \frac{\partial w}{\partial z} = 0 \quad (2.11)$$

Equations (2.9) and (2.10) can be combined to define the natural frequency N such that

$$N^2 = \frac{-g}{\rho_0} \frac{d\rho}{dz} \quad (2.12)$$

The previous equations with their five unknowns can be rearranged to form one equation with w , t , and N as

$$\frac{\partial^2}{\partial t^2} (\nabla^2 w) + N^2 \nabla_{\text{H}}^2 w = 0 \quad (2.13)$$

where ∇_{H}^2 is the Laplace operator in the horizontal directions of x and y . The solution to Eq. (2.13) is a wave form solution with

$$w = w_0 \exp[i(kx + ly + mz - \omega t)] \quad (2.14)$$

where w_0 is the wave amplitude, k , l , and m are the wavenumbers in the x , y , and z directions, and ω is the frequency of the wave. This equation will be further simplified in this work by assuming two-dimensional waves and thus $l = 0$.

For evanescent waves, the form of the solution is different as the vertical wavenumber m must be imaginary in order to account for the decay of the waves. A standard form for the velocity of evanescent waves for regions where N is constant can be written as

$$w = w_0 \exp[i(kx + ly - \omega t)] \exp(mz) \quad (2.15)$$

Equations 2.14 and 2.15 will be used (with some variations) in the analytical model presented next, the synthetic schlieren experiments in Sec. 2.3.2, and the numerical simulations in Sec. 2.4.

2.2 Analytical model

A linear, Boussinesq, 2D model was used to calculate the kinetic energy that passes from the evanescent region through the turning depth and into the propagating region, accounting for the exponential natural frequency profile. Linear theory is a good approximation for the cases presented here because $u_{\text{top}}/(\omega W) < 1$ [75], where u_{top} is the average velocity of the topography, and W is the width of the topography. The WKB approximation, which assumes that wave amplitudes vary slowly in z , is also applied [74]. This approximation is valid away from the turning depth where $N^2 \gg \lambda_z(\partial N^2/\partial z)$ [74]. In the following sections I will analytically calculate kinetic energy in the evanescent region and the propagating region, and then demonstrate how the two regions can be matched at the turning depth where the WKB approximation is not valid. Because the waves are first generated within the evanescent region, this region will be denoted with the sub-

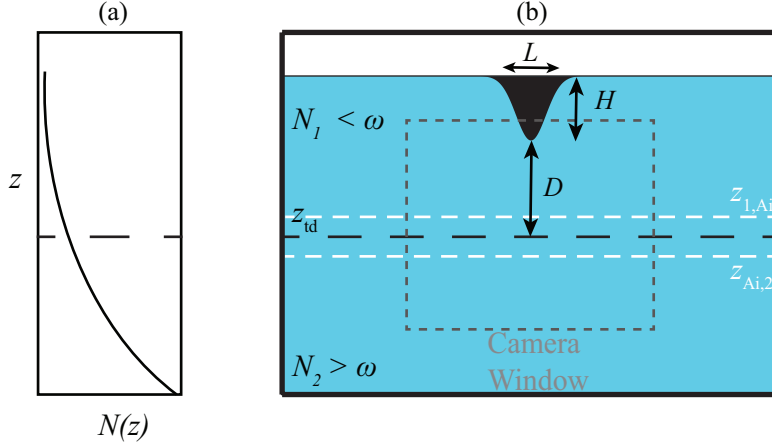


Figure 2.1: An example of the natural frequency profile in the tank (a) shown relative to the experimental setup (b).

script 1, with a subscript 2 for the propagating region. A subscript “Ai” will be used for the Airy region which links the evanescent and propagating region. Details on the size of this region are provided in Sec. 2.2.3. Within each region the vertical velocity (w) is defined and the horizontal velocity (u) is found from the 2D continuity equation

$$\frac{\partial u}{\partial x} + \frac{\partial w}{\partial z} = 0 \quad (2.16)$$

Figure 2.1 provides an example of the natural frequency profile (a) and the domain for the experiments and linear theory (b). In Fig. 2.1(b), evanescent and propagating regions are labeled as $N_1 < \omega$ and $N_2 > \omega$, respectively. The excursion length (L), height of the topography (H), and distance between the topography and the turning depth (D) are indicated. The grey dashed box shows the approximate location of the camera window, while the beginning and end of the Airy region ($z_{1,Ai}$, $z_{Ai,2}$) is shown with white dashed lines (see Sec. 2.2.3).

With both u and w defined, the kinetic energy is defined as

$$KE = u^2 + w^2 \quad (2.17)$$

for comparison with experiments. Each case is reproduced with a linear theory analysis using the given experimental parameters; however, no data from the synthetic schlieren experiments are needed to initialize the theoretical analysis.

2.2.1 Evanescent region

The vertical velocity in the evanescent region varies since N is a function of height, which affects the vertical wavelength. First, in the evanescent region, q is defined as

$$q^2(z) = k^2(1 - N^2(z)/\omega^2) \quad (2.18)$$

where $m = iq$ is the imaginary vertical wavenumber in the evanescent region. Following the work of Pedlosky [74] in a propagating region with $N = f(z)$, θ_1 is introduced for the evanescent region:

$$\theta_1(z) = \int_{z_{1,0}}^z q dz \quad (2.19)$$

$A_{1,0}$ and $q_{1,0}$ are defined at a reference height $z_{1,0}$ which varies based on the shape of the topography used. The reference location will change the overall kinetic energy throughout the evanescent and propagating region. However, if the kinetic energy is normalized by the energy at the tip of the topography, $z_{1,0}$ will not change the relative energy. Using q and θ , the vertical velocity can be defined as

$$w_1(x, z, t) = A_1 \exp[i(kx - \omega t)] \exp(\theta_1) \quad (2.20)$$

$$A_1(z) = A_{1,0}/(q/q_{1,0})^{1/2} \quad (2.21)$$

Assuming a slip condition at the topography [34], the wave velocity can be calculated by matching the velocity of the topography to Eq. (2.20). Using continuity [Eq. (2.16)], the horizontal

velocity is computed as

$$u_1(x, z, t) = \frac{-w_1}{ik} \left[\frac{-dq/dz}{2q} + q \right] \quad (2.22)$$

The kinetic energy in the evanescent region is calculated using $KE_1 = u_1^2 + w_1^2$.

2.2.2 Propagating region

Following the work of Pedlosky [74] and solving the NS equations in Sec. 2.1, velocities in the propagating region, assuming a varying natural frequency, are defined by

$$w_2(x, z, t) = A_2 \exp(i(kx - \omega t + \theta_2)) \quad (2.23)$$

$$u_2(x, z, t) = \frac{-w_2}{k} \left[\frac{-dm/dz}{2im} + m \right] \quad (2.24)$$

$$A_2(z) = A_{2,0}/(m/m_0)^{1/2} \quad (2.25)$$

$$\theta_2(z) = \int_{z_0}^z m dz \quad (2.26)$$

$$m^2(z) = k [N(z)^2/\omega^2 - 1] \quad (2.27)$$

where continuity has again been used to define u_2 . Note that the subscript 2 refers to the propagating region. The kinetic energy in the propagating region is calculated by $KE_2 = u_2^2 + w_2^2$. In both the evanescent and propagating regions, the amplitude, A , of the velocities varies with height. This is due to the varying natural frequency, which causes the varying vertical wavenumber, and is necessary to conserve energy [74].

2.2.3 Airy integral matching

As the evanescent wave moves from the topography toward the turning depth, the WKB assumptions are violated near the turning depth because $N^2 \sim \lambda_z(\partial N^2/\partial z)$. This also causes q to decrease to zero, creating a discontinuity at the turning depth as the velocity amplitudes increase towards infinity. In order to prevent this discontinuity and predict the correct amplitude of the prop-

agating velocity, the Airy function can be used in this region [91,92] if the WKB approximation is extended past where it is valid [81]. Although the equation for w_2 has been defined, the amplitude $A_{2,0}$ was not and needs to be derived from w_{Ai} , or the vertical velocity in the Airy region. This section will describe how the Airy region connects the velocities of the evanescent and propagating region.

Following Lighthill [91], the vertical wave velocity with the Airy integral is

$$w_{\text{Ai}}(x, z, t) = Q_{0,w} \text{Ai}(\beta^{1/3}z - \beta^{1/3}z_{\text{td}}) \exp[i(kx - \omega t)] \quad (2.28)$$

where β is defined by $\beta = m^2/(z_{\text{td}} - z)$. The amplitude of $Q_{0,w}$ is found by matching Eq. (2.28) to Eq. (2.20) at $z_{1,\text{Ai}} = z_{\text{td}} + 0.01(2\pi/\bar{q})$, or 1% of the average vertical wavelength (λ_z) above the turning depth in the evanescent region. A range of percentages from 0.1% to 10% of λ_z was compared to understand the effect of the locations of the start and end points of the Airy integral. Decreasing the percentage causes a decrease in the average kinetic energy, but the changes of kinetic energy below 1% were minimal, both for the medium and steep topographies. This percentage away from the turning depth should be altered if there is a significant increase in the model domain and may be dependent on the vertical resolution of the model.

Continuity (Eq. (2.16)) and Eq. (2.28) are used to derive the form of the horizontal velocity in the Airy integral

$$u_{\text{Ai}}(x, z, t) = Q_{0,u} \frac{i\beta^{1/3}}{k} \text{Ai}'(\beta^{1/3}z - \beta^{1/3}z_{\text{td}}) \exp[i(kx - \omega t)] \quad (2.29)$$

where Ai' is the first derivative of the Airy function with respect to z .

Above the turning depth, the vertical velocities are set equal such that $w_1 = w_{\text{Ai}}$ at $z = z_{\text{Ai},1}$ and $Q_{0,w}$ is solved. This procedure is repeated for the horizontal velocity with $u_1 = u_{\text{Ai}}$ at $z = z_{1,\text{Ai}}$ to find $Q_{0,u}$. It is assumed that both $Q_{0,w}$ and $Q_{0,u}$ are constant through the Airy integral region as the variation in the natural frequency is small over the small change in height. $A_{2,0}$ is calculated

by setting $w_{\text{Ai}} = w_2$ at $z_{\text{Ai},2} = z_{\text{td}} - 0.01(2\pi/\bar{m})$, and continuity is used to define u_2 from w_2 , as shown in the previous section.

2.2.4 Accuracy of analytical model

The importance of the terms $(-dq/dz)/2q$ and $(-dm/dz)/2im$ in Eqs. (2.22) and (2.24), respectively, will be explored in this section. These higher order terms, which are not usually found in the horizontal velocity, appear because the amplitude of the velocity is a function of depth. When assuming that the amplitude, natural frequency, and vertical wavenumbers vary slowly, these variations (dq/dz and dm/dz) are included, and thus are neglected. This assumption breaks down near the turning depth, due to the rapid variation of q and m in that region, indicating they should remain in the equations for velocity. However, the use of the Airy integral to connect the evanescent and propagating regions does not include these terms. Figure 2.2 depicts the two different scenarios with height on the ordinate and kinetic energy on the abscissa. The dashed line indicates the location of the turning depth with the evanescent region above the turning depth and the propagating region below. The horizontal dash-dot line below the turning depth marks the height corresponding to a 10% increase in N relative to the excitation frequency of 0.95 s^{-1} . Kinetic energy with the higher order terms included is indicated by the solid line, while the dotted line represents kinetic energy when these terms are neglected. For both scenarios, kinetic energy begins at a maximum at the top of the figure and then decreases as the wave moves through the evanescent region. An increase in energy is seen near the turning depth, with a larger increase when the higher order terms are included. Below the turning depth, both scenarios decrease in kinetic energy through the propagating region. Away from the turning depth, the kinetic energy collapses to a single line. Each of the 24 experimental cases in Ch. 3 were compared with and without the higher order terms and the average error from the region between the end of the Airy integral and a 10% increase in N is 20%. However, the majority of this error is due to the increase in amplitude at the end of the Airy integral. Neglecting this increase and again comparing the kinetic energy, the average error is

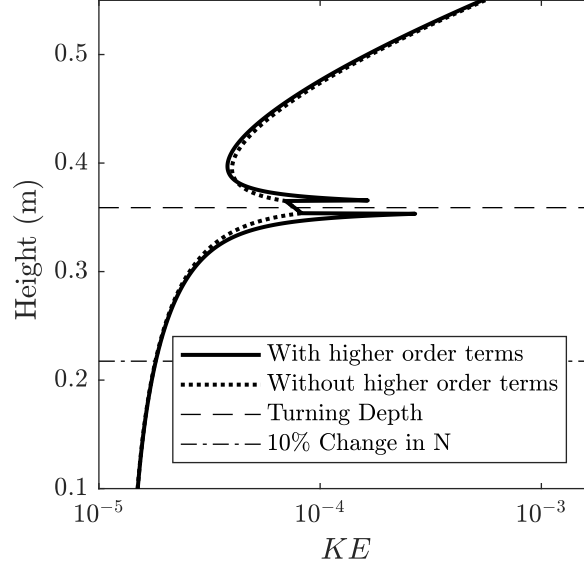


Figure 2.2: The kinetic energy as a function of height is shown for the scenarios of including or excluding dq/dz and dm/dz when calculating the horizontal velocity. The turning depth is shown by the dashed horizontal line and the dash-dot line indicates the height of a 10% increase in N from the turning depth.

13%. The higher order terms in this work will be ignored, but it may be necessary to retain them in future work if more rapid changes in natural frequency are of interest.

An example of the MATLAB file used to calculate the kinetic energy in all three regions is given in Appx. B and includes code for different topography shapes and different density profiles. To use the MATLAB files, an equation describing the motion of the topography, based on topography shape, as a function x and t is required. For example,

$$z_{\text{top}}(x, t) = H \exp \left[\frac{-(x - L \sin \omega t)^2}{B^2} \right] \quad (2.30)$$

defines the equation of motion for a Gaussian topography. Assuming a slip condition at the topography [34], the wave velocity can be calculated by using the time derivative of Eq. (2.30) and setting it equal to Eq. (2.20) such that $dz_{\text{top}}/dt = w_1(x = B, t = 0)$. Here, the location $x = B$ as a matching condition is chosen arbitrarily. Although the matching location does change the absolute value of kinetic energy, it does not affect normalized values. Currently a topography shape that can be defined analytically can be used in the model.

2.3 Experimental processes

2.3.1 Tank preparation

This section will outline the steps to create a stratified salt water mixture in an experimental tank as well as how to setup and control topography which oscillates on a track. These processes remain unchanged regardless of the experimental method used after the stratification is created.

Filling the tank

The experimental tank is an acrylic tank that is 2.45 m long, 0.15 m wide, and 0.91 m tall and is shown in Fig. 2.3. Before filling, cross beams are clamped to the top of the tank to maintain the width of the tank (not shown in Fig. 2.3). Without the cross beams, the tank will bow in the center, which will cause distortions when images are taken during the experimental process. Also before filling, air filter matting, cut to the width of the tank, is placed two layers deep along the bottom of the tank to dampen reflections. A single layer is placed along the width of the tank. Each filter is washed and dried before being placed again in the tank. It is recommended that the filters be replaced every few months as they begin to wear out. Although it is easier to place the track in the tank before placing the cross beams, it can also be placed after the beams are on, as long as two people are doing it together. In general, all process of setup, performing experiments, and cleaning the tank should be done with two people for safety purposes.

The experimental tank is filled with a modified version of the “two-tank” or “double bucket” method described by Hill [93]. Two peristaltic pumps are used to control the flow rate from a salt water and a fresh water bucket separately. The pumps are calibrated by first allowing them to run at high speed for at least 5 minutes to warm up, and then each pump is tested for flow rates at 25, 50, 100, and 175 rpms, with three tests at each speed. Flowrate and voltage input have been previously calibrated and tested to ensure they remain constant. Knowing the desired N profile, the density of the saltwater bucket, and values from pump calibration, conservation of mass is used to define flowrates necessary from each bucket to create N . These flowrates are then converted back



Figure 2.3: An example of a topography attached to the track in the experimental tank. The two buckets used to fill the tank are on the left side, while the lightbox and mask are behind the tank.

to voltages based on the calibration. All calculations are done in MATLAB and then calculated values are input into a LabView program which outputs voltages to the peristaltic pumps. Fresh water and salt water streams are mixed in a T-connection to create the needed density immediately before entering the tank. Although it is necessary for the fresh water and salt water streams to mix to create the required density, it is also important that the flow into the tank does not generate significant mixing with the water already in the tank. To prevent this secondary mixing (which would create a uniform density within the tank), the mixed stream enters the tank through a sponge, effectively spreading out the stream and minimizing mixing. Flow rates are kept low, such that the height of the water of the tank increases at a rate below 15 cm/hr. Higher flow rates cause more mixing in the tank, which is undesirable. The slow filling rate generally means the tank will take 4-6 hours to fill, depending on the desired height of the water.

After the tank is filled, it is left to settle, generally overnight. Density measurements are then taken throughout the tank to find the exact density profile. When density measurements are first taken, the distance between density measurements is 2 to 3 cm. After a set of tests (usually 4), the density is checked again every 5 cm to ensure the density profile has not varied. The values

from the density tests are input into a MATLAB program which interpolates the density for the entire height of the water, $\rho(z)$, and from this the natural frequency can be calculated from Eq. (1.1) and the smoothed density profile (See Appx. B.1.2). A mixed region, or a region of constant density, usually occurs near the surface of the water. Once this region is large enough to interfere with the tests, the tank is emptied and cleaned.

Controlling the topography

All topographies are built with a dovetail on the base which allows for an easy connection between the topography and the track on which the topography oscillates, shown in Fig. 2.3. The current track was built by two undergraduate students, Jordan Freeman and Katie Pusey, specifically to oscillate the topography at a set frequency ω and to allow for quick changes of topography shapes with the dovetail attachment. Three of the topographies in this work are similar lengths of about 20 cm, while the steep topography is only 4.5 cm long. Each topography about 13 cm wide to fit in the tank and also be away from the walls to reduce the influence of viscosity and other edge effects. An ARDUINO controller and small motor are used to run the topography (See Appx. B.2). The code which controls the oscillations takes as inputs the time period (or frequency) and the desired excursion length, L , which is the distance the topography moves in half an oscillation. It is recommended that the actual frequency be tested and adjusted as needed to ensure the correct frequency of the topography based on the needs of the test.

2.3.2 Synthetic schlieren and Digiflow

Figure 2.4 gives a sketch of the experimental setup. Figure 2.4(a) specifically displays the SS setup, showing a side view of the camera, mask, and light box used in SS. The camera focuses on the mask, which is a random patterned of dots illuminated by the light box, and captures the apparent motion of the dots needed for the SS process [58]. Figure 2.4(b) indicates the PIV setup where the front view shows the general location of the laser sheet relative to the topography (See Sec. 2.3.3).

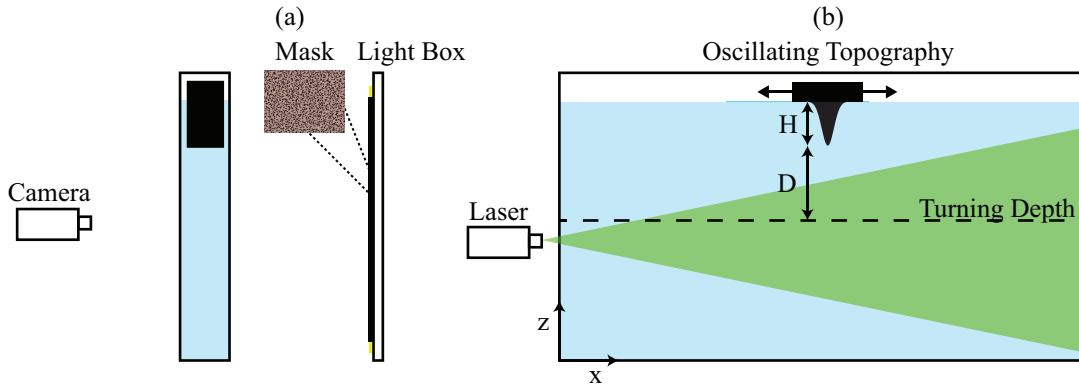


Figure 2.4: Experimental setup of (a) SS and (b) PIV experiments

When running a synthetic schlieren test, the lights in the room must be turned off and the lightbox which illuminates the randomized dot pattern is turned on. The camera needs to be placed at least 3 m in front of the lightbox. This measurement and all of the values listed in Fig. 1.6 need to be recorded in Digiflow, which is a free software used to process the images of all SS tests to calculate the density perturbation field as described in Sec. 1.5.2 [94].

Once the frequency of the topography has been set, two groups of pre-test images are taken. In the first, a ruler is slowly placed into the tank and one picture is taken. In the code used for Digiflow, this picture is referred to as the “with_stick” image and is the reference picture needed to establish the relationship between camera coordinates and real world coordinates. After the ruler is removed and the water has again settled, a background image is taken. This image must exactly match the images taken in the test, meaning that the lights in the room are turned off, the lightbox is on, and the camera is focused. This background image is used as the reference image and is compared against each image in the actual test. If the camera is accidentally bumped after this background image is taken, it must be retaken. A new background image is needed for every set of tests.

Once the pre-test images are taken, the topography is run for at least 15 periods to create a steady-state experiment. The camera runs at 24 fps and should be set for 4320 images, or 3 minutes worth of tests. Because of the large number of images, the computer must have RAM available for

the capturing process, otherwise the images will overload the computer and the test will be lost. After completing a test, the images are saved and then processed on Digiflow.

All experiments are processed at 6 fps, instead of the full 24 fps. The frequency of internal waves is low enough that 6 fps is a good enough resolution to capture the motion of the waves and is fast enough to prevent aliasing. This also saves on disk space, as the 1080 .dfl files (created by Digiflow) for each test are each approximately 32GB. In Digiflow, the “with_stick” image is used to set the length scale of the test, and the background image is used in the Pattern Matching process. Full details of the exact steps are given in Appx. A. One test takes about 4 hours to process.

Estimating kinetic energy

After the tests are processed, kinetic energy can be estimated. Outputs from Digiflow include the x -gradient and z -gradient of density perturbations in a nondimensional form; $\rho_0^{-1}d\rho'/dx$ and $\rho_0^{-1}d\rho'/dz$. The Digiflow files are exported as .dat files, which are then read by MATLAB using the BYU supercomputer, due to the large size of the files. By multiplying $\rho_0^{-1}d\rho'/dz$ by the gravitational constant, g , the data then represents the variation in the natural frequency between the initial undisturbed image and each subsequent image, and an equation similar to Eq. (1.1) is derived:

$$\Delta N^2 = \frac{-g}{\rho_0} \frac{\partial \rho'}{\partial z} \quad (2.31)$$

With ΔN^2 , the kinetic energy of the internal waves can be estimated using the method described by Wunsch and Brandt [20]. By using the continuity equation (Eq. (2.16)) and defining

$$\frac{\partial \Delta N^2}{\partial t} = -\frac{\partial (N^2 w)}{\partial z} \quad (2.32)$$

Wunsch and Brandt used the WKB approximation to estimate kinetic energy. Internal wave velocities and the natural frequency are defined as planar waves multiplied by slowly varying amplitudes:

$$u(x, z, t) = \int \tilde{U} \exp[i(kx + mz - \omega t)] dk d\omega \quad (2.33)$$

$$w(x, z, t) = \int \tilde{W} \exp[i(kx + mz - \omega t)] dk d\omega \quad (2.34)$$

$$\Delta N^2(x, z, t) = \int \Delta \tilde{N}^2 \exp[i(kx + mz - \omega t)] dk d\omega \quad (2.35)$$

where \tilde{U} , \tilde{W} and $\Delta \tilde{N}^2$ are Fourier amplitudes. Using Eqs. (2.16) and (2.32), where the derivatives of the amplitudes are assumed negligible, and taking a two dimensional Fourier transform along the horizontal (x) direction and through time (t), Wunsch and Brandt derive

$$KE_2 = \frac{\omega^2 N^2}{k^2(N^2 - \omega^2) + (\omega \partial_z N^2 / N^2)^2} \left| \frac{\Delta \tilde{N}^2}{N^2} \right|^2 \quad (2.36)$$

where $KE = |\tilde{U}|^2 + |\tilde{W}|^2$, k is the horizontal wavenumber, and the subscript “2” indicates the propagating region. Unfortunately, this equation is not valid in the evanescent region because of the exponential decay of evanescent wave amplitudes and imaginary vertical wavenumber. These are accounted for by first using q as defined in Eq. (2.18). The velocities and natural frequency then become

$$u(x, z, t) = \int \tilde{U} \exp(qz) \exp[i(kx - \omega t)] dk d\omega \quad (2.37)$$

$$w(x, z, t) = \int \tilde{W} \exp(qz) \exp[i(kx - \omega t)] dk d\omega \quad (2.38)$$

$$\Delta N^2(x, z, t) = \int \Delta \tilde{N}^2 \exp(qz) \exp[i(kx - \omega t)] dk d\omega \quad (2.39)$$

Following the same methodology described above for Eq. (2.36), evanescent region kinetic energy can be estimated with

$$KE_1 = \left| \frac{-q\omega\Delta\tilde{N}^2}{k(\partial_z N^2 + qN^2)} \right|^2 + \left| \frac{i\omega\Delta\tilde{N}^2}{\partial_z N^2 + qN^2} \right|^2 \quad (2.40)$$

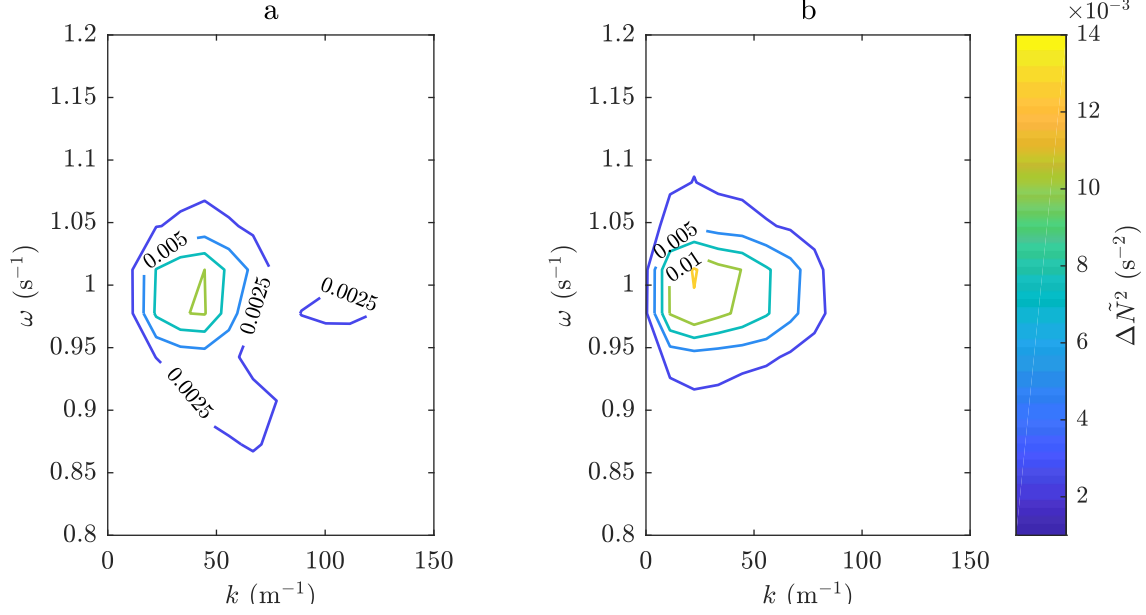


Figure 2.5: Fourier amplitudes of ΔN^2 in the evanescent region (a) and propagating region (b) are shown in contours increasing by 0.0025 for each line. Both figures use the same scaling. The highest value for the contour lines for (a) is 0.01 s^{-2} and for (b) is 0.0125 s^{-2} .

for the evanescent region. As this region is the first region where waves are formed, the kinetic energy is denoted as KE_1 .

To use Eq. (2.36) and Eq. (2.40), the data is sorted into a timeseries of rows representing horizontal slices of the experimental data. Each row is the height of a single pixel. A two-dimensional Fourier transform in x and t is then performed on a timeseries row to create $\Delta \tilde{N}^2$. Results are shown for Case 2 from Tab. 3.1 of Ch. 3 at two different locations in Fig. 2.5 with contours of $\Delta \tilde{N}^2$ plotted against frequency (ω) and horizontal wavenumber (k). In Fig. 2.5(a), the horizontal slice is at $z = 0.4 \text{ m}$, in the evanescent region, while the data in Fig. 2.5(b) is in the propagating region at $z = 0.22 \text{ m}$. The excitation frequency for this case is $\omega_f = 1$. Comparing the two figures, this frequency peak is seen clearly. The expected dominant horizontal wavenumber, k_d , for a specific case is found by defining the horizontal wavelength, λ_x , as the width of the topography plus the excursion length or

$$\lambda_x = W + L \quad (2.41)$$

Then the wavenumber for each case, $k_d = 2\pi/\lambda_x$, gives $k_d = 28.26 \text{ m}^{-1}$ for Fig. 2.5. Although the Fourier amplitudes show a peak near the expected wavenumber and excitation frequency, $\Delta\tilde{N}^2$ amplitudes do not match exactly with the expected frequency and wavelength and there is some energy in nearby frequencies and wavenumbers. The kinetic energy is calculated at all wavenumbers and frequencies for each individual row with its corresponding N^2 and $\partial_z N^2$ values using Eq. (2.36) and Eq. (2.40). Kinetic energy data can then be filtered and averaged over a range of wavenumbers or frequencies as required. Because of the topography and the local turbulence in its wake, the kinetic energy of the evanescent region is only calculated below the tip of the topography.

Sample MATLAB and supercomputer files used to process synthetic schlieren data in MATLAB and on the supercomputer are in Appx. B. An uncertainty analysis of the calculation of $\Delta\tilde{N}^2$ and kinetic energy density is performed with sequential perturbation in Appx. C.

2.3.3 Particle image velocimetry

Particle image velocimetry (PIV) uses lasers to illuminate relatively small particles seeded into a flow in order to map the velocity field of the flow. Experiments in this work all used dual ND:YAG lasers that were fired at a rate of 4.5 Hz with a 90 ms separation between the lasers. Each test was run for over 3.7 minutes, capturing 1000 pairs of images. To perform the PIV experiments, the tank was seeded with titanium dioxide particles, filtered to diameters between $150 \mu\text{m} - 850 \mu\text{m}$. With a large diameter, and relatively large specific gravity of 4.23, some of the larger particles fell quickly to the bottom of the tank, disturbing the water. The settling velocity of the smaller particles was much lower (3 cm/min), and these particles needed almost half an hour to completely fall to the bottom of the tank. Because of this, after seeding, the water was allowed to sit for 5-10 minutes to allow larger particles to fall away and smaller particles to fill the experimental window. Once the water was again quiescent, the motorized track was turned on and the topography oscillated for multiple periods (at least 10) to reach steady state conditions for wave generation.

Tests using (PIV) were always performed following SS tests in order to correlate the two experimental methods. SS images were processed and reviewed to locate areas of strong wave activity in the evanescent and propagating regions of the tank and PIV tests were performed in those regions. A ruler was placed in the tank at these regions, and a correlation picture was taken with both the PIV and SS camera in order to correlate the locations of the two images with each other. Care was taken to ensure that the track was not moved when particles were placed and when the calibration images were taken, thus ensuring that the PIV and SS tests were performed under the same conditions. PIV tests were run immediately after each SS test in the same tank and under the same steady state conditions. A LaVision Imager Intense camera with a resolution of 1376 x 1040 pixels captured the PIV images. The camera was positioned approximately 3.5 m from the front of tank.

After the test, the images were processed with DaVis software using cross-correlation between image pairs with two passes over the experiment window. The first pass used an interrogation window of 64 x 64 pixels with a 50% window overlap. Then the interrogation window was narrowed to 16 x 16 pixels with 75% overlap. DaVis processing generated horizontal (u) and vertical (w) velocities in matrices of 344x256 points. This data was output as .DAT files from Davis and then imported into MATAB. In order to compare the PIV results to those obtained with SS, a 2D Fourier transform in x and t was performed on the velocities and the Fourier amplitudes were used to calculate kinetic energy following Eq. 2.17. Examples of the MATLAB import files and kinetic energy calculation files are shown in Appx. B

2.4 Numerical Simulations

All numerical simulations were performed by Yuxuan Liu and Michael Allshouse at Northeastern University. A summary of their methods is included here as a reference.

A CDP-2.4 algorithm was implemented to perform direct numerical simulations of the Navier-Stokes equations under the Boussinesq approximation. This algorithm is a finite volume solver that uses a fractional-step time-marching scheme [95,96]. This code was chosen because it

has previously been used to study internal waves and has been validated with experiments [18, 86, 88, 97–100]. Simulations provided both the velocity and density perturbation fields.

Equations solved in the 2D simulations result in the total density ρ , pressure p , and velocity \mathbf{u}_T over the domain $x \in [-400, 400]$ cm and $z \in [0, 150]$ cm. Equations include

$$\frac{\partial \mathbf{u}}{\partial t} + \mathbf{u}_T \cdot \nabla \mathbf{u}_T = -\frac{1}{\rho_0} \nabla p + \nu \nabla^2 \mathbf{u}_T - \frac{g\rho}{\rho_0} \hat{\mathbf{z}} + \mathbf{f}_{\text{tidal}} \quad (2.42)$$

$$\frac{\partial \rho}{\partial t} + \mathbf{u}_T \cdot \nabla \rho = \kappa_s \nabla^2 \rho \quad (2.43)$$

$$\nabla \cdot \mathbf{u}_T = 0 \quad (2.44)$$

where $\rho_0 = 1000 \text{ kg/m}^3$ (density of water), $\nu = 10^{-6} \text{ m}^2/\text{s}$ (kinematic viscosity of water at 20°C), and $\kappa_s = 2 \times 10^{-9} \text{ m}^2/\text{s}$ (the diffusivity of NaCl in water). All simulations used the same domain, with a structured grid containing resolutions that ranged from 0.02 to 10 cm, where the resolution was increased for the complex topography cases due to the significant turbulence seen in preliminary tests. Initially, the system was set at rest with an unperturbed density field. The density field matched the density profiles of the experiments. For the simulations, the topography was at the bottom of the domain, with a no slip boundary condition. At the top of the domain, the boundary condition was set to be free slip. Periodic boundary conditions with Rayleigh damping were implemented along the left and right edges to force negligible velocities at both boundaries. In addition, to reduce reflections, a sponge layer was placed at the top of the domain.

Each case was run twice, with an excursion length matching the experimental details, and again with an excursion length 1/10 of the original value. These low amplitude cases were run to investigate the importance of both excursion length and turbulence on the steeper sloped topographies. They will be referred to as the low amplitude or 1/10 amplitude cases. Simulations were performed at temporal resolutions of 0.002 and 0.004 s for the low and high amplitude simulations, respectively. Convergence studies were performed for each topography. Because the system was initially at rest, each case was run for 30 periods to reach a steady state, and then an additional 30 periods which were used in the energy analysis.

Kinetic energy density for the simulations was calculated either directly, using the Fourier amplitudes of the velocity fields with Eq. (2.17), or indirectly. Indirect methods used the density perturbation field to calculate ΔN^2 and followed the same methodology as the experiments using Eqs. (2.40) and (2.36).

CHAPTER 3. TURNING DEPTHS: EVANESCENT TO PROPAGATING WAVE KINETIC ENERGY DENSITY

This chapter is published in the journal *Physical Review Fluids*. The formatting of this paper has been modified to meet the stylistic requirements of this dissertation.

3.1 Contributing authors and affiliations

Allison Lee, Julie Crockett, Department of Mechanical Engineering, Brigham Young University, Provo, UT 84602

3.2 Abstract

Tidal flow over oceanic topography generates internal waves when the natural frequency (N) of the water is greater than the tidal frequency (ω). When $N < \omega$, evanescent waves are generated. Although the amplitude and kinetic energy of evanescent waves decay rapidly, if the wave reaches a turning depth, where $N = \omega$, and moves into a region where $N > \omega$, the evanescent wave becomes an internal wave. This work expands upon previous research of varying stratifications by investigating the kinetic energy density in internal waves generated by evanescent waves passing through a turning depth. An analytical model is presented and compared to synthetic schlieren experiments of two Gaussian shaped topographies. The model and experiments both indicate that the kinetic energy density of internal waves increases with decreasing topographic slope, when the distance between the topography and the turning depth decreases, and when the average Froude number in the evanescent region is close to one. The model is used to estimate the normalized kinetic energy density of internal waves generated from an oceanic feature located within an evanescent region.

3.3 Introduction

Internal waves are uniquely formed in stratified fluids such as the atmosphere and ocean. The strength of the stratification is proportional to the variation in density in a fluid and is defined by the natural frequency of unforced oscillations, N which is defined as

$$N^2 = \frac{-g}{\rho_0} \frac{d\rho}{dz} \quad (3.1)$$

where g is the gravitational constant, ρ_0 is a reference density, and $d\rho/dz$ is the change in density with respect to height. One well known generator of internal waves in the ocean is tidal flow over oceanic bathymetry, specifically the M2 semidiurnal tide, with a frequency $\omega_{M2} = 1.4052 \times 10^{-4} \text{ s}^{-1}$ [19]. The kinetic energy of internal waves generated from oceanic topography depends on many factors, including the strength of the stratification and the shape of the topography. The strength of the stratification defines whether internal waves or evanescent waves will be formed. Internal waves are formed when N is greater than the excitation frequency (ω) and they suffer little to no viscous dissipation as they propagate. Figure 3.1(a) depicts an internal wave generated by tidal motion across an idealized oceanic topography. Evanescent waves form in the opposite scenario, where $N < \omega$ as depicted in Fig. 3.1(b). An evanescent wave has no vertical structure as a propagating wave does and as it transmits energy vertically the amplitude decays at an exponential rate [5]. King et al. [19] used data from the World Ocean Circulation Experiment (WOCE) to estimate variations in N across the oceans in order to locate evanescent regions and turning depths, or locations where the natural frequency is equal to the forced wave frequency associated with ω_{M2} . They found that these turning depths occur frequently in deep oceans where east-west tides dominate. If an evanescent wave reaches a turning depth, it becomes a propagating internal wave, as shown in Fig. 3.1(c) where the evanescent wave reaches the turning depth (dashed line) and then forms a propagating internal wave [5]. While internal waves are known to have significant energy and are widely studied, evanescent waves are not often considered to have an impact on the ocean due to the rapid decay rate of the amplitude and energy content. However, if a significant portion

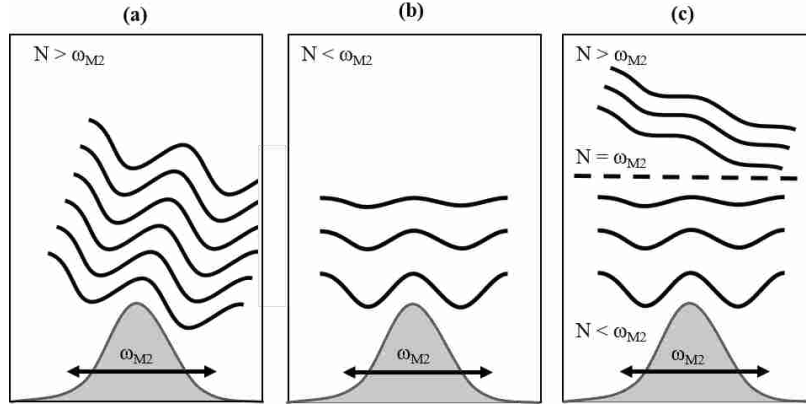


Figure 3.1: A propagating internal wave is shown in (a) and the vertically decaying evanescent wave is seen in (b). In (c), the a turning depth indicates the boundary between the evanescent and propagating regions, with the evanescent wave becoming an internal wave as it pass through the turning depth.

of the original evanescent wave energy reaches a propagating region, the internal waves formed may have an important impact on the ocean energy budget.

Significant research has been accomplished in both varying stratifications and internal waves approaching evanescent regions. Pedlosky [74] used linear theory and the WKB approximation to account for wave propagation in non-uniform stratifications in propagating regions. For multi-layered stratification profiles, internal waves have been shown to tunnel through an evanescent region of fluid and the transmission coefficient of incident internal wave energy across the evanescent region can be calculated with linear theory [80]. Further work on tunneling includes smooth changes in natural frequency and the inclusion of a shear flow [77,81]. Gregory and Sutherland [79] found that the transmission coefficient was larger for internal waves that tunneled through a weakly stratified region instead of a well-mixed region. Mathur and Peacock [78] extended this work for transmission and reflection of internal waves and varied the scale of the transitional region. They found that a wave beam will adjust to a varying stratification and be either amplified or diminished based on the characteristics of the stratification, as long as the changes in the stratification occurred over a sufficiently large distance. Rapid changes in stratification led to wave scattering. Sutherland [82] found an analytical solution for the transmission coefficient for an arbitrary number of density staircases that are all equal in size, and also used simulations to calculate

the transmission coefficient for uneven length staircases. Sutherland found, similar to the results of Ghaemsaïdi et al. [83], that density staircases can act as a filter allowing only internal waves with long horizontal wavelengths and high frequencies to completely pass through the staircase region. Paoletti and Swinney [64] used exponential density profiles and stratifications to investigate internal wave reflection and transmission from a turning depth. Their results compared well with the viscous theory of Kistovich and Chashechkin [84] which allowed for arbitrary stratifications. Each of these cases assumed that internal waves were formed in a propagating region and then pass into an evanescent region, but did not investigate waves formed in an evanescent region passing into a propagating region.

Few studies have been conducted which investigate both evanescent and propagating regions. Using linear theory, Nappo [5] showed that in a two-layer, constant N fluid, with an abrupt change from an evanescent to a propagating region, propagating internal wave energy is dependent upon the strength of the stratification in the propagating region. Paoletti et al. [18] used numerical simulations validated with experiments to characterize the radiated power of internal waves generated from a turning depth with varying stratifications and compared their results to an estimated maximum tidal power. The radiated power was calculated at a fixed location near the topography while the turning depth location was varied. They found that steep-sloped topography generated waves with less power than topography with more gentle slopes. They also saw that the presence of a turning depth greatly reduced the radiated power compared to the internal waves formed in a propagating region from the same topography. Their work provides valuable insight on relative power transferred from the tides into wave motion near topography. In this work, we investigate the kinetic energy transmitted to propagating waves only. We will use experiments and a linear theory analysis to explore the effect of non-uniform stratification on wave generation in evanescent regions and focus on the resultant internal wave kinetic energy in propagating regions.

As mentioned previously, the shape of the topography from which waves are generated has an important affect on the energy content of the waves. When investigating topographically generated internal waves, topographies are frequently divided into different categories based on

criticality. Criticality is defined $\varepsilon = S_{\text{top,m}}/S_{\text{wave}}$ where $S_{\text{top,m}}$ is the maximum topographical slope and $S_{\text{wave}} = \sqrt{\omega^2/(N^2 - \omega^2)}$ is the slope of the generated waves (assuming no rotation). Topographies in propagating regions are considered subcritical ($\varepsilon < 1$), critical ($\varepsilon = 1$), or supercritical ($\varepsilon > 1$). Internal wave energy has been estimated for subcritical topography for constant stratifications [29], depth varying stratifications and a finite depth ocean [75, 85]. Work has also been done for supercritical topographies both experimentally and with a viscous linear theory model [86, 87]. However, for evanescent waves, ε is undefined because S_{wave} is imaginary in an evanescent region. Paoletti et al. [18] used a novel technique to define an effective height of the topography, based on both the slope of the topography and the stratification profile. Using this, they could estimate radiated power for internal waves generated from evanescent waves formed from topography. They found that internal wave power is significantly decreased in the presence of a turning depth. Their results compared well with previous research on topographically generated internal waves and varying stratifications.

In this work we account for the effects of topography shape and the distance from the topography to the turning depth in realistic stratifications to investigate the influence of turning depths on the local kinetic energy of internal waves generated from evanescent regions. Specifically, experiments and a new linear model are used with an exponential N profile such that waves are generated in an evanescent region and pass into a propagating region. Average internal wave kinetic energy is quantified in the propagating region as a function of average Froude number in the evanescent region ($\overline{Fr}_1 = \omega/N$) and H/D , the relative distance between the topography and the turning depth. These results represent the first ever analytical model of an evanescent wave generating an internal wave through a turning depth with varying natural frequency and the kinetic energy associated with each wave. The numerical theory is supported by experiments.

The paper is outlined as follows. Section 3.4 describes the experimental setup and analysis, and details the analytical model. Results are given in Section 3.5, with an oceanic case study in 3.6. Section 3.7 concludes with a summary of the work.

3.4 Methodology

3.4.1 Experimental procedures

All experiments were performed in an acrylic tank with a length, width, and height of 2.45 m, 0.15 m, and 0.91 m, respectively. To create the density profile, a modified version of the double bucket method was used [93]. Two peristaltic pumps controlled the flow rates of fresh and salt water which were joined and slowly filled the tank. Density measurements using an Anton Par density meter were taken every 2 cm before experiments began, and then every 5 cm after every fourth experiment. Density measurements were fit to the equation

$$\rho = a \exp(bz) + c \quad (3.2)$$

where ρ and z have units of kg/m^3 and meters, and a (kg/m^3), b (m^{-1}), and c (kg/m^3) are coefficients calculated from the exponential fit with an average $R^2 = 0.997$ for all cases. This density profile ensures a varying N profile for every experiment, with N defined by Eq. (3.1) and ranging from 0.3 to 2.0 s^{-1} . In Fig. 3.2 the measured density and calculated exponential curve fit is shown. These data come from Case 17 shown in Table 3.1. The density increases with decreasing height, starting at the top of the tank ($z = 0.6 \text{ m}$) and moving down to the bottom at $z=0 \text{ m}$.

As shown in Fig. 3.3, the ocean-topography system is inverted with the topography at the surface and lower values of N at the base of the topography. As z decreases, N increases. A stepper motor controls the oscillation frequency and excursion length of the topography generating waves. Matting was placed at the bottom of the tank to dampen reflections. Two Gaussian topographies were used in the experiments with curves of the form

$$h = H \exp(-x^2/B^2) \quad (3.3)$$

where H is the peak height of the topography and $B^2 = W^2/18$. Here, W is the width of the topography when the height of the topography has decayed to 1% of H . The first topography is

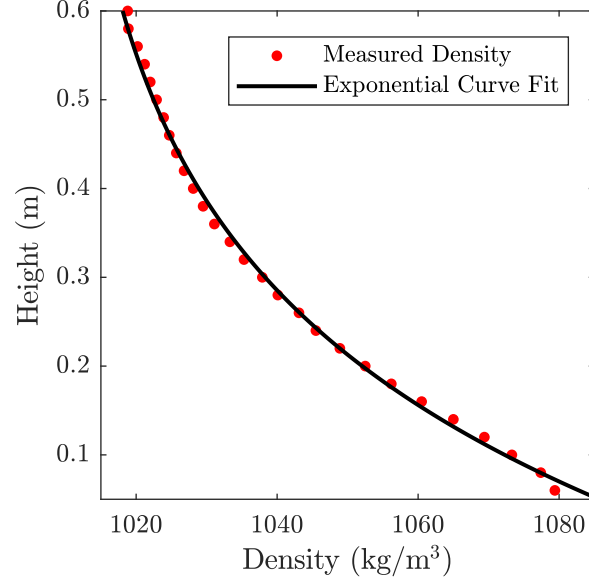


Figure 3.2: The measured density is shown in red points and the exponential curve fit is the black line.

defined by $W/H = 1.8$ (medium topography) and the second by $W/H = 0.45$ (steep topography). $H = 10$ cm for both topographies.

Two non-dimensional numbers were used to describe each experimental setup. First, H/D is a ratio of the height of the topography to the distance between the tip of the topography and the turning depth (D in Fig. 3.3(a)). This ratio provides a relative measure of the number of topographic heights between the source and propagating region. Values of H/D ranged from 0.311 to 2.128, where the higher values indicate that the topography is closer to the turning depth. The other non-dimensional number is the average Froude number in the evanescent region which is defined as

$$\overline{Fr}_1 = \omega_f / \overline{N}_1 \quad (3.4)$$

where the subscript “1” refers to the evanescent region (see Fig. 3.3(a)) and ω_f is the forcing frequency of the topography. The Froude number is used to characterize the stratification profile in the evanescent region. Table 3.1 provides the details of each case, including the coefficients for the density profile [Eq. (3.2)], the height of the water in the tank, the horizontal wavenumber, the

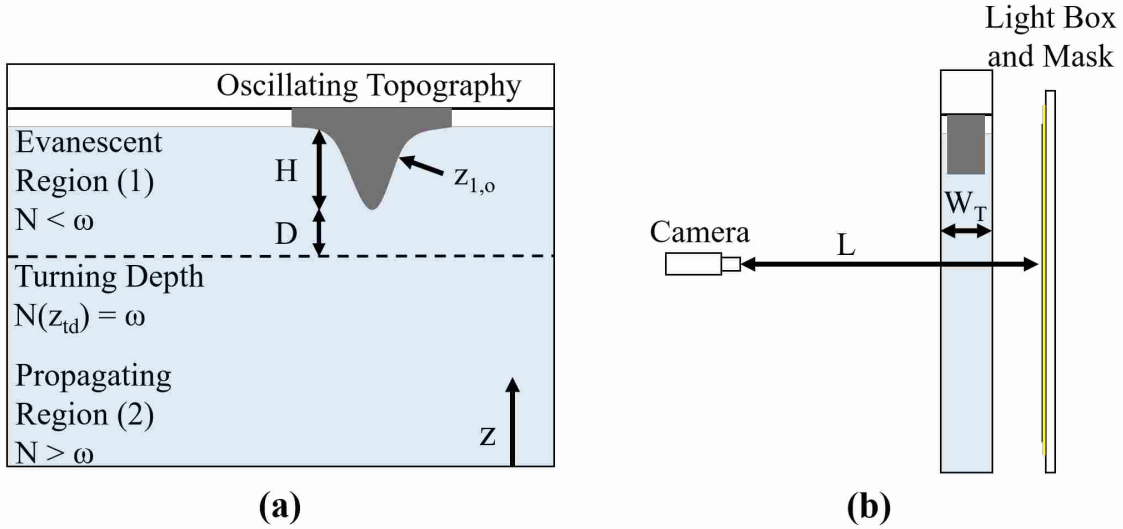


Figure 3.3: Experimental tank and visualization system schematic. In (a), the front view of tank is shown with internal wave regions and turning depth as labeled. In (b), the side view of the setup with camera for synthetic schlieren imaging is shown.

oscillation frequency of the topography, the height of the turning depth, the excursion length of the topography, and values for H/D and \overline{Fr}_1 .

The topography was forced at an oscillation frequency ω_f . The location of the Gaussian profile in space and time is described as

$$z_{\text{top}}(x, t) = H \exp \left[\frac{-(x - L \sin \omega t)^2}{B^2} \right] \quad (3.5)$$

where L is the excursion length of the topography, $-0.09 \leq x \leq 0.09$ m for the medium topography, and $-0.0225 \leq x \leq 0.0225$ m for the steep topography. After 15 oscillation periods of the topography, which allowed the waves to reach steady state, images were recorded with a jAi Cv-M4+Cl progressive scan camera for three minutes at 6 fps and processed with the commercial software DigiFlow [58]. The camera shown in Fig. 3.3(b) was focused on the mask of random dots illuminated by a light box behind the tank and synthetic schlieren was used to calculate variations in density for each experiment. DigiFlow calculates values of $\nabla \rho' / \rho_0$, where ρ' is the density perturbation. Using the z derivative and multiplying these values by the gravitational constant, an

Table 3.1: A summary of experiments and experimental parameters. Cases 1-14 used the medium topography ($W/H = 1.8$), while cases 15-24 used the steep topography ($W/H = 0.45$). Water height, z_{td} , and L are given in centimeters.

Case	a (kg/m^3)	b (m^{-1})	c (kg/m^3)	Water Height	k_d (m^{-1})	ω_f (s^{-1})	z_{td}	L	H/D	\overline{Fr}_1
1	100	-2.36	993	57.5	28.39	1.04	32.7	4.13	0.67	1.15
2	97.7	-2.35	994	57.3	28.26	1.00	34.9	4.23	0.81	1.14
3	95.2	-2.55	998	57.3	28.48	0.95	38.1	4.07	1.09	1.13
4	110.4	-1.35	975	67.3	28.57	0.95	35.9	3.99	0.47	1.11
5	101.6	-1.51	984	67.2	28.26	1.04	21.9	4.23	0.28	1.18
6	89.8	-2.17	999	63.4	28.29	0.85	45.3	4.21	1.23	1.10
7	84.9	-2.48	1005	63.3	28.09	0.85	42.4	4.37	0.92	1.14
8	92.6	-2.39	997	61.7	28.28	0.86	45.5	4.22	1.62	1.10
9	86.9	-2.81	1004	61.1	28.51	0.81	46.5	4.04	2.15	1.11
10	92.6	-2.39	997	57.5	28.26	0.93	38.4	4.24	1.10	1.12
11	95.2	-2.64	1003	61.7	32.29	1.21	19.8	1.46	0.31	1.30
12	95.2	-2.64	1003	61.4	31.04	1.08	28.1	2.24	0.43	1.24
13	119	-1.87	982	63.5	28.39	1.13	28.8	4.14	0.41	1.17
14	117	-1.76	981	63.3	28.15	1.00	40.3	4.32	0.77	1.10
15	88.8	-3.71	1008	69.3	67.64	1.04	29.7	4.34	0.38	1.41
16	87.8	-3.50	1007	69.3	62.85	1.24	19.3	5.05	0.28	1.50
17	87.8	-3.50	1007	60.6	63.95	1.17	22.6	4.88	0.41	1.37
18	92.2	-4.01	1011	60.5	70.96	0.96	34.1	3.90	0.71	1.29
19	94.7	-4.49	1014	61.0	57.67	0.81	41.2	5.94	1.25	1.24
20	85.1	-4.27	1014	60.9	67.38	0.86	36.9	4.38	0.85	1.28
21	89.6	-4.38	1014	60.8	65.76	0.86	37.8	4.61	0.91	1.27
22	91.8	-4.54	1014	60.5	67.57	0.77	42.7	4.35	1.62	1.22
23	91.8	-4.54	1014	60.4	67.52	1.00	31.1	4.36	0.60	1.37
24	89.8	-4.52	1015	60.2	66.03	1.00	30.6	4.57	0.59	1.37

equation for the variation in the natural frequency between the initial undisturbed image and each subsequent image, similar to Eq. (3.1) is derived:

$$\Delta N^2 = \frac{-g}{\rho_0} \frac{\partial \rho'}{\partial z} \quad (3.6)$$

With ΔN^2 , the kinetic energy of the internal waves can be estimated using the method described by Wunsch and Brandt [20]. By using the continuity equation

$$\frac{\partial u}{\partial x} + \frac{\partial w}{\partial z} = 0 \quad (3.7)$$

and defining

$$\frac{\partial \Delta N^2}{\partial t} = -\frac{\partial (N^2 w)}{\partial z} \quad (3.8)$$

the WKB approximation is used to approximate kinetic energy. Internal wave velocities and the natural frequency are defined as planar waves multiplied by slowly varying amplitudes:

$$u(x, z, t) = \int \tilde{U} \exp[i(kx + mz - \omega t)] dk d\omega \quad (3.9)$$

$$w(x, z, t) = \int \tilde{W} \exp[i(kx + mz - \omega t)] dk d\omega \quad (3.10)$$

$$\Delta N^2(x, z, t) = \int \Delta \tilde{N}^2 \exp[i(kx + mz - \omega t)] dk d\omega \quad (3.11)$$

where \tilde{U} , \tilde{W} and $\Delta \tilde{N}^2$ are Fourier amplitudes. Using Eqs. (3.7) and (3.8), where the derivatives of the amplitudes are assumed negligible, and taking a two dimensional Fourier transform along the horizontal (x) direction and through time (t), Wunsch and Brandt derive

$$KE_2 = \frac{\omega^2 N^2}{k^2 (N^2 - \omega^2) + (\omega \partial_z N^2 / N^2)^2} \left| \frac{\Delta \tilde{N}^2}{N^2} \right|^2 \quad (3.12)$$

where $KE = |\tilde{U}|^2 + |\tilde{W}|^2$, k is the horizontal wavenumber, and the subscript “2” indicates the propagating region. Unfortunately, this equation is not valid in the evanescent region because of the exponential decay of evanescent wave amplitudes and imaginary vertical wavenumber. These are accounted for by first defining

$$q^2(z) = k^2 (1 - N^2(z) / \omega^2) \quad (3.13)$$

where $m = iq$ is the imaginary vertical wavenumber in the evanescent region [5,74]. The velocities and natural frequency then become

$$u(x, z, t) = \int \tilde{U} \exp(qz) \exp[i(kx - \omega t)] dk d\omega \quad (3.14)$$

$$w(x, z, t) = \int \tilde{W} \exp(qz) \exp[i(kx - \omega t)] dk d\omega \quad (3.15)$$

$$\Delta N^2(x, z, t) = \int \Delta \tilde{N}^2 \exp(qz) \exp[i(kx - \omega t)] dk d\omega \quad (3.16)$$

Following the same methodology described above for Eq. (3.12), we find

$$KE_1 = \left| \frac{-q\omega\Delta\tilde{N}^2}{k(\partial_z N^2 + qN^2)} \right|^2 + \left| \frac{i\omega\Delta\tilde{N}^2}{\partial_z N^2 + qN^2} \right|^2 \quad (3.17)$$

for the evanescent region. We will denote this by KE_1 as it is the first region where waves are formed.

To use Eq. (3.12) and Eq. (3.17), the experimental data are first filtered by performing a Fourier transform in the vertical direction. The vertical wavenumber will vary throughout the experiment due to the variation in N . The Fourier coefficients corresponding to the lowest possible vertical wavenumber ($m = 0$) and above the highest expected wavenumber are zeroed. The highest expected wavenumber is defined as $m_{\max}^2 = k^2(N_{\max}^2/\omega^2 - 1)$. An inverse Fourier transform is then applied to the filtered data and is sorted into a timeseries of rows representing horizontal slices of the experimental data. Each row is the height of a single pixel. A two-dimensional (2D) Fourier transform in x and t is then performed on a timeseries row to create $\Delta\tilde{N}^2$. Results are shown for Case 2 at two different locations in Fig. 3.4 with contours of $\Delta\tilde{N}^2$ plotted against frequency (ω) and horizontal wavenumber (k). In Fig. 3.4(a), the horizontal slice is at $z = 0.4$ m, in the evanescent region, while the data in Fig. 3.4(b) is in the propagating region at $z = 0.22$ m. The excitation frequency for this case is $\omega_f = 1.00$. Comparing the two figures, this frequency peak is seen clearly. The expected dominant horizontal wavenumber, k_d , for a specific case is found by

defining the horizontal wavelength, λ_x , as the width of the topography plus the excursion length or

$$\lambda_x = W + L \quad (3.18)$$

Then the wavenumber for each case, $k_d = 2\pi/\lambda_x$, gives $k_d = 28.26 \text{ m}^{-1}$ for Fig. 3.4. Although the Fourier amplitudes show a peak near the expected wavenumber and excitation frequency, $\Delta\tilde{N}^2$ amplitudes do not match exactly with the expected frequency and wavelength and there is some leakage into nearby frequencies and wavenumbers. The kinetic energy is calculated at all wavenumbers and frequencies for each individual row with its corresponding N^2 and $\partial_z N^2$ values using Eq. (3.12) and Eq. (3.17). Kinetic energy data is then filtered by summing energy values for the three wavenumbers and three frequencies nearest to the expected values. This is done to allow for a comparison to the linear theory model, which uses only one wavenumber, k_d , and the forcing frequency, ω_f , while also preventing an underestimate of kinetic energy due to the $k - \omega$ spreading. Also, because of the topography and the local turbulence in its wake, the kinetic energy of the evanescent region is only calculated below the tip of the topography.

3.4.2 Theory

Using the WKB approximation, a linear, Boussinesq, 2D model was used to calculate the kinetic energy that passes from the evanescent region through the turning depth and into the propagating region, accounting for the exponential natural frequency profile. Linear theory is a good approximation because $u_{\text{top}}/(\omega_f W) < 1$ for all cases [75], where u_{top} is the average velocity of the topography, and W is the width of the topography. The maximum value in our cases is 0.38 and the effects of this will be discussed further in Section 3.5. The WKB approximation is valid away from the turning depth where $N^2 \gg \lambda_z(\partial N^2/\partial z)$ [74]. In the following sections we will analytically calculate kinetic energy in the evanescent region and the propagating region, and then demonstrate how the two regions can be matched at the turning depth where the WKB approximation is not

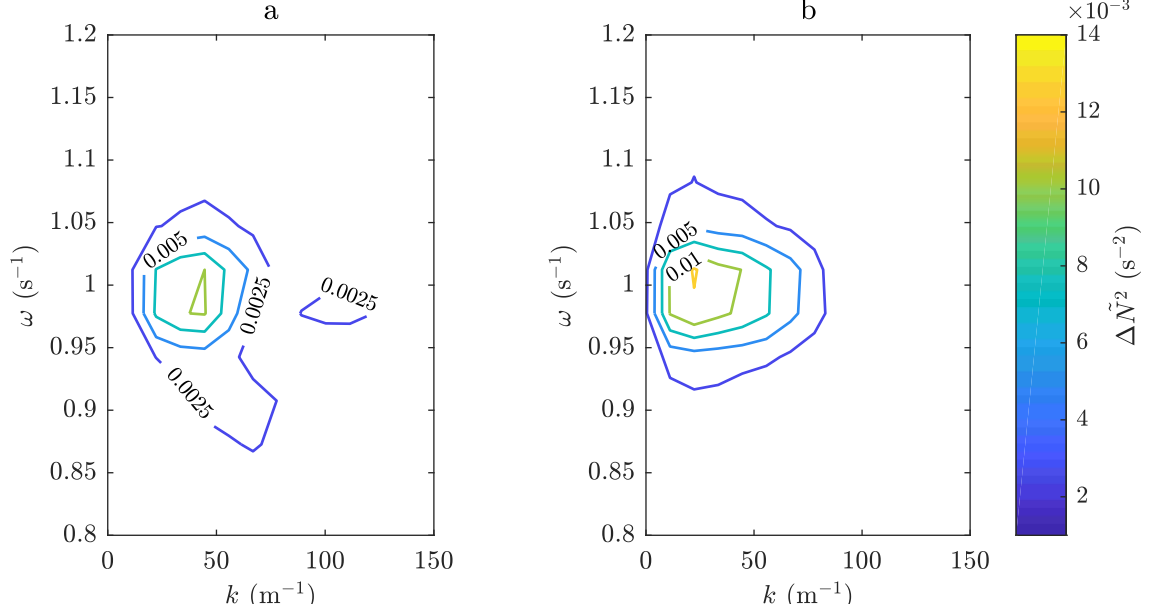


Figure 3.4: Fourier amplitudes of ΔN^2 in the evanescent region (a) and propagating region (b) are shown in contours increasing by 0.0025 for each line. Both figures uses the same scaling. The highest value for the contour lines for (a) is 0.01 s^{-2} and for (b) is 0.0125 s^{-2} .

valid. Within each region the vertical velocity (w) is defined and the horizontal velocity (u) is found from continuity [See Eq. (3.7)].

With both u and w defined, the kinetic energy is defined as

$$KE = u^2 + w^2 \quad (3.19)$$

for comparison with experiments. Each case in Table 3.1 is reproduced with a linear theory analysis using the given experimental parameters, including the calculated λ_x and k_d from Eq. (3.18). No other data from the synthetic schlieren experiments are needed to initialize the theoretical analysis.

Evanescent region

The vertical velocity in the evanescent region varies due to the variation in the N profile which affects the vertical wavelength. In the same manner as the experimental energy calculations in Section 3.4.1, the vertical wavenumber will be defined as $m = iq$, with q defined by Eq. (3.13).

Following the work of Pedlosky [74] in a propagating region with $N = f(z)$, for the evanescent region we introduce θ_1 ,

$$\theta_1(z) = \int_{z_{1,0}}^z q dz \quad (3.20)$$

where the subscript “1” refers to the evanescent region. $A_{1,0}$ and $q_{1,0}$ are defined at the height $z_{1,0} = h(B)$ as shown in Fig. 3.3(a) for the medium Gaussian topography. Using q and θ , the vertical velocity can be defined as

$$w_1(x, z, t) = A_1 \exp[i(kx - \omega t)] \exp(\theta_1) \quad (3.21)$$

$$A_1(z) = A_{1,0}/(q/q_{1,0})^{1/2} \quad (3.22)$$

Assuming a slip condition at the topography [34], the wave velocity can be calculated by using the time derivative of Eq. (3.5) and setting it equal to Eq. (3.21) such that $dz_{\text{top}}/dt = w_1(x = B, t = 0)$ [See Eq. (3.3)]. Using continuity [Eq. (3.7)], the horizontal velocity is computed as

$$u_1(x, z, t) = \frac{-w_1}{ik} \left[\frac{-dq/dz}{2q} + q \right] \quad (3.23)$$

The kinetic energy of the evanescent region is calculated using $KE_1 = u_1^2 + w_1^2$.

Propagating region

Following the work of Pedlosky [74], velocities in the propagating region, assuming a varying natural frequency, are defined by

$$w_2(x, z, t) = A_2 \exp(i(kx - \omega t + \theta_2)) \quad (3.24)$$

$$u_2(x, z, t) = \frac{-w_2}{k} \left[\frac{-dm/dz}{2im} + m \right] \quad (3.25)$$

$$A_2(z) = A_{2,0}/(m/m_0)^{1/2} \quad (3.26)$$

$$\theta_2(z) = \int_{z_0}^z m dz \quad (3.27)$$

$$m^2(z) = k [N(z)^2/\omega^2 - 1] \quad (3.28)$$

where continuity has again been used to define u_2 . Note that the subscript 2 refers to the propagating region. The kinetic energy in the propagating region is calculated by $KE_2 = u_2^2 + w_2^2$. In both the evanescent and propagating regions, the amplitude, A , of the velocities varies with height. This is due to the varying natural frequency, which causes the varying vertical wavenumber, and is necessary to conserve energy [74].

Airy integral matching

As the evanescent wave moves from the topography toward the turning depth, the WKB assumptions are violated near the turning depth because $N^2 \sim \lambda_z(\partial N^2/\partial z)$. This also causes q to decrease to zero, creating a discontinuity at the turning depth. The Airy function can be used to patch over the discontinuity [91, 92] if the WKB approximation is extended past where it is valid [81]. This patch is used to match the vertical velocity of the evanescent wave to the propagating region. Following Lighthill [91], the vertical wave velocity with the Airy integral is

$$w_{\text{Ai}}(x, z, t) = Q_{0,w} \text{Ai}(\beta^{1/3}z - \beta^{1/3}z_{\text{td}}) \exp[i(kx - \omega t)] \quad (3.29)$$

where β is defined by $\beta = m^2/(z_{\text{td}} - z)$. The amplitude of $Q_{0,w}$ is found by matching Eq. (3.29) to Eq. (3.21) at $z_{1,\text{Ai}} = z_{\text{td}} + 0.01(2\pi/\bar{q})$, or 1% of the average vertical wavelength (λ_z) above the turning depth in the evanescent region. A range of percentages from 0.1% to 10% was compared to understand the effect of the start and end points of the Airy integral. Decreasing the percentage causes a decrease in the average kinetic energy, but the changes of kinetic energy below 1% were minimal, both for the medium and steep topographies. This percentage should be altered if there is a significant increase in the model domain and may be dependent on the vertical resolution of the model.

Continuity and w_{Ai} , Eq. (3.7) & Eq. (3.29) are used to derive the form of the horizontal velocity in the Airy integral

$$u_{\text{Ai}}(x, z, t) = Q_{0,u} \frac{i\beta^{1/3}}{k} \text{Ai}'(\beta^{1/3}z - \beta^{1/3}z_{\text{td}}) \exp[i(kx - \omega t)] \quad (3.30)$$

where Ai' is the first derivative of the Airy function with respect to z .

Above the turning depth, the vertical velocities are set equal such that $w_1 = w_{\text{Ai}}$ at $z = z_{1,\text{Ai}}$ and $Q_{0,w}$ is solved. This procedure is repeated for the horizontal velocity with $u_1 = u_{\text{Ai}}$ at $z = z_{1,\text{Ai}}$ to find $Q_{0,u}$. While continuity is used to find the form of u_{Ai} , using the same amplitude as w_{Ai} defines a horizontal velocity in the Airy region that is inconsistent with the horizontal velocity in the evanescent and propagating regions. The amplitude $Q_{0,u}$ provides better consistency throughout the Airy region, but is not used in the propagating region. Instead, the wave amplitude below the turning depth, $A_{2,0}$ is calculated by setting $w_{\text{Ai}} = w_2$ at $z_{\text{Ai},2} = z_{\text{td}} - 0.01(2\pi/\bar{m})$, and continuity is used to define u_2 from w_2 , as defined in the previous section. It is assumed that both $Q_{0,w}$ and $Q_{0,u}$ are constant through the Airy integral region as the variation in the natural frequency is small over the small change in height.

Completed model

We now explore the importance of the terms $(-dq/dz)/2q$ and $(-dm/dz)/2im$ in Eqs. (3.23) and (3.25), respectively. These higher order terms, which are not usually found in the horizontal velocity, appear because the amplitude of the velocity is a function of depth. When assuming that the amplitude, natural frequency, and vertical wavenumbers vary slowly, the variation of the vertical wavenumbers (dq/dz or dm/dz) is relatively small and can be neglected. This assumption breaks down near the turning depth, due to the rapid variation of q and m in that region, indicating they should remain in the equations for velocity. However, the use of the Airy integral to connect the evanescent and propagating regions does not include these terms. Figure 3.5 depicts the two different scenarios for Case 4 with height on the ordinate and kinetic energy on the abscissa.

The dashed line indicates the location of the turning depth with the evanescent region above the turning depth and the propagating region below. The horizontal dash-dot line below the turning depth marks the height corresponding to a 10% increase in N relative to the excitation frequency of 0.95 s^{-1} . Kinetic energy with the higher order terms included is indicated by the solid line, while the dotted line represents kinetic energy when these terms are neglected. For both scenarios, kinetic energy begins at a maximum at the top of the figure and then decreases as the wave moves through the evanescent region. An increase in energy is seen near the turning depth, with a larger increase when the higher order terms are included. Below the turning depth, both scenarios decrease in kinetic energy through the propagating region. Away from the turning depth, the kinetic energy collapses to a single line. Each of the 24 experimental cases were compared with and without the higher order terms and the average error from the region between the end of the Airy integral and a 10% increase in N is 20%. However, the majority of this error is due to the sharp increase that comes from the sharp increase in amplitude at the end of the Airy integral. Neglecting this increase and again comparing the kinetic energy, the average error is 13%. We will ignore the higher order terms in this work, but it may be necessary to retain them in future work if more rapid changes in natural frequency are of interest.

3.5 Results

First, the normalized kinetic energy, KE^* , over the height of the experiment is analyzed. Figure 3.6 shows both the experimentally calculated and theoretically predicted KE^* over height for four cases. The ordinate is height in meters where $z = 0$ is at the bottom of the tank. The abscissa is KE^* , or KE/KE_{norm} where KE_{norm} is the average of the kinetic energy of the three pixel locations below the topography height, $z = z_{\text{total}} - H$. Because the presence of the topography generated spurious values near the topography in the experimental data, only data below the topography was analyzed. To maintain consistency between the model and the experimental analysis, the kinetic energy at the same three height locations were averaged to calculate KE_{norm} in the theoretical model as well. However, the model was averaged over only one period and one hori-

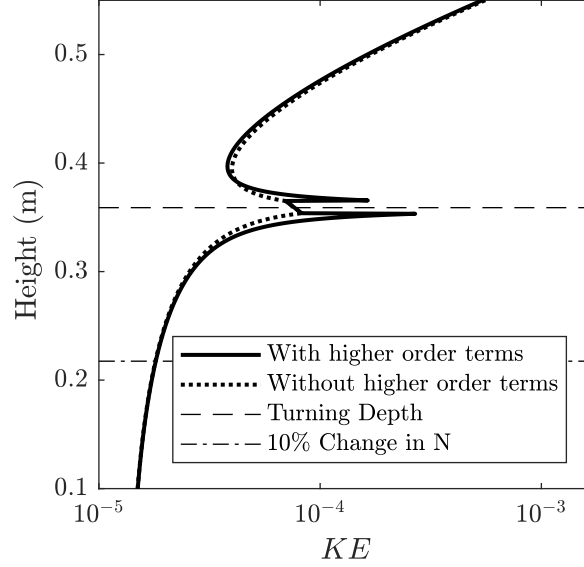


Figure 3.5: The kinetic energy as a function of height is shown for the scenarios of including or excluding dq/dz and dm/dz when calculating the horizontal velocity. The turning depth is shown by the dashed horizontal line and the dash-dot line indicates the height of a 10% increase in N from the turning depth.

zonal wavelength because of its periodic nature. All experimental tests were run for three minutes which provided between 21 and 35 periods for the different test cases. At least two horizontal wavelengths were captured in the field of view in the experiments for the medium topography and at least five for the steep. Figures 3.6(a) and 3.6(b) compare the model and experimental KE^* values for Cases 1 and 8 respectively, where the medium topography was explored. Figures 3.6(c) and 3.6(d) are Cases 18 and 20, steep topography test cases. In all graphs, the solid line represents experimental data while the dotted line represents model results. The horizontal dashed line shows the location of the turning depth (z_{td}), which is determined by $N(z_{td}) = \omega_f$. Although the ordinate is the same across all four plots, the abscissa varies for each. Starting in the upper right hand corner of each plot (near the topography), normalized kinetic energy is at a maximum; as height decreases and N increases, the normalized kinetic energy decreases exponentially as the evanescent wave travels downward and decays. At the turning depth there is a slight increase in energy due to the decrease in q as N approaches ω_f , which causes an increase in the amplitudes of u and v [See Eqs. (3.21) and (3.22)]. The Airy integral is used to connect the two evanescent and propagating

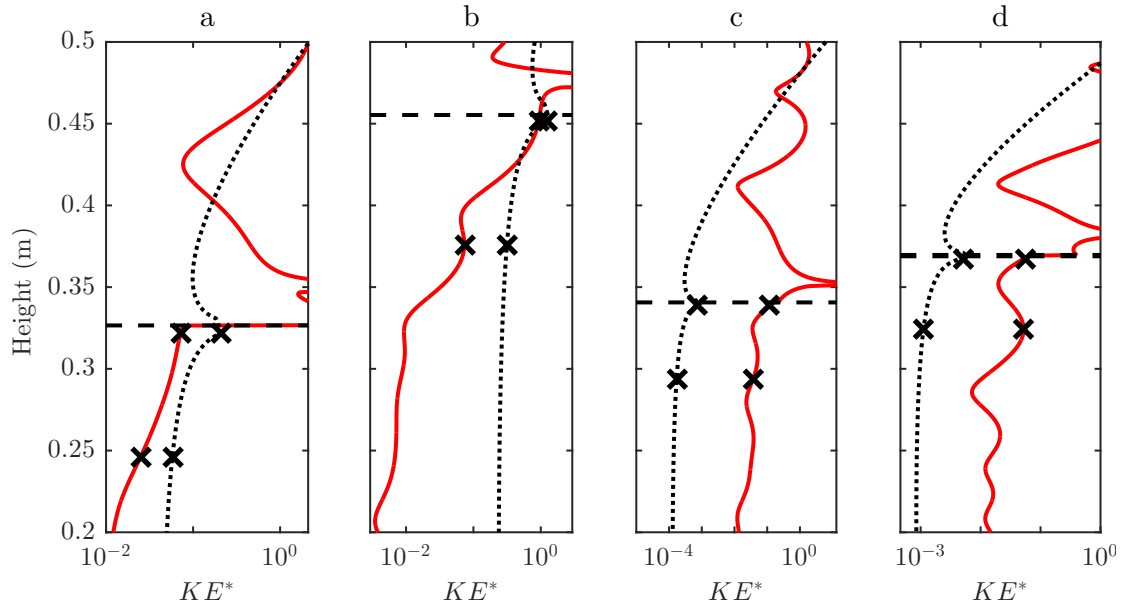


Figure 3.6: Normalized kinetic energy is shown as a function of height for two cases. The solid lines are experimentally calculated KE^* while the dotted represent model results. Data from (a) and (b) come from Cases 1 and 8 which used the medium topography, while (c) and (d) are Cases 18 and 20 and used the steep topography. The turning depth location, z_{td} is marked with a dashed line. The black x markers indicate the distance over which kinetic energy is averaged in the propagating region.

region. Below this, a propagating internal wave exists with relatively constant normalized kinetic energy. Within Fig. 3.6, there are variations in the vertical structure of the experimental energy, the model generally overestimates the kinetic energy for the medium topography, and the model significantly underestimates kinetic energy of the steep topography. Each of these results will be explored in the following paragraphs.

Differences in the vertical structure of KE^* between the model and the experiments may be partially explained by the density profile. In Fig. 3.2, although the curve fit used in the model follows the density measurements well, with $R^2 = 0.997$, there are some local variations in the density profile within the experimental tank that do not match exactly with the curve fit. Density values vary both slightly above and slightly below the curve fit. These local fluctuations can lead to variations in the experimental energy profile that is not reflected in the model. Also, because each of the four cases shown here have different density profiles and experimental setups, they all

have different structures so an averaging scheme is introduced below. The experimental energy for Fig. 3.6(a) and (b) show an added decay in kinetic energy far from the turning depth. This decay is possibly due to reflected wave beams destructively interfering with the main propagating wave as it nears the bottom of the tank. For all cases, this interference was not seen near the turning depth. Because of this, the kinetic energy in the propagating region was averaged over a region below the turning depth by

$$\overline{KE}_2 = \frac{1}{\Delta z_{Fr2}} \int KE dz \quad (3.31)$$

where Δz_{Fr2} is the height from the end of the Airy integral ($z_{2,Ai}$) to the height where the average Froude number in the propagating region is 0.952. This corresponds to a 10% increase in N from the turning depth into the propagating region. This relatively short distance is considered here to focus directly on kinetic energy transferred through the turning depth and into the propagating region. Starting and ending locations of Δz_{Fr2} are demarcated in Fig. 3.6 with black x's for each case. This average kinetic energy is also normalized giving $\overline{KE}_2^* = \overline{KE}_2 / KE_{norm}$.

For the medium topography in Figs. 3.6(a) and 3.6(b), the average, normalized kinetic energy of the experiment is $\overline{KE}_2^* = 0.048$ and $\overline{KE}_2^* = 0.335$, respectively. This means that approximately 5% and 34% of the kinetic energy near the topography is transferred into the propagating region. The model predicts percentage of kinetic energy transfer for these two cases to be 9% and 48%. This overestimate is most likely due to non-linearities, such as viscosity, within the experiment that are not accounted for in the model.

In the steep topography cases shown in Fig. 3.6(c) and Fig. 3.6(d), the experiment and model follow the same qualitative trends, however the model underestimates \overline{KE}^* throughout the majority of both the evanescent region and propagating region. For Fig. 3.6(c), the model predicts $\overline{KE}_2^* = .00028$ while the experiment indicates $\overline{KE}_2^* = 0.049$. Similarly for Fig. 3.6(d), $\overline{KE}_2^* = 0.00026$ for the model and $\overline{KE}_2^* = 0.033$ for the experiment. We explain this difference by noting the movement of the steep topography creates turbulence near the topography and turbulence generated internal waves are seen within the experiments. These turbulence generated waves have a variety of wavelengths, but also show signs of resonant triad behavior in some cases. Near

the turning depth, an exchange of energy was seen between the turbulence generated waves and the topographically generated waves. For example, in Cases 15 and 16 the turbulence generated waves had a frequency of approximately half of the forcing frequency, and as the topographically generated evanescent wave passed into the propagating region, the turbulence waves lost energy while the newly formed internal waves increased in energy. Similar to Fig. 3.4, Fig. 3.7 shows the Fourier amplitudes of $\Delta\tilde{N}^2$ (scaled by a factor of 10^3) in the evanescent (a) and propagating (b) regions of Case 15. The scales for both (a) and (b) are the same, but here the frequency is normalized by the forcing frequency, ω_f , and the horizontal wavenumber is normalized by k_d from Table 3.1. In Fig. 3.7(a), there are peaks at $k^* = 0.15$ and 0.95 , with $\omega_f^* = 0.5$. These peaks are no longer clear in Fig. 3.7(b), but these two waves approximately sum to 1 in both frequency and wavenumber, forming a triad with the expected frequency and wavenumber, and could be feeding into the peak seen at (1,1) in Fig. 3.7(b). Because the linear theory model does not take into account the generation or interaction of turbulence generated waves, there are steep topography cases where the model underestimates KE^* . Further investigation into the combined effect of turning depths and resonant triads could provide new information into the influence of turbulence generated waves in the ocean, but is beyond the scope of this work.

To understand the effects of topography placement relative to the turning depth (see D in Fig. 3.3(a)) on propagating internal wave energy, Fig. 3.8 shows \overline{KE}_2^* as a function of H/D for all 24 cases. Circles represent the medium topography and triangles represent the steep topography. Filled in markers are values from experiments and open markers are calculated using the linear theory model. Normalized average kinetic energy is shown on the ordinate with a logarithmic scale, and H/D is the abscissa with a linear scale. Four trend lines have been added to the data, one for each of the four symbols. In all cases, the data show that increasing H/D , which decreases the relative distance from the topography to the turning depth, leads to an increase in kinetic energy in the propagating region. Since the evanescent wave decays over a shorter distance for high values of H/D , more kinetic energy is present at the turning depth and is subsequently transferred to the propagating region.

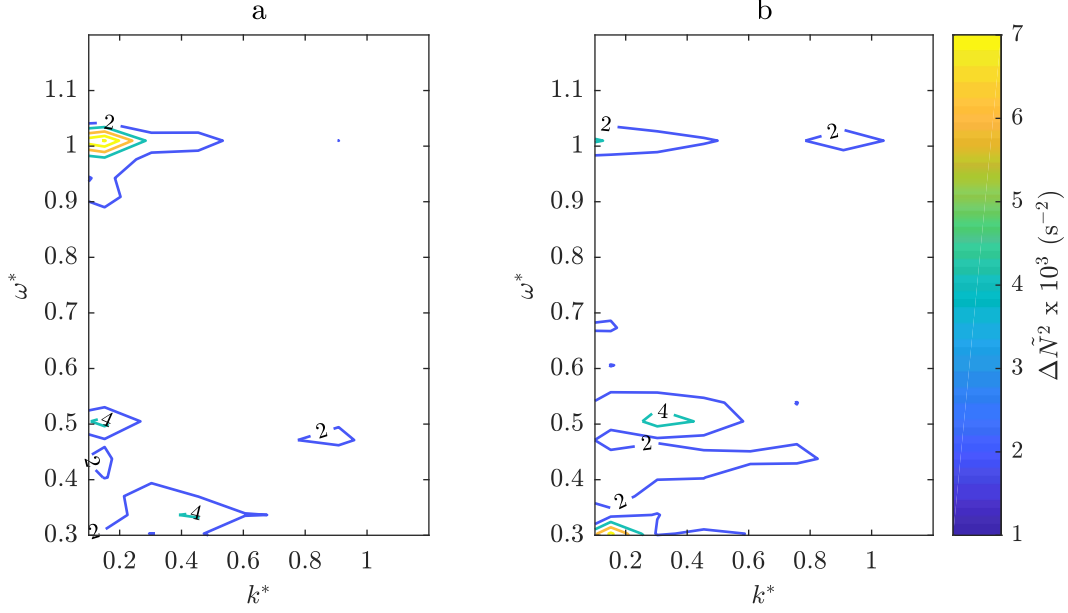


Figure 3.7: Contours of $\Delta\tilde{N}^2$ for Case 15 as a function of ω^* and k^* in the evanescent (a) and propagating (b) regions. $\Delta\tilde{N}^2$ values have been scaled by a factor of 10^3 .

For the medium topography, the model trend line is similar to the experimental trend line.

Each fit is defined by

$$\overline{KE}_2^* = \exp[C_1(H/D)^{C_2}] \quad (3.32)$$

The experimental values of C_1 and C_2 are -1.68 and -1.89 with $R^2 = 0.86$, while the model values are -1.42 and -1.40 with $R^2 = 0.98$. Here R^2 refers to the goodness of fit between the trend line and the data points, with $R^2 = 1$ indicating a perfect fit. For $H/D < 0.72$, both the model and the experiment trend lines show $\overline{KE}_2^* < 0.1$ and further decreases in H/D leads to a large decrease in kinetic energy transmitted into the propagating region. For $H/D > 0.72$, the model over estimates the normalized kinetic energy of the experiment. At $H/D = 2.2$, the experiment trend indicates that 43.5% of the initial energy from the evanescent region will pass into the propagating region, while the model predicts 62.5%. When $H/D > 0.72$, the experiment and model values match well, with the model indicating, on average, 11.9% more energy passing into the propagating region.

For the steep topography, the model generally underestimates the experimental values. Equation (3.32) was also used to fit trend lines to the data with $C_1 = -5.04$, $C_2 = -0.42$ and

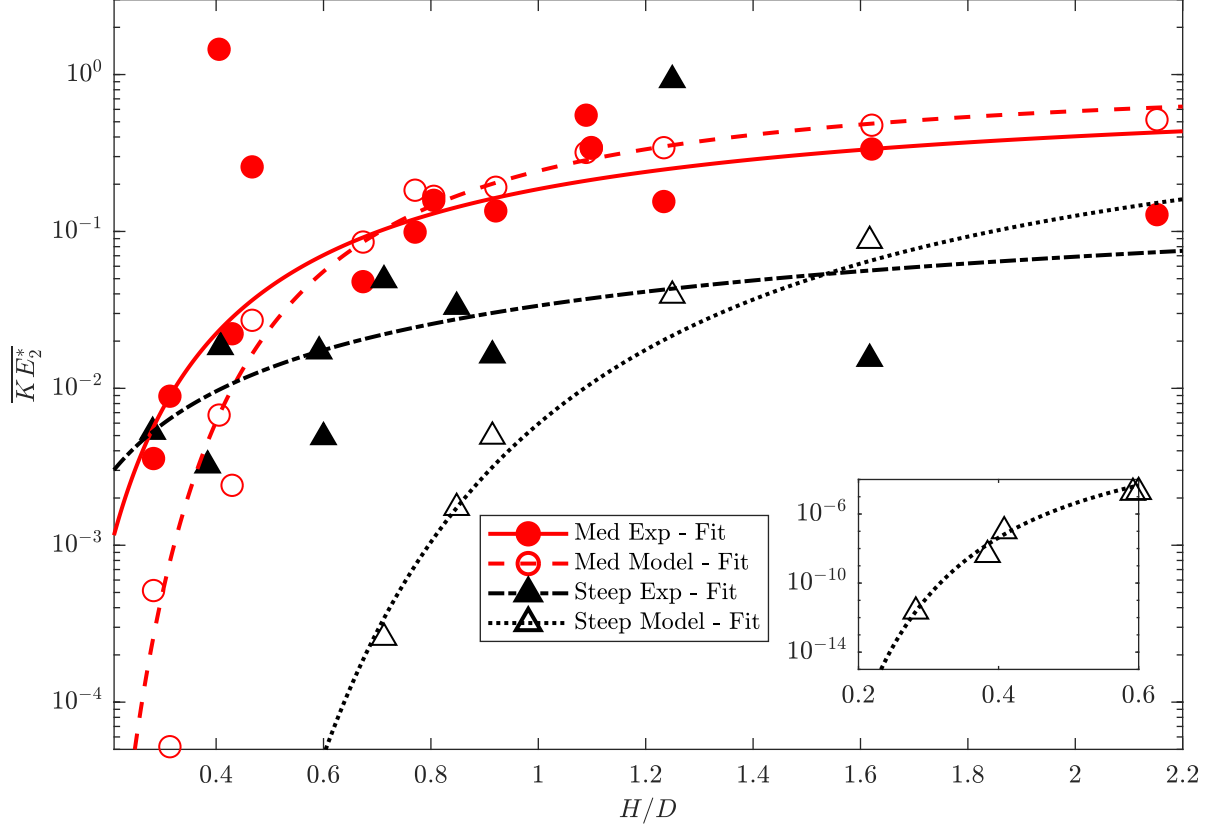


Figure 3.8: The average, normalized, kinetic energy in the propagating region as a function of H/D for both the medium and steep topographies with experimental and model values. Red circles represent the medium topography, with closed filled circles representing experimental data and open for the model. Steep topography data is represented with black triangles, again with the filled triangles representing experimental data and open for the model. The inset contains five steep topography model points with normalized kinetic energy values less than 10^{-5} .

$R^2 = 0.53$ for the experimental data and $C_1 = -5.13$, $C_2 = -1.30$ and $R^2 = 0.99$ for the model data. As mentioned previously, some of the tests showed an interaction between the turbulence generated waves and the internal waves in the propagating region. The large difference in experimental and model values occurs for low values of H/D and for $\overline{KE}_2^* < 0.001$. It is possible that the turbulence generated waves contribute a relatively constant amount of energy to the internal wave field, and at lower values of H/D this is more significant because less topographically generated energy is present. Also, one of the requirements for using linear theory is that the $u_{\text{top}}/(\omega_f W) < 1$, meaning that the excursion length must be less than the length scale of the topography [75]. While

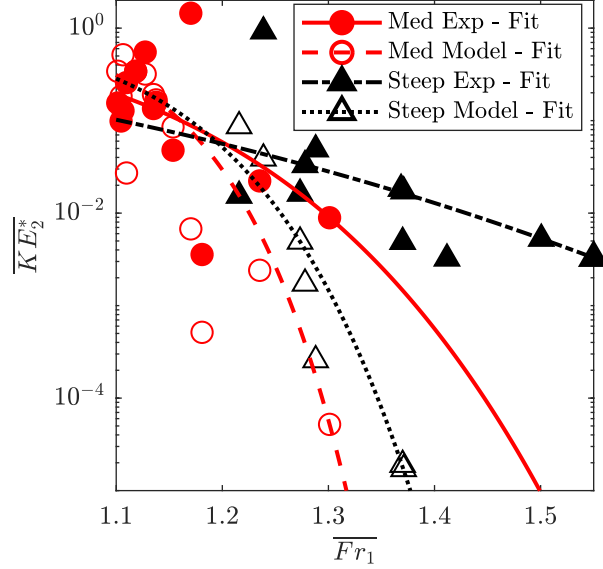


Figure 3.9: \overline{KE}_2^* is shown as a function of \overline{Fr}_1 . The symbols and lines follow the same legend as shown in Fig. 3.8.

the medium topography always met this criteria with values of $O(10^{-2})$ the steep topography had values of $O(10^{-1})$.

Figure 3.8 also indicates that for $H/D > 0.25$, the medium topography has a higher relative kinetic energy in the propagating region than the steep topography. Linear theory shows that without a turning depth present, a steep, narrow topography generates internal waves with higher kinetic energy than shallower, wide topography [3]; however, the presence of a turning depth introduces new dynamics. The medium topography, which has a larger wavelength, generates more kinetic energy in the propagating region than the steep topography, which has a smaller wavelength. This phenomena was seen by Paoletti et al. in their experiments and numerical models [18]. They also used a medium and steep topography with the same W/H ratios as reported here and found that in the presence of a turning depth, the medium topography has about an order of magnitude higher radiated internal wave power. We also see this trend for normalized kinetic energy for $H/D > 0.25$.

An approximation of the strength of the evanescent region can be represented by \overline{Fr}_1 [Eq. (3.4)]. As \overline{Fr}_1 increases, the strength or size of the evanescent region also increases. The averaged,

normalized kinetic energy in the propagating region as a function of \overline{Fr}_1 is shown in Fig. 3.9. For both the medium and the steep topographies, increasing \overline{Fr}_1 decreases \overline{KE}_2^* and at $\overline{Fr}_1 > 1.2$, \overline{KE}_2^* decreases rapidly. A higher value of \overline{Fr}_1 is indicative of a high ω_f or low N and thus a relatively weak wave as the fluid cannot sustain the motion of the evanescent wave [See Eqs. (3.20)-(3.23)]. \overline{Fr}_1 has less of an influence on normalized, propagating kinetic energy for the steep topography in the experiments than is seen for the medium topography. The greatest discrepancy between the model and the experiments for the steep topography occurs when $\overline{Fr}_1 > 1.3$ and $\overline{KE}_2^* < 10^{-3}$. This discrepancy for the steep topography is likely due to the non-linear effects seen in the steep topography experimental data that are not accounted for in the model.

The curve fits follow Eq. (3.32), replacing H/D with \overline{Fr}_1 . The medium topography experimental curve fit to the data ($C_1 = -0.90$, $C_2 = 6.29$, $R^2 = 0.37$) follows the general trends of the model curve fit ($C_1 = -0.35$, $C_2 = 12.72$, $R^2 = 0.94$), but with greater kinetic energy when $\overline{Fr}_1 > 1.16$. The curve fits for the steep topography experiment ($C_1 = -1.76$, $C_2 = 2.68$, $R^2 = 0.36$) and model ($C_1 = -0.49$, $C_2 = 9.85$, $R^2 = 0.90$) show significant differences, but the model line follows the trend of the medium topography curves, especially for the experimental values. While not all of the cases are shown in Fig. 3.9, each curve was fit to the entire applicable set of data. For high \overline{Fr}_1 , the steep topography maintains more kinetic energy in the propagating region than the medium topography. This will be explored further with the model in the following paragraphs. The medium and steep topography trend lines for the model predict a maximum \overline{KE}_2^* of 0.30, meaning 30% of the original kinetic energy is retained in the propagating region. However, the experiment trend line for the medium topography indicates almost 20%, while the steep topography experiments are just over 10%.

With the experimental and model relation established, we now exercise the model further to explore a more direct relationship between the different dimensionless variables. Figure 3.10 shows \overline{KE}_2^* as a function of both H/D (shown with different line markers) and \overline{Fr}_1 (abscissa). Here three different values of H/D are chosen for each topography and \overline{Fr}_1 is varied by changing the height of the evanescent region and the height of the topography while other variables (ω_f , W/H ,

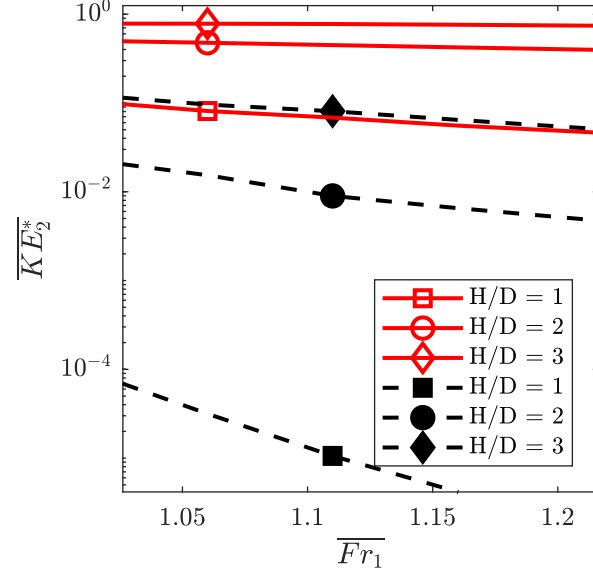


Figure 3.10: \overline{KE}_2^* as a function of H/D and \overline{Fr}_1 for the analytical model. The solid red line indicates the medium topography, while the dashed black line is the steep topography. Markers for H/D as shown.

and N profiles) are held constant. As seen in the previous figures, increasing H/D and decreasing \overline{Fr}_1 leads to an increase in relative kinetic energy. For the medium topography at $\overline{Fr}_1 = 1.11$, the average kinetic energy transmitted into the propagating region increases from 6% to 78% by increasing $H/D = 1$ to $H/D = 3$. This increase is larger for the steep topography under the same condition and \overline{KE}_2^* increases from less than 0.001% to 8%. The model also shows that with a high H/D for the steep topography and low H/D for the medium topography, the steep topography can transmit greater kinetic energy to the propagating region than the medium topography for the same \overline{Fr}_1 . This was seen in Fig. 3.8 where some cases of the steep topography had higher kinetic energy than the medium topography, but only when the steep topography has a higher H/D value.

Figure 3.11 depicts scenarios for varying topographic slope and stratification profiles. In Fig. 3.11(a), \overline{KE}_2^* increases with increasing W/H , which represents the relative slope of the topography. The width of the topography was varied while maintaining a constant height of 10 cm, which also varied the horizontal wavelength according to Eq. (3.18). The Gaussian parameter B [Eq. (3.3)] was varied based on W . Parameters for the density profile were held constant and follow Case 4 from Table 3.1. The excursion length and excitation frequency were also maintained

as values from Case 4. With $W/H = 10$, almost 80% of the kinetic energy from the evanescent region is transmitted into the propagating region. For Case 4, with $W/H = 1.8$, marked on Fig. 3.11(a) as a red circle, only 2.5% of the initial kinetic energy passes into the propagating region. As shown previously, in the presence of a turning depth, topography with steep slopes generate internal waves with less kinetic energy in the propagating region for a given H/D or \overline{Fr} . Also W , the width of the topography, indicates an increase in the wavelength of the topography. A topography with a larger wavelength will generate evanescent waves with higher kinetic energy which will then pass into the propagating region.

In Fig. 3.11(b) and 3.11(c), the influence of the exponential stratification is explored. With a density profile of $\rho = a \exp(bz) + c$, the stratification is defined as $N^2 = -gab \exp(bz)/\rho_0$. For both Fig. 3.11(b) and 3.11(c), H/D , ω_f , W/H , L , and \overline{Fr}_1 are held constant and match Case 4. The topography height varies to maintain H/D , and width is defined by $W = 1.8H$, maintaining the same W/H ratio as the medium topography. In Fig. 3.11(b), a is normalized by the reference density ρ_0 . Increasing a/ρ_0 from 0.092 to 0.149 causes a 95% decrease in the normalized, average kinetic energy in the propagating region. Although a weaker stratification leads to initially more energetic evanescent waves, the stratification also increases more rapidly throughout the evanescent region with a larger value of a , causing an overall decrease in the kinetic energy in the propagating region. However, as shown in Fig. 3.11(c), increasing bH causes an overall increase in the kinetic energy in the propagating region. Here, b is normalized by H , the height of the topography. Increasing bH causes an initially weaker stratification but a larger b , meaning a value that is less negative, causes the stratification to increase at a slower rate. Thus the evanescent wave does not decay as rapidly and more kinetic energy passes through the evanescent region into the turning depth. Although bH changes by less than one order of magnitude, \overline{KE}^* increases by three orders of magnitude.

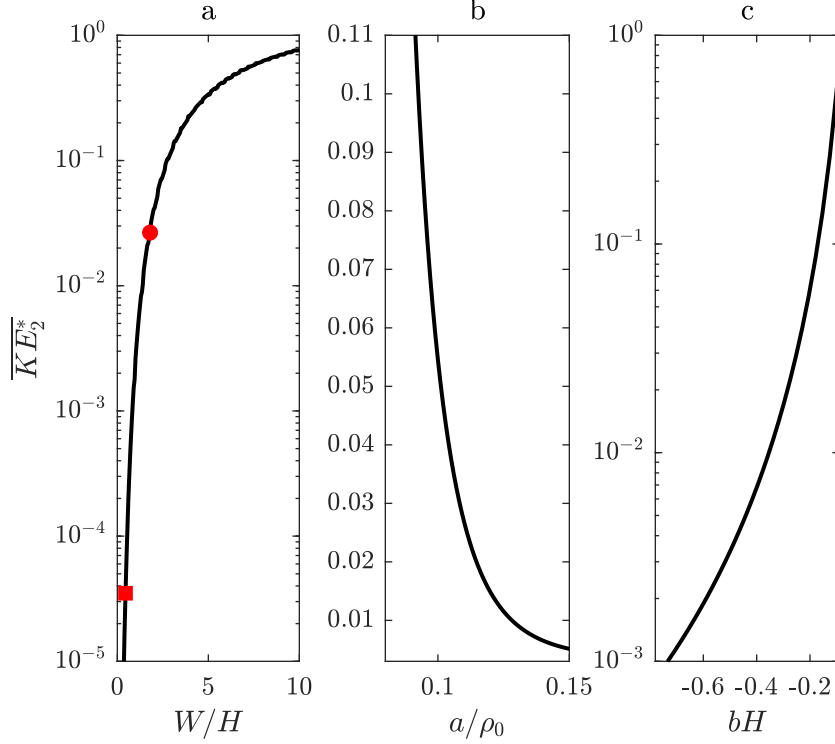


Figure 3.11: \overline{KE}_2^* is shown as a function of W/H , a/ρ_0 , and bH , showing the effects of topographic shape (a) and an exponential density profile in (b) and (c). In (a), the square and circle indicate $W/H = 0.45$ and 1.8 , or the steep and medium topographies, respectively.

3.6 Ocean case study

We now use the linear model to investigate the propagating internal wave kinetic energy generated by an oceanic feature. To use the linear model we estimate the shape of the topography, the natural frequency profile, and the velocity of the tide and assume a frame of reference where the topography moves through quiescent water. Feature data comes from the *Ocean Data View 4* using a GEBCO 2014 6' worldwide bathymetry map [101]. The feature is at 15° N, ranges from 129.6° to 130.2° E, and can be approximated as a Gaussian topography as seen in Fig. 3.12. In the figure, the data from the GEBCO bathymetry map is shaded and the Gaussian curve fit laid over the feature of interest with a dashed line. For use in the linear theory model, the Gaussian curve fit is centered at zero. The equation for the fit is given by

$$z_{\text{top,ocean}} = 5868 - 831.3 \exp\left(\frac{-x^2}{10970^2}\right) \quad (3.33)$$

with $-20000 < x < 20000$ m and the base of the feature at a depth of 5868 m. In order to apply the feature to the model, it is assumed that the feature is two dimensional. We assume a tidal velocity of 4 cm/s for the M2 semidiurnal tide based on the work by Poulain and Centurioni [102], who also indicate that in the Philippine Sea the M2 tide oscillates zonally, or left to right over the topography shown in Fig. 3.12.

Using data from the World Ocean Circulation Experiment (WOCE) for cruise P08N located at 129.99° E, 15.01° N, the natural frequency profile was calculated. This location is the closest data near the chosen oceanic topography [50]. We followed the method of King et al. [19] to smooth and average the CTD data. Temperature and salinity data is averaged over a set depth or bin size and then the natural frequency is calculated with the Gibbs Sea Water TEOS-10 Matlab tool box [103]. King et al. recommend a bin size of between 100 and 200 m and we chose 200 m for this data set because it provided a smooth curve while retaining the major characteristics of the profile. The natural frequency profile indicates a turning depth at a height of 4367 m, which is above the topography. However, the profile does not extend down to the bottom of the oceanic feature. A curve fit was applied to the smoothed data to extend the profile to the bottom of the topography. The curve fit is given by

$$\ln(N^2) = a_1 \exp \left[\frac{-(z - b_1)^2}{c_1} \right] + a_2 \exp \left[\frac{-(z - b_2)^2}{c_2} \right] \quad (3.34)$$

where $a_1 = -15.14$, $b_1 = 4831$, $c_1 = 6553$, $a_2 = -5.788 \times 10^{12}$, $b_2 = 3.658 \times 10^4$, and $c_2 = 5993$ and \ln refers to the natural logarithm. The natural frequency profile is plotted in Fig. 3.13(a). To maintain consistency between this figure and those given previously, the evanescent region is at the top of the figure with the propagating region beginning at 4367 m.

Based on the oceanic feature and natural frequency profile, we use the analytical model to calculate a kinetic energy profile shown in Fig. 3.13(b). Kinetic energy is again normalized by the evanescent wave energy at the tip of the topography to be consistent with the previous results. Starting at the top left corner, KE^* decreases rapidly through the evanescent region until

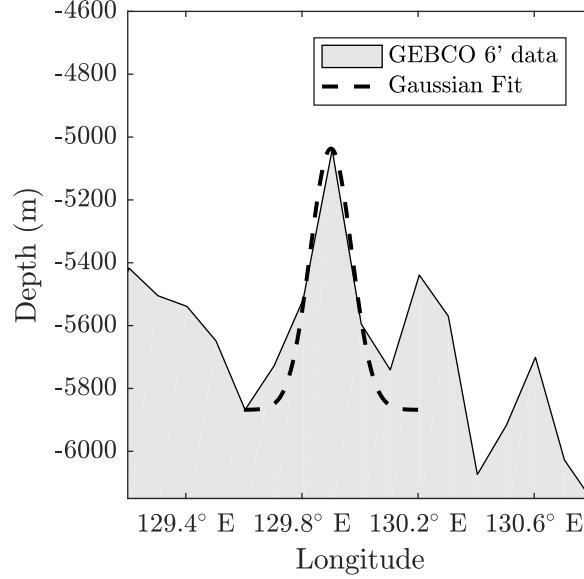


Figure 3.12: Data from the GEBCO worldwide bathymetry map is indicated by the shaded portion, with a Gaussian curve fit through topographical feature analyzed in this work.

it reaches the turning depth. The Airy integral provides the needed patch into the propagating region, where the kinetic energy of the internal wave at first decreases and then increases. In the experimental cases, shown previously, this increase was not seen due to the limited depths of the propagating region. Kinetic energy increases due to increasing N which causes an increase in m as well. Although the velocity amplitudes are inversely proportional to $m^{1/2}$, kinetic energy is proportional to A^2 and m^2 , leading to an overall increase in energy. However, the energy flux, $c_{gz}\{E\} = -\rho_0 A^2 m \omega / (2k^2)$, is constant throughout the propagating region [74].

The Airy integral in Fig. 3.13(b) uses a smaller percentage of the vertical wavelength than the experiments. Testing the model with the experiments indicated that using 1% of the vertical wavelength to start and end the Airy integral minimized the effects of the matching condition (See Section 3.4.2). For this oceanic scenario, this percentage is reduced to 0.001%. Increasing or decreasing this value led to an increase in the overall kinetic energy in the propagating region. The minimum value was chosen to prevent an overestimate of the kinetic energy.

The average, normalized kinetic energy from the end of the Airy region to $\overline{Fr}_2 = 0.952$ at a depth of 4587 m is $\overline{KE}_2^* = 0.57$. The minimum KE^* in the propagating region occurs near the

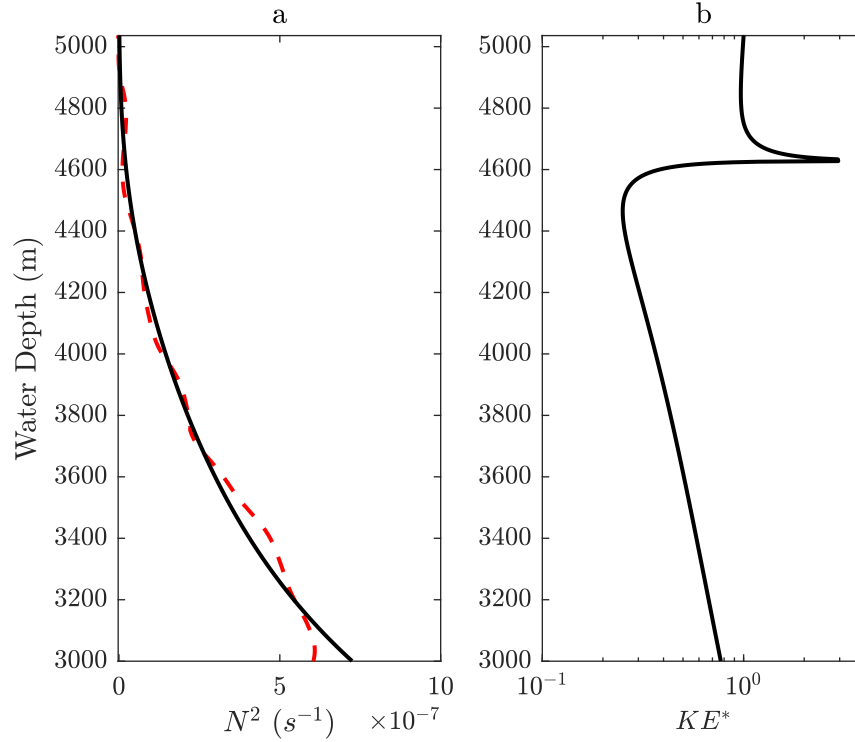


Figure 3.13: WOCE data is used to calculate N^2 indicated by the red dashed line in (a), while the black line is the curve fit of the data used for the model analysis. The normalized kinetic energy calculated from the model is shown in (b) as a function of depth.

turning depth at a depth of 4466 m with a value of 0.25. This 25% transmission could be taken as the energy that is able to pass through the turning depth and into the propagating region, and is a nontrivial portion of the original kinetic energy of the evanescent wave. While this model is a linear approximation of a non-linear event, it does indicate that internal waves generated from evanescent waves passing through the turning depth can still maintain a significant portion of the original kinetic energy formed from M2 tidal oscillations across oceanic bathymetry within evanescent regions.

3.7 Conclusion

Past investigations of the influence of evanescent regions on internal waves have focused on an internal wave approaching an evanescent region and the subsequent reflection and/or transmission of internal wave energy at the turning depth. Here, we studied the scenario where evanescent

waves approach a turning depth and become propagating internal waves. We expanded upon the work of Paoletti et al [18] by creating an analytical model which predicts the kinetic energy of internal waves generated from an evanescent region. The model is then compared to experiments and the effects of topographical shape, stratification profile ($\overline{Fr_1}$), and the relative distance between the topography and the propagating region (H/D) on internal wave kinetic energy were explored.

Similar to Paoletti et al [18], we found that the medium Gaussian topography, with a more gentle slope, has a higher kinetic energy in the propagating region than the steep Gaussian topography. For high H/D and low $\overline{Fr_1}$, the medium topography theory showed that the evanescent waves transmit up to 62.5% of the kinetic energy at the topography surface into internal waves in the propagating region, while the experiments indicated a maximum of 43.5% (See Fig. 3.8). While not an exact match, the model predicts similar values to the experiment. However, the model does not match well with the steep topography as it approaches the limit of criticality. The experiments for the steep topography indicate the maximum kinetic energy in the propagating region is near 10% of the original kinetic energy at the tip of the topography, while the model indicates closer to 20% (See Fig. 3.9). As seen in Fig. 3.11, decreasing the slope, indicated by an increasing W/H , increases the percentage of energy transmitted into the propagating region. Also, Fig. 3.10 indicates that only with larger values of H/D does steep topography generate internal waves with higher kinetic energy than medium topography.

The experiments and model also indicate the importance of the stratification in estimating internal wave kinetic energy. Increasing $\overline{Fr_1}$, indicating a large, or strong, evanescent region, causes a decrease in propagating region kinetic energy. For the exponential density profile, the model indicates that low values of a/ρ and high values of bH increase \overline{KE}_2^* due to a slow increase in the natural frequency in the evanescent region, causing a slower decay of the evanescent waves and more kinetic energy transferred into the propagating region.

To show a potential use of this analytical model, an oceanic case study was also explored and results show the average kinetic energy that passed from the evanescent region, through the turning depth and into the propagating region had 25% of the original kinetic energy of the evanes-

cent wave. While this is only one case, it indicates that evanescent waves that become internal waves could transfer significant energy from tidal motions away from the topography and into the general ocean.

Future work with this model could include applying it to more oceanic topographies which are situated in evanescent regions (relative to the M2 tidal frequency) to provide an overall estimate of the kinetic energy of internal waves generated from tidal motions across topography. Also, continued investigations into the turbulence generated waves could provide insight in how to improve the model, possibly by including viscosity. As both topography shape and stratification profile impact the overall kinetic energy, this work could also be expanded upon by exploring more complex topographies and other realistic stratification profiles.

CHAPTER 4. EVANESCENT TO PROPAGATING INTERNAL WAVES IN SIMULATIONS, EXPERIMENTS, AND LINEAR THEORY

This chapter was submitted to the journal Experiments in Fluids.

4.1 Contributing authors and affiliations

Allison Lee, Kyle Hakes, Julie Crockett, Department of Mechanical Engineering, Brigham Young University, Provo, UT 84602

Yuxuan Liu, Michael R. Allshouse, Mechanical and Industrial Engineering, Northeastern University, Boston, Massachusetts 02115

All simulations were performed at Northeastern University through the Texas Advanced Computing Center.

4.2 Abstract

Internal waves can be generated by evanescent waves which pass through a turning depth. The kinetic energy density of these waves is investigated with experiments, numerical simulations, and linear theory using a Gaussian shaped topography placed in an exponential density profile. Kinetic energy density is estimated in two manners: directly calculating kinetic energy from velocity and indirectly by relating variations in the natural frequency to kinetic energy. All methods show similar trends in the percentage of energy retained by the internal waves as a function of $\overline{Fr}_1 D/H$. A correlation between linear theory and numerical simulations is presented, along with guidelines for when each of the discussed methods is most accurate.

4.3 Introduction

Internal waves play an important role in both the ocean and atmosphere as they transfer energy and effect mixing in both mediums [3, 8, 11]. However, observing internal waves in the ocean or atmosphere is complex due to their lack of visibility: they only exist as small variations in density within a fluid, which are generally imperceptible to the eye. Field observations must rely on direct readings of density whereas experimental methods can use optical techniques such as synthetic schlieren (SS), which uses the variation in the index of refraction of different salinity water, or particle image velocimetry. However, experiments must be confined, and even these techniques have disadvantages. Mathematical analysis is another option, but significant assumptions must be made to solve spatially varying, three-dimensional, velocity, pressure, and density fields through time. Numerical methods may be used to provide traction to the problem, but issues of resolution are regularly present. A discussion of the state of these methodologies, SS, theory, and numerical methods, with specific examples relating to internal waves in nonuniform stratifications (which will be explored here) follows.

A common experimental methodology for studying internal waves over the past few decades has been synthetic schlieren. This represents a variation on schlieren imaging where the index of refraction associated with water salinity is used to evaluate the apparent motion of a mask consisting of a series of dark lines or dots placed behind a tank filled with varying salinity water. A comparison between the mask with no disturbance of the stratified liquid and the perceived displacement of the mask during wave propagation can be related to the density perturbation [58, 104, 105]. The density perturbation defines the natural or buoyancy frequency, N , through

$$N^2 = \frac{-g}{\rho_0} \frac{d\rho}{dz} \quad (4.1)$$

where g is the gravitational constant, ρ_0 is a reference density, and z is the vertical coordinate. An estimate of the variation in N is often accomplished experimentally and the ΔN^2 field, which is directly related to the apparent displacement of the mask, is displayed to show general wave

propagation dynamics including flow field amplitudes and spectra. This methodology has been used to explore internal wave dynamics ranging from simple wave generation by an oscillating cylinder [86, 104] or two dimensional topography [28, 34] to more complex wave fields expected from wave generation by three dimensional objects [106] or wave-wave interactions [46]. SS has even been extended to three-dimensions [107–109] and microscale applications [110]. It can be used with varying N profiles as well [20, 100]. Most of these prior works display the general dynamics of the flow field, including wave amplitude, wavenumber, and frequency in conjunction with a visual image of the propagating wave. Recently, however, it was shown that the ΔN^2 field could also be manipulated mathematically to estimate kinetic energy density [20, 100] as well as energy flux and the pressure field [99, 111].

Theoretical methods to analyze internal wave generation and propagation must use a variety of assumptions if an exact solution is to be found. These assumptions may include that the flow is inviscid, that waves have small amplitudes, or that wave amplitude, wavenumber, frequency, and N slowly vary over wavelengths. Frequently, the Boussinesq approximation, indicating the variation in density is small relative to the background density [4], is valid for oceanic internal wave investigations. Many or all of these may be used to more quickly analyze wave propagation. Ray theory represents one of the simplest mathematical methods, which results in tracing the path of wave energy. It has been used throughout the ocean and atmosphere for waves propagating through varying velocity and N profiles with great success [69–73]. Other analytical methods have been used for a plethora of internal wave dynamics analysis: linear theory of wave generation over weak two-dimensional topography [75]; Green’s function methods for wave generation by a moving point mass source [76]; small-amplitude, inviscid flow analysis in the Boussinesq approximation for wave propagation through a sharp N profile [77]; linear theory for a two-dimensional plane wave at an N interface [78]; linear theory for two dimensional, small amplitude wave beam transmission and reflection [79]; linear theory with the Boussinesq and small amplitude approximations with Airy function matching for evanescent waves travelling through a turning depth due to varying stratification [100]; to name a few. Although significant assumptions must be made for

these exact solutions, each result has contributed to our understanding of internal wave generation and propagation in variable stratifications and flow situations.

Using numerical methods, the full equations of wave motion in two or three dimensions can be solved. Nonlinearities can be included and assumptions regarding the scales of the waves and changing parameters are no longer necessary. Although considerable effort has been made to model internal waves in a variety of applications [11], we will focus on prior work involving two-dimensional solutions in varying stratification conditions. Gravity wave packets, as opposed to beams, can transmit energy through an evanescent level through the wave-induced mean flow [66]. Effects of finite amplitude on internal wave propagation in an abruptly changing N profile is explored numerically in the Boussinesq approximation [67]. An extreme change in N occurs in the ocean at the pycnocline where the generation of harmonics from incident internal wave beams was shown to be a strong function of pycnocline thickness using fully nonlinear direct numerical simulations [68]. Turning depths in exponential N stratified Boussinesq flows have been analyzed numerically and showed relatively good agreement with nonlinear theory [64]. Paoletti et al. [18] used 2-D numerical simulations in the Boussinesq approximation to study wave generation by tidal flow over primarily Gaussian topographies in exponential N profiles. In these types of numerical simulations, the kinetic energy density can be estimated directly from the velocity field or using the ΔN^2 field, similar to how it must be estimated when analyzing SS data. Thus a direct comparison between the two methods can be made.

Here we present the effect of the difference in methodology on the kinetic energy density approximation using a direct calculation or the ΔN^2 field. In SS, only the ΔN^2 field can be used. For analytical solutions, however, kinetic energy may be calculated directly from the velocity field. With numerical simulations both methods of estimating kinetic energy can be assessed and each are used to explore both large amplitude (to compare with experiments) and small amplitude (to verify large) topographic disturbances. Differences between the capabilities of the testing methods and kinetic energy calculation methods are discussed for lab based wave generation and propagation. Specifically, an exponential N profile is used such that generated waves will be evanescent and then

undergo a transition (at the turning depth) to propagating waves as N increases, similar to what is seen in deep ocean regions [19]. Recent works have shown that these resultant propagating waves contribute to the overall global energy balance within the ocean [18, 100].

This investigation provides significant insight into the strengths and weaknesses of the different methods, with a specific emphasis on the kinetic energy density in the propagating region. Mathematically, the region of the turning depth must be estimated using an Airy function approximation and these are found to hold quite well. In the SS experiments, the region where the approximation of kinetic energy from ΔN^2 is valid is clarified and described. Numerical simulations provide a bridge between the methods and show good agreement with both. In Sec. 4.4 all three methodologies are described in detail. Results are presented in Sec. 4.5, a discussion of the efficacy of each method is given in 4.6, and conclusions of the work are discussed in Sec. 4.7.

4.4 Methodology

This section begins with the parameters that were constant for each method and then details the three different processes used to investigate the kinetic energy of internal waves generated from an evanescent region. Figure 4.1 provides an example of the natural frequency profile (a) and the domain for the experiments and linear theory (b). In Fig. 4.1(b), evanescent and propagating regions are labeled as $N < \omega$ and $N > \omega$, respectively. The excursion length (L), height of the topography (H), and distance between the topography and the turning depth (D) are indicated. The grey dashed box shows the approximate location of the camera window, while the beginning and end of the Airy region ($z_{1,Ai}$, $z_{Ai,2}$) (See Sec. 4.4.1) is shown with white dashed lines. The simulations were performed with a flipped domain (topography at the bottom of the domain), but will be discussed throughout this work in the same orientation shown in Fig. 4.1(b).

A Gaussian topography was used and is given by the profile

$$h = H \exp(-x^2/B^2) \quad (4.2)$$

$$B^2 = W^2/18 \quad (4.3)$$

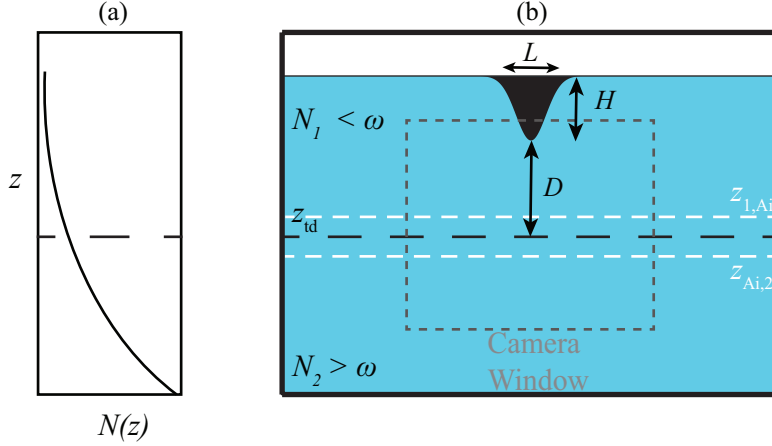


Figure 4.1: An example of the natural frequency profile in the tank (a) shown relative to the experimental setup (b)

where $H = 0.10$ m is the peak height of the topography. For this topography, $W = 0.18$ m is the width of the topography where the height of the topography is 1% of H . For the experiments and linear theory analysis, the topography oscillated back and forth, while the simulations set a fixed topography and used tidal oscillations to generate waves.

Density profiles used in the simulations and theory were based off the actual density profiles from the experiments. A modified version of the double bucket method [93] was used to create an exponential density profile. After filling the tank, density measurements were taken every 3 cm and the points were fit to the equation

$$\rho = a \exp(bz) + c \quad (4.4)$$

where ρ and z have units of kg/m^3 and meters, and a (kg/m^3), b (m^{-1}), and c (kg/m^3) are coefficients calculated from the exponential fit. The goodness of fit parameter, R^2 , was above 0.99 for all cases. Cases 1 through 4 used the same density profile with coefficients for Eq. (4.4) were $a = 109.1 \text{ kg/m}^3$, $b = -2.57 \text{ m}^{-1}$, and $c = 1016.3 \text{ kg/m}^3$, while the coefficients for Case 5 were $a = 106.2 \text{ kg/m}^3$, $b = -2.76 \text{ m}^{-1}$, and $c = 1020.1 \text{ kg/m}^3$. In all cases, the water height was 68.0 cm, such that the tip of the topography is at 58.0 cm. The natural frequency profile was

Table 4.1: A summary of the parameters of each case.

Case	k_L (m ⁻¹)	ω_f (s ⁻¹)	z_{td} (cm)	L (cm)	D/H	\overline{Fr}_1	$\overline{Fr}_1 D/H$
1	25.0	0.80	56.4	5.1	0.13	1.01	0.13
2	25.0	0.89	48.5	5.1	0.95	1.06	1.00
3	24.4	1.01	39.3	5.7	1.87	1.13	2.11
4	24.4	1.10	32.0	5.7	2.60	1.18	3.06
5	24.6	1.21	24.5	5.5	3.35	1.25	4.18

calculated with Eq. (4.1). N is plotted against height in Fig. 4.1(a) with the turning depth ($N = \omega$) labeled in Fig. 4.1(b).

A complete set of case parameters is given in Table 4.1 where k_d is the dominant horizontal wavenumber, ω_f is the topography or tidal forcing frequency, z_{td} is the location of the turning depth. The horizontal wavenumber is calculated as $k_L = 2\pi/\lambda_x$ where λ_x is the horizontal wavelength which, based on the results of Lee and Crockett [100], can be defined as

$$\lambda_x = W + L \quad (4.5)$$

Also listed in Table 4.1 are three non-dimensional numbers: D/H , \overline{Fr}_1 , and $\overline{Fr}_1 D/H$. D is the distance between the tip of the topography and the turning depth [see Fig. 4.1(b)]. The ratio D/H indicates the number of topographic heights between the topography and the turning depth, and provides a measure of the distance evanescent waves will travel and decay before reaching the propagating region. \overline{Fr}_1 is the average Froude number in the evanescent region and is used to describe the stratification strength of that region. It is defined as $\overline{Fr}_1 = \omega/\overline{N}_1$, where \overline{N}_1 is the average natural frequency over the height D . Throughout this work the subscript 1 refers to the evanescent region. Because $\omega > N$ throughout the evanescent region, \overline{Fr}_1 is always greater than unity. Combining D/H and \overline{Fr}_1 gives a non-dimensional number that provides insight into the combined effects of topography placement and the influence of the stratification.

Kinetic energy density is calculated as

$$KE = \tilde{U}^2 + \tilde{W}^2 \quad (4.6)$$

where U and W are the horizontal and vertical wave velocities, respectively, and the tilde indicates Fourier amplitudes. Kinetic energy, in this work, is either calculated directly using the amplitudes of velocity, or it is estimated indirectly by relating ΔN^2 to \tilde{U} and \tilde{W} . Further details on the indirect method are given in Sec. 4.4.2. The indirect method is used in the experimental analysis while the direct calculation is used in the theory. Both methods are used with the numerical simulations and compared to the experimental results and theoretical calculations.

4.4.1 Theory

Linear theory is used to calculate the horizontal and vertical velocity of the waves in the evanescent and propagating regions. Following the work of Lee and Crockett [100], the velocity can be calculated starting at the topography into the evanescent region, through the discontinuity of the turning depth with the Airy function, and into the propagating region. Full details for this method can be found in [100], but the main points are summarized here.

In the evanescent region, the Gaussian topography oscillates in space and time as

$$z_{\text{top}}(x, t) = H \exp \left[\frac{-(x - L \sin \omega t)^2}{B^2} \right] \quad (4.7)$$

with $z_{1,0} = z_{\text{top}}(B, 0)$ as a matching location between the topography and the vertical velocity of the generated waves. The vertical velocity is defined as

$$w_1(x, z, t) = A_1(z) \exp[i(kx - \omega t)] \exp[\theta_1(z)] \quad (4.8)$$

Taking the time derivative of Eq. (4.7) and matching it to Eq. (4.8) at $z_{1,0}$ provides the initial amplitude of the velocity $A_{1,0}$ such that

$$A_{1,0} = \frac{dz/dt}{\exp[i(kB)] \exp[\theta_1(z_0)]} \quad (4.9)$$

Both the amplitude, A_1 , and the term θ_1 vary with height to account for the varying stratification. They are defined as

$$A_1(z) = A_{1,0}/(q/q_{1,0})^{1/2} \quad (4.10)$$

$$\theta_1(z) = \int_{z_{1,0}}^z q dz \quad (4.11)$$

where $q^2 = k^2[1 - N(z)^2/\omega^2]$ is the imaginary vertical wavenumber in the evanescent region, again with q_0 calculated at $z_{1,0}$. Using the continuity equation

$$\frac{\partial u}{\partial x} + \frac{\partial w}{\partial z} = 0 \quad (4.12)$$

the horizontal velocity in the evanescent region is calculated as

$$u_1(x, z, t) = \frac{-w_1}{ik} \left[q - \frac{dq/dz}{2q} \right] \quad (4.13)$$

where it is assumed that dq/dz is negligible [100]. This assumption fails near the turning depth, where the assumption of a slowly varying amplitude breaks down. To account for this failing assumption and the singularity at the turning depth, the Airy function is used.

The Airy region begins at $z_{1,Ai} = z_{td} + 0.01(2\pi/\bar{q})$, or 1% of the average vertical wavelength (λ_z) above the turning depth in the evanescent region. It passes through the turning depth and ends at $z_{Ai,2} = z_{td} - 0.01(2\pi/\bar{m})$, 1% of average vertical wavelength in the propagating region

(See Fig. 4.1). Following Lighthill [91], the equations for velocity in the Airy region are

$$w_{\text{Ai}}(x, z, t) = Q_{0,w} \text{Ai}(\beta^{1/3}z - \beta^{1/3}z_{td}) \exp[i(kx - \omega t)] \quad (4.14)$$

$$u_{\text{Ai}}(x, z, t) = Q_{0,u} \frac{i\beta^{1/3}}{k} \text{Ai}'(\beta^{1/3}z - \beta^{1/3}z_{td}) \exp[i(kx - \omega t)] \quad (4.15)$$

where $\beta = m^2/(z_{td} - z)$ and Ai' is the first derivative of the Airy function with respect to z . The amplitudes $Q_{0,w}$ and $Q_{0,u}$ are found by matching Eq. (4.14) to Eq. (4.8), and Eq. (4.15) to Eq. (4.13), with each matching condition at $z_{1,\text{Ai}}$. It is assumed that both $Q_{0,w}$ and $Q_{0,u}$ are constant through the Airy region. The wave amplitude below the turning depth, $A_{2,0}$ is calculated by setting w_{Ai} equal to the vertical velocity in the propagating region, w_2 , at $z_{\text{Ai},2}$. This region specifically will be explored further and compared to the numerical simulations in Sec. 4.5 and 4.6 to quantify the accuracy of the kinetic energy calculations.

Following the work of Pedlosky [74], the propagating region equations for velocity can be found by assuming a wave equation for the vertical velocity (w_2) and using the continuity equation (4.12) to define the horizontal velocity (u_2). The vertical velocity again includes the terms $A_2(z)$ and $\theta_2(z)$ to account for the variation in N with height. These are defined as

$$w_2(x, z, t) = A_2(z) \exp \left[i(kx - \omega t + \theta_2(z)) \right], \quad (4.16)$$

$$A_2(z) = A_{2,0} / (m/m_0)^{1/2}, \quad (4.17)$$

$$\theta_2(z) = \int_{z_{\text{Ai},2}}^z m dz, \quad (4.18)$$

$$u_2(x, z, t) = \frac{-w_2 m}{k} \left[m - \frac{dm/dz}{2im} \right] \quad (4.19)$$

where the vertical wavenumber m is also a function of height, but dm/dz is assumed negligible [100].

Because a Gaussian topography is made of a range of wavenumbers, the waves generated by an oscillating Gaussian topography will also have a range of wavenumbers. Nappo [5] showed that for internal waves generated by a constant background wind over a Gaussian topography the

waves with the most energy correspond to

$$k_{\max} = \sqrt{2}/B \quad (4.20)$$

where B is defined in Eq. (4.3). However, Lee and Crockett [100] found that, for oscillating topography, the wavenumber associated with the peak energy would include the excursion length, and B is re-defined to include the excursion length as

$$B_L^2 = (W + L)^2/18 \quad (4.21)$$

Nappo [5] also found that the amplitude of the generated wave velocity as a function of wavenumber could be defined according to the response function

$$C_A(k) = kB_L \exp[-(kB_L/2)^2] \quad (4.22)$$

Thus, the velocity amplitude of a wave generated at any wavenumber for a Gaussian topography could be defined as

$$A_k = A_{1,0} \frac{C_A}{C_{A,\max}} \quad (4.23)$$

where the amplitude of the main wave generated, $A_{1,0}$, is calculated from Eq. (4.9) and all others are attenuated by this response function. Note for Eq. (4.22), C_A increases from $k = 0$ until it reaches a maximum at $C_{A,\max}(k_{\max}) = \sqrt{2} \exp(-1/2)$ [Eq. (4.20)]. For $k > 5/B_L$, C_A becomes negligible [5]. Thus, waves with wavenumbers in the range $0 < kB_L < 5$ will have the most energy, while waves outside of this range have negligible energy. This was seen in the results presented here, however because of the resolution limitations on the experiments, the lower limit of the wavenumber range must be adjusted. Thus the kinetic energy for all methods will be averaged over $0.5 < kB_L < 5$.

With initial velocities defined for a range of wavenumbers, the velocities of the waves in the evanescent, Airy, and propagating regions are calculated, and then averaged over one horizontal

wavelength and one period. Kinetic energy is calculated by squaring and summing the amplitudes of velocity for each wavenumber.

4.4.2 Experimental procedure

Experiments were performed in an acrylic tank with the topography oscillating on a track situated at the top of the tank. In order to maintain two-dimensional (2D) waves, the tank is 2.45 m long, 0.91 m tall, and only 0.15 m wide. An exponential density profile was created using two peristaltic pumps and the density was measured every 3 cm using an Anton Par density meter and then interpolated to generate a complete density profile for the tank.

In all cases, the topography oscillated for 15 periods before a jAi Cv-M4+Cl progressive scan camera with a resolution of 1360x1080 pixels was focused on a random dot pattern behind the tank and recorded three minutes of images at 6 frames per second. A sketch of the experimental window is outlined by a box with dashed lines in Fig. 4.1(b). Two tests were run for each case, with time in between the tests to allow the water to again become quiescent. Images were analyzed using synthetic schlieren [58] and the software Digiflow [94]. This process provides values of ΔN^2 , or the squared perturbation of the natural frequency. From this data an estimate of kinetic energy can be made by assuming plane waves with slowly varying amplitudes. Based on the work of Lee and Crockett [100] and Wunsch and Brandt [20] for the evanescent and propagating regions, respectively, the Fourier amplitudes of ΔN^2 can be used to estimate kinetic energy density in each region using Eq. (4.6).

For the evanescent region, the equations for velocity and the variation in the natural frequency are

$$u(x, z, t) = \int \tilde{U} \exp(qz) \exp[i(kx - \omega t)] dk d\omega \quad (4.24)$$

$$w(x, z, t) = \int \tilde{W} \exp(qz) \exp[i(kx - \omega t)] dk d\omega \quad (4.25)$$

$$\Delta N^2(x, z, t) = \int \Delta \tilde{N}^2 \exp(qz) \exp[i(kx - \omega t)] dk d\omega \quad (4.26)$$

where \tilde{U} , \tilde{W} and $\Delta\tilde{N}^2$ are Fourier amplitudes from a 2D Fourier transform taken through time and the horizontal direction (x). The vertical wavenumber m is imaginary in the evanescent region and q is defined as $m = iq$. Because the evanescent wave energy travels downward, the negative branch of q is used in all calculations. Using the continuity equation (4.12) and by defining

$$\frac{\partial\Delta N^2}{\partial t} = -\frac{\partial(N^2 w)}{\partial z} \quad (4.27)$$

the kinetic energy of the evanescent region can be estimated by combining (4.24) - (4.26) with (4.27). Rearranging all the terms generates an equation for kinetic energy in terms of $\Delta\tilde{N}^2$ such that

$$KE_1 = \left| \frac{-q\omega\Delta\tilde{N}^2}{k(\partial_z N^2 + qN^2)} \right|^2 + \left| \frac{i\omega\Delta\tilde{N}^2}{\partial_z N^2 + qN^2} \right|^2. \quad (4.28)$$

This equation is valued if the temporal and spatial (vertical) derivatives of the amplitudes are assumed to be negligible. This assumption is known to be accurate away from the turning depth, but will be further explored near the turning depth in this work.

Similarly, in the propagating region, the velocities and natural frequency are defined as

$$u(x, z, t) = \int \tilde{U} \exp[i(kx + mz - \omega t)] dk d\omega, \quad (4.29)$$

$$w(x, z, t) = \int \tilde{W} \exp[i(kx + mz - \omega t)] dk d\omega, \quad (4.30)$$

$$\Delta N^2(x, z, t) = \int \Delta\tilde{N}^2 \exp[i(kx + mz - \omega t)] dk d\omega. \quad (4.31)$$

Again, using Eq. (4.12) and Eq. (4.27) with Eqs. (4.29)-(4.31) and assuming that the derivatives of the amplitudes are negligible, the kinetic energy of the propagating region can be estimated as

$$KE_2 = \frac{\omega^2 N^2}{k^2(N^2 - \omega^2) + (\omega\partial_z N^2/N^2)^2} \left| \frac{\Delta\tilde{N}^2}{N^2} \right|^2. \quad (4.32)$$

From these equations, kinetic energy is found at all frequencies and wavenumbers present. To compare with the theoretically estimated kinetic energy, the kinetic energy of the experiments is

averaged over the same wavenumber range of $0.5 < kB_L < 5$. As will be shown in Sec. 4.5, the peak kinetic energy varies slightly over a small range of frequencies, specifically just above and just below ω_f . Because of this, the kinetic energy is also averaged over those three frequencies.

4.4.3 Numerical simulations

To model the generation of internal waves, we perform direct numerical simulations of the Navier-Stokes equations in the Boussinesq approximation. These simulations provide the density perturbation and velocity fields. The density perturbation field is needed to calculate ΔN^2 and subsequently the kinetic energy, which is used to compare to the experiments, while the velocity fields are used to directly calculate kinetic energy and can be compared to the theoretical energy calculations. The simulations use the CDP-2.4 algorithm, which is a finite volume solver that implements a fractional-step time-marching scheme [95, 96]. This code has previously been used to simulate internal waves and has been validated with experiments [18, 86, 88, 97–99].

The 2D simulations span the domain $x \in [-400, 400]$ cm and $z \in [0, 150]$ cm. The simulation solves for the total density ρ , pressure p , and velocity \mathbf{u}_T :

$$\frac{\partial \mathbf{u}}{\partial t} + \mathbf{u}_T \cdot \nabla \mathbf{u}_T = -\frac{1}{\rho_0} \nabla p + \nu \nabla^2 \mathbf{u}_T - \frac{g\rho}{\rho_0} \hat{\mathbf{z}} + \mathbf{f}_{\text{tidal}}, \quad (4.33)$$

$$\frac{\partial \rho}{\partial t} + \mathbf{u}_T \cdot \nabla \rho = \kappa_s \nabla^2 \rho, \quad (4.34)$$

$$\nabla \cdot \mathbf{u}_T = 0, \quad (4.35)$$

where $\rho_0 = 1000 \text{ kg/m}^3$ (density of water), $\nu = 10^{-6} \text{ m}^2/\text{s}$ (kinematic viscosity of water at 20°C), and $\kappa_s = 2 \times 10^{-9} \text{ m}^2/\text{s}$ (the diffusivity of NaCl in water). The tidal flow is implemented using a body force on the cells as was performed by [86, 88, 97, 98]. The system is initially at rest and the density field is unperturbed. The initial density field is analytically derived from Eq. (4.4). The simulations used a unstructured grid with resolutions that ranged from 0.02 to 10 cm. Boundary conditions at the bottom and top are no slip and free slip, respectively, where the topography is positioned at the bottom of the domain. The left and right boundaries are set to be periodic;

however, Rayleigh damping is used along the perimeter of the domain, thus forcing the velocity perturbation to be negligible at the left and right boundary. Rayleigh damping is also used at the top of the domain to minimize any reflections off the top boundary. To investigate the impact of the excursion length on each case, the simulations were performed with two different excursion lengths while all remaining parameters were held constant. First, the simulation was run with the excursion length $L_{10} = L/10$, and then again at L (see Tab 4.1). Temporal resolution was 0.002 and 0.004 s for the low and high amplitude simulations, respectively. Convergence studies were performed to ensure that the energy profiles changed by less than 1% when the spatial and temporal resolution were varied. A total of 60 periods were simulated with the last 30 periods being at steady state and used for the Fourier analysis. Simulations using the $L/10$ amplitude will be referred to as 1/10-amplitude cases throughout the remainder of this work. The smaller excursion length directly impacts the initial amplitude of evanescent wave velocity. A comparison of the two scenarios, full and 1/10 amplitude, also provides information about how turbulence affects the kinetic energy density in the evanescent and propagating waves and will be discussed in Sec. 4.5.

4.5 Results

This section presents physical, spectral, and kinetic energy density results of each of the four methods and provides comparisons of each. The kinetic energy density is shown both as a function of height and nondimensional numbers. An estimate of the differences between the direct and indirect methods is presented to explore where the WKB assumptions are valid away from the turning depth. Finally, the kinetic energy of the direct simulations is estimated using the theoretical calculations, and a function relating these variables and $\overline{Fr_1}D/H$ is presented.

4.5.1 Qualitative comparison

First, the results of the experiments and simulations are compared to each other qualitatively using ΔN^2 and vertical velocity fields for case 1. Figure 4.2 shows snapshots in time for three of the four methods for case 1. A horizontal green dashed line in each figure represents

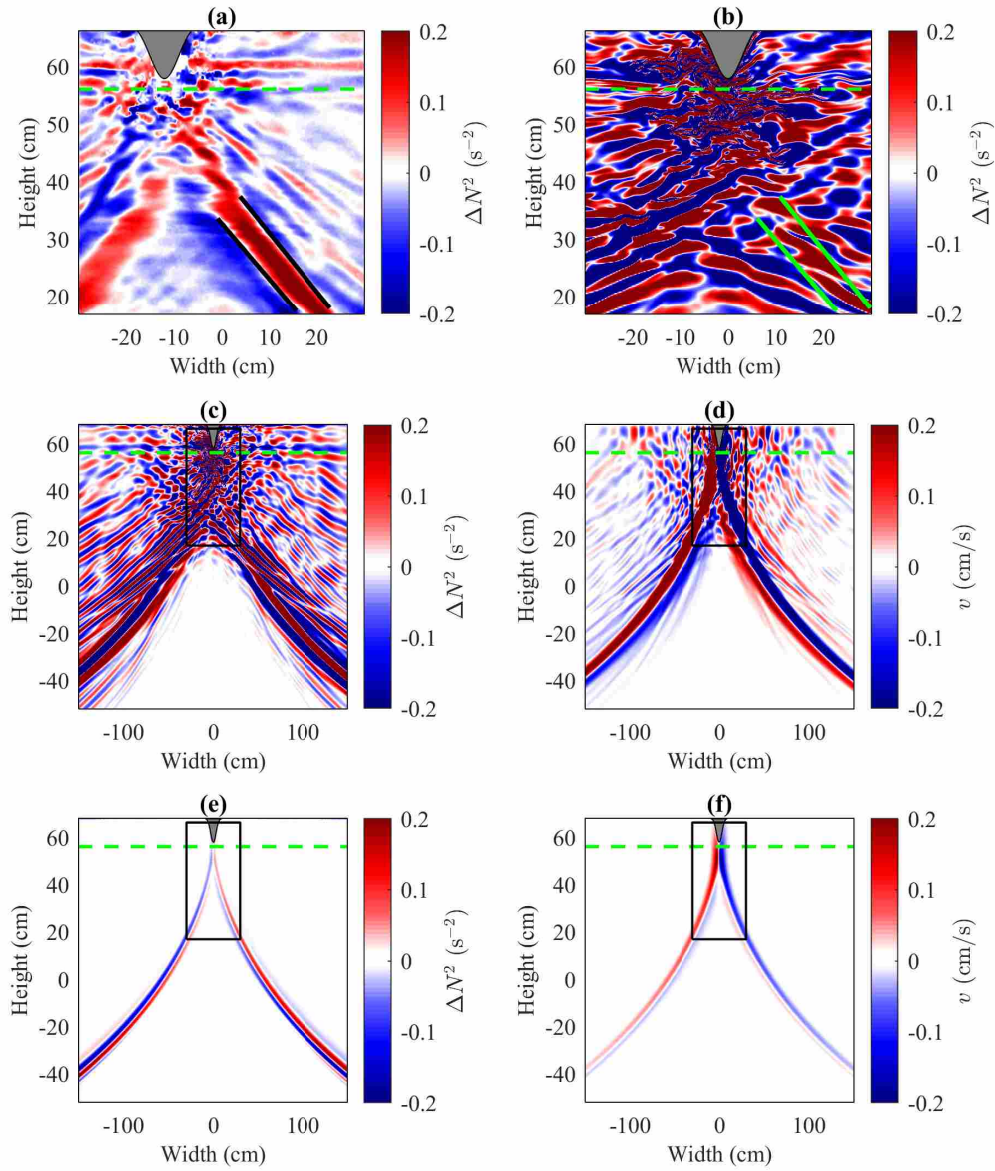


Figure 4.2: Snapshots in time of experimental ΔN^2 data (a), full amplitude ΔN^2 simulation data (b,c), full amplitude simulation velocity field (d), 1/10 amplitude ΔN^2 simulation data (e), and 1/10 amplitude simulation velocity field (f) for case 1. The topography location is masked in grey

the location of the turning depth ($z_{td} = 0.56$ m) and the topography is at the top of the image. In Fig 4.2(a), the experimental ΔN^2 field is shown. Figures 4.2(b) and 4.2(c) are the full amplitude simulation ΔN^2 field, where (b) is set to the same vertical and horizontal axis as (a). Note that the all simulation images have been flipped to match the domain of the experiments. However, the horizontal and vertical distances are much larger than the image of Figs. 4.2(a) and (b), causing the angles of propagation to look different relative to Fig. 4.2(c)-(f). To provide perspective, a rectangle indicating the location of the experiment window has been added to (c)-(f). This box matches the full size of (a) and (b). Figures 4.2(e) and (f) are similar images to Figs.4.2(c) and (d), but are the results from the 1/10 amplitude simulation.

For case 1, the topography is 2 cm away from the turning depth, resulting in a relatively small evanescent region and large propagating region. The wave beam begins at the topography and then moves vertically through the evanescent region and across the turning depth. In the propagating region, the internal wave beam near the turning depth begins with a very steep slope that gradually decreases as the natural frequency increases. Turbulence generated by the topography is manifest in Figs. 4.2(a)-(d) where the vertical velocity deviates from the dominant waves. Because of this turbulence in Fig. 4.2(b), guide lines for the wave beams have been added as green lines. These guide lines were created for Fig. 4.2(a) first (black lines), and then added to Fig. 4.2(b), and shifted 7 cm in the x -direction to match the actual location of the beam. From these guide lines, it is easier to see that the wave angles match well between the experiments and simulations. Wave beams are clearer in Fig. 4.2(c) away from the topography, and also throughout Fig. 4.2(d) Low amplitude simulations of 4.2(e) and (f) show only clear beams, without any interference because the lower amplitude does not induce overturning and turbulence in the evanescent region.

As mentioned in Sec. 4.4, a Gaussian shaped topography will generate waves at a range of wavelengths and this work focuses on the energy in a specific range of wavelengths and frequencies. Contour plots of $\Delta \tilde{N}^2$ are shown in Fig. 4.3 to demonstrate this range, provide a general comparison of the experiments and simulations, and illustrate the dynamics of waves moving through an evanescent region into a propagating region. The abscissa in the nine figures is the

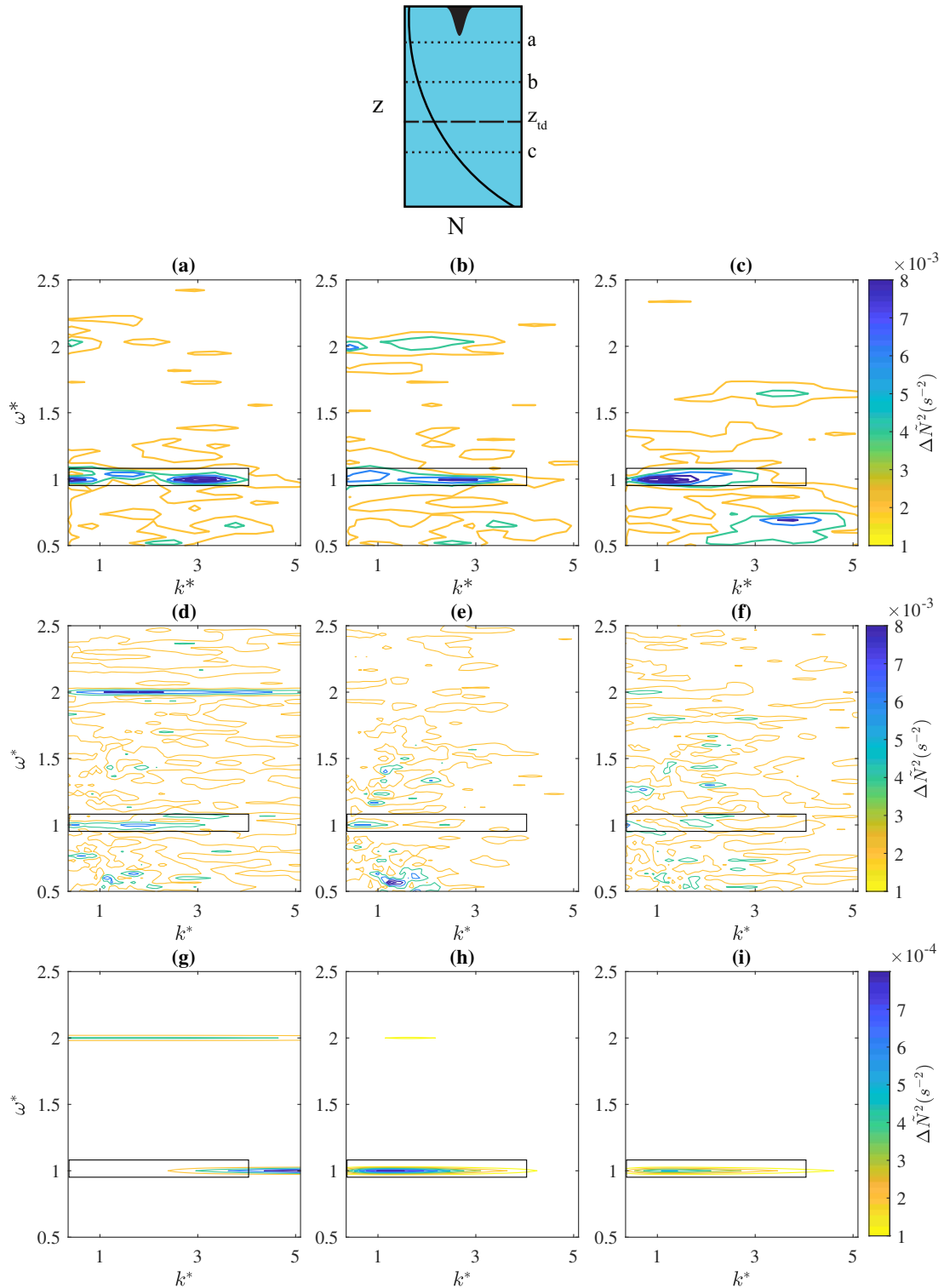


Figure 4.3: Contour plots of the experiments (a-c), full amplitude simulation (d-f) and 1/10 amplitude simulation (g-i) for case 1. A sketch of the relative height of each scenario is shown on the left. Each column of figures is at the same location, meaning figures (a), (d), and (g) are at the tip of the topography

normalized wavenumber, $k^* = k/k_N$, with the normalized frequency $\omega^* = \omega/\omega_f$ on the ordinate. Each figure corresponds to data from case 1 from three different heights for three of the methods: experiment (a-c), full amplitude simulation (d-f), and low amplitude simulation (g-i). A schematic of the relative depths for each contour plot is shown at the top of the figure: (a), (d), and (g) are located at the tip of the topography; (b), (e), and (h) are in the evanescent region halfway between the topography and the turning depth; (c), (f), and (i) are in the propagating region at the height corresponding to $N/\omega = 1.1$. Scales for $\Delta\tilde{N}^2$ are the same for the experiments and full amplitude simulation, but are an order of magnitude lower for the 1/10 amplitude simulations. In each figure, a box is plotted indicating the values of $0.3 < k^* < 3.7$, which is equivalent to $0.5 < kB_L < 5$ or the range of wavenumbers over which the kinetic energy is averaged (See Sec. 4.4.1).

For all methods and heights, there is a large peak at $\omega^* = 1$ in $\Delta\tilde{N}^2$, which corresponds to high wave energy. However, the energy is more spread in wavenumber space with the largest peaks generally within the plotted box. These peaks are most clearly seen in the experiments and 1/10 amplitude simulation, but the full amplitude simulation has a less pronounced peak at the expected values. The turbulence and noise seen in Fig. 4.2(b) results in $\Delta\tilde{N}^2$ spreading over a larger range of ω^* and k^* for the full amplitude simulation, especially near the topography [Fig. 4.3(d)]. Also, near the topography in the 1/10 amplitude simulation [Fig. 4.3(g)] it is clear that $\Delta\tilde{N}^2$ extends above $kB_L = 5$ (outside the rectangle), but that energy quickly dies away with depth and is not present as the wave propagates.

In Fig. 4.3 a harmonic is present in each of the evanescent region figures (columns 1 and 2) at $\omega^* = 2$, which is consistently a smaller peak than the peaks seen at $\omega^* = 1$. This harmonic decays and is generally not visible in the propagating region. Note also that the harmonic of $\omega^* = 2$ is strongest in the low amplitude case and remains throughout the evanescent region, in both Fig. 4.3(g) and (h), but is nearly imperceptible approaching the turning depth and below it. In the full amplitude simulation, the harmonic decays quickly in the evanescent region and is not clearly visible in Fig. 4.3(e), but the harmonic wave does remain in the propagating region in (f).

These results confirm that the kinetic energy is spread over a range of wavenumbers and also indicates that there is energy within the harmonics of the excitation frequency near the topography. However, throughout the remainder of this work, the kinetic energy is averaged only at the excitation frequency ω_f and excludes the energy at the harmonics as these are shown to be unimportant in the propagating region. The 1/10 amplitude data is not quite exactly 1/10 smaller than the experiments and full amplitude simulation data, due to the lack of turbulence, but it is clear it will still be necessary to individually normalize the data from each of the methods. Additionally, Fig. 4.3 shows that turbulent fluctuations are more prominent in the numerical simulations than in the experiments, which is possibly due to the increased resolution of the simulations.

Throughout the remainder of this work, directly calculating kinetic energy from the velocity fields or indirectly estimating kinetic energy based on the derived relationship between ΔN^2 and velocity, will be referred to as the direct or indirect methods using equations (4.28) and (4.32), respectively. The experiments exclusively used the indirect method of kinetic energy calculations, while the theory used only the direct methods, and each will be discussed as such throughout the work.

4.5.2 Kinetic energy variation with depth

In Fig. 4.4 kinetic energy density (J/kg) is plotted against height for all cases and compares the experiments to the full amplitude simulations with (a)-(e) corresponding to cases 1-5, respectively. Experimental kinetic energy is indicated by a red line with a diamond marker, the indirect simulation is a black line, the direct simulation is represented by a black dashed line, and the turning depth is shown with a horizontal dotted line. In all cases and for all methods, the kinetic energy starts at a high value near the topography at $z = 0.58$ cm, and then decreases through the evanescent region. In the propagating region, the kinetic energy is nearly constant for the simulations once a sufficient distance from the turning depth has been reached. For the experiments and indirect simulations, there are oscillations in the energy. It has been seen previously that small variations in the actual density field in the experimental tank can cause oscillations in the kinetic

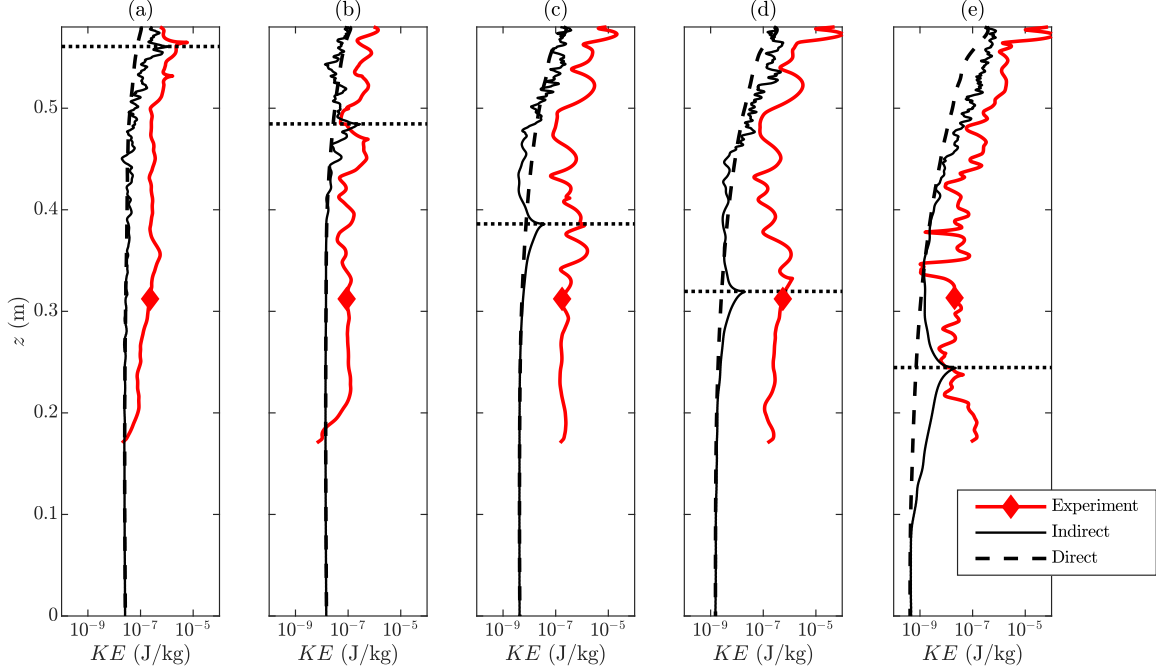


Figure 4.4: Kinetic energy of the experiments (red line with diamond marker), indirect simulations (black line), and direct simulations (black dashed line) are compared for each of the five cases. Case 1 corresponds to (a), case 2 to (b), etc.

energy calculations [100], which is one cause of the variations in the experiments. Although the simulations were performed using a smoothed density profile, there are still some oscillations in the kinetic energy obtained indirectly from the simulations, which could be due to the ΔN^2 calculation. A second order method was used to find gradients of $d\rho'/dz$ in the simulations. These values are then directly related to ΔN^2 . The oscillations would potentially decrease if higher order methods for calculating $\nabla\rho'$ were implemented. In addition, the oscillations are more significant in the evanescent region, which could be due to wave overturning and turbulence in the region, especially near the topography. Overturning has a detrimental affect on the density perturbation field, and thus would present as errors of the data for the indirect analysis of the simulations and for the synthetic schlieren experiments, but would not be present in the propagating region. However, these small variations in kinetic energy do not greatly affect the average kinetic energy of the indirect simulations in the propagating region in this work and were thus not explored further.

Comparing each of the cases, it is most noticeable that the experimental energy is generally greater than that of the simulations throughout the depth. This will be addressed through normalizing. Also, the kinetic energy in the propagating region is the smallest for case 5, Fig. 4.4(e), which has the highest value of $\overline{Fr}_1 D/H$, meaning that the turning depth is far from the topography with a relatively weak stratification. In addition, the two methods for analyzing the simulations match each other best far from the evanescent region. In the evanescent region, the two methods have similar values and are the same order of magnitude, but there are fluctuations in the indirect method throughout the region preventing the methods from matching well. There is also an increase in kinetic energy density in the indirect and experimental methods near the turning depth. Near the turning depth the vertical wavenumbers, which are found in the denominators of Eq. (4.28) and (4.32), approach zero and cause an increase in KE. This increase is an artifact of the WKB approximation no longer being valid. After the increase in KE, which dies away quickly in the simulations, the indirect and direct methods match well in the propagating region away from the turning depth. This trend will be discussed further later in this section and an estimate for the region where the indirect methods is valid will be given.

In order to make a quantitative comparison between each of the four methods, the kinetic energy density is normalized by the energy generated near the topography for each method. This normalization is necessary to accurately compare the relative amount of energy transferred into the propagating region, especially for the 1/10 amplitude simulation, which contains less overall kinetic energy relative to the other four methods. Also, the value of the theoretical energy is dependent upon the input boundary conditions, but the normalized energy remains constant regardless of the initial condition. Due to the oscillations of the experiments and indirect simulations within the evanescent region, curve fits were applied to these methods within the evanescent region near the tip of the topography. The first three points immediately below the tip of the topography were then averaged together to create KE_{norm} . These values are shown in Figure 4.5 as a function of $\overline{Fr}_1 D/H$. The solid symbols represent indirect methods of calculating KE, while the open symbols are the direct methods. Along with the experiments (red diamonds) and full amplitude simulations (black

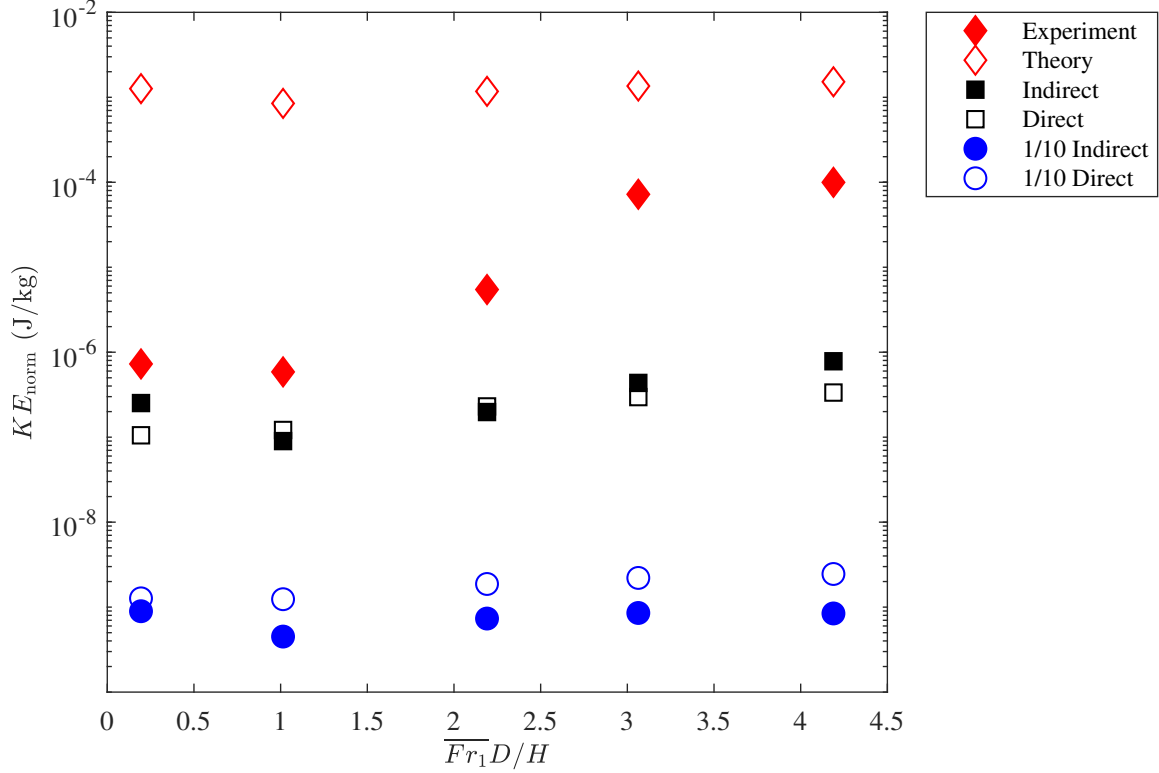


Figure 4.5: Normalizing values for the kinetic energy density for each of the methods as a function of $\overline{Fr}_1 D/H$

squares), we now include the theoretical calculations (open red diamonds) and 1/10 amplitude simulations (blue circles). The 1/10 amplitude simulations used the same setup as the full amplitude simulations except the excursion length is 1/10 the size of the value listed in Tab. 4.1 (see Sec. 4.4.3). KE_{norm} for the full amplitude simulations are approximately 2 orders of magnitude higher than the 1/10 amplitude simulations, as expected due to the order of magnitude higher velocity amplitude. For increasing $\overline{Fr}_1 D/H$, it is expected the initial kinetic energy would also increase because a high value of \overline{Fr}_1 indicates a relatively large ω_f , causing a larger initial velocity of the topography and evanescent wave. The direct simulation shows this expected increase for all values of $\overline{Fr}_1 D/H$. However, the experiments, theory, and indirect analysis of the simulations only follow this expected behavior when $\overline{Fr}_1 D/H > 1$. Case 1, with $\overline{Fr}_1 D/H = 0.13$, has the smallest evanescent region of the cases with the turning depth very near the topography, which we note causes

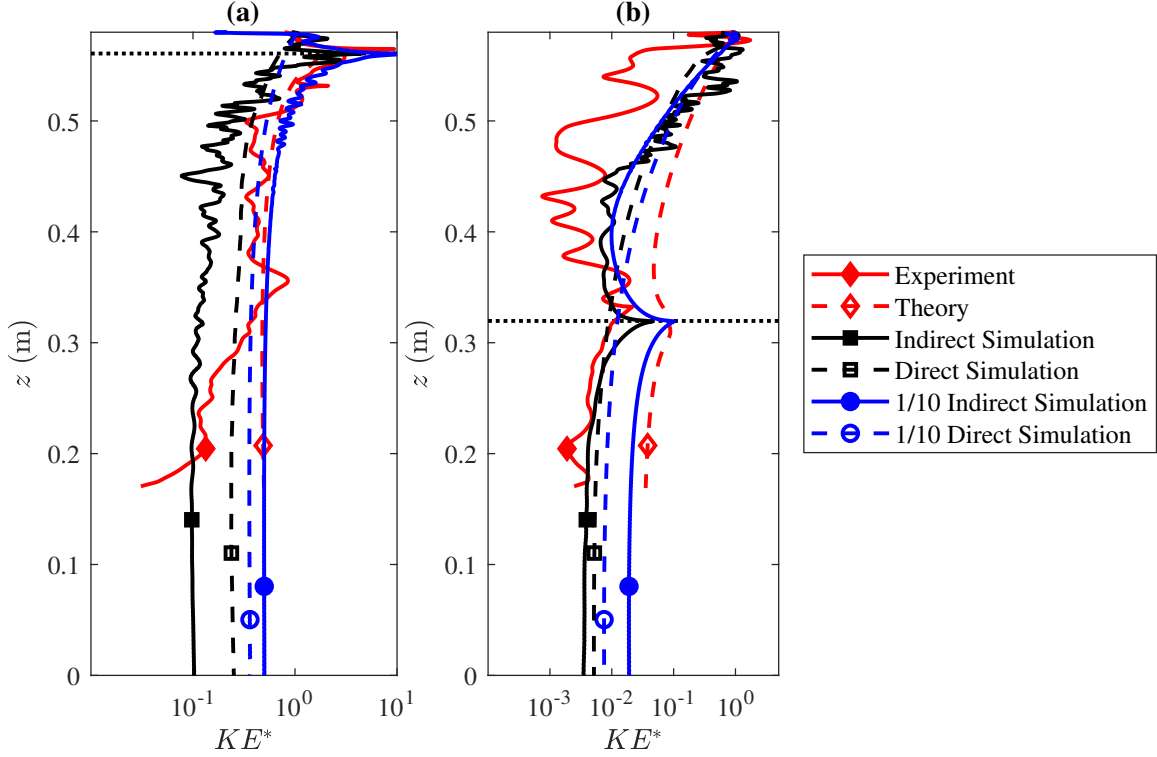


Figure 4.6: Normalized kinetic energy for each of the four methods for case 1 (a) and case 4 (b)

errors to arise even near the topography in the methods which use the WKB approximations. The direct simulations, for the full and 1/10 amplitude, do not use these approximations.

Examples of the normalized kinetic energy density as a function of height for each method are shown in Fig. 4.6(a) and (b), for cases 1 and 4, which represent extreme cases with relatively small and large evanescent regions respectively. $KE^* = KE/KE_{\text{norm}}$ is on the abscissa with water height on the ordinate. There are six sets of lines and symbols. Similar to the previous figure, solid lines and filled symbols represent indirect KE calculation methods, where $\Delta\tilde{N}^2$ is used to estimate KE, while dashed lines and open symbols are a direct calculation of KE using velocities. Thus the experiments are shown in red with the closed diamond, while the model is the red dash line with the open diamond. Full amplitude simulations using the indirect method of estimating kinetic energy are a solid black line and filled square, with the direct calculation method in the dashed black line and open square. Finally, the 1/10 amplitude simulation indirect calculation is depicted with a solid blue line and filled blue circle and the direct calculation is a blue dashed

line with an open blue circle. A horizontal black dotted line indicates the height of the turning depth which is 56.1 cm for case 1 and 32 cm for case 4. In each case, the kinetic energy starts at a high value near the topography at the top of the figure. As z decreases, the normalized kinetic energy decreases through the evanescent region until there is an increase near the turning depth for all of the methods except the simulation with the direct calculations, which is also seen in Fig. 4.4. For the experiments, theory, and indirect simulations, the kinetic energy always increases close to the turning depth. With the theoretical calculations of kinetic energy, this increase is caused by the relationship between vertical wavenumber and velocity amplitude (Eq. (4.10) & (4.17)), such that a decreasing vertical wavenumber increases the amplitude and thus the kinetic energy. Experiments, theory, and indirect simulations all use the same equations based on the WKB approximation, which fails near the turning depth. The increase in energy for the theory and indirect methods is due to these approximations. The direct simulations do not use the WKB approximations and show no increase in energy near the turning depth. Within the propagating region, the kinetic energy decreases after the turning depth and then remains nearly constant, and the direct and indirect simulations match each other very well.

In case 1, Fig. 4.6(a), a very small evanescent region exists with $D/H = 0.13$. Here, the 1/10 amplitude indirect simulations closely match the theoretical calculations, such that the two lines are almost directly on top of each other. No turbulent losses would occur in either of these methods. Experimental results are more similar to the 1/10 direct and full amplitude direct KE^* . The full amplitude indirect simulation indicates the lowest normalized energy, while the other methods are all within the same order of magnitude for the majority of the propagating region. Far from the turning depth, the experimental energy decays and matches more closely with the full amplitude indirect simulation. Differences in the propagating region kinetic energy for this case will be discussed further later in this section.

For case 4, Fig. 4.6(b), the evanescent region is much larger than in case 1, with $D/H = 3.35$. Similar to case 1, the theory and 1/10 amplitude indirect simulations maintain the highest KE^* throughout the majority of the evanescent and propagating regions. Unlike case 1, experi-

Table 4.2: N/ω shown for each case indicates where in the propagating region the difference between the direct and indirect methods is less than 5%.

Case	1	2	3	4	5
N/ω Full Amplitude	1.48	1.12	1.12	1.30	1.60
N/ω 1/10 Amplitude	1.11	1.11	1.11	1.11	1.10

mental energy is much smaller than the other methods in the evanescent region, but similar to the indirect simulation in the propagating region. There are also significant oscillations in both the experiments and full amplitude simulations within the evanescent region due to the turbulence caused by the vortex shedding at the topography peak. These oscillations decay in the propagating region and both the full amplitude simulation methods show similar average KE^* , 0.003 and 0.006 for the direct and indirect methods, respectively. Direct and indirect estimates of kinetic energy from the simulations match best far from the turning depth because the indirect calculations are based on WKB theory. This theory fails near the turning depth where the evanescent and internal waves experience relatively rapid variations in m and A instead of the slow variations required by the WKB assumptions. However, once the wave is far from the turning depth, the energy calculated by both simulations and predicted by the theory match well, such that variations due to poor local assumptions are not propagated. An exploration of when the linear theory and indirect calculations closely approximate the direct methods is discussed next.

To quantify the distance away from the turning depth where the indirect method closely approximates the kinetic energy of the direct method, the two calculation methods in the simulations are compared. The error, calculated as a percent difference between the two methods, is reported in Tab. 4.2 and the non-dimensional value of N/ω is used to compare all of the cases. Because $N = f(z)$, comparing N and ω provides a relative height at which the effects of the WKB approximation are negated for each case. The tabulated values indicate where the error between the two methods is less than 5%. Looking first at the full amplitude simulations, the value of N/ω decreases with increasing $\overline{Fr}_1 D/H$ and then gradually increases with a larger N/ω indicating that

the two methods do not coincide until farther from the turning depth. This increase in $\overline{Fr}_1 D/H$ indicates an increasing excitation frequency and larger evanescent regions. This may be the cause of the increasing N/ω for the full amplitude cases, as the larger evanescent region may allow for the growth of nonlinear terms which will eventually need to be damped out in the propagating region. The decrease from case 1 to case 2 could be due to the small and relatively weak evanescent region in case 1, indicated by $\overline{Fr}_1 D/H = 0.13$, which is an order of magnitude smaller than the other 4 cases. There is also evidence of turbulence generated waves and noise in case 1 (See Fig. 4.2(b)). In contrast, the 1/10 amplitude simulations show very similar values of $N/\omega \geq 1.11$ for all cases. In the smaller amplitude cases there was little to no turbulence and the wave beams in the propagating region were very smooth as seen in Figs. 4.2(e) and (f). With a low amplitude, the 1/10 amplitude simulations fall well within the small amplitude approximations needed for linear theory, and increasing $\overline{Fr}_1 D/H$ has almost no effect on N/ω . The full amplitude cases are further from the small amplitude assumptions than the 1/10-amplitude cases, and thus the linear theory equations which dictate the indirect method need a larger distance in the propagating region to overcome the non-linearities generated by these poor assumptions and turbulence.

These results indicate that for low amplitude scenarios with little turbulence, the indirect methods will be most accurate when $N/\omega > 1.1$, or a distance corresponding to a 10% increase in N away from the turning depth. Given the current trends, this is true for a wide range of $\overline{Fr}_1 D/H$. However, when turbulence is present, as would be expected in many oceanic situations, indirect methods should only be trusted further away from the turning depth, depending on $\overline{Fr}_1 D/H$. From the data in Tab. 4.2, a minimum N/ω can be chosen for large amplitude cases based on $\overline{Fr}_1 D/H$ with the equation

$$N/\omega = 0.1028(\overline{Fr}_1 D/H)^2 - 0.4035\overline{Fr}_1 D/H + 1.507. \quad (4.36)$$

As the only topography used in this work is the Gaussian shaped profile (See Sec. 4.4), Eq. 4.36 is only valid for this profile. Further research with multiple topographies would be needed to generate

an equation which covers more scenarios. However, this equation does provide a good baseline for future work.

4.5.3 Average kinetic energy

In order to further compare each of the methods and investigate the kinetic energy transferred from the evanescent region into the propagating region, we find an average, normalized kinetic energy in the propagating region. The average kinetic energy is calculated from the location where the Airy region ends ($z_{\text{Ai},2}$) until the bottom of the experimental window, (z_w). General locations of these values are shown on Fig. 4.1b by white dashed lines and can be written as $\Delta z_{\text{prop}} = z_{\text{Ai},2} - z_w$. The average KE is defined as

$$\overline{KE}_2 = \frac{1}{\Delta z_{\text{prop}}} \int_{z_{\text{Ai},2}}^{z_w} KE \, dz \quad (4.37)$$

Using the normalizing values described above, the non-dimensional kinetic energy in the propagating region is $\overline{KE}_2^* = \overline{KE}_2 / KE_{\text{norm}}$. It would be beneficial to perform all averaging starting at the locations indicated in Sec. 4.5.2. However, the experiments were limited base on the size of the tank. Although the numerical simulations could be averaged over specific heights corresponding to N/ω , this could not be matched in the experimental domain and a smaller Δz_{prop} was chosen to maintain consistency across the methods.

Figure 4.7 is \overline{KE}_2^* as a function of $\overline{Fr}_1 D/H$. The symbols are the same as Fig. 4.5, with the addition of three lines, which are curve fits to the model data (red dashed line), full amplitude direct simulation data (black dotted line), and 1/10 amplitude direct simulation data (blue dash-dot line). The curve fits for each scenario follow the equation

$$\ln(\overline{KE}_2^*) = C_1(\overline{Fr}_1 D/H) + C_2 \quad (4.38)$$

where C_1 and C_2 are constants for each scenario. These values are listed in Table 4.3. For almost every method, \overline{KE}_2^* decreases with increasing $\overline{Fr}_1 D/H$. Although the kinetic energy of the

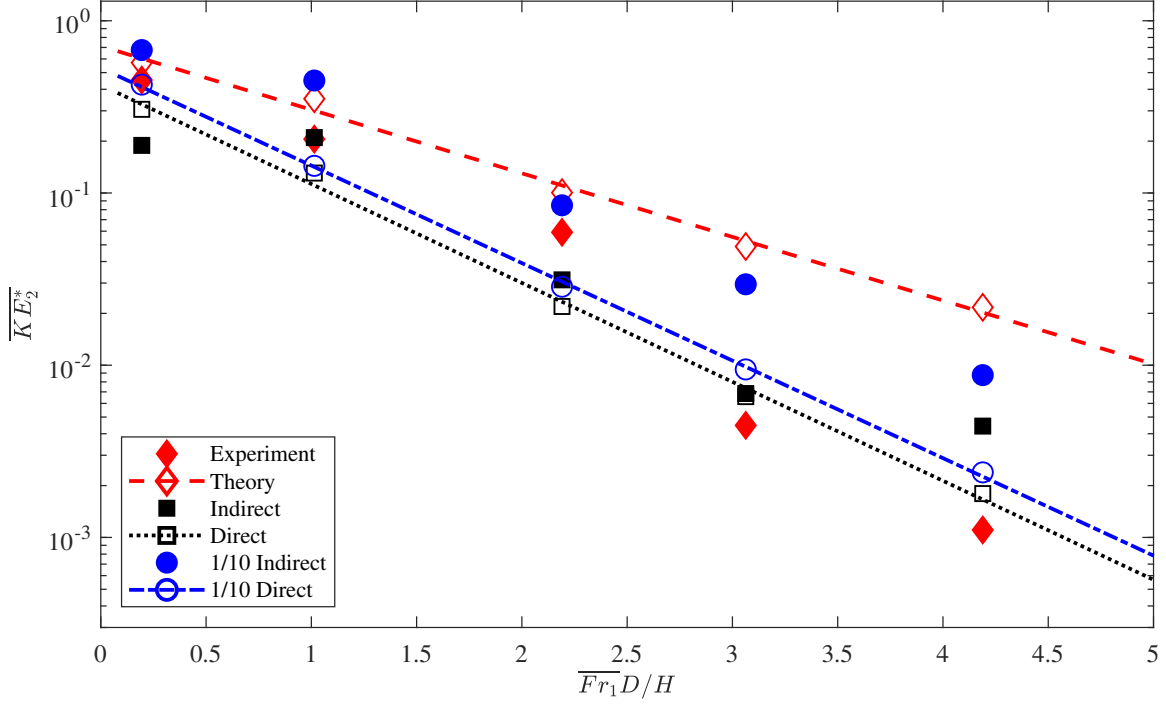


Figure 4.7: Average, normalized kinetic energy in the propagating region as a function of $\overline{Fr}_1 D/H$, with curve fits for the theory, direct simulations, and 1/10 amplitude direct simulations

Table 4.3: Constants and goodness of fit values for Eq. (4.38).

Method	C_1	C_2	R^2
Theory	-0.8503	-0.339	0.9935
Direct Simulation-Full Amplitude	-1.323	-0.859	0.9969
Direct Simulation-1/10 Amplitude	-1.340	-0.632	0.9994

normalizing value will increase with increasing $\overline{Fr}_1 D/H$ because of the increased initial energy from a relatively larger forcing frequency (see Fig. 4.5), the evanescent waves will decay more rapidly with an increased difference between N at the turning depth and ω_f . Also, the larger distance between the tip of the topography and the turning depth, indicated by an increasing D/H , allows a larger distance for the evanescent wave to decay, decreasing the internal wave energy in the propagating region.

\overline{KE}_2^* is greatest in the theory, where inviscid, linear theory was utilized and there were no losses due to turbulence, viscosity, or wave-wave interactions. Because of this, the linear theory

can be assumed to be an upper limit for kinetic energy transfer from the evanescent region to the propagating region. For $\overline{Fr}_1 D/H < 2$, the experiments show the second highest normalized kinetic energy, but the 1/10 indirect simulations are larger than the experiments for $\overline{Fr}_1 D/H > 2$. The 1/10 indirect simulations always indicate a larger kinetic energy than the full amplitude simulations, where turbulence is present. For direct KE calculations, the difference between the large and small amplitude simulations is very small, and each case has the same order of magnitude of \overline{KE}_2^* . Note that for case 5, with $\overline{Fr}_1 D/H = 4.18$, the indirect, full amplitude simulation significantly overestimates the direct simulation. From Tab. 4.2, it is indicated that for case 5 the indirect method will be valid below $N/\omega = 1.6$, however the experiments only reach a depth of $N/\omega = 1.11$. Thus the indirect simulation for case 5 is averaged over a region where it is known that the effects of the WKB approximation are still important and \overline{KE}_2^* will be too high. Therefore, the gap between the points is expected.

Figure 4.7 can also be viewed as the percentage of initial kinetic energy from the topography that passes into the propagating region. Case 1, corresponding to the lowest value of $\overline{Fr}_1 D/H$, results in the greatest propagating energy. For this case, the largest and smallest \overline{KE}_2^* values are 1/10 amplitude indirect and full amplitude indirect methods at 70% and 20%, respectively. However, the indirect methods are not as reliable for this case due to the relatively small separation between the topography and turning depth. It is more likely that the upper limit of energy transfer at this $\overline{Fr}_1 D/H$ is defined by the theoretical value of $\overline{KE}_2^* = 60\%$. Yet, a more realistic upper estimate of \overline{KE}_2^* would be the experimental value of $\overline{KE}_2^* = 45\%$. Similarly, a more accurate lower limit is the full amplitude direct value of 30%. Thus, we predict that 30-45% of the initial kinetic energy associated with waves at the excitation frequency will pass from the evanescent region into the propagating region for $\overline{Fr}_1 D/H < 0.5$, with 60% being the highest possible transmission percentage. This percentage decreases with increasing $\overline{Fr}_1 D/H$ and the propagating energy becomes negligible when $\overline{Fr}_1 D/H > 3$ as less than 1% of the initial energy is transferred into the propagating region for all methods.

Evaluating only the 1/10 amplitude simulations, the indirect method shows a much higher \overline{KE}_2^* than the direct method for all cases. Although the 1/10-amplitude cases had little turbulence, there was still some noise near the topography which generates errors in the normalizing values for the indirect simulations. Although the average kinetic energy between the direct and indirect simulations for the 1/10-amplitude cases differed by only 25% or less for all 5 cases, there is a significant difference in the normalizing values (See Fig. 4.5). For cases 2-5, the normalizing value of the direct simulations is a different order of magnitude. Thus, while the actual kinetic energy values are very similar, the variations of the normalization values cause an artificial separation between the indirect and direct methods, such that the indirect cases have similar values \overline{KE}_2^* compared to the theoretical cases.

For the full amplitude simulation, the greatest difference between the direct and indirect methods of calculating \overline{KE}_2^* occurs at the lowest $\overline{Fr}_1 D/H$, where the indirect method is four times greater than the direct. The smallest difference occurs at $\overline{Fr}_1 D/H = 3.06$ with only a 0.04% increase from the direct to the indirect method. In the other cases, all values of \overline{KE}_2^* are the same order of magnitude and show little variation. Only in case 1, where the turning depth is close to the topography, the indirect method is an underestimate of the direct method. This, along with the variation in the 1/10 amplitude simulations for case 1, lead to the idea that for very small evanescent regions, $\overline{Fr}_1 D/H < 1$, the indirect methods are less accurate, due to inaccurate calculations even near topography.

Based on Fig. 4.7, it can be seen that the theory follows the same trends as the full amplitude simulations, although it over predicts those trends because of turbulence in the simulations. As the theory is less expensive than the simulations and experiments both computationally and financially, we use Eq. (4.38) to create a relationship between the theory and the full simulations. A ratio of \overline{KE}_2^* of the simulations to the theory is shown as a function of $\overline{Fr}_1 D/H$ in Fig. 4.8. Triangles are actual ratios from each of the 5 cases and a curve fit is applied to the points. With

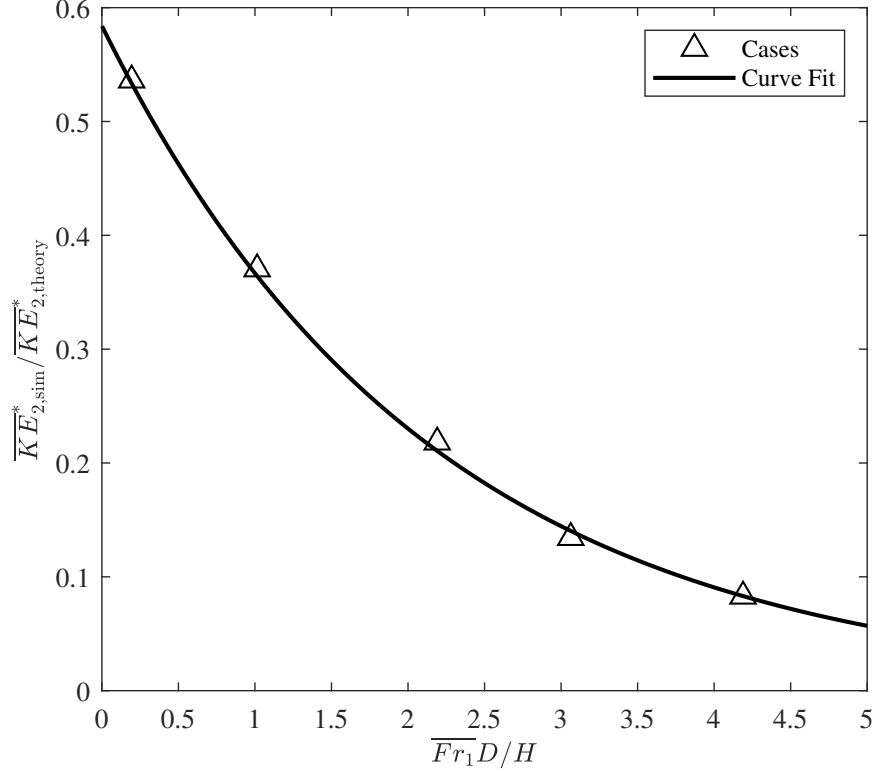


Figure 4.8: A ratio of the full amplitude simulation and theory kinetic energies as a function of $\overline{Fr}_1 D/H$

$R^2 = 0.9991$, the curve fit is defined as

$$\overline{KE}_{2,\text{sim}}^*/\overline{KE}_{2,\text{theory}}^* = 0.5894 \exp(0.465 \overline{Fr}_1 D/H) \quad (4.39)$$

With this equation, a prediction of the realistic kinetic energy in the propagating region can be formed without performing a complete series of simulations or experiments for the medium topography in an exponential profile. Further work is needed to explore if this equation is valid for different topographies and varying stratification profiles.

4.6 Summary of methodologies

Of the four methods presented in this work, the theory is the fastest and least expensive. It is a direct method of calculating the kinetic energy, but uses the WKB approximations which

fail near the turning depth. It also does not take into account any nonlinearities such as viscosity or turbulence that would decrease the overall kinetic energy density throughout the evanescent and propagating regions. This method is presented as an upper limit of kinetic energy density that passes into the propagating region (see Fig. 4.7) and is best used for scenarios where average energy in a propagating wave region is desired. However, it can also be related to the full amplitude simulations using Eq. (4.38) and a more realistic estimate of \overline{KE}_2^* can then be calculated for the medium Gaussian topography in an exponential density profile.

Although computationally expensive, the direct analysis of numerical simulations provides a significant amount of data and insight into regions where assumptions such as the WKB and small amplitude approximations fail and where nonlinearities are present. This occurs near the turning depth and very near the topography. In addition, the direct simulations show that the full and 1/10 amplitude simulations have similar percentages of kinetic energy passed from the evanescent region to the propagating region, with the trend line for the 1/10 amplitude approximately 30% higher than the full amplitude in Fig. 4.7 for the regions shown. Although the excursion length for the smaller amplitude simulations is 1/10 that of the full amplitude, the relative energy is comparable. It is possible that turbulence or turbulence generated internal waves cause the difference between the two methods. For scenarios where the main interest is the relative amount of wave energy generated from topography, performing simulations at 1/10 the amplitude will still provide accurate data. Investigations focused on turbulence or other nonlinearities should use full amplitude simulations.

The indirect analysis of simulations was accomplished in this work to provide insight on when the indirect methods of the synthetic schlieren experiments were valid, and should not necessarily be used as a specific method for investigating internal wave kinetic energy. In general, the direct analysis of numerical simulations can provide data needed to estimate kinetic energy without the added WKB assumptions used by the indirect analysis methods.

Synthetic schlieren experiments were performed to help ensure that the theory and simulations accurately model the kinetic energy density of the evanescent and internal waves. Based on

the information of Tab. 4.2, it is recommended that experiments investigating the kinetic energy of evanescent to propagating waves should have a propagating region large enough that there is an increase in N of at least a 10%. A larger propagating region will provide better estimates of the energy in that region. In addition, case 1 shows that kinetic energy density estimates are poor when the topography and turning depth are relatively close ($\overline{Fr_1}D/H < 1$).

4.7 Conclusion

This work compared four methods of estimating the kinetic energy density of internal waves generated by evanescent waves passing through a turning depth. Kinetic energy was calculated directly with velocity using linear theory and numerical simulations, and estimated indirectly using a derived relationship between velocity and the Fourier amplitudes of ΔN^2 in experiments and simulations for comparison. For each method, kinetic energy was averaged over a narrow band of frequencies near ω_f and over a wide range of wavenumbers of $0.5 < kB_L < 5$, which was necessary because a range of wavenumbers is generated by a Gaussian topography.

Kinetic energy density was calculated over the height domain with each method and compared to the nondimensional $\overline{Fr_1}D/H$. A small value of $\overline{Fr_1}D/H$ indicates that the topography is far from the turning depth and that the oscillation frequency is similar to the average natural frequency of the evanescent region. When $\overline{Fr_1}D/H < 1$, all methods indicate between 10% and 80% of the initial kinetic energy generated at the topography passes into the propagating region, with the theory, experiments, and 1/10 indirect method simulations predicting that over 30-60% of the initial energy is retained from evanescent waves.

Numerical simulations provided insight into the validity of the indirect calculations, indicating that the direct and indirect methods collapse far from the turning depth, where $N/\omega > 1.1$ for the 1/10 amplitude simulations. With the full amplitude, a larger propagating region is required to minimize the difference between the methods. Based on this, it is recommended that any calculations of kinetic energy in the propagating region of experiments involving turning depths also use

Eq. (4.36) to ensure that the errors associated with the WKB approximation failing at the turning depth do not artificially increase the estimate of propagating wave energy..

A correlation between the direct simulations and theory provides a future research opportunity to estimate the kinetic energy density of internal waves generated by tidal motions over actual oceanic topography. Theoretical estimates of \overline{KE}_2^* can be calculated quickly and Eq. (4.38) provides an estimate of the predicted simulation energy, which would more closely correlate to realistic situations. However, this work used only one topography shape and one density profile. Further investigations into the effects of topography shape and density profiles are needed to increase the usability of this function.

This work has been supported by the Utah NASA Space Grant Consortium and by NSF Grant CBET-1606040. The authors would also like to acknowledge the support of Harry Swinney and the Texas Advanced Computing Center.

CHAPTER 5. EFFECTS OF STRATIFICATION AND TOPOGRAPHY SHAPE ON KINETIC ENERGY DENSITY OF EVANESCENT AND INTERNAL WAVES

This chapter represents a full manuscript in preparation for submission to Physical Review Fluids.

5.1 Contributing authors and affiliations

Allison Lee, Kyle Hakes, Julie Crockett, Department of Mechanical Engineering, Brigham Young University, Provo, UT 84602

Yuxuan Liu, Michael R. Allshouse, Mechanical and Industrial Engineering, Northeastern University, Boston, Massachusetts 02115

All simulations were performed at Northeastern University through the Texas Advanced Computing Center.

5.2 Abstract

Evanescent waves formed from tidal motions over oceanic topography can generate internal waves as they pass through a turning depth, or the location where the natural frequency (N) of the fluid is equal to the excitation frequency. The kinetic energy density of these internal waves is dependent upon the shape of the topography and the relative strength of the natural frequency in the evanescent region. Using experiments, analytical theory, and numerical simulations, the kinetic energy density of internal waves generated from evanescent regions is compared for multiple topography shapes and multiple density profiles using $\overline{Fr}_1 D/H$. Propagating internal wave kinetic energy relative to the initial evanescent wave kinetic energy decreases with increasing $\overline{Fr}_1 D/H$,

and can be assumed negligible for $\overline{Fr}_1 D/H > 4$. Effects of topography shape and average natural frequency on kinetic energy predictions are also discussed.

5.3 Introduction

As the tides oscillate over oceanic topography, internal waves are generated when the local stratification of the ocean water is greater than the oscillation frequency (ω). Fluid stratification is indicated by the natural frequency (N) which is defined as

$$N^2 = \frac{-g}{\rho_0} \frac{\partial \rho}{\partial z} \quad (5.1)$$

where g and ρ_0 are the gravitational constant and a reference density for the fluid. Smaller values of N are indicative of a weak stratification, while larger values indicate a strong stratification. Internal waves generated where N is strong relative to the excitation frequency, or $N > \omega$. These waves suffer little to no viscous dissipation and are important factors in the ocean energy budget and oceanic mixing [30]. In contrast, when $N < \omega$, evanescent waves are generated. The amplitudes of these waves decay at an exponential rate as they move vertically away from their generation site [5]. Because of the rapid decay, researchers generally do not focus on the impact of evanescent waves. However, in regions where the stratification increases with height, evanescent waves can pass through a turning depth and become propagating internal waves [5, 18]. A turning depth is the location where the local stratification is equal to the original excitation frequency such that $N(z_{td}) = \omega$. Previous investigations have found that under certain conditions a significant portion of the kinetic energy of the generated evanescent wave can pass through the turning depth and be retained in the internal waves which propagate away [18, 100, 112]. This work explores the impact of topographical shape and density profile on the relative kinetic energy density of propagating internal waves formed from evanescent waves.





When exploring topographical shape, it is standard to investigate the criticality of the topography where criticality is defined as $\varepsilon = S_{top,m}/S_{wave}$ [3, 18]. Here, $S_{top,m}$ is the maximum

slope of the topography and $S_{\text{wave}} = \sqrt{\omega^2/(N^2 - \omega^2)}$. A topography is considered subcritical, critical, or supercritical when $\varepsilon < 1$, $\varepsilon = 1$, or $\varepsilon > 1$, respectively. Criticality defines the type of internal waves and possibility of wave breaking. It has been explored for multiple topography types [11, 34, 39, 40, 86]. Unfortunately, this definition of criticality and resultant wave generation parameters requires the topography to be in a propagating region, where $N > \omega$. In all of the cases presented here, the topography is in an evanescent region, where $N < \omega$, and thus S_{wave} is undefined. Because of this, we will focus on $S_{\text{top,m}}$ and the presence of multiple peaks and investigate how these parameters affect the kinetic energy of the generated waves.

Density profiles throughout the ocean were mapped with 18,000 World Ocean Circulation Experiment casts in an effort to find oceanic locations where the local stratification is less than the M2 semidiurnal tide [19]. It was found that the natural frequency of the deep ocean can frequently be described with an exponential equation with density as a function of depth [19, 64]. Although the effect of varying stratification on internal wave generation has been explored [75, 84, 113], few studies have investigated the impact of stratification on evanescent wave generation. Lee and Crockett [100] used an average N in the evanescent region to characterize the relative energy of internal waves generated from an evanescent region with exponential density profiles. They found that both the average strength of the stratification and the distance from the topography to the turning depth defined propagating wave energy, where large average evanescent stratifications and shorter distances resulted in significant kinetic energy transfer to propagating waves.

Internal and evanescent waves can be studied through observations, analytical solutions to linear and nonlinear equations, experiments, and numerical simulations. Of those methods, three will be used in this work. Synthetic schlieren experiments, analytical calculations, and numerical simulations will each be presented and compared. Synthetic schlieren uses the relationship between the index of refraction and the density of a fluid to find variations in the natural frequency, or ΔN^2 [58]. This, in turn, can be used to estimate kinetic energy of evanescent [100] and internal waves [20]. Using the WKB approximation, linear theory can be applied throughout the evanescent region and propagating region, individually, to calculate horizontal (u) and vertical (v)

Table 5.1: Names, equations and images of the four topography profiles. All units are in meters.

Name	Equation	Range (m)	Profile
Medium Gaussian	$h = 0.1e^{-x^2/0.0424^2}$	$-0.09 < x < 0.09$	
Steep Gaussian	$h = 0.1e^{-x^2/0.0106^2}$	$-0.0112 < x < 0.0112$	
Sinusoidal	$h = 0.0355 \sin(2\pi x/0.11)$	$-0.0275 < x < 0.1925$	
Complex	$h = 0.1672e^{-x^2/0.0566^2} \frac{1}{4} \sin(520x) + \cos(115x) $	$-0.1214 < x < 0.1214$	

velocities [100]. Numerical simulations expound upon the data available through experimentation and allow for a direct comparison with both the theoretical velocities and the experimental variation in stratification [112]. Lee et al. [112] used each of these methods to investigate the validity of the methods, but was limited to a singular topography and density profile. By including more topographies and density profiles, this work will expand upon the previous research to allow for a stronger relationship between each of the methods and a better understanding of other realistic oceanic scenarios of tidally generated internal waves.

5.4 Methods

This section will first describe in detail the four topographies and density profiles, along with the parameters of each case. Details of the three methods and the corresponding kinetic energy calculations will then be summarized.

Table 5.2: Density Profile Equations

Profile Number	Profile	Equation
1	Two Layer Linear	$\rho_1 = az + b; \rho_2 = cz + d$
2	Quadratic	$\rho = az^2 + bz + c$
3	Cubic	$\rho = az^3 + bz^2 + cz + d$
4	Exponential	$\rho = ae^{bz} + c$

To explore the effects of maximum topography slope and varying number of peaks, four different topographies were chosen for the cases. Each is listed in Tab. 5.1 and will be referred to as the medium, steep, sinusoidal, and complex topographies. Each topography was 3D printed to ensure the shape matched the desired equation. Both the medium and sinusoidal topographies have the same maximum slope of $S_{\text{top,m}} = 2.02$, while the steep and complex have maximum slopes of 8.09 and 39.05, respectively. Although the medium topography is taller than the sinusoidal, the width of the sinusoidal is slightly greater than the medium. With these small differences, maintaining the same maximum slope between the medium and sinusoidal topographies allows for a comparison of the effect of multiple peaks. The steep topography represents an increase in maximum slope, while the complex topography provides a more realistic topography and can be seen as an approximation of the ocean floor [18]. Results based on each topography will be presented in Sec. 5.5.

Density profiles are listed in Tab. 5.2. From the work of King et al. [19], it is known that the density in the deep ocean can often be described as an exponential profile. However, varying oceanic conditions can create other density profiles that are better fit with linear, quadratic or cubic curves as shown in Tab. 5.2. Because the kinetic energy of evanescent and internal waves is dependent on N , the rate of density change will affect the overall energy of the internal waves. In addition, a comparison of two layer profiles to average N values in each of the other density profiles will provide insight on the effect of averaging the natural frequency of non-uniform stratifications.

Summarized details for all cases are listed in Tab. 5.3 with the topography used, the density profile (associated with Tab. 5.2), the number of cases for each profile, and ranges for ω , D/H ,

Table 5.3: Summarized details of all cases including the topography shape and density profile listed in Tab. 5.2 and the range of values for ω , D/H , \overline{Fr}_1 , and $\overline{Fr}_1 D/H$.

Topography	Density Profile	Number of Cases	ω	D/H	\overline{Fr}_1	$\overline{Fr}_1 D/H$
Medium	1	4	0.80-1.40	2.90	1.38-2.40	4.00-6.97
	2	9	1.00-1.30	0.45-3.52	1.02-1.12	0.45-2.87
	3	2	1.21-1.30	1.50-2.66	1.09-1.11	1.63-2.95
	4	5	0.81-1.21	0.19-3.35	1.01-1.25	0.19-4.19
Steep	1	4	0.80-1.40	2.89	1.37-2.39	3.97-6.92
	2	5	1.01-1.29	0.61-3.01	1.03-1.10	0.63-3.32
	3	3	1.10-1.30	1.37-4.17	1.07-1.13	1.47-4.71
	4	5	0.80-1.20	0.61-3.34	1.05-1.28	0.63-4.26
Sinusoidal	1	4	0.81-1.44	4.49	1.40-2.47	6.28-11.1
	2	4	1.09-1.30	1.00-5.08	1.03-1.11	1.03-5.65
	3	5	0.81-1.21	0.80-3.65	1.13-1.25	0.90-4.55
	4	6	0.81-1.30	1.21-5.73	1.06-1.33	1.29-7.62
Complex	1	5	0.90-1.40	0.87	1.61-4.71	1.40-4.10
	2	1	1.13	0.78	1.05	0.81
	3	3	1.10-1.30	0.19-1.59	1.02-1.09	0.19-1.73
	4	3	0.19-1.10	0.32-1.08	1.04-1.16	0.33-1.26

and \overline{Fr}_1 and $\overline{Fr}_1 D/H$. D is the distance between the tip of the topography and the turning depth and H is the height of the topography. This ratio indicates a relative size of the evanescent region, with larger values indicating a larger region as the topography is farther away from the turning depth. \overline{Fr}_1 is the average Froude number in the evanescent region, defined as the ω_d/\overline{N}_1 . The natural frequency is also averaged over the distance D . Because all cases involve an evanescent region, \overline{Fr}_1 is always larger than 1. This value provides a relative strength for the evanescent region. As \overline{Fr}_1 increases, the stratification decreases causing evanescent waves to decay more rapidly. Combining the two terms into $\overline{Fr}_1 D/H$ illustrates the importance of both density profile and relative topography distance in the overall kinetic energy density of the resultant internal waves in the propagating region. Full details of each case including the case number, parameters of the density profile, excursion length L , the overall water height Z_H , and height of the turning depth z_{td} are all listed in Appendix A.1.

5.4.1 Experiments

Experiments were performed and data was captured using synthetic schlieren imaging methods [58]. An inverted topography was placed at the water line in an acrylic tank with dimensions of 2.45 x 0.91 x 0.15 m, corresponding to length, height and width. The tank was filled to a water height between 0.55-0.75 m using a modified double bucket method [93] to match one of the density profiles outlined in Table 5.2. Matting was placed along the bottom of the tank to reduce reflections. Before each test, the density was measured every 3 cm, then every 5 cm after the fourth test. The topography was oscillated 15 times before starting the imaging to ensure a steady state had been reached. Experiments were processed at 6 fps in the commercial software Digiflow [94], which uses the apparent motion of a random dot pattern behind the experiment to estimate $\nabla\rho'/\rho_0$, or dimensionless variations in density in the horizontal and vertical directions. By multiplying the z derivative by gravity, this data becomes ΔN^2 such that

$$\Delta N^2 = \frac{-g}{\rho_0} \frac{\partial \rho'}{\partial z} \quad (5.2)$$

which is similar to Eq. (5.1). From this data, a relationship can be made between the Fourier amplitudes ΔN^2 and those of the horizontal (u) and vertical (v) velocity of both evanescent and internal waves. Because the vertical velocity of evanescent waves must take into account the imaginary vertical wavenumber, the relationships between natural frequency and velocity varies based on the type of wave. However, both functions assume a kinetic energy density defined as

$$KE = \tilde{U}^2 + \tilde{W}^2 \quad (5.3)$$

where the tilde indicates Fourier amplitudes. Lee and Crockett [100] found that kinetic energy can be estimated in an evanescent region with

$$KE_1 = \left| \frac{-q\omega\Delta\tilde{N}^2}{k(\partial_z N^2 + qN^2)} \right|^2 + \left| \frac{i\omega\Delta\tilde{N}^2}{\partial_z N^2 + qN^2} \right|^2 \quad (5.4)$$

where k is the horizontal wavenumber and q is the imaginary vertical wavenumber such that $m = iq$. The subscript 1 indicates the evanescent region and the subscript on the partials indicate the dimension of the derivative. Similarly, Wunsch and Brandt [20] defined the kinetic energy density of propagating internal waves as

$$KE_2 = \frac{\omega^2 N^2}{k^2(N^2 - \omega^2) + (\omega \partial_z N^2 / N^2)^2} \left| \frac{\Delta \tilde{N}^2}{N^2} \right|^2. \quad (5.5)$$

Experiments were imaged with a jAi Cv-M4+Cl progressive scan camera with a resolution of 1360x1080 pixels. A 2D Fourier transform in x and t was performed for each row of pixels and amplitudes from the transform were entered into either Eq. (5.4) or Eq. (5.5) depending on the height of the pixel row.

5.4.2 Linear theory

To calculate the kinetic energy of the evanescent and internal waves in a non-uniform stratification, the WKB approximation can be applied to both regions and the velocities of the waves can be calculated. WKB approximations are valid where $N^2 \gg \lambda_z (\partial N^2 / \partial z)$ [74], where λ_z is the vertical wavelength of the wave. These assumptions breakdown near the turning depth as λ_z varies rapidly. By applying the Airy function instead of the standard velocity equations, it is possible to smoothly transition from the evanescent region to the propagating region [91, 100].

In both regions, the natural frequency is a function of height, which must be accounted for in both the vertical wavenumber and the amplitude of the velocities [74]. This is done by introducing θ , or the integrated wavenumber in each region, and allowing the amplitude, A , to also

be a function of height. Starting with the evanescent region, the equations for velocity include

$$\theta_1(z) = \int_{z_{1,0}}^z q dz \quad (5.6)$$

$$w_1(x, z, t) = A_1 \exp[i(kx - \omega t)] \exp(\theta_1) \quad (5.7)$$

$$u_1(x, z, t) = \frac{-w_1}{ik} \left[q - \frac{dq/dz}{2q} \right] \quad (5.8)$$

$$A_1(z) = A_{1,0}/(q/q_{1,0})^{1/2} \quad (5.9)$$

Here, it is assumed that the term $(dq/dz)/2q$ is negligible [100]. The continuity equation

$$\frac{\partial u}{\partial x} + \frac{\partial w}{\partial z} = 0 \quad (5.10)$$

is used to calculate u . An initial amplitude of $A_{1,0}$ is defined by the velocity of the topography and matched at the height $z_{1,0}$. $q_{1,0}$ is the vertical wavenumber at the height $z_{1,0}$.

Before reaching the turning depth, the evanescent region velocity equations are matched with the Airy region equations. This region begins at the height corresponding to 1% of the average vertical wavelength (λ_z) above the turning depth, or $z_{1,Ai} = z_{td} + 0.01(2\pi/\bar{q})$. The Airy region continues to $z_{Ai,2} = z_{td} - 0.01(2\pi/\bar{m})$, which is 1% of the average λ_z in the propagating region defined by the experimental domain. Based on the work of Lighthill [91] and Lee and Crockett [100], the Airy region equations for velocity are

$$w_{Ai}(x, z, t) = Q_{0,w} \text{Ai}(\beta^{1/3}z - \beta^{1/3}z_{td}) \exp[i(kx - \omega t)] \quad (5.11)$$

$$u_{Ai}(x, z, t) = Q_{0,u} \frac{i\beta^{1/3}}{k} \text{Ai}'(\beta^{1/3}z - \beta^{1/3}z_{td}) \exp[i(kx - \omega t)] \quad (5.12)$$

where $Q_{0,w}$ and $Q_{0,u}$ are constant amplitudes in the region, $\beta = m^2/(z_{td} - z)$, and Ai' is the first derivative of the Airy function with respect to the vertical. $Q_{0,w}$ and $Q_{0,u}$ are found by matching Eq. (5.11) to Eq. (5.7) and Eq. (5.12) to Eq. (5.8) at $z_{1,Ai}$.

In the propagating region, the amplitude of vertical velocity is found by matching w_{Ai} to w_2 at $z_{Ai,2}$, and then continuity (Eq. (5.10)) is used to defined the horizontal velocity. These equations

for velocity are similar to those for the evanescent region and are defined by Pedlosky [74] as

$$w_2(x, z, t) = A_2 \exp(i(kx - \omega t + \theta_2)) \quad (5.13)$$

$$A_2(z) = A_{2,0}/(m/m_0)^{1/2} \quad (5.14)$$

$$\theta_2(z) = \int_{z_{Ai,2}}^z m dz. \quad (5.15)$$

$$u_2(x, z, t) = \frac{-w_2 m}{k} \left[m - \frac{dm/dz}{2im} \right] \quad (5.16)$$

and again, dm/dz is considered to be negligible [100].

With u and w fully defined in all three regions, the kinetic energy can be calculated by squaring and summing their amplitudes as in Eq. (5.3).

5.4.3 Numerical simulations

A CDP-2.4 algorithm was implemented to perform direct numerical simulations of the 2D Navier-Stokes equations under the Boussinesq approximation. This algorithm is a finite volume solver that uses a fractional-step time-marching scheme [95,96]. This code was chosen because it has previously been used to study internal waves and has been validated with experiments [18, 86, 88, 97–100]. Simulations provided both the velocity and density perturbation fields. Thus kinetic energy can be estimated directly using velocity or indirectly using ΔN^2 with Eqs. (5.4) and (5.5). These two methods will be referred to as such throughout the work.

The equations solved by the 2D simulations calculate the total density ρ , pressure p , and velocity \mathbf{u}_T over the domain $x \in [-400, 400]$ cm and $z \in [0, 150]$ cm with the following equations:

$$\frac{\partial \mathbf{u}}{\partial t} + \mathbf{u}_T \cdot \nabla \mathbf{u}_T = -\frac{1}{\rho_0} \nabla p + \nu \nabla^2 \mathbf{u}_T - \frac{g\rho}{\rho_0} \hat{\mathbf{z}} + \mathbf{f}_{\text{tidal}} \quad (5.17)$$

$$\frac{\partial \rho}{\partial t} + \mathbf{u}_T \cdot \nabla \rho = \kappa_s \nabla^2 \rho \quad (5.18)$$

$$\nabla \cdot \mathbf{u}_T = 0 \quad (5.19)$$

where $\rho_0 = 1000 \text{ kg/m}^3$ (density of water), $\nu = 10^{-6} \text{ m}^2/\text{s}$ (kinematic viscosity of water at 20°C), and $\kappa_s = 2 \times 10^{-9} \text{ m}^2/\text{s}$ (the diffusivity of NaCl in water). All simulations used the same domain, with a structured grid containing resolutions that ranged from 0.02 to 10 cm though the resolution was increased for the complex topography cases due to the significant turbulence seen in preliminary tests. Initially, the system was set at rest with an unperturbed density field. The density field matched the density profiles of the experiments. For the simulations, the topography was at the bottom of the domain, with a no slip boundary condition. At the top of the domain, the boundary condition was set to be free slip. Periodic boundary conditions with Rayleigh damping were implemented along the left and right edges to force negligible velocities at both boundaries. In addition, to reduce reflections, a sponge layer was placed at the top of the domain.

Each case was run twice, with an excursion length matching the above tables, and again with smaller excursion length such that $L_{low} = L/10$. These low amplitude cases were run to both investigate the importance of excursion length and to minimize turbulence for the steeper sloped topographies. They will be referred to as the low amplitude or 1/10 amplitude cases. Simulations were performed at temporal resolutions of 0.002 and 0.004 s for the low and high amplitude simulations, respectively. Convergence studies were performed for each topography. Because the system was initially at rest, each case was run for 30 periods to reach a steady state, and then an additional 30 periods which were used in the energy analysis.

5.4.4 Average kinetic energy

Prior experiments and simulations indicate that waves generated by any topography result in energy in a narrow range of frequencies, but a wide range of horizontal wavenumbers. This spread is dependent upon the topography. To accurately compare the three methods and four topographies used here, it is necessary to average kinetic energy over a range of k values in a manner individual to the topography. Nappo [5] showed that the magnitude of the vertical velocity of internal waves generated by oscillating flow over Gaussian shaped topography is defined by the function $kB \exp[-(kB/2)^2]$, where B is a term in a Gaussian equation such that $h_{\text{Gaus}} = \exp(-x^2/B^2)$.

Vertical velocity is a maximum at a wavenumber such that

$$k_{\max}B = \sqrt{2} \quad (5.20)$$

However, Lee et al. [112] showed that the predicted peak wavenumbers based on this value do not match with what is seen both in experiments and in numerical simulations. Instead they found that a new Gaussian parameter which takes into account an adjusted wavelength based on the width and excursion length is needed. By defining $\lambda_L = W + L$, where W is the width associated with the location where height of the topography has decreased to 1% of the maximum height, the new Gaussian parameter is

$$B_L = \frac{\lambda_L \sqrt{2}}{6} \quad (5.21)$$

By combining Eqs. (5.20) and (5.21), the new predicted maximum wavenumber matches that of the experiments and simulations. In addition, Nappo indicated that the function $kB \exp[-(kB/2)^2]$ decayed significantly for $kB > 5$. Similarly, Lee et al. saw a rapid decay in the kinetic energy associated with $kB > 5$. Because of this, kinetic energy will be averaged over the range $0.5 < kB_L < 5$.

For the complex topography, although the Gaussian curve is multiplied by sine and cosine terms, B from the original equation in Tab. 5.1 still applies to the general shape. A Gaussian fit can be applied a single peak of the sinusoidal topography with with $B = 0.0314$. To encompass both peaks, B is doubled and the resulting fit is $h_{\text{sin,Gaus}} = 0.071 \exp[-(x - 0.0819)^2/0.0628^2]$. Even though this shape has only one peak, it matches the overall width of the sinusoidal topography. To include the excursion length, according to experiments, B_L for the medium topography is approximately equal to $B + L/4$. As both the sinusoidal and complex topographies are similar widths to the medium Gaussian, this was used to account for the excursion length for these two topographies.

Experimental and simulation data were averaged over $0.5 < kB_L < 5$ for each topography. Because the frequency band in the experiments and simulations was so narrow, it is assumed that

only waves at the forcing frequency are present. To account for a changing k in the analytical theory, for each distinct k , an initial amplitude is calculated by

$$A_{k,0} = A_{1,0} \frac{kB_L \exp[-(kB_L/2)^2]}{k_p B_L \exp[-(k_p B_L/2)^2]} \quad (5.22)$$

where $A_{1,0}$ is calculated by matching the velocity of the topography to the vertical velocity at the expected peak wavenumber as detailed in Sec. 5.4.2. This equation forces a decreasing amplitude away from the peak wavenumber allowing for a more accurate representation of the range of kinetic energy seen in the experiments and simulations.

5.5 Results

This section will compare the general trends of kinetic energy density for each of the methods indicated in Sec. 5.4 based on topography shape and density profile. Both of these factors will also be discussed individually and estimates of the percentage of kinetic energy that passes into the propagating region will be provided.

To compare the kinetic energy of each method, all kinetic energy will each be normalized by the energy near the tip of the topography. Referred to as KE_{norm} , it is the average of the kinetic energy at the tip of the topography and at the first three locations below the topography (moving into the evanescent region). Normalized kinetic energy is then calculated as $KE^* = KE/KE_{\text{norm}}$. For experiments and indirect simulations kinetic energy fluctuates in the evanescent region and thus curve fits are applied to each case individually and KE_{norm} is calculated from the fit.

Four steep topography cases with four density profiles are shown in Fig. 5.1. From left to right, the density profiles for each figure are two layer linear, parabolic, cubic, and exponential which correspond to cases 20, 27, 31, and 34 (See Tab. A.2). Each figure shows the normalized kinetic energy (KE^*) on a log scale on the abscissa with height on the ordinate. There are six lines plotted in the figures indicating kinetic energy from the experiments (blue line), theory (red line), indirect simulation (green line), direct simulation (green dashed line), 1/10 indirect simulation

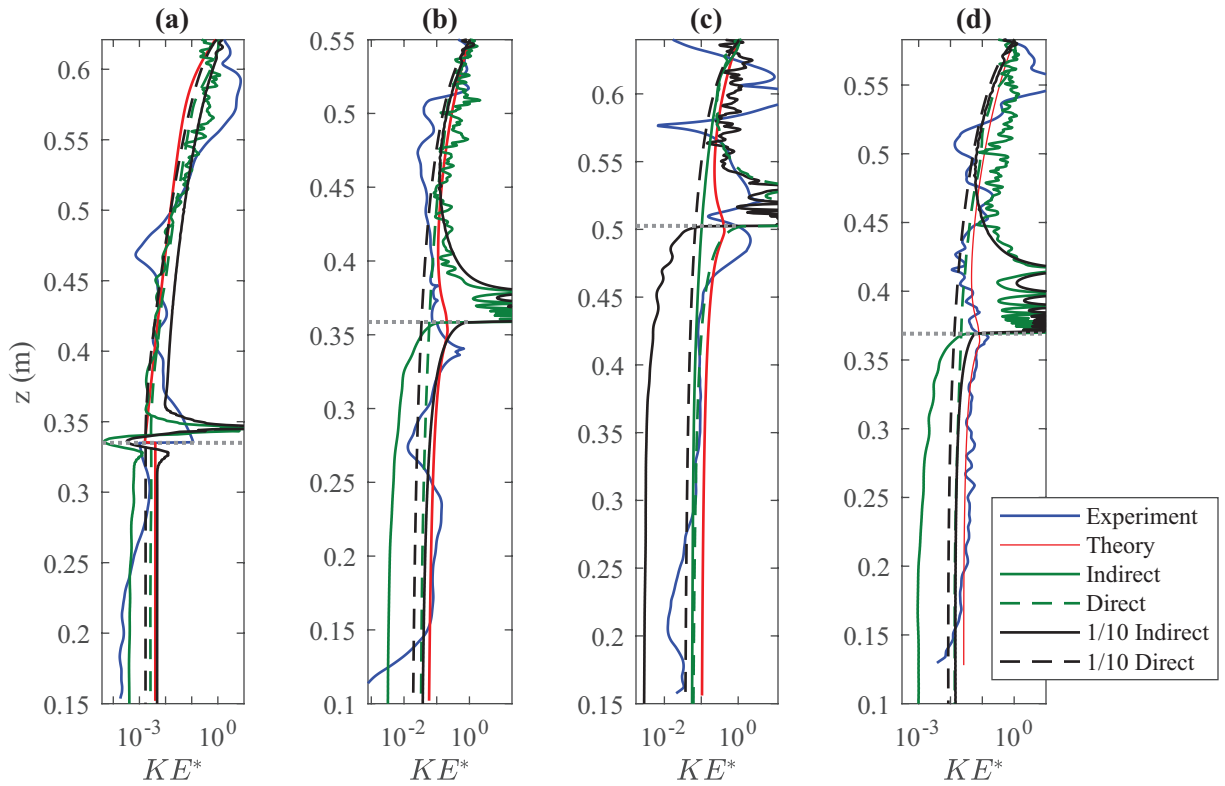


Figure 5.1: Normalized kinetic energy for the steep topography with (a) two layer, (b) parabolic, (c) cubic, and (d) exponential density profiles. Each method of estimating kinetic energy is indicated in the legend and the location of the turning depth is the horizontal dotted line.

(black line), and 1/10 direct simulation (black dashed line). The final line is a horizontal grey dotted line marking the location of the turning depth (z_{td}).

In each figure, the kinetic energy is greatest at the top where the top of the topography resides. Away from the topography, kinetic energy decreases through the evanescent region until the turning depth. It then remains fairly constant within the propagating region where the parabolic and cubic density profiles keep more energy in the propagating region than the two layer and exponential cases. These two high energy cases also have the smaller values of $\overline{Fr}_1 D/H$ compared to the low energy cases, which has been shown to influence the relative kinetic energy of internal waves [112]. This will be explained further for this work later in this section.

In all cases, the theory matches very well with the direct simulation, both the full and 1/10 amplitude, in the evanescent and propagating regions. There is some separation in these methods

near the turning depth due to the transition in the Airy region, but in the propagating region the theory follows the same trends as the direct methods. Because the theoretical calculations do not include any losses, such as turbulence, the theory generally indicates the largest kinetic energy, especially within the propagating region. Near the turning depth the indirect simulations show a significant increase in energy just before and at the turning depth. In Fig. 5.1(a), a sudden spike is seen 0.02 m above the turning depth at $z = 0.35$ m, followed by a rapid decrease. In the other three cases, the increase in energy occurs larger distances away from the turning depth and is accompanied by rapid oscillations in energy until the turning depth. Experimental data also show some oscillations, but they are not as severe as the simulation data. Variations in kinetic energy near the turning depth are expected for these indirect methods because the small amplitude approximations fail near the turning depth because m decreases causing the amplitudes of velocity to increase towards infinity [112]. Although each graph in Fig. 5.1 corresponds to a different density profile, the methods show similar trends for kinetic energy in the propagating region, with the highest energy indicated by the theory and then the direct simulations. In Fig. 5.1(d), the experimental energy is almost an exact match for the theoretical energy, but that is not generally the case.

While Fig. 5.1 compared kinetic energy for one topography and multiple density profiles, Fig. 5.2 compares kinetic energy for one density profile and each of the four topographies: (a) medium, (b) steep, (c) sinusoidal, and (d) complex. The four figures correspond to cases 13, 31, 46, and 62. This figure matches the setup of Fig. 5.1 with the same legends and axes. Similar to the previous figure, the kinetic energy decays in the evanescent region and then remains relatively constant in the propagating region. In Fig. 5.2, the oscillations of the indirect methods are larger and more frequent, especially for the sinusoidal topography in Fig. 5.2(c) and the complex topography in Fig. 5.2(d). This is likely due to the multiple peaks of each topography. Although the maximum slope ($S_{\text{top},m}$) of the sinusoidal topography is the same as the medium, two peaks generated more turbulence, which the indirect methods struggle to represent accurately. For the complex topography, the large value of $S_{\text{top},m}$ and the multiple peaks create significant error for

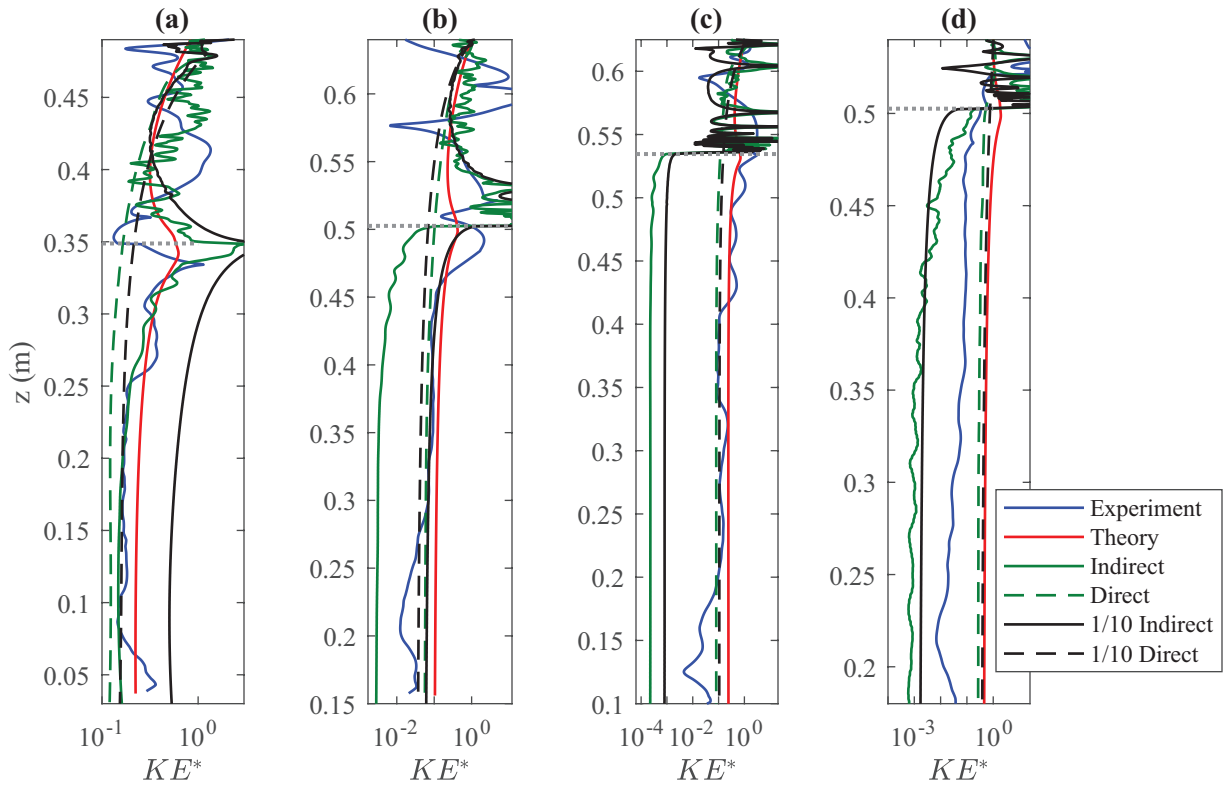


Figure 5.2: Normalized Kinetic energy of cubic density profiles corresponding to the (a) medium, (b) steep, (c) sinusoidal, and (d) complex topographies. Data for (b) is the same as Fig. 5.4(c).

the indirect methods in the evanescent region. In Fig. 5.2, the propagating kinetic for the medium topography is the largest, followed by the steep, complex and sinusoidal topographies. Note that there is a spread in the energy for each of the methods due to the normalizing process.

In Fig. 5.2(a), the kinetic energy associated with the 1/10 indirect simulation is larger than the other methods and also follows closely with the direct simulation in Fig. 5.2(b). In both cases, the full amplitude indirect kinetic energy shows significantly less energy relative to the direct methods. One of the errors that can be associated with indirect methods is an under/over estimate of the energy in the evanescent region. Because of this, the normalized energy is much larger/smaller than the other methods, but these values been inflated (deflated) by the normalizing process. Lee et al. [112] found that the indirect simulations are good estimates of kinetic energy, but only far from the turning depth and the topography. However, in Fig. 5.2(a), the 1/10 indirect simulation underestimates the kinetic energy in the evanescent region, causing a very large relative

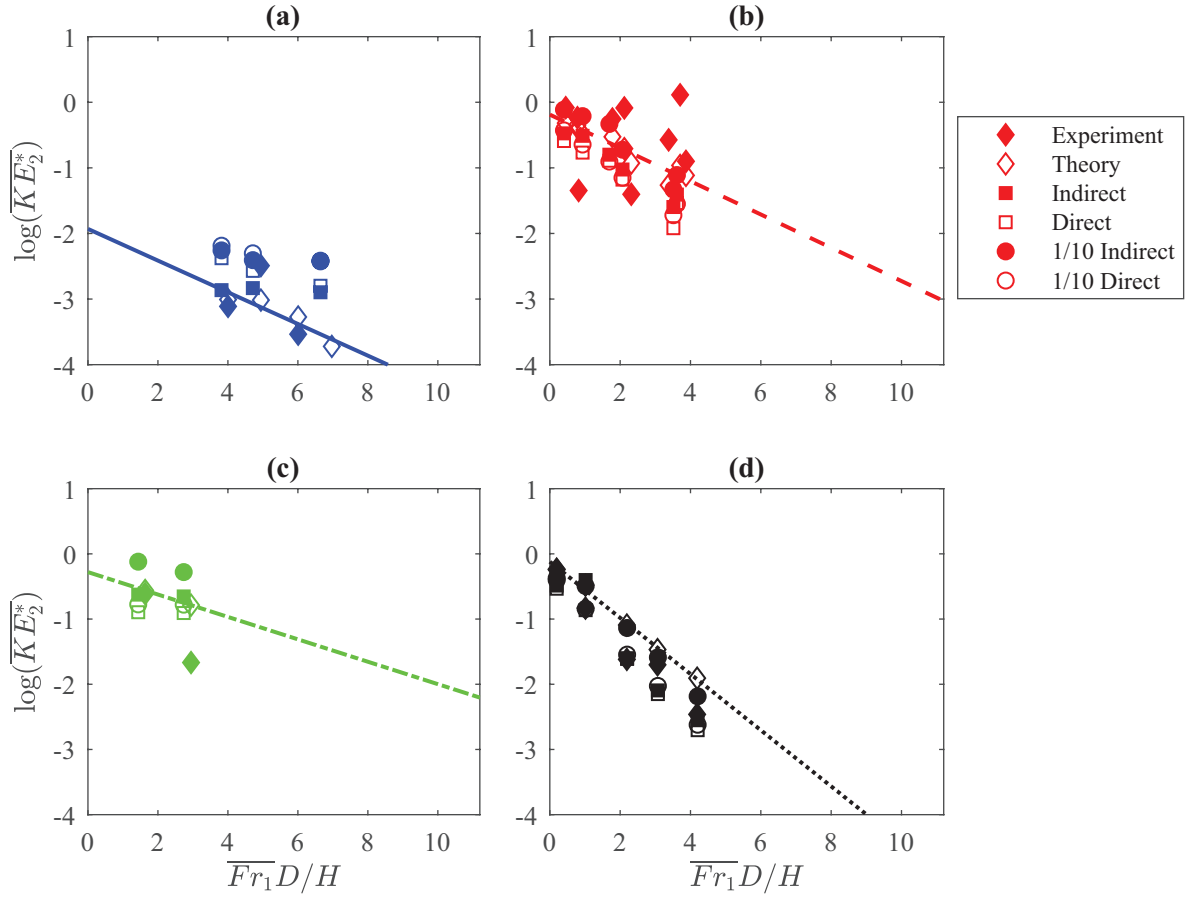


Figure 5.3: \overline{KE}_2^* as a function of $\overline{Fr}_1 D/H$ for the medium topography for cases with (a) two layer, (b) parabolic, (c) cubic, and (d) exponential density profiles.

energy in the propagating region. Conversely, the full amplitude indirect method overestimates the direct method by two orders of magnitude in the evanescent region of Fig. 5.2(b)-(d), leading to an underestimate of the normalized energy in the propagating region. Interestingly, the experimental data, while not a perfect match with the direct methods or the theory, does not show near the variation of energy in the evanescent region. This is unusual as both the experiments and the indirect methods use the same set of equations to estimate energy.

Kinetic energy is averaged in the propagating region and normalized for easier comparison and is denoted as \overline{KE}_2^* . It can be considered as the percentage of kinetic energy of the evanescent waves generated by the topography at the forcing frequency that passes into the propagating re-

gion. \overline{KE}_2^* is calculated for each case and shown as a function of $\overline{Fr}_1 D/H$ for the medium, steep, sinusoidal, and complex topographies in Figs. 5.3-5.6, providing a relative percentage of energy that passes from the evanescent waves generated at the topography into the internal waves in the propagating region. In each figure, the four graphs correspond to the four density profiles: (a) two layer, (b) parabolic, (c) cubic, and (d) exponential. Kinetic energy corresponding to each of the methods are indicated with different shapes with the experimental data as closed diamonds, theory as open diamonds, full amplitude indirect simulation as closed squares, direct simulations as open squares, 1/10 indirect simulations as closed circles, and 1/10 direct simulations as open circles. We note that not all of the experimental and theoretical data points have corresponding simulation data. Because of this, and as a guide for a simple comparison between each of the density profiles, a trendline fit only to the theoretical data is included in each figure and the scales for all of the figures are the same to quickly compare each figure. In all cases, the trendline is a linear fit with a constant slope such that

$$\log(\overline{KE}_2^*) = C_1 x + C_2 \quad (5.23)$$

R^2 values are not included because some topography and density profiles have only a few data points, which would increase this value for those fits without actually indicating the confidence in the data as a whole.

A consistent trend in Figs. 5.3-5.6 is that as $\overline{Fr}_1 D/H$ increases, there is a decrease in \overline{KE}_2^* . As \overline{Fr}_1 increases, the evanescent region has a relatively weaker stratification, meaning the evanescent waves will decay more rapidly. In addition, increasing D/H increases the distance the evanescent waves travel and decay before crossing the turning depth. Combining the two effects shows a clear trend of decreasing energy transmitting into the propagating region. With this trend established for each of the four topographies, we will now explore each topography individually.

In Fig. 5.3, with the medium topography, the theoretical estimate of energy is the largest in only the exponential density profile, (a). Here, all simulation methods indicate higher energy than the theory and experiments. Experiments and 1/10 indirect simulations are the largest in Fig. 5.3(b) when a parabolic density exists. Direct simulations match well with the theoretical values

Table 5.4: Slopes of the trendlines based on the theoretical data points in Figs. 5.3-5.6 for each topography and each density profile using Eq. 5.23.

	Two layer	Parabolic	Cubic	Exponential
Medium	-0.24	-0.25	-0.17	-0.43
Steep	-0.06	-0.37	-0.25	-0.45
Sine	-0.22	-0.22	-0.26	-0.28
Complex	-0.36		-0.47	-0.95

for parabolic and cubic profiles. All plots show that each method varies somewhat in the estimate of \overline{KE}_2^* , with the exponential density profile indicating the least separation between the methods.

To compare the propagating kinetic energy for each density profile, the slopes of the trendlines are listed in Tab. 5.4. As each topography will be discussed in a similar manner, the slopes for all topographies and all density profiles are listed. Comparing the decay rate for each density profile for the medium topography of Fig. 5.3, it is clear that the kinetic energy in the exponential profile decays the most rapidly, while the two layer and parabolic trends indicate very similar slopes. The smallest decay is seen in the theoretical trend of the cubic profile, but there are only two cases for this profile.

\overline{KE}_2^* for the steep topography and individual densities is plotted in Fig. 5.4, with the two layer, parabolic, cubic, and exponential density profiles in Figs. 5.4(a), (b), (c), and (d) respectively. Here, the exponential density profile again has the largest slope with a value similar to the medium topography (See Tab. 5.4). Following the exponential density slope are the parabolic, cubic, and the two layer density slopes. For the two layer density, in Fig. 5.4(a), the range of $\overline{Fr}_1 D/H$ values is higher than in Figs. 5.4(b)-(d), which could account for the significantly smaller slope of the trendline.

Although the theoretical trendline and direct simulation data in Fig. 5.4 all show that \overline{KE}_2^* decreases with increasing $\overline{Fr}_1 D/H$, the trend is not as clear in the experimental data for this topography. A slight increase in energy is seen in Figs. 5.4(b) and (c), while the experimental energy in Fig. 5.4(d) stays fairly constant. Simulation data for Figs. 5.4(a), (b), and (d) follow the

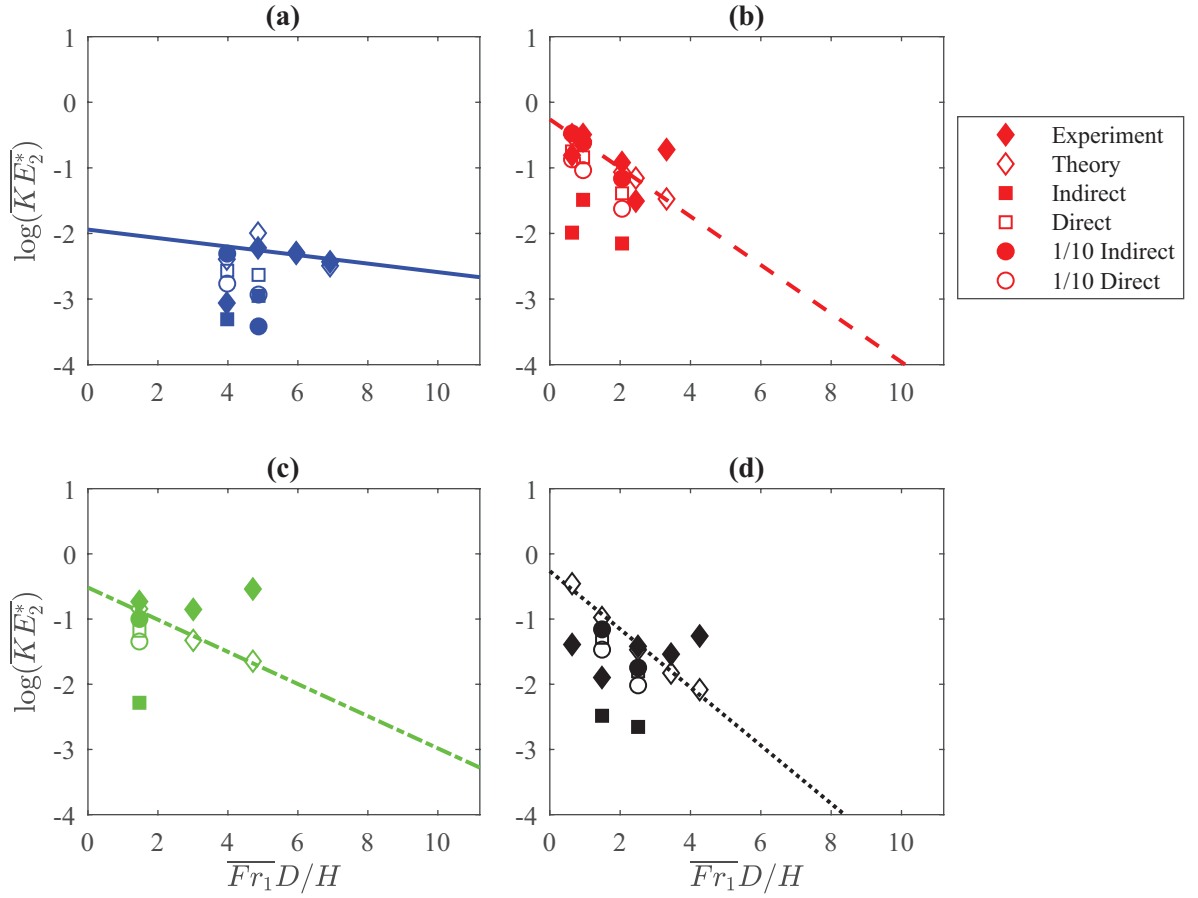


Figure 5.4: \overline{KE}_2^* as a function of $\overline{Fr}_1 D/H$ for the step topography for cases with (a) two layer, (b) parabolic, (c) cubic, and (d) exponential density profiles.

same trends as the theoretical data, including the indirect methods, which use the same equations as the experiments. Experimental data may contain more errors associated with the steep topography because of the increased $S_{\text{top,m}}$ relative to the medium topography. As the physical slope of the topography increases, it is more likely that turbulence will be generated by the topography, which leads to errors in the indirect methods near the topography where KE_{norm} is calculated. In an effort to overcome these errors, curve fits are applied to the data near the topography to smooth out the oscillations and noise. Unfortunately, the effectiveness of the curve fits decreases with increasing turbulence, causing both over and underestimates of the normalizing values for the experimental kinetic energy, and thus the almost constant energy regardless of $\overline{Fr}_1 H/D$.

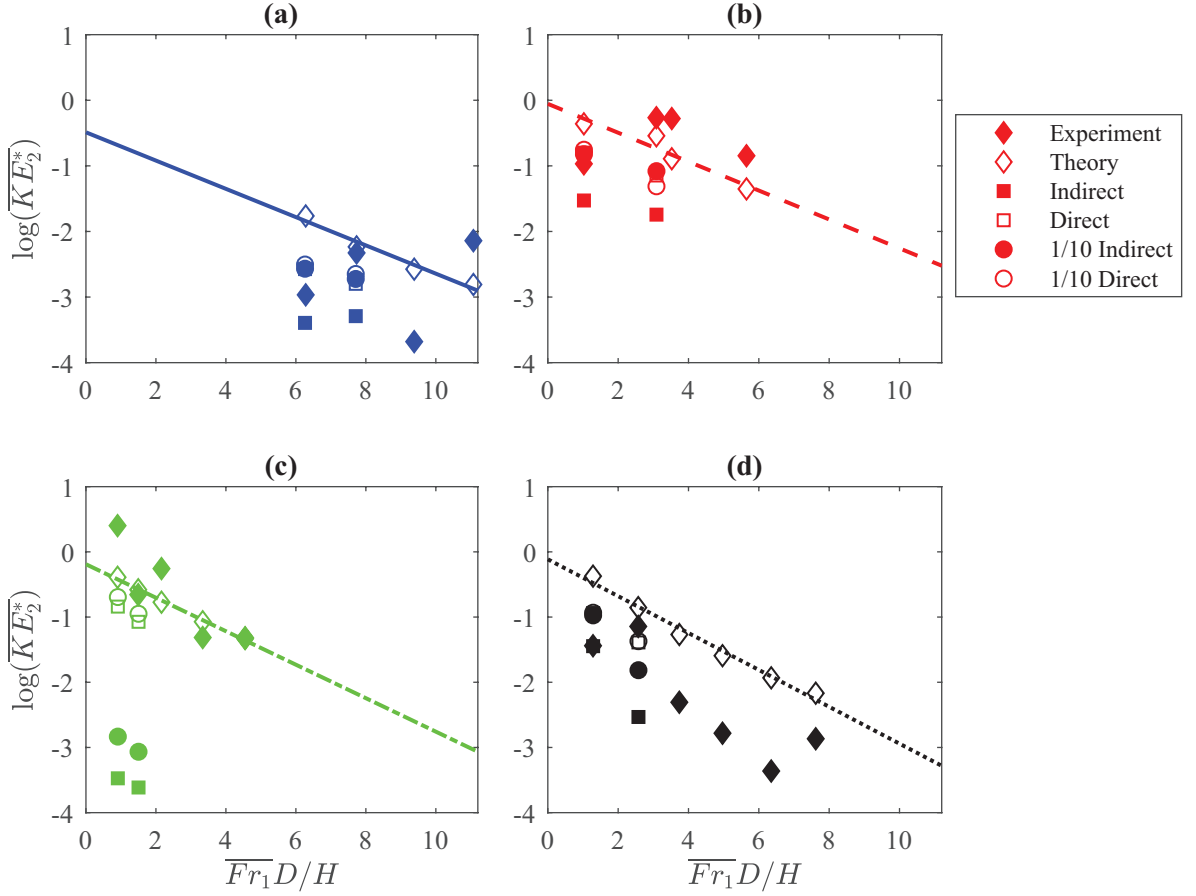


Figure 5.5: \overline{KE}_2^* as a function of $\overline{Fr}_1 D/H$ for the sinusoidal topography for cases with (a) two layer, (b) parabolic, (c) cubic, and (d) exponential density profiles.

All the trendlines for the sinusoidal topography indicated in Tab. 5.4 and Fig. 5.5 are nearly the same. While the exponential density profile still indicates the most rapid decay, similar to the medium and steep topographies, it is only slightly larger than the other three density profiles for the sinusoidal topography. This consistency across all density profiles leads to the idea that topographical shape is a more important factor than density profile when predicting internal wave kinetic energy.

For the data of the sinusoidal topography, shown in Fig. 5.5, the theoretical energy is almost always the largest energy, except for one or two experimental data points in Figs. 5.5(a), (b) and (c). Although the sinusoidal topography has two peaks, it has the same $S_{\text{top,m}}$ as the medium

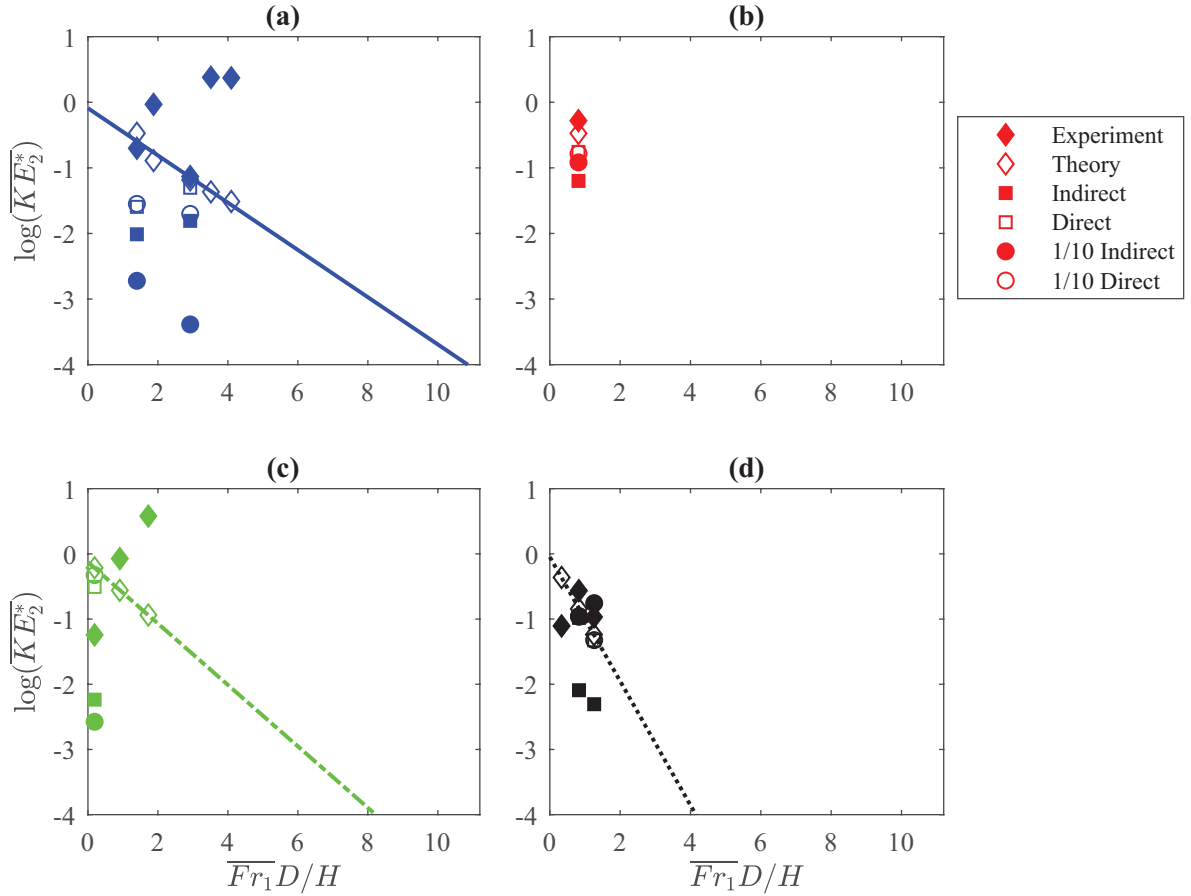


Figure 5.6: \overline{KE}_2^* as a function of $\overline{Fr}_1 D/H$ for the complex topography for cases with (a) two layer, (b) parabolic, (c) cubic, and (d) exponential density profiles.

topography, which decreases the variations in the experimental data seen in Fig. 5.4 with the steep topography. In each figure, simulation data always indicates less energy than the theoretical data, but the data points follow a similar decay in energy as the theoretical trendline.

For the complex topography in Figure 5.6, there is only one set of data for the parabolic density profile in Fig. 5.6(b), and a trendline is not included. Following the same trend as the previous three figures, the exponential density profile has the largest slope of the density profiles and is more than twice as large as the other topographies for exponential densities (Tab. 5.4). Slopes for the two layer and cubic profiles are also larger than the corresponding profiles for the other topographies. Comparing all of the decay rates for the theoretical trends in Tab. 5.4, there

is more variability in the kinetic energy of the propagating internal waves for one density profile across multiple topographies than there is for one topography across multiple density profiles, even with the variation in decay rates indicated by the complex topography.

With multiple peaks and the largest $S_{\text{top,m}}$, nonlinearities and turbulence become more important for the complex topography. Although the theoretical model is a linear model, it still matches well with the direct simulations in Fig. 5.6, which does account for turbulence generation. Smaller values of $\overline{Fr}_1 D/H$ indicate a relatively smaller excitation frequency, which would decrease the turbulence generation of the complex topography, allowing for the theory and direct methods to indicate similar energy. In contrast, the experiments and indirect methods are negatively affected by low $\overline{Fr}_1 D/H$ because it also indicates the topography is relatively close to the turning depth. Even if the turbulence generation is low, it will still cause inaccuracies in estimating KE_{norm} for these methods and causes the experiments to indicate an increasing kinetic energy with increasing $\overline{Fr}_1 D/H$. Each experimental data point indicating $\log(\overline{KE}_2^*) > 0$ is indicative of an underestimate of KE_{norm} .

Figure 5.7 combines individual density profiles of the medium topography data of Fig. 5.3 into one graph, now with \overline{KE}_2^* as a function of \overline{Fr}_1 in Fig. 5.7(a), D/H in (b), and $\overline{Fr}_1 D/H$ in (c). Each graph contains data for the four density profiles and six methods, along with a trendline created from a curve fit of all the data associated with the specific abscissa. Trends in each figure indicate that \overline{KE}_2^* decreases with increasing \overline{Fr}_1 , D/H , and $\overline{Fr}_1 D/H$ as is expected. In Fig. 5.7(a), the data for $\overline{Fr}_1 = 1 - 1.5$ shows a sharp decrease in energy, with the two layer cases indicating a slower decay rate. This slower rate of decay seen in the two layer cases could be an inherent problem with calculating energy with constant N in the evanescent region. However, these two layer cases do not overlap with the other density profiles, so it is possible that the overall decay of \overline{KE}_2^* does slow for all density profiles. In Fig. 5.7(b), there is more of an overlap between the two layer and the other density profiles, but each of the two layer cases were completed with the same experimental setup such that D is constant for all experiments tests. Slight differences in the setup between the simulations and experiments indicate two values of D/H , but they are very similar

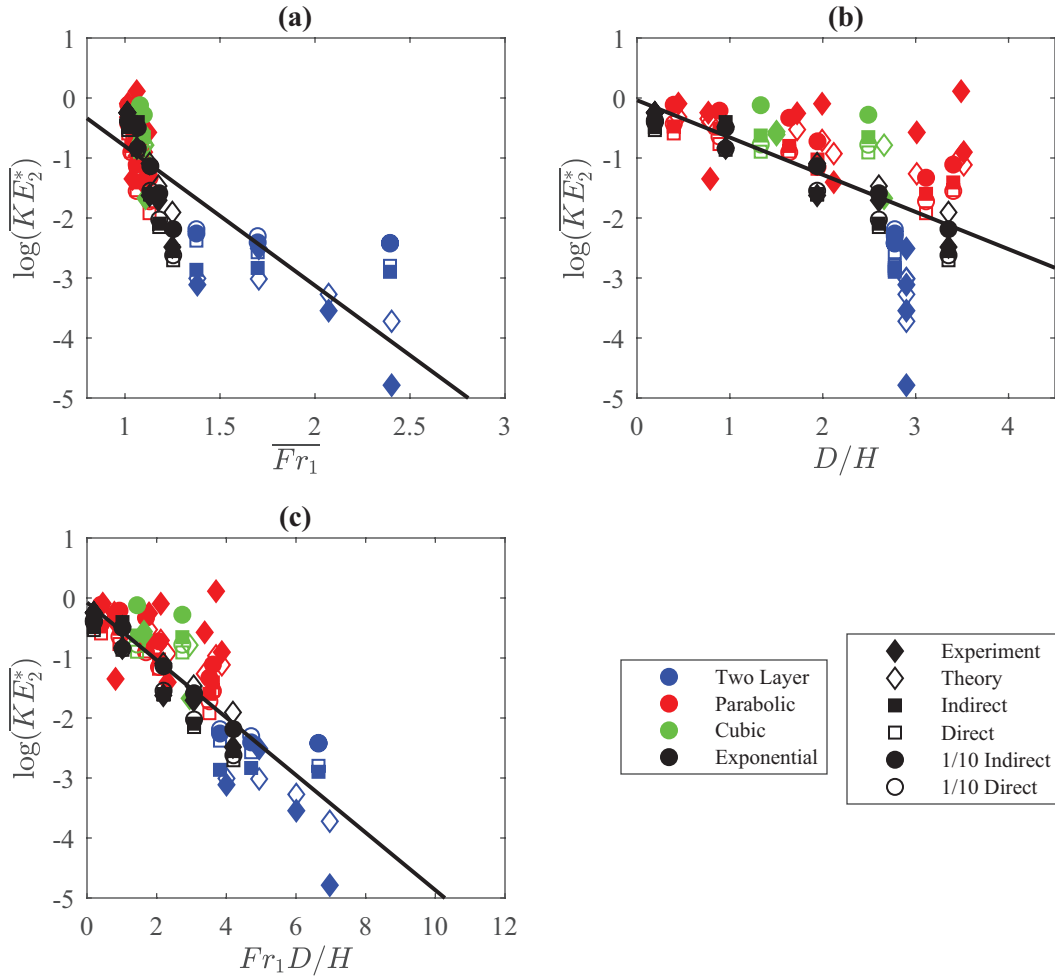


Figure 5.7: \overline{KE}_2^* as a function of (a) \overline{Fr}_1 , (b) D/H , and (c) $\overline{Fr}_1 D/H$ for all density profiles.

values. By plotting \overline{KE}_2^* as only D/H , the two layer cases do not follow the same trends as the other density profiles.

Figure 5.7(c) combines the previous two nondimensional numbers and creates a better collapse of all the data, including the two layer cases. One of the purposes of this paper is to investigate whether or not assuming a two layer linear density profile is accurate for investigations of varying density profiles. Based on the trendlines of Fig. 5.7, the two layer density data follows the same trends as the data for the other density profiles for $\overline{Fr}_1 D/H$, but not for each term individually. Although small, there is an overlap of the two layer and exponential data for this topography also

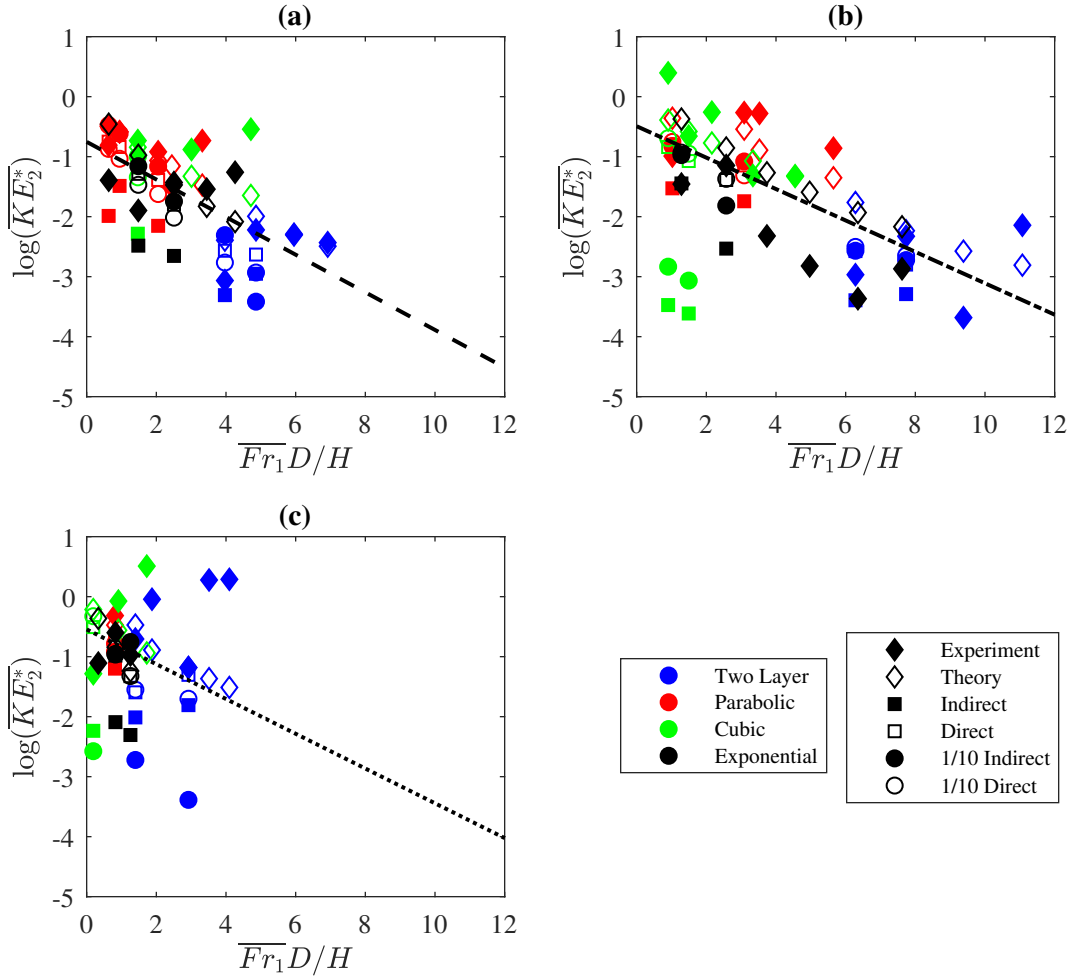


Figure 5.8: \overline{KE}_2^* as a function of $\overline{Fr}_1 D/H$ for the (a) steep, (b) sinusoidal, and (c) complex topographies.

providing evidence that two layer cases can approximate the same conditions as the varying density cases as long as both \overline{Fr}_1 and D/H are included when estimating \overline{KE}_2^* .

With all of the density profiles for the medium topography in Fig. 5.7(c), the data from the three remaining topographies from Figs. 5.4-5.6 are shown in Fig. 5.8 with data from the steep topography in Fig. 5.8(a), sinusoidal in (b), and complex in (c). Each graph, including the medium topography data in Fig. 5.7(c), contains a curve fit of all the data associated with the specific topography, except for the complex topography where theory and direct simulation data are the best fit as proximity to the topography and turning depth decrease confidence in the other methods.

Table 5.5: Coefficients corresponding to Eq. (5.23) for the trendlines associated with each topography.

Topography	C_1	C_2	R^2
Medium	-0.4793	-0.0758	0.7234
Steep	-0.3015	-0.8051	0.4275
Sinusoidal	-0.2617	-0.4930	0.3593
Complex	-0.2898	-0.5462	0.4971

Coefficients and R^2 values for the trendlines in Figs. 5.7(c) and 5.8 are listed in Tab. 5.5. Comparing these values to those listed for individual density profiles in Tab. 5.4, we note that the sinusoidal topography has the most similar slope (C_1) between the two tables, though it also has the smallest R^2 value indicating the largest differences between each of the methods. Interestingly, the slope of the curve fit for all the medium topography data is larger here than for any of the fits listed in Tab. 5.4, though it is similar to the exponential density profile. Ranges of $\overline{Fr}_1 D/H$ for the different density profiles for the medium topography vary, but the data together shows a clearer overlap of the methods and the density profiles, and the trendline fits the data very well. This improved fit is due to the medium topography having the smallest slope, $S_{\text{top,m}}$, which generates the least amount of turbulence so the indirect simulations and experiments are more accurate.

To better understand the impact of topography shape on the relative kinetic energy in the propagating region, the trendlines from Figs. 5.7(c) and 5.8 are plotted together in Fig. 5.9. Although the trendline for the complex topography is a fit only to the theory and direct simulation data, it is still included here as general estimate of \overline{KE}_2^* . For $\overline{Fr}_1 D/H < 2$, the highest propagating energy is from waves generated by the medium topography because it has the smallest maximum slope and generates the least turbulence. Sinusoidal and complex topographies have nearly the same propagating energy, and the steep topography has the lowest. Both the medium and sinusoidal topographies have the same $S_{\text{top,m}}$ and similar widths, but the kinetic energy of the medium topography internal waves decays more rapidly with $\overline{Fr}_1 D/H$, such that the waves associated with sinusoidal topography will have a larger energy when $\overline{Fr}_1 D/H > 2$. A higher overall propagating

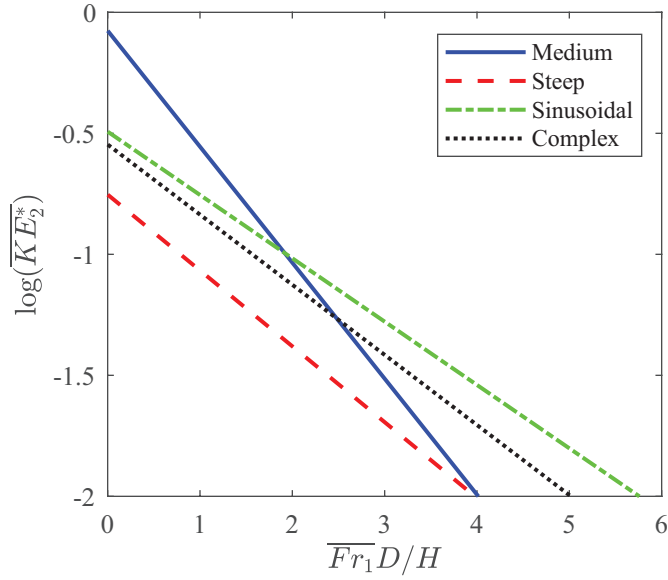


Figure 5.9: Trendlines for each topography matching those from Fig. Figs. 5.7(c) and 5.8.

kinetic energy is also seen for the complex topography compared to the steep topography, although the complex topography has a larger $S_{\text{top},m}$ based on the individual peaks. When calculating $S_{\text{top},m}$ for the overall Gaussian fit of the complex topography excluding the peaks, $S_{\text{top},m} = 2.5$, which is only slightly larger than the medium and sinusoidal topographies. Past research has shown a topography with a smaller $S_{\text{top},m}$ will have generally result in internal waves with more kinetic energy [64, 100]. Based on actual values of $S_{\text{top},m}$, the steep topography would have greater \overline{KE}_2^* than the complex topography, but the Gaussian fit and the trendlines of Fig. 5.9 indicate the opposite. In this case, although there are many peaks in complex topography, the overall energy transfer is based more on the general shape of the topography. However, this is not true for the sinusoidal topography where, based on the Gaussian fit described in Sec. 5.4.4, $S_{\text{top},m} = 0.98$, smaller than the medium topography. It is likely that the relative closeness of the individual peaks of the topography affects whether or not the energy in the propagating region is affected more by the individual peaks or the overall shape of the topography [90]. Thus, both $S_{\text{top},m}$ and the actual shape of the topography, including peaks, must be taken into account in predicting \overline{KE}_2^* .

With trendlines defined for both density and topography, estimates of \overline{KE}_2^* can be made for a wide variety of scenarios using Eq. 5.23 and Tab. 5.5. Based on these equations, an estimate of the kinetic energy of internal waves generated from an evanescent region can be made for oceanic scenarios where the topographies are similar to those listed here. In addition, the trends of Fig. 5.9 provide general guidelines for all topographies and density profiles. When $\overline{Fr}_1 D/H > 4$ internal wave kinetic energy is between 1.5 and 2 orders of magnitude less than the kinetic energy of the originally generated evanescent wave. From this, we recommend using $\overline{Fr}_1 D/H = 4$ as a limit for when non-negligible kinetic energy may pass from evanescent waves into a propagating region.

5.6 Conclusion

This work has presented a comparison of the kinetic energy density of four topographical shapes and four density profiles using six different methods. Each of the methods showed similar trends in energy. Based on trends in the average, normalized propagating wave energy, \overline{KE}_2^* , the effects of topography slope ($S_{\text{top,m}}$), the presence of multiple peaks, and density profile were each explored.

Direct comparisons of the different methods for normalized energy, KE^* , were made in Figs. 5.1 and 5.2, where it was seen that the indirect simulations and experiments show significant oscillations in the data in the evanescent region and near the turning depth. These methods perform best when far from either a topography or a turning depth. Also, the direct simulation data showed very similar values to the theoretical data, both for the full and 1/10 amplitude simulations.

In Figs. 5.3-5.6, comparisons of the methods were discussed for \overline{KE}_2^* . In general, all methods follow the same trends as indicated by the theoretical data that propagating kinetic energy decreases with increasing $\overline{Fr}_1 D/H$. Experimental data did not follow the trends as well for steep and complex topographies, both of which have the highest values for $S_{\text{top,m}}$ while the complex topography cases had the smallest evanescent regions. From the slopes of the density data for each topography in Tab. 5.4, the data collapses best when all density data is combined for one topography, indicating the importance of \overline{Fr}_1 over individual density profiles.

From Fig. 5.7, the two layer density profiles only follow the same propagating kinetic energy trends as the other density profiles when \overline{KE}_2^* is calculated as a function of the combined nondimensional term $\overline{Fr}_1 D/H$. This provides evidence that using a two layer density profile can approximate the kinetic energy density of constantly varying density scenarios when both the effects of stratification and the relative location of the topography are included.

Figures 5.7(c) and 5.8 includes all methods and all density profile data for each individual topography, along with trendlines based on all (medium, steep, sinusoidal), or some (complex) of the data. These trends are explored Fig. 5.9. While the medium and sinusoidal topographies have the same $S_{\text{top,m}}$, the medium topography has greater \overline{KE}_2^* for $\overline{Fr}_1 D/H < 2$, and the sinusoidal is greater for $\overline{Fr}_1 D/H > 2$. Similarly, the complex topography has the largest $S_{\text{top,m}}$, but indicates more energy than the steep topography. These findings indicate that a combination of both $S_{\text{top,m}}$ and the actual topography shape, including peaks, directly influence the amount of kinetic energy transferred into the propagating region. Based on the trends, we recommend that $\overline{Fr}_1 D/H = 4$ be set as an upper limit for estimating propagating energy from an evanescent region. In these situations, a simple estimate of \overline{KE}_2^* can be made using Eq. (5.23) and Tab. 5.5.

CHAPTER 6. SYNTHETIC SCHLIEREN AND PARTICLE IMAGE VELOCIMETRY: AN INVESTIGATION OF TWO EXPERIMENTAL TECHNIQUES FOR INTERNAL WAVE KINETIC ENERGY DENSITY

This chapter represents a full manuscript in preparation for submission to Experiments in Fluids.

6.1 Contributing authors and affiliations

Allison Lee, Kyle Hakes, Julie Crockett, Department of Mechanical Engineering, Brigham Young University, Provo, UT 84602

6.2 Abstract

Kinetic energy density of internal waves generated from evanescent regions is compared for two different experimental methods: synthetic schlieren (SS) and particle image velocimetry (PIV). Multiple topography shapes and density profiles are used with each method. Both experimental processes show similar wave beam characteristics in the evanescent and propagating regions, and the same trends for variations in the kinetic energy density of the propagating internal waves. Specifically, kinetic energy decreases as (1) the relative strength of the natural frequency in the evanescent region decreases and (2) the size of the evanescent region increases. SS experimental methods generally overestimate kinetic energy relative to PIV methods. However, SS and PIV data correlate well in both the evanescent and propagating regions away from the topography and turning depth, regions where SS processing assumptions break down.

6.3 Introduction

The density of stratified fluids, such as the ocean and atmosphere, varies with height. When a stratified fluid is disturbed, for instance by the tides in the ocean or winds in the atmosphere over topography, internal waves can be generated. If the frequency of the disturbance (ω) is less than the natural frequency of the fluid (N), internal waves are generated. Stratification strength is based on the rate of density change, which defines N ,

$$N^2 = \frac{-g}{\rho_0} \frac{d\rho}{dz} \quad (6.1)$$

where g is the gravitational constant and ρ_0 is a reference density. When $N < \omega$, evanescent waves are formed. Evanescent waves move vertically and their amplitude decays at an exponential rate. Previous work has shown that evanescent waves can become propagating waves if they pass into a propagating region ($N > \omega$) [5, 18, 82, 100]. The location where the evanescent wave becomes a propagating wave ($N = \omega$) is called a turning depth.

To investigate the amount of energy in internal waves passing through a turning depth, experiments can be a valuable addition to observations and simulations. Synthetic schlieren (SS) is a prevalent experimental method for internal wave studies as seen by the work of [20, 34, 58, 63, 99, 104, 108], among others. SS takes advantage of the deflection of light rays passing through a fluid. In a stratified fluid, as both evanescent and internal waves travel away from their generation point, the waves heave the fluid up and down altering the local density. A camera focused on a random dot pattern behind the experimental apparatus captures the apparent movement of the dots created by local variations in density which leads to local variations in index of refraction. Comparing the refracted image to an image taken of the undisturbed stratified water in the tank, the change in N can be obtained. Further processing allows pressure and kinetic energy estimates [20, 58, 99, 100]. SS has been used previously to investigate number of internal waves flows including harmonic generation [20], microscale waves [110], and colliding wave beams [46]. Here, our interest is in internal waves propagating through varying density profiles.

SS has been used to study internal waves tunneling through multi-layered density profiles, where the waves move from a propagating region, through a mixed ($N = 0$) or evanescent region, and into another propagating region. A transmission coefficient (T) describes the percentage of incident internal wave energy that passes through the weakly stratified region and into a propagating region. Sutherland and Yewchuk [80] used SS to confirm linear theory results for the transmission coefficient for internal waves passing through a mixed region, and this work was expanded by Gregory and Sutherland [79] who found T based on evanescent regions. Tunneling has also been studied with SS by Mathur and Peacock [78] who found transmission and reflection coefficients for variety of nonuniform density profiles. In each of these scenarios, the time rate of change of N^2 gathered from SS experiments is used to approximate T and compare experimental data to linear theory. These examples also focused on internal waves passing through small evanescent regions. Here, we will use the methods described by Wunsch and Brandt [20] concerning SS data to directly estimate kinetic energy of both evanescent and internal waves.

Another imaging method has also been used with internal waves, Particle Image Velocimetry (PIV) [63]. With PIV, neutrally buoyant particles are seeded into a fluid flow and tracked to estimate the velocity field in the fluid [62]. PIV can be used to study both internal and evanescent waves. To characterize the decay of evanescent waves, [64] used PIV to validate numerical simulations of internal waves entering an evanescent region. These experiments are different than tunneling examples provided earlier because there were only two regions being explored. Looking at both evanescent and internal waves, Paoletti et al. [18] used PIV to estimate radiated power of internal waves formed from an evanescent region and their results matches very well with their numerical simulations.

Inherent to all stratified flow experiments is that the index of refraction of the fluid being studied will vary as waves move through the fluid. While SS uses this in order to define variations in N^2 , a varying index of refraction could cause inaccurate particle tracking in PIV. To address this problem, Dalziel et al. [63] used simultaneous SS and PIV experiments in a stratified flow. SS data was used to define the density field while PIV defined the velocity field. Corrections were made to

the velocity field based on the SS data, and they found that particle movement caused by the index of refraction is small, but not completely negligible. Using SS density field data is important to correct PIV data when there are significant variations in the density field.

Although both PIV and SS can be used to study internal waves, the kinetic energy results of each method have not been directly compared. It is known that the cost of setting up a PIV experiment can be prohibitive, but the results easily translate from velocity fields to energy or power. In contrast, SS experiments are less expensive to setup, but results are generally used to define density fields or stratification profiles. Recent work by Lee et al. [111] used SS experiments to estimate energy flux by from density field data, which can be used to estimate internal wave energy flux in the ocean. Here, we present a comparison of kinetic energy estimates using both PIV and SS in order to allow confident use of the best or cheapest method available. To explore capabilities of each method in a range of situations, a variety of density profiles are used. The majority of the generated waves are initially evanescent that pass through a turning depth becoming propagating internal waves. Kinetic energy is estimated throughout the wave depths for a variety of topographic shapes. Both PIV and SS are performed for all tests and regions where each are accurate are defined.

In Sec. 6.4 experimental setup for both the SS and PIV methods are described. Section 6.5 contains results and side by side comparisons of each method, with a discussion of the results and future work presented in Sec. 6.6.

6.4 Methods

This section will outline the density profiles and topographies used for each set of experiments, provide information on the individual processes of SS and PIV, and describe the filtering process used to estimate final propagating wave kinetic energy.

Figure 6.1 is a sketch of the experimental setup. Figure 6.1(a) specifically displays the SS setup, showing a side view of the camera, mask, and light box used in SS. The camera focuses on the mask, which is a random patterned of dots illuminated by the light box, and captures the

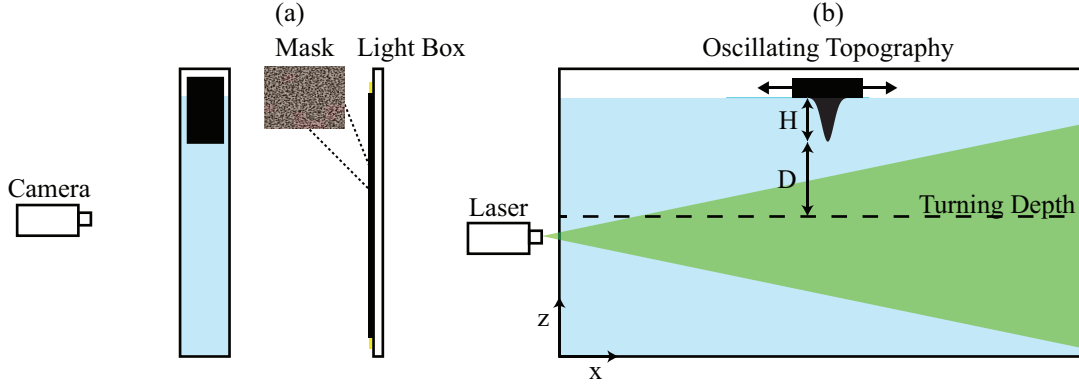



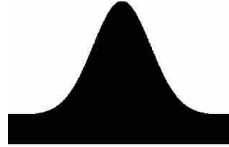

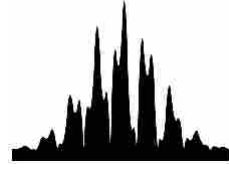
Figure 6.1: Experimental setup of (a) SS and (b) PIV experiments

Table 6.1: Equations for each of the density profiles.

Profile Number	Profile	Equation
1	One Layer Linear	$\rho = az + b$
2	Two Layer Linear	$\rho_1 = az + b; \rho_2 = cz + d$
3	Quadratic	$\rho = az^2 + bz + c$
4	Cubic	$\rho = az^3 + bz^2 + cz + d$
5	Exponential	$\rho = ae^{bz} + c$

apparent motion of the dots needed to for the SS process [58]. Figure 6.1(b) indicates the PIV setup where the front view shows the general location of the laser sheet relative to the topography. The tank shown is acrylic with a length, width and height of 0.15 m, 2.45 m, and 0.91 m. To reduce wave reflections in the tank, the bottom was lined with matting. A modified version of the double bucket method [93] was used to fill the tank to a height between 0.55 m and 0.75 m with one of the following density profiles: one layer linear, two layer linear, quadratic, cubic, or exponential. These correspond with N^2 profile types; uniform, two layer uniform, linear, quadratic, and exponential, respectively. Specific density profiles fit the equations outlined in Table 6.1 where ρ has units of kg/m^3 , z has units of meters, and a , b , and c are coefficients calculated from the corresponding curve fit. Units for each coefficient vary based upon density profile. Density profile curve fits had an average $R^2 = 0.997$ for all cases. Due to mixing, tank was emptied, cleaned, and re-filled every 10 tests. Before the first test, density measurements were taken every 3 cm, and then every 5 cm after every fourth test.

Table 6.2: Names, equations and images of the four topography profiles. All units are in meters.

Name	Equation	Profile
Medium Gaussian	$h = 0.1e^{-x^2/0.0424^2}$	
Steep Gaussian	$h = 0.1e^{-x^2/0.0106^2}$	
Sinusoidal	$h = 0.0355 \sin(2\pi x/0.11)$	
Complex	$h = 0.16715e^{-x^2/0.0566^2} \frac{1}{4} \sin(520x) + \cos(115x) $	

To create internal waves, a topography was inverted and placed at the water line of the tank (Fig. 6.1), with $z = 0$ at the bottom of the tank. Four topography profiles were used and they will be referenced in this paper as medium, steep, complex, and sinusoidal topographies. Governing equations and profiles for each topography are listed in Table 6.2. Medium and steep topographies are based on Gaussian distributions whereas the complex topography was modeled after the topography outlined by [18]. For comparison, the sinusoidal topography consisted of two periods with a maximum slope that is equivalent to the maximum slope of the medium topography. All density profiles are with the medium topography and all topographies are tested with the exponential density profile.

Specific details for each experimental case are listed in Tab. 6.3 including case number, excitation frequency ω_d , height of the turning depth z_{td} , total water height Z_H , excursion length L , and three nondimensional numbers, D/H , \overline{Fr}_1 , and $\overline{Fr}_1 D/H$. D/H is a ratio of the distance between the tip of the topography and the turning depth (D) to the height of the topography (H)

Table 6.3: Experimental details for each case. The medium topography was used for cases 1-12, steep for case 13, sinusoidal for cases 14 and 15, and complex for case 16. All lengths are in meters. The units of a, b, c, and d are defined by the appropriate density profile in Tab. 6.1.

Case	Density	a	b	c	d	ω_d	z_{td}	Z_H	L	\overline{Fr}_1	D/H	$\overline{Fr}_1 D/H$
1	1	-166	1123	0	0	0.8	NA	0.61	0.05	NA	NA	NA
2	1	-166	1123	0	0	0.9	NA	0.61	0.05	NA	NA	NA
3	1	-146	1117	0	0	0.81	NA	0.70	0.05	NA	NA	NA
4	1	-146	1117	0	0	1.41	NA	0.70	0.05	1.18	NA	NA
5	2	-215	1114	-13	1031	0.8	0.41	0.63	0.045	2.25	1.2	2.70
6	2	-215	1114	-13	1031	1.0	0.41	0.62	0.045	2.77	1.1	3.05
7	3	59	-161	1109	0	1.01	0.48	0.66	0.05	1.02	0.77	0.79
8	4	-27	172	-230	1097	1.22	0.24	0.61	0.044	1.16	2.65	3.08
9	4	-27	172	-230	1097	1.12	0.24	0.61	0.045	1.07	2.65	2.83
10	5	104	-3	995	0	1.05	0.34	0.66	0.05	1.15	2.21	2.53
11	5	118	-2	1000	0	0.91	0.51	0.70	0.045	1.05	0.87	0.91
12	5	114	-2	1003	0	1.09	0.34	0.70	0.048	1.16	2.56	2.98
13	5	129	-2	984	0	1.0	0.45	0.63	0.04	1.03	0.85	0.87
14	5	121	-2	979	0	1.05	0.39	0.59	0.049	1.07	1.93	2.06
15	5	129	-2	984	0	1.0	0.45	0.63	0.041	1.05	1.64	1.72
16	5	131	-2	980	0	1.04	0.4	0.63	0.04	1.01	0.17	0.17

as shown in Fig. 6.1(b). $\overline{Fr}_1 = \omega_d / \overline{N}_1$ is the average Froude number in the evanescent region. \overline{N}_1 is the average natural frequency over the height D . Combining the two terms, $\overline{Fr}_1 D/H$ provides insight on the combined effect of the distance the evanescent wave travels and the strength of the stratification in the evanescent region. Note that cases 1-4 are one layer, uniform N cases. As such, there is no turning depth and D/H does not exist. In cases 1-3, $N > \omega$ and thus no evanescent region exists and \overline{Fr}_1 is not applicable.

For both methods, the kinetic energy density of the waves is calculated as

$$KE = \tilde{U}^2 + \tilde{W}^2 \quad (6.2)$$

where \tilde{U} and \tilde{W} are the Fourier amplitudes of the horizontal and vertical velocities, respectively. Only kinetic energy near the excitation frequency ($\pm 5\%$) are included.

6.4.1 Average kinetic energy

Previous research has shown that each of the topographies used here generate evanescent and internal waves at a narrow range of frequencies, but a wide range of horizontal wavenumbers depending on the topography [100, 112]. To accurately compare the two experimental methods and four topographies used here, it is necessary to average kinetic energy over a range of k values in a manner individual to the topography. Nappo [5] showed that the vertical velocity of internal waves from a Gaussian shaped topography is dependent upon the term $kB \exp[-(kB/2)^2]$ and is at a peak where

$$kB = \sqrt{2} \quad (6.3)$$

where k is the horizontal wavenumber of the wave and B is the Gaussian parameter of the topography. For the medium and steep topographies, $B = 4.24$ cm and 1.06 cm, respectively (See Tab. 6.2). However, Lee et al. [112] showed the predicted peak wavenumbers based on this value do not match with what is seen both in the experiments and the numerical simulations. Instead, they found a new Gaussian parameter, based on both the width of the topography and the excursion length is needed. By defining

$$B_L = \frac{W + L}{6} \sqrt{2} \quad (6.4)$$

where W is the width of the topography, then the new predicted dominant wavenumber calculated from Eq. 6.3 matches that of the experiments and numerical simulations. Based on Nappo's work, kinetic energy was averaged over the range of $0.5 < kB_L < 5$ for the Gaussian topographies as the kinetic energy decayed rapidly for $kB_L > 5$.

For the complex topography, although the Gaussian curve is multiplied by sine and cosine terms, B from the original equation in Tab. 6.2 still applies to the general shape. A Gaussian fit can be applied a single peak of the sinusoidal topography with with $B = 0.0314$. To encompass both peaks, B is doubled and the resulting fit is $h_{sine,gaus} = 0.071 \exp[-(x - 0.0819)^2 / 0.0628^2]$. Even though this shape has only one peak, it matches the overall width of the sinusoidal topography. To include the excursion length in B , it was found that B_L for the medium topography is approximately

equal to $B + L/4$. As both the sinusoidal and complex topographies are similar widths to the medium Gaussian, this was used to account for the excursion length for these two topographies.

With B_L full defined for each topography, kinetic energy for both SS and PIV was averaged over $0.5 < kB_L < 5$ for each of the topographies to provide a uniform way to accurately compare the two experimental methodologies.

6.4.2 Synthetic schlieren

For the SS experiments, a light box behind the tank illuminated a matrix of dots. The topography was oscillated at the set frequency, ω , for 15 periods to bring the experiment to steady state conditions. Images were taken with a jAi Cv-M4+Cl progressive scan camera for three minutes. Images then were processed at 6 fps through the commercially available software, Digiflow [58]. Processing the data in Digiflow provides $\nabla\rho'/\rho_0$, or the variation in density with respect to x and z . Using the $\partial\rho'/\partial z$ component and multiplying by gravity, a variation on Eq. 6.1 can be written as

$$\Delta N^2 = \frac{-g}{\rho_0} \frac{\partial\rho'}{\partial z} \quad (6.5)$$

which represents the local difference in natural frequency.

By assuming that the generated waves are planar with small amplitude, a relationship between \tilde{U} , \tilde{W} , and $\Delta\tilde{N}^2$ (Fourier amplitudes of ΔN^2) can be made for the evanescent and propagating regions. Kinetic energy density is calculated using Eq. 6.2. Complete details of the process are found in [20]. Specifically, in the evanescent region, [100] defined

$$KE_1 = \left| \frac{-q\omega\Delta\tilde{N}^2}{k(\partial_z N^2 + qN^2)} \right|^2 + \left| \frac{i\omega\Delta\tilde{N}^2}{\partial_z N^2 + qN^2} \right|^2 \quad (6.6)$$

where k is the horizontal wavenumber and q is the imaginary vertical wavenumber such that $m = iq$ in the evanescent region. The subscript 1 refers to the evanescent region. For the propagating

region, [20] defined

$$KE_2 = \frac{\omega^2 N^2}{k^2(N^2 - \omega^2) + (\omega \partial_z N^2 / N^2)^2} \left| \frac{\Delta \tilde{N}^2}{N^2} \right|^2 \quad (6.7)$$

with the subscript 2 denoting the propagating region. Near the turning depth, the small amplitude approximation breaks down and [100] recommend using kinetic energy away from the turning depth beginning at heights where $N/\omega > 10\%$. However, due to experimental setup limitations, this is not always possible.

6.4.3 Particle image velocimetry

SS test images were processed and reviewed to locate areas of strong wave activity in the evanescent and propagating regions and PIV tests were performed in those regions. A ruler was placed in the tank at these regions, and a correlation picture was taken with both the PIV and SS camera in order to correlate the locations of the two images with each other. PIV tests were run immediately after each SS test in the same tank and under the same steady state conditions. A LaVision Imager Intense camera situated 3.5 m from the tank with a resolution of 1376 x 1040 pixels captured the PIV images.

To perform the PIV experiments, the tank was seeded with titanium dioxide particles with a settling velocity of 3 cm/min. Dual ND:YAG lasers were fired at a rate of 4.5 Hz with a 90 ms separation between the lasers. Test were run for 3.7 minutes, capturing 1000 pairs of images which were processed by DaVis software using cross-correlation between image pairs with two passes over the experiment window. The first pass used an interrogation window of 64 x 64 pixels with a 50% window overlap. Then, the interrogation window was narrowed to 16 x 16 pixels with 75% overlap. DaVis processing generated horizontal (u) and vertical (w) velocities in matrices of 344x256 points. In order to compare the PIV results to those obtained with SS, a 2D Fourier transform in x and t was performed on the velocities and the Fourier amplitudes were used to calculate kinetic energy using Eq. 6.2.

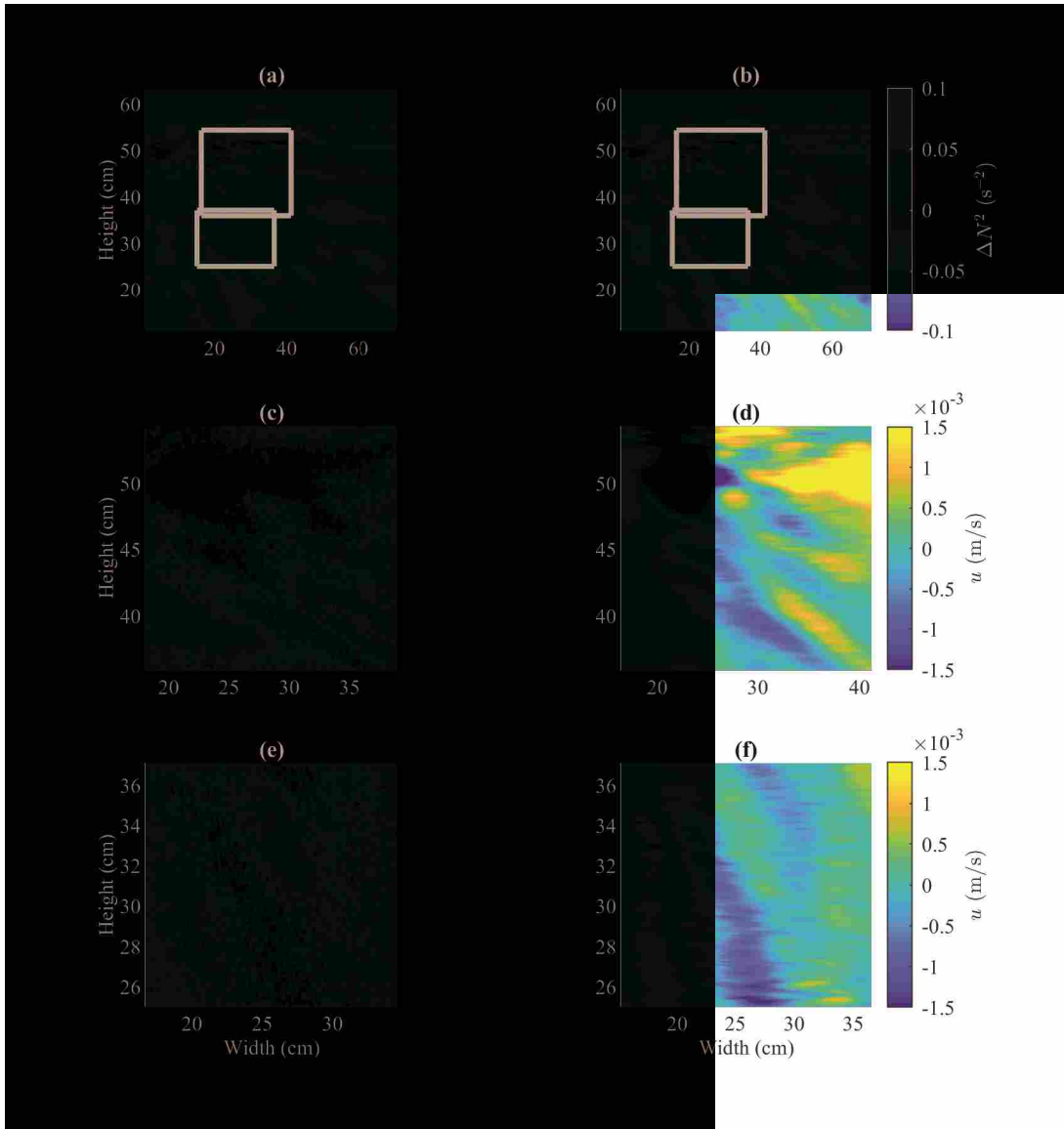


Figure 6.2: ΔN^2 data from case 14 for SS tests in (a) and (b), u data from PIV tests in (c)-(f). Unfiltered data is shown in the left column, while the right column shows data that has been filtered.

6.5 Results

To compare the SS and PIV imaging methods, experimental results will be compared both qualitatively and quantitatively. First, two cases will be explored in depth with experimental images and analysis. Then, the two methods will be compared across varying topographies and density profiles to explore the validity of SS and PIV in different applications.

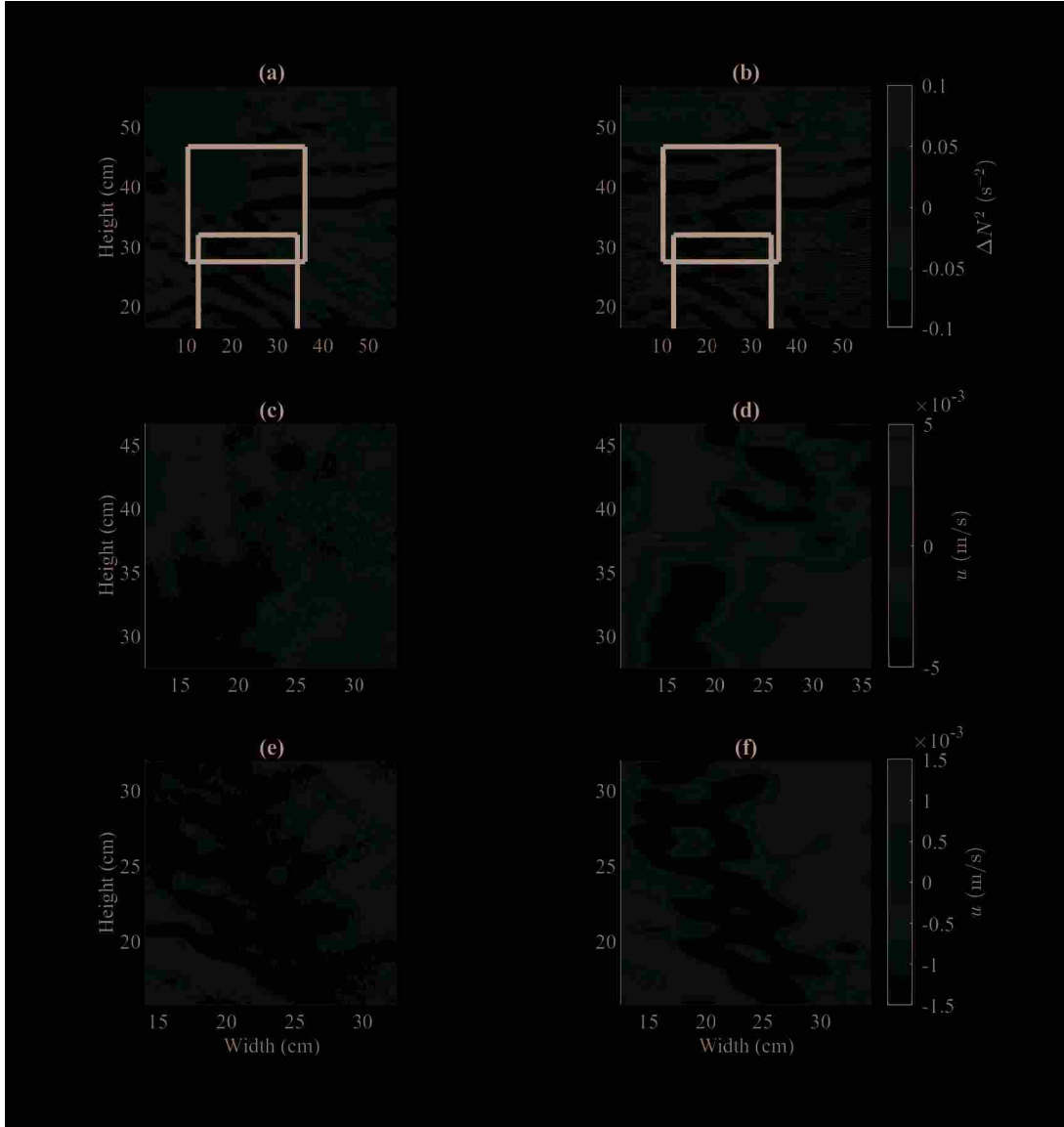


Figure 6.3: Images from case 16 with the same setup as Fig. 6.2, including both SS and PIV data.

Figs. 6.2 and 6.3 are ΔN^2 and horizontal velocity (u) fields for cases 14 (sinusoidal) and 16 (complex) with exponential density profiles. Each image is the view from the camera looking at the experimental tank, with height (cm) on the abscissa and width (cm) on the ordinate. SS images are shown in (a) and (b) and the colorbar corresponds to ΔN^2 (See Eq. 6.5). In the SS images, two black boxes outline the location of the PIV images of u shown in (c)-(f). In (a), (c), and (e), the figures are not filtered and in the second column, images (b), (d), and (f) are filtered in k . A

band pass filter was applied to include only the wavenumbers $k = 8.6 - 76.0 \text{ cm}^{-1}$ (wavelengths of 8.2-73.1 cm) to enhance visual clarity and to isolate wavenumbers used in the energy calculations.

Regarding Fig. 6.2, associated with case 14, both the SS and PIV data show clear wave beams at similar angles in the experimental window although the type of data is different between the methods. Here, the turning depth is located at $z_{td} = 0.39$ which is near the intersection of the two PIV tests. Near the topography, turbulence from the oscillations is observed in both methods and can be visualized by non-coherent variations in ΔN^2 or u magnitudes. Interestingly, the evanescent region wave beams captured by both the SS and PIV tests are not vertical as would be expected because $N < \omega$ in this region. However, there is a distinct difference in beam angle between the evanescent and propagating region as seen in Figs. 6.2(d) and (e). This difference is caused by turbulence generated waves, which have a smaller frequency such that they are propagating internal waves, are overlapping the topographically generated evanescent waves in (d). However, the evanescent waves generated by topographic oscillations clearly become propagating internal waves, which are the waves in (e) and (f).

In case 16, shown in Fig. 6.3, the turning depth is at $z_{td} = 0.4 \text{ m}$ where significant noise can be seen in the SS image in (a) due to the complex topography. Filtering removes this noise and show horizontal wave beams from $25 < x < 50 \text{ cm}$. Here the topography is very close to the turning depth such that general fluid oscillates back and forth with the topography are more apparent. In the PIV images of the evanescent region, (c) and (d), vertical beams of evanescent waves are apparent, with a discontinuity in the waves right below the turning depth. Propagating waves are clear in (e) and (f) especially in the lower left corner with an angle about 24° below the horizontal and a horizontal wavelength of 6 cm. In the same region of Fig. 6.3(b), the SS data indicates a wave angle near 28° with a wavelength of 8 cm. Again, the SS and PIV data are showing qualitatively similar wave beam phenomena in both sets of images.

To further explore the makeup of the waves indicated by both PIV and SS, Figs. 6.4 and 6.5 compare Fourier amplitudes of horizontal velocity, \tilde{U} , (PIV) and $\Delta\tilde{N}^2$ (SS) in the evanescent and propagating regions for cases 14 and 16, respectively in phase space. Wavenumber (k) is plotted

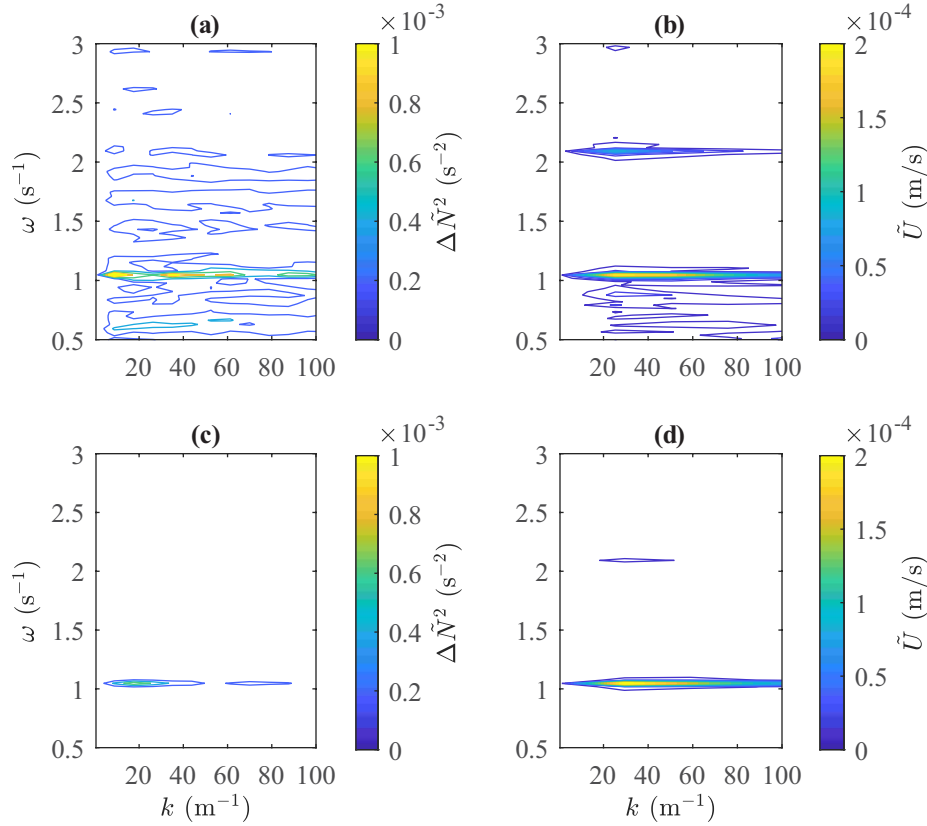


Figure 6.4: Contours of Fourier amplitudes of velocity in the left column and ΔN^2 in the right for case 14 in the evanescent region (a,b) and propagating region (c,d).

on the abscissa and frequency (ω) is on the ordinate. In both figures, (a) and (c) are from SS tests, while (b) and (d) are from PIV. Data for (a) and (b) are at $z = 0.45$ m and $z = 0.43$ m, respectively. These heights correspond to the horizontal lines halfway between the tip of the topography and the turning depth in each case. Data for (c) and (d) are in the propagating region along a horizontal line where $N/\omega = 1.1$, or a 10% increase in N away from the turning depth at $z = 0.28$ m (case 14) and $z = 0.25$ m (case 16).

In case 14, the excitation frequency is $\omega = 1.05$, which also corresponds to the large amplitudes present in (a)-(d) of Fig. 6.4. In the evanescent region both methods show a spread of energy to a range of frequencies. A particularly clear peak in the second harmonic is captured by the PIV which is not seen in the SS. This trend holds for many other cases as well. Both methods appear to

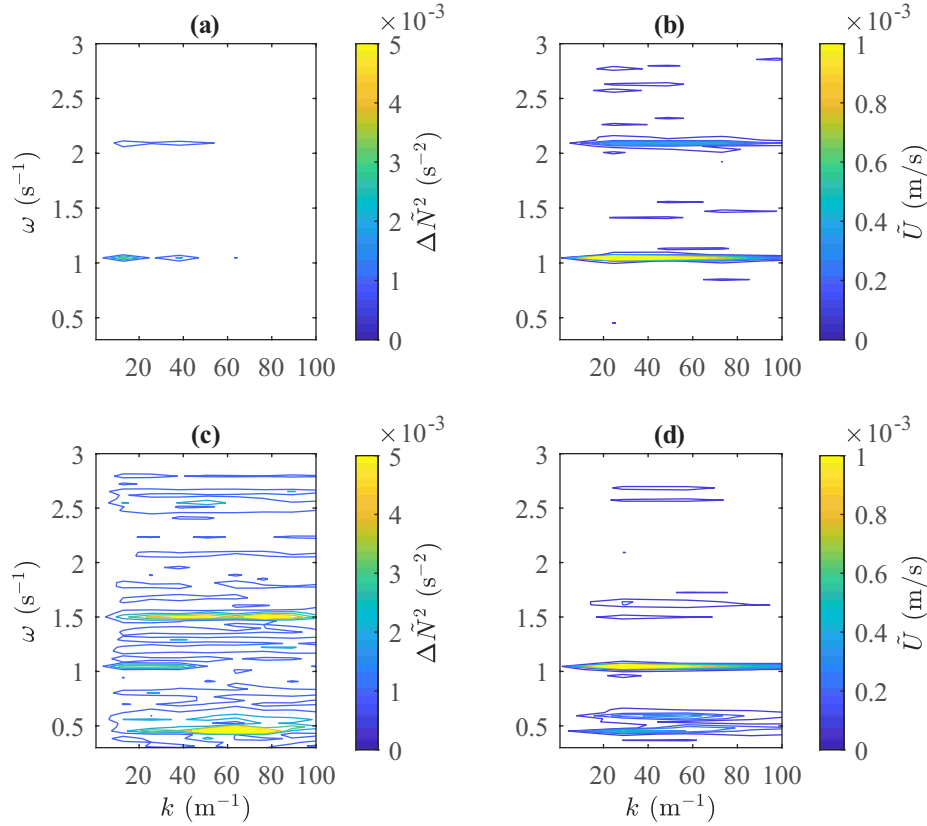


Figure 6.5: Fourier amplitudes of velocity and ΔN^2 as in Fig. 6.4 for the complex topography (case 16).

capture the propagating waves well. The spread in wavenumber is expected due to the two peaks of the topography.

Next we explore the waves generated by the complex topography in Fig. 6.5. Here in the evanescent region, relatively clear waves are seen at the excitation frequency $\omega_d = 1.05$ and harmonics, however the waves are less clear in the propagating region. This more realistic topography consists of varying slopes and multiple peaks resulting in a wider range of generated waves. In addition, the multiple peaks and steep slopes lead to greater turbulence further increasing the range of generated waves. Due to these multiple waves it seems triad interactions are occurring and in the propagating region for both PIV and SS tests, there are peaks in amplitude near $\omega = 0.55$, 1.05 (ω_d), and 1.50 . These peaks in frequency are more clear in the SS test. However, in calculating the kinetic energy, we will focus only on the energy at the forcing frequency.

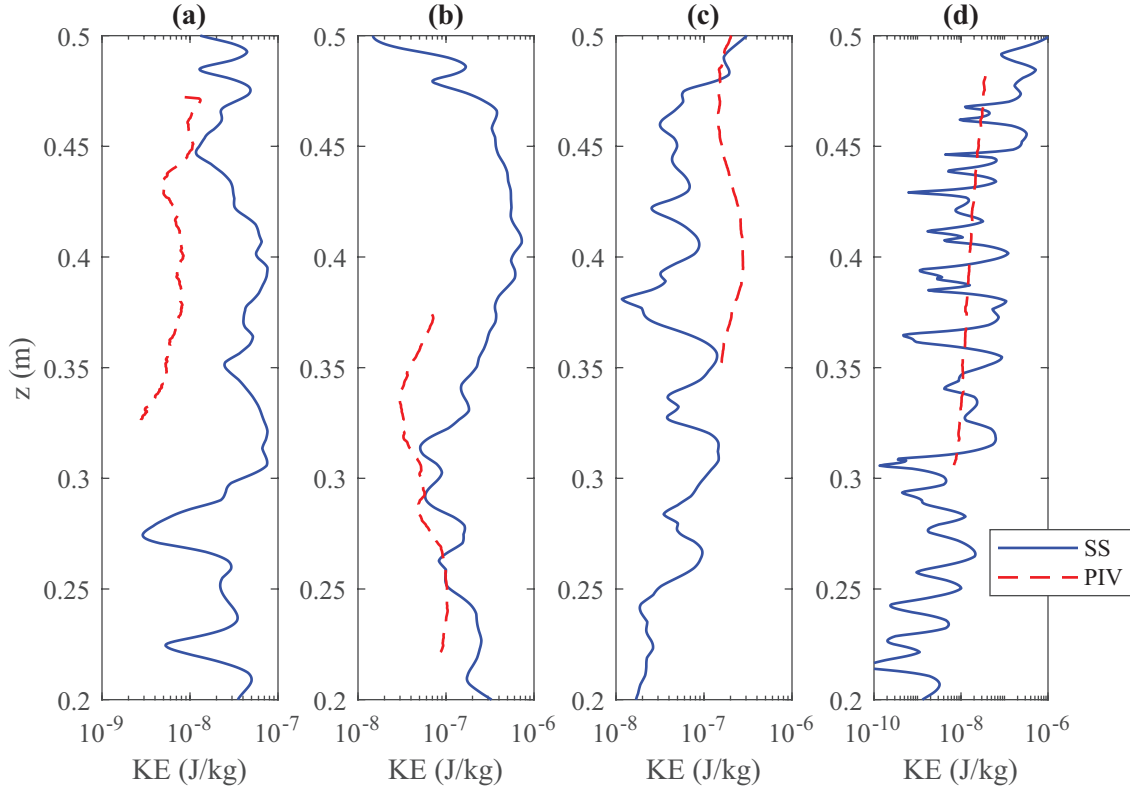


Figure 6.6: Kinetic energy density for case (a) 1, (b) 2, (c) 3, and (d) 4 each with one layer density profiles. Cases 1-3 are full propagating regions while case 4 is an evanescent region.

To begin a more qualitative comparison between the SS and PIV data, cases 1-4 are plotted in Figs. 6.6(a)-(d), respectively. All four cases used the medium topography and each have a one layer linear density profile and thus do not contain turning depths. Figures 6.6(a)-(c) are entirely propagating regions, while Fig. 6.6(d) is an evanescent region. SS energy is the blue solid line, while PIV energy is the red dashed line. Kinetic energy on the abscissa with varying scales for each figure, while the scales are the same for the height on the ordinate. SS energy shows some local oscillations in each figure, with significant variations in Fig. 6.6(d), while the PIV energy is smoother, especially in Fig. 6.6(d). These oscillations were also seen in the SS data and numerical simulation data of Lee et al. [112] and are likely inherent to the ΔN^2 data used to estimate kinetic energy.

Because Figs. 6.6(a)-(c) are wholly in a propagating region, we use $\overline{Fr}_2 = \omega_d/N_2$ to define the region, where N_2 is the natural frequency of that region. $N_2 = 1.276\text{s}^{-1}$ for cases 1 and 2, and

$N_2 = 1.197s^{-1}$ for case 3. As such, $\overline{Fr}_2 = 0.63, 0.70,$ and 0.67 for cases 1-3 respectively. Internal waves are known to increase in energy as \overline{Fr}_2 approaches unity [4]. Figures 6.6(a)-(c) do show an increase in the overall kinetic energy for PIV and SS with Fig. 6.6(a) indicating the least energy, followed by (c), and finally (b). Also, the PIV and SS energy follow similar trends and have similar values for different portions of the data. In Figs. 6.6(a) and (b), the SS energy is larger than the PIV energy, while the opposite is true for the majority of Fig. 6.6(c). As Fig. 6.6(c) has the same excitation frequency as (a), and neither the largest nor smallest \overline{Fr}_2 value, there is not a distinct reason as to why the PIV energy is greater than SS in that particular case.

In Fig. 6.6(d) there is an excellent agreement between the SS and PIV tests. Kinetic energy decreases throughout this evanescent region, as is expected for decaying evanescent waves. Although there are more oscillations in the SS data for this figures compared to Fig. 6.6(a)-(c), the PIV energy passes directly through the oscillations and matches the average trend of the SS data very well. In all of the graphs of Fig. 6.6, the PIV and SS data show good agreement.

Continuing the comparison between the SS and PIV data, four cases, all with exponential density profiles, have been chosen and plotted in Fig. 6.7 with kinetic energy on the ordinate and height on the abscissa. As before, SS energy is plotted as a solid blue line, PIV energy is the dashed red line. In addition, the turning depth is the horizontal black dash-dot line. Note that the scales are different for each individual figure. In Fig. 6.7(a) and (b), cases 14 and 16 are shown, which are the same cases from Figs. 6.2-6.5 with the sinusoidal and complex topographies. Figures 6.7(c) and (d) are the kinetic energy of case 13 (steep topography) and case 12 (medium topography).

In Figs. 6.7(a), (c), and (d), the kinetic energy decreases through the evanescent region, and then remains relatively constant through the propagating region. In the SS data, there is an increase near the turning depth due to the breakdown of the low amplitude assumption needed to estimate the kinetic energy. Because of this, the energy in the evanescent in Fig. 6.7(b) shows an immediate increase due to the relatively close proximity of the turning depth. In contrast, the PIV data does not indicate a significant increase or decrease of energy at the turning depth and there is a decay of the kinetic energy in the evanescent region in each of the figures.

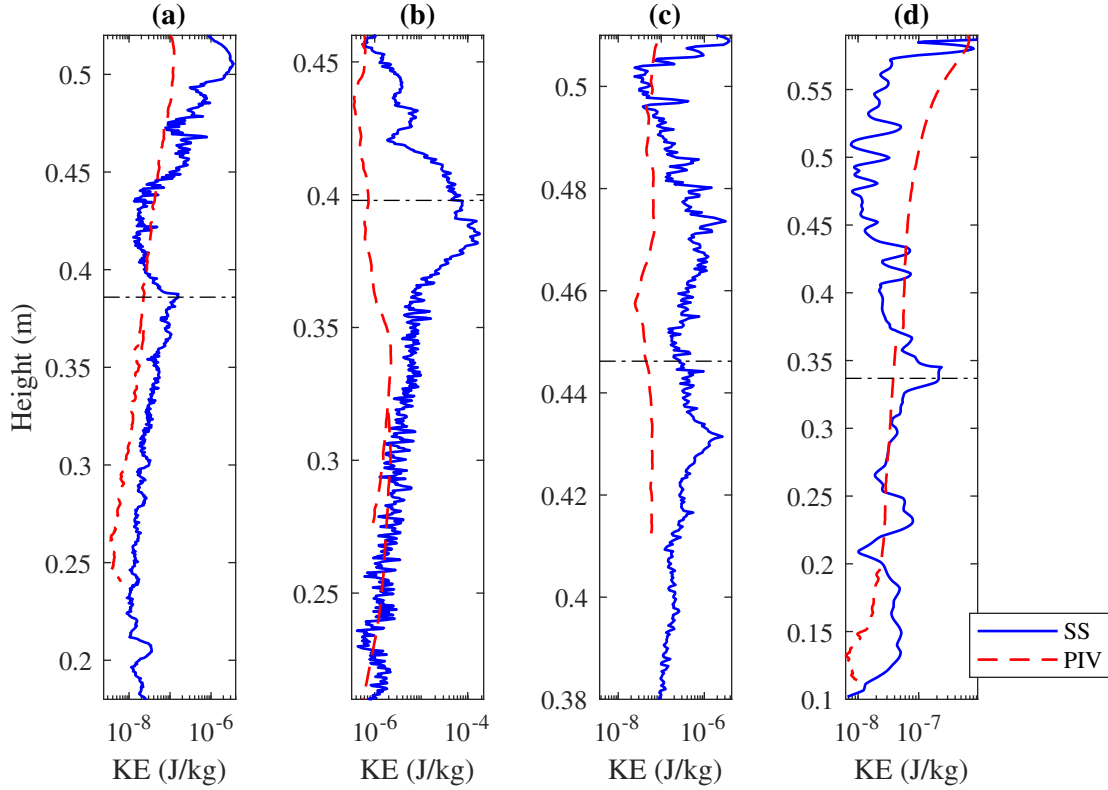


Figure 6.7: Kinetic energy as a function of height for the (a) sinusoidal, (b) complex, (c) steep, and (d) medium topographies in an exponential density profile.

For case 14, the energy estimates from PIV decreases through the evanescent region, across the turning depth, and into the propagating region with almost no visible variations between the upper and lower PIV tests. The two PIV tests overlap at 0.37 m. There is some overlap of PIV and SS kinetic energy in the evanescent region, and the general trend of a decrease in KE in the evanescent region is seen, but then there is an increase in SS energy at the turning depth, which is to be expected with the breakdown of assumptions [100]. In the propagating region, both the PIV and SS show a slight decrease in energy, but the SS energy is larger.

In case 16, which used the complex topography, there is a significant separation between the PIV and SS energy in the evanescent region. The complex topography is known to generate turbulence near the topography due to the multiple sharp-sloped peaks. This creates nonlinear effects, which adversely affects the SS method of estimating kinetic energy seen by the separation between the PIV and SS energy. Also, the topography is very near to the turning depth, which also

negatively impacts SS estimates of energy. This separation remains until the internal waves have propagated away from the turning depth. Once the nonlinear elements of the wave have decayed, the two methods again match well in the propagating region, with the second PIV test lying almost exactly on top of the SS kinetic energy.

Figure 6.7(c) shows the energy associated with the steep topography (case 13). Here, in the single PIV test performed, the kinetic energy is generally less than the SS kinetic energy, similar to the previous two cases. Significant turbulence is generated near the steep topography, which accounts for the separation in the evanescent region. Unfortunately, since the PIV test does not extend for into the propagating region, it is not possible to see if the two methods match away from the turning depth, though the SS values do seem to be approaching the PIV.

In the final case of the medium topography, Fig. 6.7(d), unlike the majority of the cases, the PIV kinetic energy is larger than the SS energy for much of the evanescent region. At the turning depth, the SS energy increases rapidly and in the propagating region, the PIV energy and SS energy match well. Both show a rapid decay in energy near the bottom of the tank, due to waves breaking up near the filtering mats places in the bottom of the tank.

Each of these four graphs in Fig. 6.7 indicate that the PIV and SS kinetic energy match quite well in the propagating region. As this is generally the region of most interest due to propagating energy, we expect either method provides similar results and thus may be used for propagating energy estimates past the evanescent region and turning depth. Greater differences within the evanescent region and near the turning depth occur regardless of topography shape and results of SS are not valid near the topography or turning depth.

The previous figure focused on four different topographies for an exponential density profile. Next, we present experiments that were performed with the medium topography for multiple density profiles. Figure 6.8 shows the kinetic energy of cases 4, 5, 7, and 8 which are the one-layer, two-layer, quadratic, and cubic density profiles, corresponding to (a)-(d) in the figure. The final density profile, the exponential profile, is Fig. 6.7(d). In case 4, previously shown in Fig. 6.6(d), there is no turning depth is present in Fig. 6.8(a) due to the constant N . Scales vary for each axis

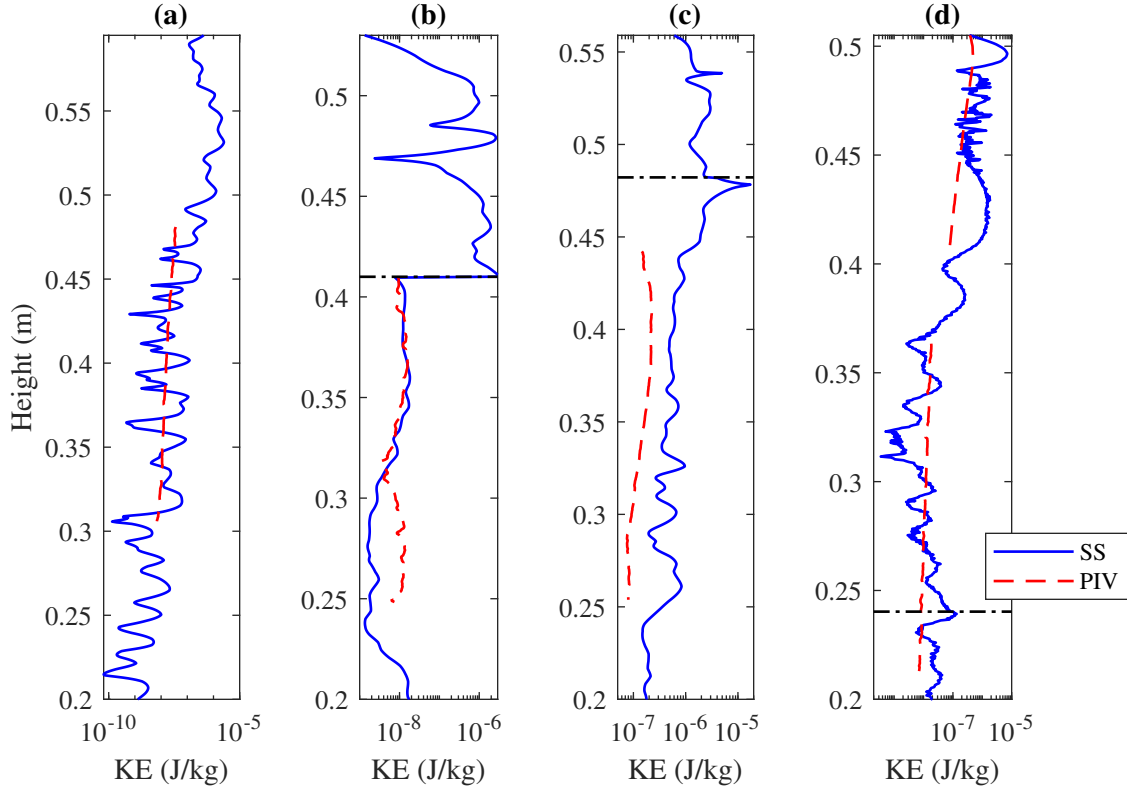


Figure 6.8: Kinetic energy as a function of height for the medium topography with (a) one layer, (b) two layer, (c) quadratic, and (d) cubic density profiles.

for each figure, which allows for a close inspection of each individual figure. Similar to Fig. 6.7, in Fig. 6.8 the SS data shows significant oscillations in energy in the evanescent region. However, in these cases, and in Fig. 6.7(d), the SS oscillations decrease in the propagating region. In both figures, the PIV data has little to no local variations. Similar oscillations were seen by Lee et al. [112] in both the SS data and in simulation data that used the SS equations to estimate kinetic energy. While some variation in the energy can be attributed to local variations of density in the experimental tank, it is likely that there is some inherent error in the SS method which causes these oscillations.

Comparing the kinetic energy of the PIV and SS data for each of the five figures, the best match is seen for Fig. 6.8(a), a portion of (b), and the lower PIV test of 6.8(d) and 6.7(d). There is no specific pattern here, as Figs. 6.8(a) and (d) are in the evanescent region, and Figs. 6.8(b) and 6.7(d) are in the propagating region, including near the turning depth.

Figure 6.8(c) is also in the propagating region, but this parabolic density profile case shows a separation between the PIV and SS energy. Similarly, in Fig. 6.8(b), the PIV and SS data is separated for $0.25 < z < 0.32$ m, but is almost an exact match between $z = 0.32$ and the turning depth. In (c), it would be expected that these values match more closely as the heights covered by the PIV test are far from the turning depth, which is the preferred scenario for the least error between the methods. However, a similar separation is seen in the propagating region for Fig. 6.7(a).

We note that in the propagating region of Fig. 6.8(b), the PIV and SS kinetic energy match well near the turning depth, but then the SS energy decreases further away. This is one of the few cases where the PIV and SS energy are so similar near the turning depth. In calculating SS kinetic energy density, the variation in the vertical wavenumber is assumed to be small, which breaks down near the turning depth. However, in this case N is constant until an abrupt change to a new constant N at the turning depth. This rapid change from low to high natural frequency does not include the transition through an undefined vertical wavenumber. Thus the SS method of energy calculation more accurately captures the energy in the internal waves for a two layer scenario.

Based on both Figs. 6.7 and 6.8, we conclude that, generally, the kinetic energy of the PIV data matches well with SS data in the propagating region, but that the SS energy will generally overestimate this energy. More details of how much of an overestimate this may be will be discussed further in this section.

Looking now at the data only in the evanescent region, note that in Fig. 6.8(a), the kinetic energy decreases throughout the entire window because this one-layer case is entirely evanescent. Although there are significant oscillations in the SS energy, the PIV energy is a good fit to the general trend. In addition, the majority of the data in Fig. 6.8(d) is in the evanescent region and both PIV tests match well with the general trends and average values of the SS energy, which again oscillates more than the PIV. In all of the graphs of Fig. 6.7, the evanescent regions have more separation between the PIV and SS data, but figures 6.8(a) and (d) indicate that it is not inherently the evanescent region which increases the error between the two methods. Instead, it is

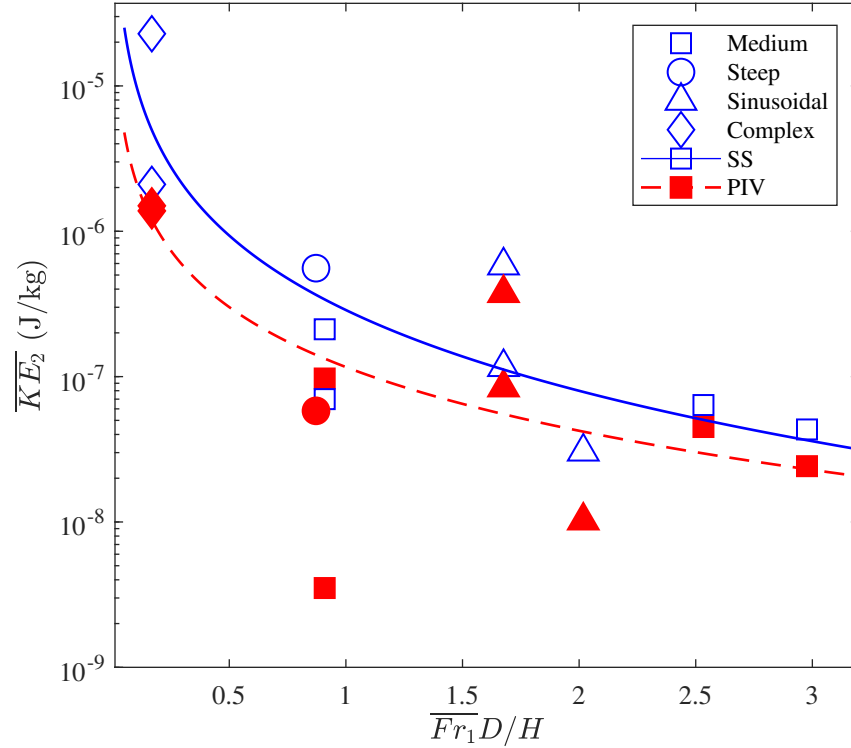


Figure 6.9: Average kinetic energy in the propagating region for all topographies. Symbols follow the legend shown, with the specific shapes for each topography. All SS points are in open blue symbols and PIV points are filled red symbols.

the relative closeness to the tip of the topography and the turning depth which cause difficulties. The tip of the topography can generate turbulence, which would affect the linear assumptions of the SS estimate, as does the turning depth and rapid decrease in wavenumber.

Kinetic energy in the propagating region was averaged and is shown as a function of $\overline{Fr_1}D/H$ in Fig. 6.9. Synthetic schlieren results are shown with open symbols, while PIV results are filled symbols. Squares represent the medium topography, circles represent the steep, triangles represent the sinusoidal, and diamonds represent complex. Since the vertical data of the PIV tests were smaller than the SS domain, averages for each were defined over the PIV window. In some cases, two PIV tests were run in the propagating region for one SS test. In these cases, averages were taken for each individual PIV test and both points are included.

Two curve fits for the two experimental methods are also plotted. Both fits use the equation

$$\ln(\overline{KE}_2) = C_1 x^{C_2} \quad (6.8)$$

with $C_1 = -15.51$ and $C_2 = 0.096$ for the SS fit and $C_1 = -16.26$ and $C_2 = 0.070$ for the PIV fit. Goodness of fit is defined by the R^2 values, with $R^2 = 0.713$ for the SS curve and $R^2 = 0.660$ for the PIV curve. Trends from the data points indicate that increasing $\overline{Fr}_1 D/H$ results in a decrease in the propagating kinetic energy. This trend is expected as an increasing \overline{Fr}_1 corresponds to a weakening evanescent region, causing the kinetic energy of the evanescent waves to decay rapidly. In addition, increasing D/H increase the space between the turning depth and providing a longer distance for the evanescent waves to decay. Although there is error between the SS and PIV points, the overall trends match well and the order of magnitudes are consistent across both methods. Based on the curve fit for the $\overline{Fr}_1 D/H$ values shown, the SS kinetic energy is, on average, 1.7 times larger than the PIV energy.

Regardless of shape, all topographies fit their respective curves well, as shown in Fig. 6.9. Difference between PIV and SS decrease with increasing $\overline{Fr}_1 D/H$, yet the error associated with each topography is not consistently above or below the fit or altered with $\overline{Fr}_1 D/H$. The largest difference between PIV and SS kinetic energy is for the medium topography at $\overline{Fr}_1 D/H = 0.91$, from data taken in the propagating region. SS kinetic energy data for this point is decreasing and approaching the PIV energy, but the average is still significantly higher than would be expected for a comparison in the propagating region. The second set of data for the medium topography at $\overline{Fr}_1 D/H = 0.91$ is closer match, though still an order of magnitude apart, as would be expected for data taken near the turning depth as these points are.

For the complex topography there are only two data points and both are for the same test [See Fig. 6.9(b)]. PIV results are the same, while one of the SS data points is significantly larger. At this point, half of the kinetic energy averaging distance is very near the turning depth, which is prone to error in SS calculations. However, the second set of PIV data, far from the turning depth,

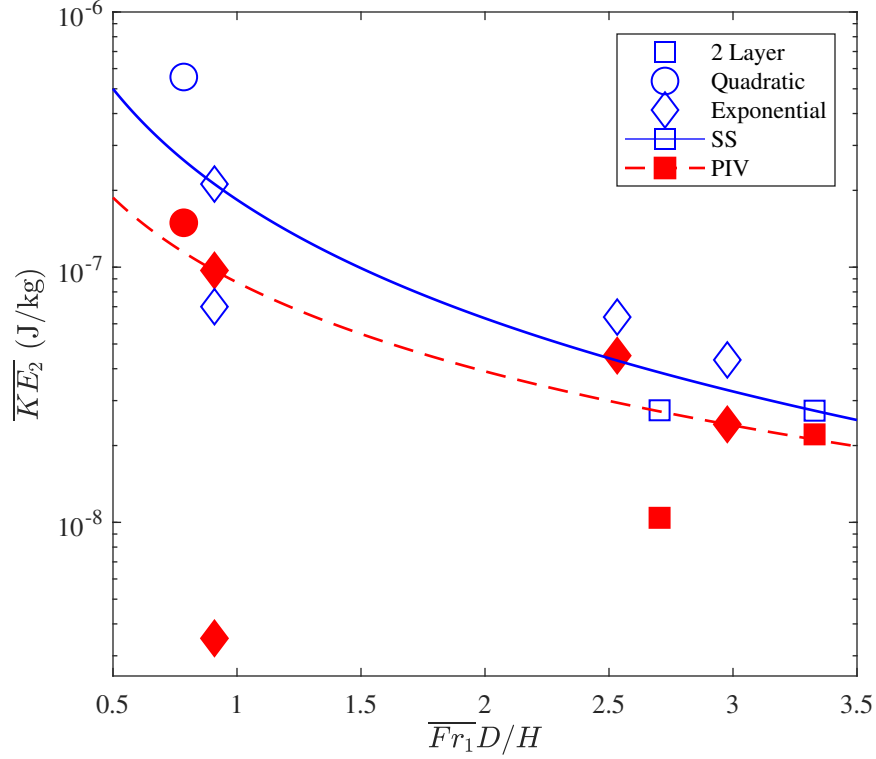


Figure 6.10: Average kinetic energy in the propagating region for the medium topography SS and PIV data with three density profiles.

matches well with the SS data, once again leading to the conclusion that PIV and SS tests indicate similar results when in the propagating region and far from the turning depth.

Exploring the effect of density profile, average kinetic energy in the propagating region of tests with the medium topography and various density profiles is shown in Fig. 6.10. As indicated by the legend, three density profiles are plotted with both SS and PIV data. Trend lines for each data set are indicated by a blue dashed line for SS and a red dotted line for PIV. Each trend line follows the same format as Eq. 6.8 with $C_1 = -15.06$ and $C_2 = 0.118$ with $R^2 = 0.702$ for the SS trend line and $C_1 = -15.97$ and $C_2 = 0.088$ with $R^2 = 0.636$ for the PIV trend line. As is also seen in Fig. 6.9, Fig. 6.10 indicates that \overline{KE}_2 decreases with increasing $\overline{Fr}_1 D/H$. Similarly, there is no distinctive trend in error between the SS and PIV data based on $\overline{Fr}_1 D/H$. However, the error between the two layer cases increases with increasing $\overline{Fr}_1 D/H$, while the opposite is true for the

exponential cases. Based solely on the trend lines, the difference between the cases is decreasing overall, with the SS curve 1.7 times larger (on average) than the PIV curve fit.

Because the two cubic cases, cases 8 and 9, had data only in the evanescent region, they are not plotted in Fig. 6.10. However, the data for case 8 was shown in Fig. 6.8(d). In addition, case 9 had relatively good agreement between the PIV and SS data in the evanescent region, but is one of the few cases where the PIV energy is higher than SS energy. Using the same averaging scheme mentioned previously, case 8 has two PIV points for the average kinetic energy in the evanescent region. Near the topography, the PIV energy is $\overline{KE}_1 = 1.82 \times 10^{-7}$ J/kg and SS is $\overline{KE}_1 = 8.76 \times 10^{-7}$ J/kg. Away from the topography the PIV energy is $\overline{KE}_1 = 1.24 \times 10^{-7}$ J/kg and the SS energy is slightly higher with $\overline{KE}_1 = 1.37 \times 10^{-7}$ J/kg. Near the topography SS overestimates the PIV energy, but matches it well away from the topography while still in the evanescent region. For case 9 the average PIV kinetic energy in the evanescent region is $\overline{KE}_1 = 5.65 \times 10^{-8}$ J/kg while the SS test is $\overline{KE}_1 = 2.40 \times 10^{-8}$ J/kg. The error for cases 8 and 9 is similar to that seen in both Figs. 6.9 and 6.10.

6.6 Discussion

This work compares data from two different experimental methodologies, particle image velocimetry (PIV) and synthetic schlieren (SS), both qualitatively and quantitatively. Processed images from the two cases show similar wave beam characteristics in the evanescent and propagating regions of Figs. 6.2 and 6.3. Also, there are similar peaks in frequency and wavenumber when the Fourier amplitudes of each method are compared in both regions (Figs. 6.4 and 6.5). Although the type of data is different, with SS providing information about changes in the natural frequency and PIV indicating velocity both are directly related to wave amplitude and properties of propagation. Each method indicates the same excitation frequency and a similar spread of energy over a range of wavenumbers.

Kinetic energy of the SS data is estimated using two different equations depending on whether the data is in the evanescent region (Eq. 6.6) or propagating region (Eq. 6.7), though both

rely on the Fourier amplitudes of ΔN^2 and the small amplitude assumption. To provide a similar data set to that of SS tests, all PIV velocities were also Fourier transformed to create \tilde{U} and \tilde{V} . Kinetic energy as a function of height for the different topographies and different density profiles indicates that the difference between the two methods is the greatest when the SS data is near the topography or the turning depth. Conversely, when far from either, the two methods match very well, though the SS energy is in general 1.5-2 times greater than the PIV energy. Normalizing the data would mitigate this difference. Exceptions include the 2 layer density profile where the PIV and SS energy were almost an exact match.

Averaging the kinetic energy in the propagating region, based on the location of the PIV data, and plotting it against $\overline{Fr_1}D/H$ indicated that $\overline{KE_2}$ decreases with increasing $\overline{Fr_1}D/H$ for all topographies and all density profiles. In addition, the various topographies collapsed well onto the same trend lines (Fig. 6.9), as did the multiple density profiles (Fig. 6.10). Based on these findings, it is recommended that SS be used in experiments that are far from a turning depth or topography. Results for SS compared well to PIV in both evanescent and propagating regions where the small amplitude approximation needed for the kinetic energy calculations is still valid. We expect SS results to be an overestimate of the data relative to PIV data in these regions, however, this effect could be mitigated in the future by using a normalizing method to compare relative energy in future experiments. For experiments involving turning depths or which focus on the generation mechanisms of waves use, we recommend PIV as the experimental process.

Acknowledgements

This work has been supported by the Utah NASA Space Grant Consortium and by NSF Grant CBET-1606040. The authors would also like to gratefully acknowledge the support of Katie Pusey, Annie Wesolek, and Heather Erickson in setting up and performing PIV experiments.

CHAPTER 7. CONCLUSION

This dissertation has investigated propagating internal wave energy from topographically generated evanescent waves passing through a turning depth. A linear theory model was created and compared to experiments and direct numerical simulations. Propagating kinetic energy results from experiments, linear theory, and numerical simulations indicate that increasing $\overline{Fr}_1 D/H$ causes a decrease in the kinetic energy of internal waves generated from an evanescent region. Based on a range of topographies and multiple density profiles, the average, normalized kinetic energy in the propagating region, \overline{KE}_2^* , is significant only when $\overline{Fr}_1 D/H < 4$. The comparison of synthetic schlieren experiments to PIV experiments and numerical simulations indicate that synthetic schlieren is a valid experimental method for both evanescent and propagating regions as long as data is taken far from the turning depth.

An analytical model using linear theory and the WKB approximation was created. Horizontal and vertical velocities are calculated for evanescent and internal waves in varying stratifications, which are then used to calculate kinetic energy density. As part of the completed model, a smooth transition over a turning depth is estimated using the Airy function. Trends from the model match those of the synthetic schlieren experiments for \overline{KE}_2^* . However, due to experimental non-linearities such as turbulence generation, the model kinetic energy is greater than that of the experiments. Both the model and experiments with the medium and steep Gaussian topographies indicate that the strength of the stratification in the evanescent region, \overline{Fr}_1 is an important factor for the total energy transfer into the propagating region. The model was also used to estimate \overline{KE}^* for a specific oceanic topography at 15°N and 130°E using data from WOCE and approximating the topography as a Gaussian shape. Given the natural frequency profile and the tidal frequency, the

model estimates 25% of the initial energy of the evanescent waves can be transferred into internal waves propagating through the open ocean (See Fig. 3.13).

Kinetic energy density results from the model and experiments were compared to direct numerical simulations for the medium Gaussian topography in an exponential density profile. To more accurately capture the range of waves generated from the topography, results were expanded such that a range of wavenumbers was included in \overline{KE}_2^* . Using an adjusted Gaussian parameter (B_L) which includes the excursion length (L), kinetic energy was averaged over $0.5 < kB_L < 5$. In numerical simulations, kinetic energy can be calculated in two ways: directly and indirectly. Direct calculations refer to using the velocity fields to find kinetic energy, while indirect methods use the density perturbation fields and the same set of equations used with the experiments to estimate kinetic energy. A comparison of the direct and indirect methods indicated that the error between the methods decreased in propagating regions away from the turning depth. For the 1/10 amplitude simulations, the height where $N/\omega = 1.1$ was sufficiently far to have less than 5% error between the two methods. For the full amplitude simulations, this distance varied based on Eq. (4.36) which is dependent upon $\overline{Fr}_1 D/H$. $\overline{Fr}_1 D/H$ is a combined parameter which accounts for both the strength of the stratification and the relative distance from the topography to the turning depth in the evanescent region. All of the methods indicated that increasing $\overline{Fr}_1 D/H$ decreased \overline{KE}_2^* . An equation which correlates the kinetic energy of the theoretical model to the full amplitude direct simulations was provided to easily estimate \overline{KE}_2^* for the medium topography in an exponential density profile for a range of $\overline{Fr}_1 D/H$.

After comparing the above mentioned methods for one topography and one density profile, this research was expanded to four topographies and four density profiles. Topography shapes included a medium Gaussian, steep Gaussian, two peak sinusoidal, and complex. Two-layer linear, parabolic, cubic, and exponential density profiles were used with all of the topographies. Again, results were consistent with previous data, indicating that increasing $\overline{Fr}_1 D/H$ results in decreased \overline{KE}_2^* . Along with this trend, results from the Gaussian and sinusoidal topographies indicated that \overline{KE}_2^* for different density profiles collapsed well for individual topographies. Curve fits for all

methods and all profiles were created for these topographies to create trendlines. Trends for the indirect simulations and experiments were more prone to error for the complex topography due to turbulence generated by the topography, and the trendline was fit only to the theoretical and direct simulation data. All trendlines for the topographies indicated that an increasing maximum slope, $S_{\text{top,m}}$, is a good indicator for decreasing \overline{KE}_2^* for single-peak topographies (See Fig. 5.9). Both the number of peaks and $S_{\text{top,m}}$ need to be taken when estimating which topography will have the largest \overline{KE}_2^* . From a comparison of the four trends for the various topographies, \overline{KE}_2^* is only significant, or greater than 0.01, for $\overline{Fr}_1 D/H < 4$.

Continuing with multiple topographies and multiple density profiles, experiments were performed both with synthetic schlieren and particle image velocimetry (PIV). Previous results indicated that indirect methods of calculating kinetic energy density were not as reliable in the evanescent region compared to the propagating region. To explore this further, the direct method of PIV was compared to the indirect method of synthetic schlieren. Different from previous results, the kinetic energy density was not normalized, but the trends between the methods matched well. Synthetic schlieren results were similar to PIV when far from a turning depth in both the evanescent and propagating regions for all topographies and the multiple density profiles used with the medium topography. Based on trendlines, synthetic schlieren experiments had 1.5-2 times more kinetic energy than the PIV experiments, but these differences would decrease if the data from each method was normalized. It is recommended that for experiments performed near topography or a turning depth, PIV be used. However, synthetic schlieren is a good option for either evanescent or propagating regions.

The material in this dissertation has been published in one archival journal, *Physical Review Fluids*, with another journal article submitted to *Experiments in Fluids*, and two more in preparation for submission. In addition, this work has been presented at the American Physical Society Division of Fluid Dynamics annual conference 5 times, with a paper presented at the International Symposium on Stratified Flows once.

Scientific contributions from this work include the completed linear theory model which is the first model to estimate kinetic energy density of topographically formed evanescent waves which move through a turning depth and become propagating internal waves. This model follows the same trends as both experiments and numerical simulations and has been used to estimate the percentage of kinetic energy for internal waves generated from an oceanic topography. Similar estimates can be made for various oceanic locations given the density profile and topography shape for the region in question. Another contribution is the comparison of synthetic schlieren and PIV experiments which indicate that synthetic schlieren experiments, which are less expensive to setup, are viable in both evanescent and propagating regions. Finally, based on the combined information of experiments, theory, and numerical simulations, the average kinetic energy density of internal waves formed from topography generated evanescent waves is significant only when $\overline{Fr}_1 D/H < 4$. A simple calculation of density profile and relative distance from the topography to the turning depth provides guidelines for where energetic internal waves could be generated and interact with the surrounding ocean.

Motivated by the work completed here, future research is encouraged in a number of areas. First, the theoretical model can be expanded to an ocean scale for easier accessibility for oceanographers and other researchers to use in understanding the impact of evanescent waves. Also, not shown in this work was that for the sinusoidal and complex topography, numerous internal waves were generated at higher harmonics of the excitation frequency, at $\omega = 2\omega_d$. All of the kinetic energy shown here isolated only the kinetic energy associated with ω_d . Future work could include an investigation of the energy within these harmonic waves and the influence of the number of peaks of a topography on the energy in harmonic waves. In addition, it was seen that the complex topography generated waves with more energy than the steep Gaussian topography, even though $S_{top,m}$ is larger for the complex topography. An investigation of the influence of the number of topography peaks relative to the maximum slope of the topography would also provide researchers with a better understanding of where evanescent and internal waves have an important influence in the ocean without need to individually model each topography in the ocean.

REFERENCES

- [1] Walker, J., 1991. “Farthest north, dead water and the ekman spiral.” *Weather*, **46**(6), pp. 158–164. 1
- [2] Pettersson, S. O., 1908. *Strömstudier vid Östersjöns portar*. Sven. Hydrogr. Biol. Komm, Göteborg. 1, 9
- [3] Garrett, C., and Kunze, E., 2007. “Internal tide generation in the deep ocean.” *Annual Review of Fluid Mechanics*, **39**, pp. 57–87. 1, 8, 65, 76, 111
- [4] Sutherland, B. R., 2010. *Internal Gravity Waves*. Cambridge University Press, Cambridge, United Kingdom. 1, 2, 3, 5, 7, 15, 16, 22, 77, 155
- [5] Nappo, C. J., 2002. *An introduction to atmospheric gravity waves*. Academic Press, San Diego, California. 1, 2, 3, 7, 16, 18, 43, 45, 52, 84, 85, 111, 120, 140, 146
- [6] Fritts, D. C., 1984. Gravity wave saturation in the middle atmosphere: A review of theory and observations. 2
- [7] Garret, C., and Munk, W., 1979. “Internal waves in the ocean.” *Annual Reviews of Fluid Mechanics*, **11**(Figure 2), pp. 339–369. 2, 8
- [8] Sutherland, B. R., Achatz, U., Caulfield, C. C. P., and Klymak, J. M., 2019. “Recent progress in modeling imbalance in the atmosphere and ocean.” *Physical Review Fluids*, **4**(1), p. 10501. 3, 4, 76
- [9] Elvidge, A. D., Vosper, S. B., Wells, H., Cheung, J. C., Derbyshire, S. H., and Turp, D., 2017. “Moving towards a wave-resolved approach to forecasting mountain wave induced clear air turbulence.” *Meteorological Applications*, **24**(3), pp. 540–550. 4
- [10] Wunsch, C., and Ferrari, R., 2004. “Vertical mixing, energy, and the general circulation of the oceans.” *Annual Review of Fluid Mechanics*, **36**(1), jan, pp. 281–314. 4, 5, 7
- [11] Sarkar, S., and Scotti, A., 2017. “From Topographic Internal Gravity Waves to Turbulence.” *Annual Review of Fluid Mechanics*, **49**(1), pp. 195–220. 4, 5, 15, 76, 78, 112
- [12] Kurup, N. V., Shi, S., Shi, Z., Miao, W., and Jiang, L., 2011. Study of nonlinear internal waves and impact on offshore drilling units Tech. rep. 4
- [13] Leichter, J. J., Stewart, H. L., and Miller, S. L., 2003. “Episodic nutrient transport to Florida coral reefs.” *Limnology and Oceanography*, **48**(4), pp. 1394–1407. 4
- [14] Little, A. D., 1966. Internal waves: their influence upon naval operations Tech. rep., Department of the Navy Bureau of Ships. 4

- [15] Apel, J. R., Holbrook, J. R., Liu, A. K., and Tsai, J. J., 1985. “The Sulu Sea Internal Soliton Experiment.” *Journal of Physical Oceanography*, **15**(12), dec, pp. 1625–1651. 4, 7
- [16] Alford, M. H., MacKinnon, J. A., Zhao, Z., Pinkel, R., Klymak, J., and Peacock, T., 2007. “Internal waves across the pacific.” *Geophysical Research Letters*, **34**, p. L24601. x, 5, 9, 10
- [17] Saenko, O. A., 2006. “The Effect of Localized Mixing on the Ocean Circulation and Time-Dependent Climate Change.” *Journal of Physical Oceanography*, **36**(1), pp. 140–160. 5
- [18] Paoletti, M. S., Drake, M., and Swinney, H. L., 2014. “Internal tide generation in nonuniformly stratified deep oceans.” *Journal of Geophysical Research: Oceans*, **119**(3), pp. 1943–1956. 5, 7, 14, 15, 18, 19, 40, 45, 46, 65, 73, 78, 79, 88, 111, 114, 119, 140, 141, 144
- [19] King, B., Stone, M., Zhang, H. P., Gerkema, T., Marder, M., Scott, R. B., and Swinney, H. L., 2012. “Buoyancy frequency profiles and internal semidiurnal tide turning depths in the oceans.” *Journal of Geophysical Research: Oceans*, **117**(C4). 5, 6, 18, 20, 43, 70, 79, 112, 114
- [20] Wunsch, S., and Brandt, A., 2012. “Laboratory experiments on internal wave interactions with a pycnocline.” *Experiments in Fluids*, **53**(6), dec, pp. 1663–1679. 7, 35, 50, 77, 86, 112, 117, 140, 141, 147, 148
- [21] Dossmann, Y., Auclair, F., and Paci, A., 2013. “Topographically induced internal solitary waves in a pycnocline: Secondary generation and selection criteria.” *Physics of Fluids*, **25**(8), aug. 7
- [22] Linden, P. F., 1975. “The deepening of a mixed layer in a stratified fluid.” *Journal of Fluid Mechanics*, **71**(2), sep, pp. 385–405. 7
- [23] Taylor, J. R., and Sarkar, S., 2007. “Internal gravity waves generated by a turbulent bottom Ekman layer.” *Journal of Fluid Mechanics*, **590**, nov, pp. 331–354. 7, 8
- [24] Dohan, K., and Sutherland, B. R., 2003. “Internal waves generated from a turbulent mixed region.” *Physics of Fluids*, **15**(2), pp. 488–498. 7
- [25] Dohan, K., and Sutherland, B. R., 2005. “Numerical and laboratory generation of internal waves from turbulence.” *Dynamics of Atmospheres and Oceans*, **40**(1-2 SPEC. ISS.), jun, pp. 43–56. 8, 15
- [26] Bonneton, P., Hopfinger, E. J., and Chomaz, J. M., 1993. “Internal waves produced by the turbulent wake of a sphere moving horizontally in a stratified fluid.” *Journal of Fluid Mechanics*, **254**, pp. 23–40. 8
- [27] Munroe, J. R., and Sutherland, B. R., 2008. “Generation of internal waves by sheared turbulence: Experiments.” In *Environmental Fluid Mechanics*, Vol. 8, pp. 527–534. 8
- [28] Aguilar, D. A., and Sutherland, B. R., 2006. “Internal wave generation from rough topography.” *Physics of Fluids*, **18**(6). 8, 22, 77

- [29] Bell, T. H., 1975. “Topographically generated internal waves in the open ocean.” *Journal of Geophysical Research*, **80**(3), pp. 320–327. 8, 19, 46
- [30] Munk, W., and Wunsch, C., 1998. “Abyssal recipes II: Energetics of tidal and wind mixing.” *Deep-Sea Research Part I: Oceanographic Research Papers*, **45**(12), dec, pp. 1977–2010. 8, 111
- [31] Baines, P. G., 1986. *Internal tides, internal waves and near-inertial motions*. American Geophysical Union (AGU), ch. 2, pp. 19–31. 8
- [32] Aguilar, D. A., Sutherland, B. R., and Muraki, D. J., 2006. “Laboratory generation of internal waves from sinusoidal topography.” *Deep-Sea Research Part II: Topical Studies in Oceanography*, **53**(1-2), pp. 96–115. 8
- [33] Gostiaux, L., and Dauxois, T., 2007. “Laboratory experiments on the generation of internal tidal beams over steep slopes.” *Physics of Fluids*, **19**(2). 8
- [34] Peacock, T., Echeverri, P., and Balmforth, N., 2008. “An Experimental Investigation of Internal Tide Generation by Two-Dimensional Topography.” *Journal of Physical Oceanography*, **38**, p. 235. 8, 26, 30, 55, 77, 112, 140
- [35] Lamb, K. G., 2004. “Nonlinear interaction among internal wave beams generated by tidal flow over supercritical topography.” *Geophysical Research Letters*, **31**(9), may. 8
- [36] Munroe, J. R., and Lamb, K. G., 2005. “Topographic amplitude dependence of internal wave generation by tidal forcing over idealized three-dimensional topography.” *Journal of Geophysical Research: Oceans*, **110**(C2). 8
- [37] Legg, S., and Huijts, K. M., 2006. “Preliminary simulations of internal waves and mixing generated by finite amplitude tidal flow over isolated topography.” In *Deep-Sea Research Part II: Topical Studies in Oceanography*, Vol. 53, pp. 140–156. 8
- [38] Legg, S., and Klymak, J., 2008. “Internal hydraulic jumps and overturning generated by tidal flow over a tall Steep Ridge.” *Journal of Physical Oceanography*, **38**(9), pp. 1949–1964. 8
- [39] Balmforth, N. J., Ierley, G. R., and Young, W. R., 2002. “Tidal conversion by subcritical topography.” *Journal of Physical Oceanography*, **32**(10), pp. 2900–2914. 8, 19, 112
- [40] Balmforth, N. J., and Peacock, T., 2009. “Tidal conversion by supercritical topography.” *Journal of Physical Oceanography*, **39**(8), pp. 1965–1974. 8, 19, 112
- [41] Phillips, O. M., 1960. “On the dynamics of unsteady gravity waves of finite amplitude Part 1. The elementary interactions.” *Journal of Fluid Mechanics*, **9**(2), pp. 193–217. 8
- [42] Müller, P., Holloway, G., Henyey, F., and Pomphrey, N., 1986. Nonlinear interactions among internal gravity waves. 8
- [43] Bourget, B., Dauxois, T., Joubaud, S., and Odier, P., 2013. “Experimental study of parametric subharmonic instability for internal plane waves.” *Journal of Fluid Mechanics*, **723**, may, pp. 1–20. 8

- [44] Tabaei, A., Akylas, T. R., and Lamb, K. G., 2005. “Nonlinear effects in reflecting and colliding internal wave beams.” *Journal of Fluid Mechanics*, **526**, mar, pp. 217–243. 8
- [45] Jiang, C. H., and Marcus, P. S., 2009. “Selection rules for the nonlinear interaction of internal gravity waves.” *Physical Review Letters*, **102**(12), mar. 8
- [46] Smith, S., and Crockett, J., 2014. “Experiments on Nonlinear Harmonic Wave Generation from Colliding Internal Wave Beams.” *Experimental Thermal and Fluid Science*, **54**. 8, 77, 140
- [47] Rainville, L., and Pinkel, R., 2006. “Baroclinic energy flux at the Hawaiian Ridge: Observations from the R/P FLIP.” *Journal of Physical Oceanography*, **36**(6), pp. 1104–1122. 9
- [48] Martin, J. P., Rudnick, D. L., and Pinkel, R., 2006. Spatially Broad Observations of Internal Waves in the Upper Ocean at the Hawaiian Ridge Tech. rep. 9
- [49] Brandt, P., Rubino, A., Alpers, W., and Backhaus, J. O., 1997. “Internal waves in the Strait of Messina studied by a numerical model and synthetic aperture radar images from the ERS 1/2 satellites.” *Journal of Physical Oceanography*, **27**(5), pp. 648–663. 9
- [50] Diggs, S., Kappa, J., Kinkade, D., and Swift, J., 2002. WHP CD_ROM Version 3.0 [CD-ROM]. 9, 18, 70
- [51] Pinkel, R., and Rudnick, D., 2006. “Editorial.” *Journal of Physical Oceanography*, **36**(6), jun, pp. 965–966. 9
- [52] Hackett, C. M., Settles, G. S., and Miller, J. D., 1994. On the gas dynamics of HVOF thermal sprays, sep. 10
- [53] Iffa, E. D., Aziz, A. R., and Malik, A. S., 2011. “Gas flame temperature measurement using background oriented schlieren.” *Journal of Applied Sciences*, **11**(9), pp. 1658–1662. 11
- [54] Soranna, F., Chow, Y. C., Uzol, O., and Katz, J., 2010. “The effects of inlet guide vane-wake impingement on the boundary layer and the near-wake of a rotor blade.” *Journal of Turbomachinery*, **132**(4), oct, pp. 1–13. 11
- [55] Görtler, H., 1943. “Über eine Schwingungserscheinung in Flüssigkeiten mit stabiler Dichteschichtung.” *Zeitschrift für Angewandte Mathematik und Mechanik*, **23**(2), pp. 65–71. 11
- [56] Mowbray, D. E., and Rarity, B. S. H., 1967. “A theoretical and experimental investigation of the phase configuration of internal waves of small amplitude in a density stratified liquid.” *Journal of Fluid Mechanics*, **28**(01), pp. 1–16. 11
- [57] Merzkirch, W., 1974. *Flow visualization*. Academic Press. 11
- [58] Dalziel, S. B., Hughes, G. O., and Sutherland, B. R., 2000. “Whole-field density measurements by ‘synthetic schlieren’.” *Experiments in Fluids*, **28**(4), pp. 322–335. 11, 13, 14, 33, 49, 76, 86, 112, 116, 140, 143, 147, 232, 233

- [59] Goldhahn, E., and Seume, J., 2007. “The background oriented schlieren technique: sensitivity, accuracy, resolution and application to a three-dimensional density field.” *Experiments in Fluids*, **43**(2-3), pp. 241–249. 11
- [60] Venkatakrishnan, L., Wiley, A., Kumar, R., and Alvi, F., 2011. “Density field measurements of a supersonic impinging jet with microjet control.” *AIAA Journal*, **49**(2), feb, pp. 432–438. 11
- [61] Aminfar, A., Cobian-Iñiguez, J., Ghasemian, M., Rosales Espitia, N., Weise, D. R., and Princevac, M., 2019. “Using Background-Oriented Schlieren to Visualize Convection in a Propagating Wildland Fire.” *Combustion Science and Technology*. 11
- [62] Raffel, M., Willert, C. E., Scarano, F., Kähler, C. J., Wereley, S. T., and Kompenhans, J., 2018. *Particle Image Velocimetry.*, 3 ed. Springer International Publishing, Cham. 14, 141
- [63] Dalziel, S. B., Carr, M., Sveen, J. K., and Davies, P. A., 2007. “Simultaneous synthetic schlieren and PIV measurements for internal solitary waves.” *Measurement Science and Technology*, **18**(3), pp. 533–547. 14, 15, 140, 141
- [64] Paoletti, M. S., and Swinney, H. L., 2012. “Propagating and evanescent internal waves in a deep ocean model.” *Journal of Fluid Mechanics*, **706**, sep, pp. 571–583. 14, 15, 17, 45, 78, 112, 136, 141
- [65] Niwa, Y., and Hibiya, T., 2004. “Three-dimensional numerical simulation of M2 internal tides in the East China Sea.” *Journal of Geophysical Research C: Oceans*, **109**(4), apr. 15
- [66] Sutherland, B. R., 1996. “Internal gravity wave radiation into weakly stratified fluid.” *Physics of Fluids*, **8**(2), pp. 430–441. 15, 78
- [67] Brown, G. L., Bush, A. B. G., and Sutherland, B. R., 2008. “Beyond ray tracing for internal waves. II. Finite-amplitude effects.” *Physics of Fluids*, **20**(10), p. 106602. 15, 78
- [68] Diamessis, P. J., Wunsch, S., Delwiche, I., and Richter, M. P., 2014. “Nonlinear generation of harmonics through the interaction of an internal wave beam with a model oceanic pycnocline.” *Dynamics of Atmospheres and Oceans*, **66**, pp. 110–137. 15, 78
- [69] Hines, C. O., 1991. “The Saturation of Gravity Waves in the Middle Atmosphere. Part II: Development Of Doppler-Spread Theory.” *Journal of the Atmospheric Sciences*, **48**(11), pp. 1361–1379. 16, 77
- [70] Buckley, G., Broutman, D., Rottman, J. W., and Eckermann, S., 1999. “On the importance of weak steady shear in the refraction of short internal waves.” *Geophysical Research Letters*, **26**(18), pp. 2877–2880. 16, 77
- [71] Sartelet, K. N., 2003. “Wave Propagation inside an Inertia Wave. Part I: Role of Time Dependence and Scale Separation.” *Journal of the Atmospheric Sciences*, **60**(12), pp. 1433–1447. 16, 77
- [72] Vanderhoff, J. C., Nomura, K. K., Rottman, J. W., and Macaskill, C., 2008. “Doppler spreading of internal gravity waves by an inertia-wave packet.” *Journal of Geophysical Research: Oceans*, **113**(C5). 16, 77

- [73] Vanderhoff, J. C., Rottman, J. W., and Broutman, D., 2010. “The trapping and detraping of short internal waves by an inertia wave.” *Physics of Fluids*, **22**(12), p. 126603. 16, 77
- [74] Pedlosky, J., 2003. *Waves in the Ocean and Atmosphere*. Springer-Verlag Berlin Heidelberg, Germany. 16, 17, 24, 26, 27, 44, 52, 53, 55, 56, 71, 84, 117, 119
- [75] Llewellyn-Smith, S. G., and Young, W. R., 2002. “Conversion of the Barotropic Tide.” *Journal of Physical Oceanography*, **32**(5), pp. 1554–1566. 16, 19, 24, 46, 53, 64, 77, 112
- [76] Voisin, B., 1994. “Internal wave generation in uniformly stratified fluids. Part 2. Moving point sources.” *Journal of Fluid Mechanics*, **261**, pp. 333–374. 16, 77
- [77] Brown, G. L., and Sutherland, B. R., 2007. “Internal wave tunneling through non-uniformly stratified shear flow.” *Atmosphere-Ocean*, **45**(1), pp. 47–56. 16, 17, 44, 77
- [78] Mathur, M., and Peacock, T., 2009. “Internal wave beam propagation in non-uniform stratifications.” *Journal of Fluid Mechanics*, **639**, pp. 133–152. 16, 17, 44, 77, 141
- [79] Gregory, K. D., and Sutherland, B. R., 2010. “Transmission and reflection of internal wave beams.” *Physics of Fluids*, **22**(10), p. 106601. 16, 17, 44, 77, 141
- [80] Sutherland, B. R., and Yewchuk, K., 2004. “Internal wave tunnelling.” *Journal of Fluid Mechanics*, **511**, pp. 125–134. 17, 44, 141
- [81] Nault, J. T., and Sutherland, B. R., 2007. “Internal wave transmission in nonuniform flows.” *Physics of Fluids*, **19**(1). 17, 28, 44, 56
- [82] Sutherland, B. R., 2016. “Internal wave transmission through a thermohaline staircase.” *Physical Review Fluids*, **1**(1), p. 13701. 17, 44, 140
- [83] Ghaemsaidi, S. J., Dosser, H. V., Rainville, L., and Peacock, T., 2016. “The impact of multiple layering on internal wave transmission.” *Journal of Fluid Mechanics*, **789**, pp. 617–629. 17, 45
- [84] Kistovich, Y. V., and Chashechkin, Y. D., 1998. “Linear theory of the propagation of internal wave beams in an arbitrarily stratified liquid.” *Journal of Applied Mechanics and Technical Physics*, **39**(5), pp. 729–737. 17, 18, 45, 112
- [85] Khatiwala, S., 2003. “Generation of internal tides in an ocean of finite depth: analytical and numerical calculations.” *Deep Sea Research Part I: Oceanographic Research Papers*, **50**(1), pp. 3–21. 19, 46
- [86] Zhang, H. P., King, B., and Swinney, H. L., 2007. “Experimental study of internal gravity waves generated by supercritical topography..” *Physics of Fluids*, **19**(9), p. 96602. 19, 40, 46, 77, 88, 112, 119
- [87] Hurley, D. G., and Keady, G., 1997. “The generation of internal waves by vibrating elliptic cylinders. Part 2. Approximate viscous solution.” *Journal of Fluid Mechanics*, **351**, pp. 119–138. 19, 46

- [88] King, B., Zhang, H. P., and Swinney, H. L., 2009. “Tidal flow over three-dimensional topography in a stratified fluid.” *Phys. Fluids*, **21**, p. 116601. 20, 40, 88, 119
- [89] King, B., Zhang, H. P., and Swinney, H. L., 2010. “Tidal flow over three-dimensional topography generates out-of-forcing-plane harmonics.” *Geophysical Research Letters*, **37**(14). 20
- [90] Zhang, L., and Swinney, H. L., 2014. “Virtual seafloor reduces internal wave generation by tidal flow.” *Phys. Rev. Lett.*, **112**(10), mar, p. 104502. 20, 136
- [91] Lighthill, J., 1978. *Waves in fluids*. Cambridge University Press. 28, 56, 84, 117, 118
- [92] Broutman, D., 1986. “On Internal Wave Caustics.” *Journal of Physical Oceanography*, **16**(10), pp. 1625–1635. 28, 56
- [93] Hill, D. F., 2002. “General density gradients in general domains: the “two-tank” method revisited.” *Experiments in Fluids*, **32**(4), pp. 434–440. 31, 47, 80, 116, 143
- [94] Dalziel Research Partners, 2018. DigiFlow. 34, 86, 116, 231
- [95] Ham, F., and Iaccarino, G., 2004. “Energy conservation in collocated discretization schemes on unstructured meshes.” In *Annual Research Briefs*. Stanford University, pp. 3–14. 39, 88, 119
- [96] Mahesh, K., Constantinescu, G., and Moin, P., 2004. “A numerical method for large-eddy simulation in complex geometries.” *Journal of Computational Physics*, **197**(1), pp. 215–240. 39, 88, 119
- [97] Lee, F. M., Paoletti, M. S., Swinney, H. L., and Morrison, P. J., 2014. “Experimental determination of radiated internal wave power without pressure field data.” *Phys. Fluids*, **26**, p. 46606. 40, 88, 119
- [98] Dettner, A., Paoletti, M. S., and Swinney, H. L., 2013. “Internal tide and boundary current generation by tidal flow over topography.” *Phys. Fluids*, **25**, pp. 1–13. 40, 88, 119
- [99] Allshouse, M. R., Lee, F. M., Morrison, P. J., and Swinney, H. L., 2016. “Internal wave pressure, velocity, and energy flux from density perturbations.” *Phys. Rev. Fluids*, **1**(1), may, p. 14301. 40, 77, 88, 119, 140
- [100] Lee, A., and Crockett, J., 2019. “Turning depths: Evanescent to propagating wave kinetic energy density.” *Phys. Rev. Fluids*, **4**(3), p. 34803. 40, 77, 79, 81, 82, 83, 84, 85, 86, 95, 111, 112, 113, 116, 117, 118, 119, 136, 140, 146, 147, 148, 156
- [101] Schlitzer, R., 2017. Ocean Data View 4. 69
- [102] Poulain, P.-M., and Centurioni, L., 2015. “Direct measurements of World Ocean tidal currents with surface drifters.” *Journal of Geophysical Research Oceans*, **120**, pp. 6986–7003. 70
- [103] McDougall, T., and Barker, P., 2011. *Getting started with TEOS-10 and the Gibbs Seawater (GSW) Oceanographic Toolbox.*, manuals an ed. SCOR/IAPSO WG127. 70

- [104] Sutherland, B. R., Dalziel, S. B., Hughes, G. O., and Linden, P. F., 1999. “Visualization and measurement of internal waves by ‘synthetic schlieren’. Part 1. Vertically oscillating cylinder.” *Journal of Fluid Mechanics*, **390**, pp. 93–126. 76, 77, 140
- [105] Sutherland, B. R., Hughes, G. O., Dalziel, S. B., and Linden, P. F., 2000. “Internal waves revisited.” *Dynamics of Atmospheres and Oceans*, **31**(1), pp. 209–232. 76
- [106] Flynn, M. R., Onu, K., and Sutherland, B. R., 2003. “Internal wave excitation by a vertically oscillating sphere.” *Journal of Fluid Mechanics*, **494**, pp. 65–93. 77
- [107] Decamp, S., Kozack, C., and Sutherland, B. R., 2008. “Three-dimensional schlieren measurements using inverse tomography.” *Experiments in Fluids*, **44**(5), pp. 747–758. 77
- [108] Hazewinkel, J., Maas, L. R. M., and Dalziel, S. B., 2011. “Tomographic reconstruction of internal wave patterns in a paraboloid.” *Experiments in Fluids*, **50**(2), feb, pp. 247–258. 77, 140
- [109] Ghaemsaïdi, S., and Peacock, T., 2013. “3D Stereoscopic PIV visualization of the axisymmetric conical internal wave field generated by an oscillating sphere.” *Experiments in Fluids*, **54**(2). 77
- [110] Yick, K., Stocker, R., and Peacock, T., 2007. “Microscale Synthetic Schlieren.” *Experiments in Fluids*, **42**(1), pp. 41–48. 77, 140
- [111] Lee, F. M., Allshouse, M. R., Swinney, H. L., and Morrison, P. J., 2018. “Internal wave energy flux from density perturbations in nonlinear stratifications.” *Journal of Fluid Mechanics*, **856**, pp. 898–920. 77, 142
- [112] Lee, A., Hakes, K., Liu, Y., Allshouse, M. R., and Crockett, J. “Evanescent to propagating internal waves in experiments, simulations, and linear theory.” *Experiments in Fluids*, *Submitted*. 111, 113, 121, 123, 124, 125, 146, 154, 158
- [113] Varma, D., and Mathur, M., 2017. “Internal wave resonant triads in finite-depth non-uniform stratifications.” *Journal of Fluid Mechanics*, **824**, pp. 286–311. 112
- [114] Manteufel, R. D., 2012. “Sequential perturbation uncertainty propagation in thermal-fluid applications.” In *ASME International Mechanical Engineering Congress and Exposition, Proceedings (IMECE)*, Vol. 5, pp. 281–289. 231
- [115] Huibers, P. D. T., 1997. “Models for the wavelength dependence of the index of refraction of water.” *Applied Optics*, **36**(16), jun, p. 3785. 232
- [116] Stone, J. A., and Zimmerman, J. H., 2004. *Engineering Metrology Toolbox*. 232
- [117] Kasarova, S. N., Sultanova, N. G., Ivanov, C. D., and Nikolov, I. D., 2007. “Analysis of the dispersion of optical plastic materials.” *Optical Materials*, **29**(11), pp. 1481–1490. 232

APPENDIX A. SUPPLEMENTAL EXPERIMENTAL DETAILS

This appendix details the experimental cases of Ch. 5 and the step by step process for filling the tank, running experiments, setting up the stepper motor, and processing experiments.

A.1 Cases of Chapter 5

Table A.1: Case details for the medium topography. All heights are given in centimeters and a , b , c , and d correspond to the density profile listed in the second column and detailed in Tab. 5.2. Simulations were performed on cases with an asterisk.

Case	Density	a	b	c	d	L	Z_H	ω	z_{TD}	D/H	\overline{Fr}_1	$\overline{Fr}_1 D/H$
1*	1	-242.3	1103	-34.39	1034	5.6	71.3	0.80	33.5	2.90	1.38	4.00
2*	1	-242.3	1103	-34.39	1034	5.4	71.3	0.99	33.5	2.90	1.70	4.94
3	1	-242.3	1103	-34.39	1034	4.8	71.3	1.20	33.5	2.90	2.06	5.99
4*	1	-242.3	1103	-34.39	1034	4.8	71.3	1.40	33.5	2.90	2.40	6.97
5*	2	70.42	-177.9	1105		5.5	68.3	1.00	54.3	0.45	1.02	0.45
6*	2	70.42	-177.9	1105		5.1	68.3	1.10	38.9	1.99	1.06	2.12
7	2	70.42	-177.9	1105		5.0	68.8	1.19	23.7	3.52	1.10	3.87
8*	2	115.1	-229.5	1129		4.6	66.0	1.09	47.1	0.79	1.04	0.82
9	2	115.1	-229.5	1129		4.6	65.0	1.22	33.8	2.12	1.09	2.32
10*	2	115.1	-229.5	1129		4.6	66.0	1.30	24.9	3.01	1.12	3.38
11*	2	52.68	-187.9	1119		5.2	66.4	1.20	40	1.72	1.03	1.78
12*	2	52.68	-187.9	1119		5.2	66.44	1.27	22.3	3.49	1.06	3.71
13	2	58.61	-160.5	1110		5.0	65.9	1.01	48.2	0.77	1.02	0.79
14*	3	150.9	-29.08	-183.3	1121	5.7	58.2	1.21	34.9	1.50	1.09	1.63
15*	3	150.9	-29.08	-183.3	1121	5.6	58.2	1.30	23.3	2.66	1.11	2.95
16*	4	109.1	-2.57	1016		5.1	68.0	0.81	56.7	0.19	1.01	0.19
17*	4	109.1	-2.57	1016		5.1	68.0	0.89	48.5	0.95	1.06	1.01
18*	4	109.1	-2.57	1016		5.7	68.0	1.01	39.3	1.94	1.13	2.19
19*	4	109.1	-2.57	1016		5.7	68.0	1.10	32	2.60	1.18	3.06
20*	4	106.2	-2.76	1020		5.5	68.0	1.21	24.5	3.35	1.25	4.19

Table A.2: Case details for the steep topography.

Case	Density	a	b	c	d	L	Z_H	ω	z_{TD}	D/H	\overline{Fr}_1	$\overline{Fr}_1 D/H$
21*	1	-242.3	1103	-34.39	1034	4.7	72.4	0.80	0.335	2.89	1.37	3.97
22*	1	-242.3	1103	-34.39	1034	5.2	72.4	0.98	0.335	2.89	1.68	4.86
23	1	-242.3	1103	-34.39	1034	4.9	72.4	1.20	0.335	2.89	2.06	5.95
24	1	-242.3	1103	-34.39	1034	4.8	72.4	1.40	0.335	2.89	2.39	6.92
25*	2	76.43	-179.6	1104		5.2	68.6	1.01	0.494	0.91	1.04	0.95
26	2	76.43	-179.6	1104		5.0	68.6	1.11	0.359	2.27	1.08	2.45
27*	2	100.3	-220.5	1128		4.6	65.0	1.10	0.488	0.61	1.03	0.63
28*	2	100.3	-220.5	1128		4.6	65.0	1.21	0.359	1.91	1.07	2.05
29	2	100.3	-220.5	1128		4.5	65.0	1.29	0.249	3.01	1.10	3.32
30	3	40.80	43.10	-197.6	1125	4.50	74.0	1.30	0.223	4.17	1.13	4.71
31	3	40.80	43.10	-197.6	1125	4.80	74.0	1.21	0.368	2.72	1.11	3.01
32*	3	40.80	43.10	-197.6	1125	4.50	74.0	1.10	0.503	1.37	1.07	1.47
33	4	104.9	-3.00	1004		4.7	68.3	0.80	0.522	0.61	1.05	0.63
34*	4	104.9	-3.00	1004		4.7	68.3	0.90	0.448	1.34	1.10	1.48
35*	4	103.2	-3.05	1006		4.7	68.3	1.00	0.387	2.14	1.17	2.51
36	4	103.2	-3.05	1006		4.7	68.3	1.11	0.302	2.81	1.23	3.45
37	4	103.2	-3.05	1006		4.7	68.3	1.20	0.249	3.34	1.28	4.26

Table A.3: Case details for the sinusoidal topography.

Case	Density	a	b	c	d	L	Z_H	ω	z_{TD}	D/H	\overline{Fr}_1	$\overline{Fr}_1 D/H$
38*	1	-242.3	1103	-34.39	1034	5.0	72.5	0.81	0.335	4.49	1.40	6.28
39*	1	-242.3	1103	-34.39	1034	4.9	72.5	1.00	0.335	4.49	1.72	7.73
40	1	-242.3	1103	-34.39	1034	4.8	72.4	1.22	0.335	4.48	2.09	9.38
41	1	-242.3	1103	-34.39	1034	4.9	72.4	1.44	0.335	4.48	2.47	11.07
42*	2	52.68	-187	1119		5.2	67.2	1.20	0.39	2.97	1.04	3.09
43*	2	89.38	-214.9	1128		5.0	67.0	1.09	0.528	1.00	1.03	1.03
44	2	89.38	-214.9	1128		5.0	67.0	1.21	0.367	3.27	1.08	3.52
45	2	89.38	-214.9	1128		4.8	67.0	1.30	0.238	5.08	1.11	5.65
46*	3	157.4	-21.46	-195.5	1124	5.0	69.6	0.81	0.568	0.80	1.13	0.90
47*	3	157.4	-21.46	-195.5	1124	5.0	69.6	0.91	0.534	1.27	1.17	1.49
48	3	157.4	-21.46	-195.5	1124	5.5	69.6	0.99	0.498	1.79	1.20	2.16
49	3	157.4	-21.46	-195.5	1124	5.5	69.6	1.11	0.432	2.71	1.23	3.34
50	3	157.4	-21.46	-195.5	1124	4.6	69.6	1.21	0.365	3.65	1.25	4.55
51*	4	106.8	-2.95	1002		5.1	68.2	0.81	0.525	1.21	1.06	1.29
52*	4	106.8	-2.95	1002		5.2	68.2	0.91	0.449	2.29	1.12	2.57
53	4	106.8	-2.95	1002		5.0	68.2	1.00	0.385	3.18	1.18	3.74
54	4	106.8	-2.95	1002		5.7	68.2	1.09	0.324	4.05	1.23	4.97
55	4	106.8	-2.95	1002		5.0	68.2	1.20	0.259	4.96	1.28	6.35
56	4	106.8	-2.95	1002		5.7	68.2	1.30	0.205	5.73	1.33	7.62

Table A.4: Case details for the complex topography.

Case	Density	a	b	c	d	L	Z_H	ω	z_{TD}	D/H	\overline{Fr}_1	$\overline{Fr}_1 D/H$
57*	1	-239.3	1102	-14.39	1021	4.5	73.9	0.60	0.365	0.87	1.61	1.40
58	1	-239.3	1102	-14.39	1021	4.5	73.9	0.81	0.365	0.87	2.16	1.88
59*	1	-237.0	1101	-9.00	1012	4.5	73.9	1.00	0.365	0.87	3.36	2.92
60	1	-237.0	1101	-9.00	1012	4.5	73.9	1.20	0.365	0.87	4.04	3.51
61	1	-237.0	1101	-9.00	1012	4.5	73.9	1.40	0.365	0.87	4.71	4.10
62*	2	76.43	-179.6	1104		4.9	68.6	1.13	0.331	0.78	1.05	0.81
63*	3	40.80	43.10	-197.6	1125	5.4	74.0	1.10	0.503	0.19	1.02	0.19
64	3	40.80	43.10	-197.6	1125	5.0	74.0	1.21	0.368	0.86	1.06	0.91
65	3	40.80	43.10	-197.6	1125	4.8	74.0	1.30	0.223	1.59	1.09	1.73
66	4	112.41	-2.70	1003		4.8	74.4	0.90	0.48	0.32	1.04	0.33
67*	4	110.12	-2.82	1006		5.4	74.4	1.00	0.395	0.75	1.11	0.83
68*	4	110.12	-2.82	1006		5.5	74.4	1.10	0.327	1.08	1.16	1.26

A.2 Filling the tank

1. Calibrate the pumps
 - (a) Allow pumps to warm up by running for at least 5 minutes
 - (b) Test flow rates at 25, 100, 175, and 250 rpms and take 3 measurements for each flow rate tested
 - i. Increase in rpms for the fresh water pump during calibration
 - ii. Decrease in rpms for the salt water pump during calibration
 - (c) Put calibration values into Excel sheet "Pump Testing.xlsx"
2. Put the green filters in the tank along the bottom (2 layers) and both sides (1 layer). Leave the laser side clear if PIV testing will occur.
3. Put the beam supports on (2 person job)
 - (a) The point of the supports is to keep the tank width constant along the whole length of the tank. Check this distance with a ruler as the width should be about 6" from outside edge to outside edge.
4. Open "Filling_Tank_Varying_Profiles_AL_10_20_17.m" (groups folder, intwaves, matlab)
 - (a) Input calibration from excel sheet
 - (b) Choose desired profile (linear, two-layer, exponential, parabolic, etc.)
 - (c) Make sure N_{low} and N_{high} are set to the desired values
5. Run program to find:
 - (a) Volume of fresh water used

- (b) How long it will take to fill the tank
 - (c) The initial volume of the salt water bucket (including salt)
6. Adjust the density and N_{low} and N_{high} values to make sure that the flow rates never go below 0 mL/s.
 7. Put salt into the salt water bucket
 - (a) Remember that we put so much salt in that the volume will change. Keep that in mind as you may need to add more salt.
 - (b) Rule of thumb: For a density of about 1080 for a final volume 80 L of water, you will use an entire bag of salt.
 - (c) This is a little bit of a guess and check game. That's ok. It's better to have too high of a density than too low. It's also ok to add more water in order to bring the density down.
 - (d) You will need about 20% more water in the salt water bucket than the matlab file calls for. So if it calls for 80L, I usually put in 100L.
 8. Get the sponges wet in the salt water tank, then put them in the sponge box and put it in the tank
 - (a) Connect one freshwater and one saltwater line in the box with the T-connection
 9. Copy and paste the "output1" matrix (first three columns) into the txt file "input_to_labview_pump_program.t
 10. Plug in the green usb cord that runs the DAQ into the computer
 - (a) This generally opens up LabVIEW. If not, then open the folder "Profiles Program", select "Run a Program", and choose "Main2_pumps.vi"
 11. Make sure that the tubing is at the bottom of the buckets to prevent the pumps from pulling air instead of water
 12. Run the saltwater pump for a moment to put saltwater through the lines
 13. Make sure the pumps say "EXT" and are turning the correct direction
 14. Go to Operate (top tool bar) then Run.
 15. In Labview, select "Load and Run Profile"
 - (a) This will open a dialog box where you can go and find "input_to_labview_pump_program.txt" in the groups folder
 16. Select "Page 2" in the LabView file to see the loop delay and pump output
 - (a) Each cycle is one complete loop, which is indicated by the loop delay in seconds
 - (b) When you first turn on the pump, there will be no flow until it's completed a cycle

- (c) If you are using more than one sponge box, check the freshwater lines to make sure that water running all the way through. You may need to clamp down on one of the lines to force water through the other one. Do not clamp down in the same place twice

17. Create a new excel file for this setup

After filling:

1. Remove the sponge box and droppers from the tank as carefully as possible to reduce mixing
2. At the end of the fill, run fresh water the through salt water lines to help clean them out
3. Take out MasterFlex tubing from pumps
4. Take density measurements the follow morning

A.3 Density measurements and finding N

This details how to find the density and N profiles

1. Take density measurements and record them in the correct location in the excel file
 - (a) If this the first time you are taking density measurements after filling the tank, take measurements every 2 cm. For subsequent times, you can do it every 5 cm.
 - (b) Add more sheets if necessary
 - (c) Record the total Height of the water in the tank.
2. Open the MATLAB file “Finding_N_and_more_Lee_6_17_16.m”
3. Copy the height and density data and paste it into the variable “excel”
4. Run the program
5. Input the total water height, in METERS.
6. It will output a curve for N .
 - (a) Check the density curve matches the given points. You may need to run it a few times for the curve fitting program to correctly match the profile.
7. Copy down the values for a, b, and c into the excel file for future reference
8. Repeat for each time you take density measurements.
9. It’s time to choose a frequency to run the topography at.
 - (a) Measure the height of the topography in the water and record it.
 - (b) The frequency will be based off either Froude number or H/D

A.4 Taking SS images

Immediately before running a test, put up the signs preventing people from coming in or out of the lab. Take them down as soon as you are ready to turn the lights back on.

You will take 3 sets of images per test (in this order):

1. With_stick

- (a) It's best to focus the camera with the lights off, then turn the lights back on to take this image
- (b) DO NOT bump the camera after this image has been taken
- (c) Slowly place the ruler in the center of the tank. This image needs to be taken in the center of the experiment. WRITE DOWN the height of the water based on this ruler. This value is needed to accurately match the density heights to locations within the image.

2. Background

- (a) Turn off the lights and shut the door for this image
- (b) DO NOT bump the camera after this image. If you think it may have been moved even a little, retake this image before performing the test

3. The actual test images

Process for running a test

1. Close Google Chrome and Matlab.

2. Tighten the turnbuckle

- (a) Check the lab notebook for the required frequency for that day's tests.
- (b) Check that the track is moving at the correct period and that the turnbuckle is working correctly (not sagging too much)

3. Put the track into the water

- (a) Don't let the string be in the water
- (b) Make sure it is level

4. Turn on the backlight

5. Plug in the camera

6. Place the camera in the correct spot and measure the distance from the camera to the dots

- (a) Fill out the requested information in the lab notebook

7. On bottom panel of the desktop, open Biflow

- (a) This is the icon in the task bar
8. Select the number of desired images
 - (a) If doing the images with the stick background, or the actual background images set the number of images to 2
 - (b) If running a full test, set number of images to 4320.
 - (c) CHECK that the max allowable frames are at least 4600. If not then:
 - (d) Set the frames to a large number near (but below) the max allowed and hit OK
 - (e) On the top toolbar, hit Acquisition→Setup.
 - (f) Once the program finishes thinking, close BiFlow, and reopen it.
 - (g) If the max allowable frames are still below 4320, you'll need to restart the computer.
 - (h) If the allowable frames are too close to 4320, the computer will freeze when you try to save and you'll lose your test images.
 9. On the top tool bar, select Preview and then Start Preview
 - (a) Focus the camera on the dots, not the topography
 - (b) Keep the image as big as possible, but avoid dead space. Don't film above or below the water. Keep the topography in the left corner so we can capture the right leg of the internal waves.
 10. On the top tool bar, select Preview and then Stop Preview
 11. DO NOT move the camera after finishing the preview.
 12. On the top tool bar, select Acquisition → Setup
 13. Select Process→Start Acquisition
 14. File-Save
 - (a) If taking images with the stick in place, save as "with_stick" (the lights should be on so you can read the ruler)
 - (b) If taking background images, save as "background" (the lights should be off, and the door shut)
 15. To run the camera again for the same number of images go to Acquisition → Clean up and then start with step 10
 - (a) Once you have done a background images, you cannot move the camera again. The Background and Test Images must be in exactly the same location.
 16. Wait at least 30 minutes before running another test. This allows the water to settle.
 17. When completely done using the camera-UNPLUG the black cord to prevent the camera from overheating.

18. Pull the track out of the water
19. Unplug the stepper motor
20. Write down all of the info needed for this test in the lab notebook (see below)
21. If you are the last person running tests, put the camera to the side.

Write in Lab notebook:

- Date
- Your name
- Test name (ex: 09-12-16-Test_a)
- Distance from camera to light box (meters)
- Actual frequency
- Total height of the water (the actual height AND the height based on the with_stick ruler)
- Type of topography and it's height
- Comments for anything unusual you noticed while running tests
- Horizontal distance the topography moves (specify if it's the full distance or only half)

A.5 Running the stepper motor

1. (This step is usually already done. As long as the board is still hooked up to the motor, skip to step 2.) Hook up wires to microcontroller
 - (a) Stepper motor wires go to the M3 and M4 connections (blue box thing at edge of controller). The center connection is not connected to anything. The red and green wire from the motor are paired together.
 - (b) Middle pin on switch goes to digital I/O pin number 2. Other two wires go to ground and +5V
2. Plug in external power source and USB cable. If it starts to move just flip the switch to the opposite position to stop after loop
3. Open Arduino on desktop, and open motor_control_AL.ino:
MyDocuments\Arduino\motor_control\motor_control_AL.ino
4. Enter desired Period and length
 - (a) Remember that $\text{Period} = 2 * \pi / \text{frequency}$

- (b) What you enter as the period may not be exactly correct. It's about 1 off. If you put in $T = 6s$, the actual period of the track will be about 7s. You will need to check the period a couple of times before it will be correct. Try to do this out of the water.
 - (c) Do not change the Excursion length unless you feel the topography is moving so slowly that it is no longer a smooth movement.
5. Hit upload (the arrow, not the check mark) in upper left corner
 6. Flip the switch hooked to microcontroller to start running
 7. Sometimes you will need to keep the motor plugged into both the computer and the wall in order to pull enough power to move the track.

A.6 Processing the images with Digiflow

1. Using the command prompt, type Digiflow64.exe to open Digiflow
2. File→Open Image → Find correct background image for test you want to process→Open
3. If the image is black: View→ Color Scheme → Default
 - (a) Or Ctrl+Shift+B → Default
 - (b) This allows you to see the corners of the sheet better for the next step
4. Edit→Coordinates → CenterRuler
 - (a) After selecting CenterRuler, hit Edit on the top right, then Edit Points
 - (b) Move the three Points to the three points on the ruler, bottom left, top left, top right. Edit the real world coordinates of these three points by double clicking on the points
 - (c) You will only need to do this once for each time you process, since every image in a run will have the same corner locations
 - (d) Ok→ Ok
5. Analyse→Synthetic Schlieren→Pattern Match
6. (Inputs) Experiment
 - (a) File→Choose the first of the actual run images
 - (b) Sift
 - i. Change fps to 24
 - ii. Select Default Colors
 - iii. Input correct Step (usually 4)
 - iv. Ok
7. Background Image

- (a) File→Choose first of Background Images
 - (b) Select Default Colors
8. Lengths (Generally only need to change Camera to Texture)
- (a) Input the correct Camera to Texture length (m)
 - (b) Experiment to Texture: 0.75
 - (c) Experiment Thickness: 0.12
 - (d) Wall Thickness: 0.018
9. Check (Shouldn't need to change)
- (a) Resolution: High
 - (b) Accuracy: High
 - (c) Fluid medium: Water_Salt
 - (d) Tank Wall: Acrylic
 - (e) Coordinate System: Four Corners
 - (f) Flow Geometry 2D
10. Outputs Tab
11. X-Gradient
- (a) File→Save files in X-gradient
 - (b) Save as type: Image files
 - (c) Save
 - (d) Options-Default Colors
12. Y-Gradient
- (a) File→Save files in Y-Gradient
 - (b) Save as type: Image files
 - (c) Save
13. Saturation Values:
- (a) Checked: Gradient: 0.1
 - (b) Not checked: Automatic
14. Ok (This begins the processing)

The previous steps only allow for processing one test at a time. To process multiple tests in a row, complete the previous list up until step 5. Instead, use the Digiflow dlq command line with the following code, replacing important information such as the actual file names and the correct distance between the camera and the topography.


```

#Synthetic Schlieren
dlgAnalyse_SyntheticSchlierenPatternMatch.Accuracy := "High";
dlgAnalyse_SyntheticSchlierenPatternMatch.Algorithm:= "Pre_2009";
dlgAnalyse_SyntheticSchlierenPatternMatch.AutomaticInterrogation := true;
dlgAnalyse_SyntheticSchlierenPatternMatch.AutomaticMeans := true;
dlgAnalyse_SyntheticSchlierenPatternMatch.AutomaticScales := false;
dlgAnalyse_SyntheticSchlierenPatternMatch.AutomaticValidation := true;
dlgAnalyse_SyntheticSchlierenPatternMatch.Background_MatchIntensity.Kind := "
    Conform";
dlgAnalyse_SyntheticSchlierenPatternMatch.Background_Options.Display:=true;
dlgAnalyse_SyntheticSchlierenPatternMatch.Background_Options.UseArchive:=
    false;
dlgAnalyse_SyntheticSchlierenPatternMatch.Background_Options.AutoPreprocess:=
    false;
dlgAnalyse_SyntheticSchlierenPatternMatch.Background_Region.Kind:= "Conform"
;
dlgAnalyse_SyntheticSchlierenPatternMatch.Background_Time.TimeStepFile :=1;
dlgAnalyse_SyntheticSchlierenPatternMatch.CompactOutput := false;
dlgAnalyse_SyntheticSchlierenPatternMatch.DensityScale := 1.00000E-02;
dlgAnalyse_SyntheticSchlierenPatternMatch.DifferentialMode := false;
dlgAnalyse_SyntheticSchlierenPatternMatch.DisplayOnExit := true;
dlgAnalyse_SyntheticSchlierenPatternMatch.Experiment_Options.Display := true;
dlgAnalyse_SyntheticSchlierenPatternMatch.Experiment_Options.UseArchive :=
    true;
dlgAnalyse_SyntheticSchlierenPatternMatch.Experiment_Options.AutoPreprocess :=
    false;
dlgAnalyse_SyntheticSchlierenPatternMatch.Experiment_Region.Kind:= "Conform";
dlgAnalyse_SyntheticSchlierenPatternMatch.Experiment_Time.TimeStepFile
:=4.16670E-02;
dlgAnalyse_SyntheticSchlierenPatternMatch.Experiment_Time.StepBy:=4;
dlgAnalyse_SyntheticSchlierenPatternMatch.Experiment_Time.ToStep:=4319;
dlgAnalyse_SyntheticSchlierenPatternMatch.Experiment_Time.FromStep:=0;
dlgAnalyse_SyntheticSchlierenPatternMatch.FlowGeometry:= "2D";
dlgAnalyse_SyntheticSchlierenPatternMatch.GradientScale:=0.10;
dlgAnalyse_SyntheticSchlierenPatternMatch.MaskZeros:=true;
dlgAnalyse_SyntheticSchlierenPatternMatch.Medium:= "Water_Salt";
dlgAnalyse_SyntheticSchlierenPatternMatch.Resolution:= "High";
dlgAnalyse_SyntheticSchlierenPatternMatch.UseOpticsCorrection:= false;
dlgAnalyse_SyntheticSchlierenPatternMatch.UseUserInterpolation:= false;
dlgAnalyse_SyntheticSchlierenPatternMatch.WallMedium:= "Acrylic";
dlgAnalyse_SyntheticSchlierenPatternMatch.XGradient_Options.Comments:= "No
    user comments";
dlgAnalyse_SyntheticSchlierenPatternMatch.XGradient_Options.Colour:= "( default
)";
dlgAnalyse_SyntheticSchlierenPatternMatch.XGradient_Options.Display := true;
dlgAnalyse_SyntheticSchlierenPatternMatch.XGradient_Options.UseArchive :=
    false;
dlgAnalyse_SyntheticSchlierenPatternMatch.XGradient_Options.Resample := "none
";
dlgAnalyse_SyntheticSchlierenPatternMatch.YGradient_Options.Comments:= "No_
    user_comments";
dlgAnalyse_SyntheticSchlierenPatternMatch.YGradient_Options.Colour := "(
    default)";
dlgAnalyse_SyntheticSchlierenPatternMatch.YGradient_Options.Display:=true;

```

```

dlgAnalyse_SyntheticSchlierenPatternMatch . YGradient_Options . UseArchive := _
false ;
dlgAnalyse_SyntheticSchlierenPatternMatch . YGradient_Options . Resample := _ " none
";
dlgAnalyse_SyntheticSchlierenPatternMatch . process := " "
Analyse_SyntheticSchlierenPatternMatch";
dlgAnalyse_SyntheticSchlierenPatternMatch . xMaxShift := 3;
dlgAnalyse_SyntheticSchlierenPatternMatch . xSpace := 8;
dlgAnalyse_SyntheticSchlierenPatternMatch . yMaxShift := 3;
dlgAnalyse_SyntheticSchlierenPatternMatch . ySpace := 8;

#_Paste_SS_info_here :
dlgAnalyse_SyntheticSchlierenPatternMatch . Background := " background#####.
tif";
dlgAnalyse_SyntheticSchlierenPatternMatch . Background_Folder := "H:\2018\Fill
-3-5-18\3-7-18-Test_f\";
dlgAnalyse_SyntheticSchlierenPatternMatch . CameraToTexture := 4.0 ;
dlgAnalyse_SyntheticSchlierenPatternMatch . CoordSystem := " center_ruler";
dlgAnalyse_SyntheticSchlierenPatternMatch . DensityScale := 1.00000E-02;
dlgAnalyse_SyntheticSchlierenPatternMatch . Experiment := " Sequence#####.tif"
;
dlgAnalyse_SyntheticSchlierenPatternMatch . ExperimentThickness := 0.120000;
dlgAnalyse_SyntheticSchlierenPatternMatch . ExperimentToTexture := 0.93;
dlgAnalyse_SyntheticSchlierenPatternMatch . Experiment_Folder := "H:\2018\Fill
-3-5-18\3-7-18-Test_f\images\";
dlgAnalyse_SyntheticSchlierenPatternMatch . WallThickness := 1.80000E-02;
dlgAnalyse_SyntheticSchlierenPatternMatch . XGradient := "H:\2018\Fill
-3-5-18\3-7-18-Test_f\xgrad\x_gradient#####.dfi";
dlgAnalyse_SyntheticSchlierenPatternMatch . YGradient := "H:\2018\Fill
-3-5-18\3-7-18-Test_f\ygrad\y_gradient#####.dfi";
process_dlgAnalyse_SyntheticSchlierenPatternMatch ;
#_Dat_files
##### Start_Here#####
dlgFile_EditStream . DisplayOnExit := false ;
dlgFile_EditStream . Input_Options . Display := true ;
dlgFile_EditStream . Input_Options . UseArchive := false ;
dlgFile_EditStream . Input_Options . AutoPreprocess := false ;
dlgFile_EditStream . Input_Region . Kind := " All";
dlgFile_EditStream . Input_Time . TimeStepFile := 0.166668;
dlgFile_EditStream . Output_Options . Display := true ;
dlgFile_EditStream . Output_Options . UseArchive := false ;
dlgFile_EditStream . ReviewCapture := false ;
dlgFile_EditStream . process := " File_EditStream";
#_Paste_dat_info_here
dlgFile_EditStream . Input := " y_gradient#####.dfi";
dlgFile_EditStream . Input_Folder := "H:\2018\Fill -3-5-18\3-7-18-Test_f\ygrad\";
dlgFile_EditStream . Output := "H:\2018\Fill -3-5-18\3-7-18-Test_f\ygrad_dat\
y_gradient#####.dat";
process_dlgFile_EditStream ;

```

APPENDIX B. COMPUTER CODE

B.1 MATLAB

B.1.1 Generating natural frequency profile and output voltages

```
clear
% close all
% clc

%% Establish Variables
% rho_f = fresh water density , set
% rho_s = salt water density , set
% rho_m = mixture density (as a function over time)
% Q_f = fresh water flowrate , to be solved
% Q_s = salt water flowrate , to be solved
% Q_m = mixture flowrate , set
% A_t = Tank area
% z_dot = Tank depth per unit time
% t = time
% Vol_f = total volume of fresh water used (L)
% Vol_s = total volume of salt water used (L)
%% User supplied inputs
% Desired height
z_total = .70; %(m)

% Density of salt water tank
rho_s = 1106.4; % kg/m^3
%% Type of profile desired
%% exponential rho = a*exp(bz)+c (b is negative)
N_profile = 1;
N_low = 0.48;
N_high = 1.95;

%% Two layer N
%% rho1 = az+b; rho2 = cz+d;
% N_profile = 2;
% N_low = .5;
% N_high = 1.5;
% switch_height = .30;

%% Constant N
%% rho = az+b
```

```

% N_profile = 3;
% N_low = 0.9;
%
%% Linear N^2
% rho = az^2 + bz + c
% N_profile = 4;
% N_low = 0.4;
% N_high = 1.5;
%
% Parabolic N^2
% rho = az^3 + bz^2 + cz + d
% N_profile = 5;
% N_low = 0.2;
% N_high = 1.7;

excel_fresh = [25          64
50          127.3333333
100         240.6666667
175         452
250         609.3333333
];

excel_salt = [250          605.3333333
175          482.6666667
100          245.3333333
50           134.6666667
25           71.333333333
];
%% Constants
g = 9.81;    %m/s^2

%Density of fresh water
rho_f = 998.5; % kg/m^3

% Standard density to calculate N
rho_o = 1000;

% Desired Volume flow rate
Q_m = 10e-06; % m^3/s
% Q_m = 5e-06; % m^3/s small fish tank

% Area of Tank
A_t = 0.117475*2.40824; % m^2 full tank
% A_t = .5127*.2651; %m^2 small fish tank

% dh_dt = Q_m/A_t*100*3600;

%% Creating z and t arrays
% Depth array
z = 0:.0005:z_total; % m
dz = (z(2)-z(1)); %delta z in m, to be used to find N

% Relations
z_dot = Q_m/A_t; % m/s

```

```

t = z/z_dot; % creating the time array

if N_profile == 1
    b = log(N_high^2/N_low^2)/(-z_total);
    a = -rho_o*N_low^2./(g*b*exp(b*z_total));
    c = rho_s-a-10;
    rho_m = a*exp(b*z)+c;
    N = sqrt(-g/rho_o*a*b*exp(b*z));
%    figure (1); clf; plot(rho_m,z); figure(2); clf; plot(N,z)
elseif N_profile == 2
    a = N_low^2*(-rho_o/g);
    c = N_high^2*(-rho_o/g);
    d = rho_s-25;
    b = (c-a)*switch_height+d;
    for i= 1:length(z)
        if z(i)<switch_height
            %profile for N2
            rho_m(i) = c*z(i)+d;
            N(i) = sqrt(-g/rho_o*c);
        else
            %profile for N1
            rho_m(i) = a*z(i)+b; %(-(N_low^2)*rho_f/g)*z_m(i)+(rho_f*
                switch_height/g*(N_low^2-N_high^2))+rho_s-25;
            N(i) = sqrt(-g/rho_o*a);
        end
    end
elseif N_profile == 3
    a = N_low^2*-rho_o/g;
    b = rho_s-15;
    rho_m = a*z+b;
elseif N_profile == 4
    b = N_high^2;
    a = (N_low^2-b)/z_total;
    rho_m = -rho_o/g*(a/2*z.^2+b*z)+rho_s-10;
    N = sqrt(a*z+b);
elseif N_profile == 5
    N_med = (N_high+N_low)/2;
    z_med = z_total/2;
    z_matrix = [0    0    1;
                z_med^2  z_med    1;
                z_total^2  z_total    1];
    N_matrix = [ N_high^2; N_med^2; N_low^2];
    A = z_matrix\N_matrix;
    a = A(1); b = A(2); c = A(3);
    rho_m = -rho_o/g*(a/3*z.^3+b/2*z.^2+c*z)+rho_s-15;
    N = sqrt(a*z.^2+b*z+c);

end
%%
% Solve for Q_f & Q_s
Q_f = Q_m * (rho_m - rho_s)/(rho_f - rho_s);
Q_s = Q_m * (rho_m - rho_f)/(rho_s - rho_f);

for n = 2:1:length(rho_m)-1

```

```

    drhodz(n) = (rho_m(n+1)- rho_m(n-1))./(2* dz);
end
drhodz(1) = drhodz(2);
drhodz(length(rho_m)) = drhodz(length(rho_m)-1);
N_calc = sqrt(-g/1000*drhodz);

if min(Q_f)<0
    fprintf('The fresh water flow rate goes below zero during the program\n')
end

if min(Q_s)< 0
    fprintf('The salt water flow rate goes below zero during the program\n')
end

%% Finding total volumes of fresh and salt water
delta_t = zeros(size(t));
delta_t(1:end-1) = diff(t);
delta_t(end) = delta_t(end-1);
Vol_f = sum(delta_t.*Q_f)*1000;
Vol_s = sum(delta_t.*Q_s)*1000;

%% On screen values

fprintf(['N at tank bottom (1/s): ', num2str(N_calc(1)), '\n'
]);
fprintf(['N at tank top (1/s): ', num2str(N_calc(end)), '\n'
]);
fprintf(['volume of fresh water used (L): ', num2str(Vol_f), '\n']);
fprintf(['volume of salt water used (L): ', num2str(Vol_s), '\n']);
fprintf(['Initial density in salt water bucket: ', num2str(rho_s), '\n']);
fprintf(['Time elapsed (hours): ', num2str(t(end)/3600), '\n'
]);

%% Setting The Pump Voltages
fresh_rpm = excel_fresh(:,1);
fresh_q = excel_fresh(:,2);
fit_order_fresh = 1;
fresh_pump_fit_rpm_to_q = polyfit(excel_fresh(:,1), excel_fresh(:,2),
    fit_order_fresh);
fresh_pump_fit_q_to_rpm = polyfit(excel_fresh(:,2), excel_fresh(:,1),
    fit_order_fresh);
salt_rpm = excel_salt(:,1);
salt_q = excel_salt(:,2);
fit_order_salt = 1;
salt_pump_fit_rpm_to_q = polyfit(excel_salt(:,1), excel_salt(:,2),
    fit_order_salt);
salt_pump_fit_q_to_rpm = polyfit(excel_salt(:,2), excel_salt(:,1),
    fit_order_salt);
bob_check_fresh = polyval(fresh_pump_fit_rpm_to_q, 0:375);
bob_check_salt = polyval(salt_pump_fit_rpm_to_q, 0:375);

dt = delta_t;

```

```

fresh_flow_desired = Q_f*1000000*60;    %mL/ min
salt_flow_desired = Q_s*1000000*60;    %mL/ min

RPM_fresh = polyval(fresh_pump_fit_q_to_rpm , fresh_flow_desired);
RPM_salt = polyval(salt_pump_fit_q_to_rpm , salt_flow_desired);

%% Finding Voltages from new RPMS–Need to check these still
% Volts_fresh = (0.0166*RPM_fresh+0.0148);
% Volts_salt = (0.0167*RPM_salt+0.0203);
Volts_fresh = round(0.0166*RPM_fresh+0.0148,2);
Volts_salt = round(0.0167*RPM_salt+0.0203,2);

%% Finding Flow rates based off of actual flows
RPM_line_fresh = 60.172*Volts_fresh -0.882;
RPM_line_salt = 60.02*Volts_salt -1.2108;

Q_line_fresh = polyval(fresh_pump_fit_rpm_to_q , RPM_line_fresh);
Q_line_salt = polyval(salt_pump_fit_rpm_to_q , RPM_line_salt);
t = (1:1:length(dt)).*dt;
t_hours = t/3600;

%% Finding new densities based off of actual flow rates
for i = 1:length(dt);
    if Q_line_fresh(i)<0
        Q_line_fresh(i) = 0;
    end
    if Q_line_salt(i)<0;
        Q_line_salt(i) = 0;
    end
end
Qm = Q_line_fresh+Q_line_salt;
rho_m_f = rho_s+Q_line_fresh./Qm.*(rho_f-rho_s);
rho_m_s = rho_f+Q_line_salt./Qm.*(rho_s-rho_f);
figure (2);clf
plot(t_hours , rho_m_f)
title('density_vs_time(hours)')
xlabel('time_(hours)')
A_t = 0.117475*2.40824; % m^2

Q_m_m_s = Qm*10^-6/60;

z_dot = Q_m_m_s./A_t; % m/s

z = t.*z_dot;

output1(:,1) = dt;
output1(:,2) = Volts_fresh;
output1(:,3) = Volts_salt;
output1(:,4) = rho_m_f';

%% Figures
figure(100); clf;

```

```

plot(z, N_calc)
plot(N_calc, z)
xlabel('Depth (cm)')
ylabel('N')
title('Natural Frequency in the Tank')

figure(3); clf;
plot(t_hours, fresh_flow_desired, t_hours, salt_flow_desired, t_hours, Q_line_fresh
, t_hours, Q_line_salt);
xlabel('Time (hours)')
ylabel('Flowrate (mL/min)')
legend('Fresh desired', 'Salt desired', 'Fresh actual', 'Salt actual')
title('Flowrates of Fresh and Salt Water Tanks');

```

B.1.2 Measuring the density profile

```

% This file allows you calculate the natural frequency of the experimental
% tank. The data for "depth" and "rho_measured" come from the density
% sheets in the excel file for each fill. The values for a,b,c, and d
% should be written down for future use, but are not necessary for running
% tests. This program will also output the N/omega and H/D values for a
% range of frequencies.

```

```

clear
% clc
% close all
%% Inputs
% Choose topography shape
% topography = 1; % Medium
% topography = 2; % steep
% topography = 3; % complex
topography = 4; % sine
if topography == 1
    H = 0.1;
elseif topography == 2
    H = 0.1;
elseif topography == 3
    H = 0.2;
elseif topography == 4
    H = .071;
end

% Choose Profile
% Exponential Profile (a*exp(-bz)+c)
density_prof=1;

% Cubic Profile (a*x^3+b*x^2+c*x+d)
% density_prof = 2;

% Quadratic Profile (a*x^2+b*x+c)
% density_prof = 3;

% Linear Profile (a*x+b)
% density_prof = 4;

```



```

% Two Layer Linear Profile (a*x+b, c*x+d)
% density_prof = 5;
% switch_height = 0.41;

% Needed Values
H_water=.663;
omega = 0.6961;

% Put in density values
%Just copy paste both columns in from excel file
excel=[1100.4    0.06
1095.7    0.08
1089.8    0.11
1086.3    0.14
1081.1    0.17
1076.4    0.2
1072.2    0.23
1067.6    0.26
1063.2    0.29
1059.1    0.32
1055.4    0.35
1051.8    0.38
1048.4    0.41
1045.0    0.44
1041.8    0.47
1039.2    0.5
1036.7    0.53
1034.7    0.56
1032.2    0.59
1030.2    0.62
];
%% Calculations
g = 9.81;
rho_o = 1000;
depth=excel(:,2);
rho_measured = excel(:,1);
drho_dz_measured = diff(rho_measured)./diff(depth);
N_measured = sqrt(-9.81/1000*drho_dz_measured);
z_fit = 0:.001:depth(end);
syms z_td % needed to find the actual td location numerically (given omega)
if density_prof ==1
    ft = fitype( 'a*exp(-b*x)+c', 'independent', 'x', 'dependent', 'y' );
    opts = fitoptions( 'Method', 'NonlinearLeastSquares' );
    opts.Algorithm = 'Levenberg-Marquardt';
    opts.Display = 'Off';
    [xData, yData] = prepareCurveData( depth, rho_measured );
    [fitresult, gof] = fit( xData, yData, ft, opts );
    coeff = coeffvalues(fitresult);
    a = coeff(1)
    b = -coeff(2)
    c = coeff(3)
    rho_plot = a*exp(b*z_fit)+c;
    N_fit = sqrt(-g/rho_o*(a*b*exp(b*z_fit)));

```

```

Nmin = sqrt(-g/rho_o*(a*b*exp(b*H_water));%c*d*exp(d*H_water)));
Nmax = sqrt(-g/rho_o*(a*b*exp(b*0));%c*d*exp(d*0)));
ztd = double(vpasolve(-omega+sqrt(-g/rho_o*(a*b*exp(b*z_td)))););
N_evan = N_fit(N_fit<omega);
D = H_water-ztd-H;
H_D = H/D;
Fr1 = omega/mean(N_evan)
D_H = D/H
Fr1D_H = Fr1*D_H
elseif density_prof ==2
ft = fitype( 'a*x^3+b*x^2+c*x+d', 'independent', 'x', 'dependent', 'y' );
opts = fitoptions( 'Method', 'NonlinearLeastSquares' );
opts.Algorithm = 'Levenberg-Marquardt';
opts.Display = 'Off';
[xData, yData] = prepareCurveData( depth, rho_measured );
[fitresult, gof] = fit( xData, yData, ft, opts );
[p,S] = polyfit(depth, rho_measured, 3);
a = p(1);
b = p(2);
c = p(3);
d = p(4);
rho_plot = polyval(p, z_fit);
N_fit = sqrt(-9.81/1000*(p(1)*3*z_fit.^2+2*p(2)*z_fit+p(3)));
Nmax = sqrt(-9.81/1000*(p(1)*3*0.^2+2*p(2)*0+p(3)));
Nmin = sqrt(-9.81/1000*(p(1)*3*H_water.^2+2*p(2)*H_water+p(3)));
ztd = double(vpasolve(-omega+sqrt(-g/rho_o*(p(1)*3*z_td.^2+2*p(2)*z_td+p(3)))););
D = H_water-ztd-H;
H_D = H/D;
N_evan = N_fit(N_fit<omega);
Fr1 = omega/mean(N_evan);
D_H = D/H
Fr1D_H = Fr1*D_H;
elseif density_prof==3
ft = fitype( 'a*x^2+b*x+c', 'independent', 'x', 'dependent', 'y' );
opts = fitoptions( 'Method', 'NonlinearLeastSquares' );
opts.Algorithm = 'Levenberg-Marquardt';
opts.Display = 'Off';
[xData, yData] = prepareCurveData( depth, rho_measured );
[fitresult, gof] = fit( xData, yData, ft, opts );
[p,S] = polyfit(depth, rho_measured, 2);
a = p(1);
b = p(2);
c = p(3);
rho_plot = polyval(p, z_fit);
N_fit = sqrt(-9.81/1000*(p(1)*2*z_fit+p(2)));
Nmax = sqrt(-g/rho_o*(p(1)*2*0+p(2)));
Nmin = sqrt(-g/rho_o*(p(1)*2*H_water+p(2)));
ztd = double(vpasolve(-omega+sqrt(-g/rho_o*(p(1)*2*z_td+p(2)))););
D = H_water-ztd-H;
H_D = H/D;
N_evan = N_fit(N_fit<omega);
Fr1 = omega/mean(N_evan);
D_H = D/H

```

```

Fr1D_H = Fr1*D_H;
elseif density_prof==4
ft = fitype( 'a*x+b', 'independent', 'x', 'dependent', 'y' );
opts = fitoptions( 'Method', 'NonlinearLeastSquares' );
opts.Algorithm = 'Levenberg-Marquardt';
opts.Display = 'Off';
[xData, yData] = prepareCurveData( depth, rho_measured );
[fitresult, gof] = fit( xData, yData, ft, opts );
[p,S] = polyfit(depth, rho_measured, 1);
a = p(1)
b = p(2)
rho_plot = polyval(p, z_fit);
N_fit = sqrt(-9.81/1000*(p(1)*2*ones(length(z_fit))));
Nmax = sqrt(-g/rho_o*(p(1)*2*0+p(2)));
Nmin = sqrt(-g/rho_o*(p(1)*2*H_water+p(2)));
ztd = double(vpasolve(-omega+sqrt(-g/rho_o*(p(1)*2*z_td+p(2)))));
D = H_water-ztd-H;
H_D = H/D;
N_evan = N_fit(N_fit<omega);
Fr1 = omega/mean(N_evan)
D_H= D/H
Fr1D_H = Fr1*D_H
elseif density_prof == 5
ft = fitype( 'a*x+b, c*x+d', 'independent', 'x', 'dependent', 'y' );
opts = fitoptions( 'Method', 'NonlinearLeastSquares' );
opts.Algorithm = 'Levenberg-Marquardt';
opts.Display = 'Off';
[xData, yData] = prepareCurveData( depth, rho_measured );
[fitresult, gof] = fit( xData, yData, ft, opts );
prop_indices = find(depth<switch_height);
evan_indices = find(depth>switch_height);
depth_prop = depth(prop_indices);
depth_evan = depth(evan_indices);
rho_measured_prop = rho_measured(prop_indices);
rho_measured_evan = rho_measured(evan_indices);
[p_prop, S] = polyfit(depth_prop, rho_measured_prop, 1);
a = p_prop(1)
b = p_prop(2)
[p_evan, S] = polyfit(depth_evan, rho_measured_evan, 1);
c = p_evan(1)
d = p_evan(2)
z_measured_evan = z_fit(z_fit >= switch_height);
z_measured_prop = z_fit(z_fit < switch_height);
rho_plot_prop = polyval(p_prop, z_measured_prop);
rho_plot_evan = polyval(p_evan, z_measured_evan);
rho_plot = [rho_plot_prop rho_plot_evan];
N_evan_extrap = zeros(1, length(z_measured_evan))+(sqrt(-g/rho_o*c));
N_prop_extrap = zeros(1, length(z_measured_prop))+(sqrt(-g/rho_o*a));
N_fit = [N_evan_extrap N_prop_extrap];
D = H_water-switch_height-H;
N_evan = N_fit(N_fit<omega);
Fr1 = omega/mean(N_evan)
D_H = D/H
Fr1D_H = Fr1*D_H

```

```

end

%%
figure (1); clf;

figure1 = figure(6);clf; hold on;
plot(z_fit ,N_fit)
plot(depth(1:end-1),N_measured)
xlabel('Depth (m)')
ylabel('N')
title ('Natural Frequency in Experimental Tank')
legend('N_Fit','N_from measurements')
hold off

```

B.1.3 MATLAB setup from Digiflow DATs

```
%% Creating Time Series Example
```

```

%% Creating Time Series
% Allison Lee, 3-21-18
% This file creates two sets of mat files. The first contains all of the
% information needed on a test such as omega and the density profile info.
% The second file creates just the timeseries with the sets of rows ready
% to be Fourier Transformed.
clear
%% %%%%%%%%%%%%%%%%%%%%%%%%%%%%%%%%%%%%%%%%%%%%%%%%%%%%%%%%%%%%%%%%%%%%%%%%%%% Variables that change with every test
%% %%%%%%%%%%%%%%%%%%%%%%%%%%%%%%%%%%%%%%%%%%%%%%%%%%%%%%%%%%%%%%%%%%%%%%%%%%%
%% Input values— These must all be checked for each test

% Date and test letter (format: 3_21_18_a)
timeseries_info.date = '3_6_19_a';

% location where program finds the ygradient files on the supercomputer
location = strcat('ygrads_to_be_run_piv/ygrad_dat_',timeseries_info.date, '/');

% location where the timeseries files will be saved
mat_fil_name = strcat('completed_timeseries_piv/timeseries_y_',timeseries_info
    .date, '.mat');

timeseries_info.end_time = 1079; % max end_time = 1079;
timeseries_info.dx = (.371+.137)/1360; % m/pixel from digiflow
timeseries_info.dz = (.351+.026)/1030; % m/pixel from digiflow
timeseries_info.omega = 0.77; % rads/sec
timeseries_info.num_rows = 1030; % number of rows to be analyzed
timeseries_info.ztd = 0.524; % Location of the turning depth (m)

timeseries_info.z_total_height = .663; % total water height (m) (density stick
)

% start and end heights of the camera image
timeseries_info.z_end = .552;

```

```

timeseries_info.z_start =timeseries_info.z_end-timeseries_info.dz*1029 ;
timeseries_info.fps = 6;    % analyzed frames per second

% Type of topography
timeseries_info.top = 'Steep'; % Options are 'Medium' 'Steep' 'Complex' 'Sine'
timeseries_info.L= .045*2; % distance topography moves during an ENTIRE period
    (left+right)
timeseries_info.u_top = timeseries_info.L/(2*pi/timeseries_info.omega);

timeseries_info.k_wave = 2*pi/(timeseries_info.L/2+.0495); % Steep ,
    calculated wavenumber (depends upon the shape of the topography)
% timeseries_info.k_wave = 2*pi/(timeseries_info.L/2+.2); % Medium,
    calculated wavenumber (depends upon the shape of the topography)
% timeseries_info.k_wave = 2*pi/(timeseries_info.L/2+.235); % Complex,
    calculated wavenumber (depends upon the shape of the topography)
% timeseries_info.k_wave = 2*pi/(.11); % .11? Sinusoidal,  calculated
    wavenumber (depends upon the shape of the topography)
% Calculated variables
g = 9.81;
rho_o = 1000;
timeseries_info.z = timeseries_info.z_start:timeseries_info.dz:timeseries_info
    .z_end;

%% Finding N
% Use the following if statements to create the correct N and dN2/dz
% profile

% Choose one of the following profile options , then adjust the a,b,c and/or
% d values in the appropriate section of the if statement
% profile = 1 ; % Two Layer
% profile = 2; % "Exponential";
% profile = 3; % Parabolic
profile = 4; % Quadratic
% profile = 5; % One Layer

timeseries_info.profile_type = profile;

if profile == 1
    % for 2 Layer N
    % Two layer profile
    timeseries_info.a = -151.96;    % Evanescent Region
    timeseries_info.b = 1115.4;    % Evanescent Region
    timeseries_info.c = -20;    % Propagating region
    timeseries_info.d = 1055.6;    % Propagating region

    for ii = 1:length(timeseries_info.z)
        if timeseries_info.z(ii)<timeseries_info.ztd
            % Prop region
            timeseries_info.N(ii) = sqrt(-g/rho_o*timeseries_info.c);
            timeseries_info.dN2_dz(ii) = 0;
        else
            % Evan region
            timeseries_info.N(ii) = sqrt(-g/rho_o*timeseries_info.a);
            timeseries_info.dN2_dz(ii) = 0;
        end
    end
end

```

```

        end
    end
elseif profile == 2
    % rho = a*exp(b*z)+c (b is negative)
    timeseries_info.a = 131.3778;
    timeseries_info.b = -1.5628;
    timeseries_info.c = 980.4197;
    timeseries_info.N = sqrt(-g/rho_o*(timeseries_info.a*timeseries_info.b*exp
        (timeseries_info.b*timeseries_info.z)));
    timeseries_info.dN2_dz = -g/rho_o*timeseries_info.a*timeseries_info.b^2*
        exp(timeseries_info.b*timeseries_info.z);

elseif profile == 3
    % rho = az^3 + bz^2 + cz + d
    timeseries_info.a = 150.8931;
    timeseries_info.b = -29.0792;
    timeseries_info.c = -183.2962;
    timeseries_info.d = 1120.5;
    timeseries_info.N = sqrt(-g/rho_o*(3*timeseries_info.a*timeseries_info.z
        .^2+2*timeseries_info.b*timeseries_info.z+timeseries_info.c));
    timeseries_info.dN2_dz = -g/rho_o*(6*timeseries_info.a*timeseries_info.z
        +2*timeseries_info.b);
elseif profile == 4
    % rho = az^2 + bz + c
    timeseries_info.a = 144.9787;
    timeseries_info.b = -212.6409;
    timeseries_info.c = 1097.5;
    timeseries_info.N = sqrt(-g/rho_o*(2*timeseries_info.a*timeseries_info.z+
        timeseries_info.b));
    timeseries_info.dN2_dz = zeros(1,length(timeseries_info.z))+(-g/rho_o*(2*
        timeseries_info.a));
elseif profile == 5
    % rho = az+b;
    timeseries_info.a = -140.82;
    timeseries_info.b = 1092.7;
    timeseries_info.N = sqrt(-g/rho_o*timeseries_info.a)+zeros(length(
        timeseries_info.z));
    timeseries_info.dN2_dz = zeros(length(timeseries_info.z));
end
%%% %%%%%%%%%%%%%%%%%%%%%%%%%%%%%%%%%%%%%%%%%%%%%%%%%%%%%%%%%%%%%%%%%%%%%%%%%%% Values that (generally) don't need to be changed
%%% %%%%%%%%%%%%%%%%%%%%%%%%%%%%%%%%%%%%%%%%%%%%%%%%%%%%%%%%%%%%%%%%%%%%%%%%%%%
% Sometimes an extra zero gets added or removed from y_gradient0000000.dat.
% Sometimes the number of rows, columns, or times might change (rarely)
%%% Read in full time series
myCluster = parcluster('local');
tic

time_steps = zeros(1030,1360,1080);
filename = 'y_gradient00000000.dat';
full_filename = strcat(location,filename);
time_steps(:,:,1) = import_full_data_set(full_filename);
toc
tic
parfor i = 1:timeseries_info.end_time

```

```

if i<10
    formatspec = 'y_gradient0000000%.dat';
    filename = sprintf(formatspec,i);
elseif i<100
    formatspec = 'y_gradient000000%.dat';
    filename = sprintf(formatspec,i);
elseif i<1000
    formatspec = 'y_gradient00000%.dat';
    filename = sprintf(formatspec,i);
else
    formatspec = 'y_gradient0000%.dat';
    filename = sprintf(formatspec,i);
end

full_filename = strcat(location,filename)
time_steps(:,:,i+1) = import_full_data_set(full_filename);
end
toc

tic
for i = 1:1030
    formatspec = 'row_%.d';
    series = sprintf(formatspec,i-1);
    full_matrix = time_steps(i, :, :);
    timeseries.(series) = squeeze(full_matrix).';
end

save(mat_fil_name, '-struct', 'timeseries')
mat_file_name_info = strcat('completed_timeseries_piv/timeseries_info_y_',
    timeseries_info.date, '.mat');
save(mat_file_name_info, '-struct', 'timeseries_info')
toc
delete(myCluster.Jobs)
clear
exit

function [time_step] = import_full_data_set(filename)%, startRow, endRow)
%IMPORTFILE Import numeric data from a text file as column vectors.
% [VARNAME1,VARNAME2,VARNAME3] = IMPORTFILE(FILENAME) Reads data from
% text file FILENAME for the default selection.
%
% [VARNAME1,VARNAME2,VARNAME3] = IMPORTFILE(FILENAME, STARTROW, ENDROW)
% Reads data from rows STARTROW through ENDROW of text file FILENAME.
%
% Example:
% [VarName1, VarName2, VarName3] = importfile('Sequence00000000.dat', 2,
% 1400801);
%
% See also TEXTSCAN.

% Auto-generated by MATLAB on 2016/05/24 17:47:17

%% Initialize variables.

```

```

if nargin <= 2
    startRow = 2;
    endRow = 1400801;
end

%% Format string for each line of text:
%   column1: double (%f)
%       column2: double (%f)
%   column3: double (%f)
% For more information, see the TEXTSCAN documentation.
formatSpec = '%5f%5f%5f%[^\\n\\r]';

%% Open the text file.
fileID = fopen(filename, 'r');

%% Read columns of data according to format string.
% This call is based on the structure of the file used to generate this
% code. If an error occurs for a different file, try regenerating the code
% from the Import Tool.
% tic
dataArray = textscan(fileID, formatSpec, endRow(1)-startRow(1)+1, 'Delimiter',
    ',', 'WhiteSpace', '', 'HeaderLines', startRow(1)-1, 'ReturnOnError',
    false);
for block=2:length(startRow)
    frewind(fileID);
    dataArrayBlock = textscan(fileID, formatSpec, endRow(block)-startRow(block)
        )+1, 'Delimiter', ',', 'WhiteSpace', '', 'HeaderLines', startRow(block)
        -1, 'ReturnOnError', false);
    for col=1:length(dataArray)
        dataArray{col} = [dataArray{col}; dataArrayBlock{col}];
    end
end

%% Close the text file.
fclose(fileID);

%% Post processing for unimportable data.
% No unimportable data rules were applied during the import, so no post
% processing code is included. To generate code which works for
% unimportable data, select unimportable cells in a file and regenerate the
% script.

%% Allocate imported array to column variable names
% x_pix = dataArray{:, 1};
% y_pix = dataArray{:, 2};
data = dataArray{:, 3};
%% Allocate imported array to column variable names
% x_total = x_pix(1);
% y_total = y_pix(1);
% x_pix(1) = [];
% y_pix(1) = [];
% data(1) = [];
time_step = zeros(1030,1360);
% tic

```



```

% for i = 1:length(data)
% %     timestep(i,i) = data(i);
%     time_step(y_pix(i)+1,x_pix(i)+1) = data(i);
% end

for i = 1:1030;
    a = (i-1)*1360+1;
    b = a+1359;
    time_step(i,:) = data(a:b);
end
% toc
end

```

B.1.4 Supercomputer MATLAB file to calculate kinetic energy

```

%% Supercomputer Calculating Experimental Energy
% This file does the initial setup and then sends data to a function
% entitled "Experimental_Energy_AL_10_26_18. That file calculates KE at a
% row and sends it back here.

% length_exp = 42; %number of experiments

%Choose topography type
topo = 1; mm = 42; %Medium 42
%topo = 2; mm = 36; %Steep 36
%topo = 3; mm = 30; %Complex 30
%topo = 4; mm = 42;% Sinusoidal 42

% kk=1;
myCluster = parcluster('local');
parfor kk = 1:5:mm

    fprintf(num2str((kk)))
    fprintf(',')
    %     if jj == 1
    %         name = '5_15_18_a';
    %     elseif jj == 2
    %         name = '5_15_18_b';
    %     end
    [test_dates ,~]= paper_3_tests_2_4_19(topo ,(kk));
    % test_dates = '5_8_18_a.mat';
    test_date = test_dates; %Replace with test_dates and comment out for loop to
        run specific tests

%% Read in timeseries data
location_data = 'completed_timeseries_piv/';
location_info = 'completed_timeseries_piv/';
name_data = strcat('timeseries_y_',test_date)
name_info = strcat('timeseries_info_y_',test_date)

mat_fil_name = strcat('Exp_Energy_no_z_filter/Energy_',name_info);
energy_calc(location_data ,location_info ,name_data ,name_info ,mat_fil_name)
end

```

```

delete(myCluster.Jobs)
clear
exit

function [] = energy_calc(location_data ,location_info ,name_data ,name_info ,
    mat_fil_name)

info_data = load(strcat(location_info ,name_info));
% The info data file needs to have other information in it including:
% N, dN^2/dz, k_wave, omega, z, number of rows,
% raw_data = load(name_data);

%% Setup basic parameters
N = info_data.N;
dN2_dz = info_data.dN2_dz;
omega = info_data.omega;
k_wave = info_data.k_wave;
z = info_data.z;
num_rows = info_data.num_rows;
rows = 0:num_rows-1;
Peak_Energy = zeros(length(z),2);
dx = info_data.dx;
fps = info_data.fps;
raw_data = load(strcat(location_data ,name_data));

%% Run experiment energy
for ii = 1:length(z)

    formatspec = 'row_%d';
    series = sprintf(formatspec ,rows(ii));
    data = raw_data.(series);
    if N(ii)<omega
        evan(ii) = 1;
        [ tmp_energy ] = Experimental_Energy_AL_10_26_18( data ,N(ii) ,dN2_dz(ii)
            ) ,dx ,fps ,evan(ii) ,k_wave ,omega) ;
        Peak_Energy(ii ,1) = tmp_energy;
        Peak_Energy(ii ,2) = z(ii);
    else
        evan(ii) = 0;
        [ tmp_energy ] = Experimental_Energy_AL_10_26_18( data ,N(ii) ,dN2_dz(ii)
            ) ,dx ,fps ,evan(ii) ,k_wave ,omega);
        Peak_Energy(ii ,1) = tmp_energy;
        Peak_Energy(ii ,2) = z(ii);
    end
end

%% Save Data
info_data .KE_exp = Peak_Energy(:,1).';
info_data .z_exp = Peak_Energy(:,2).';
save(mat_fil_name ,'-struct' , 'info_data')
clear raw_data
end

```

```

function [ Peak_Energy , Energy_range ] =
    Experimental_Energy_full_range_AL_9_16_19( data ,N,dN2_dz ,dx ,fps ,evan ,
        k_wave ,omega )
%Experimental_Energy_AL_10_26_17
% This function sends the data to either the propagating or evanescent
% function nested in this file
g = 9.81;

% Synthetic Schlieren comes in the form (1/_rho_o)*drho/dz. Need to
% multiply by gravity to have N^2 values

data_N2 = data*-g;

% Take the 2D Fourier Transform
[ frq ,k ,amp] = IW_FFT2(data_N2 ,fps ,dx);

if evan==1
    [ E_sum , E_range ] = IW_Evan_Energy(frq , k , N ,dN2_dz ,amp ,omega ,k_wave);
else
    [ E_sum , E_range ] = IW_Prop_Energy( frq , k , N ,dN2_dz ,amp ,omega ,k_wave);
end

Peak_Energy = E_sum;
Energy_range = E_range;
% figure;
% contour(k,frq ,amp); xlim([0 150]); ylim([0 3])
% title('\Delta N^2 amplitude')
% figure
% contour(k,frq ,Energy_range); xlim([0 150]); ylim([0 3])
% title('Energy')

end

function [ frq ,k ,amp] = IW_FFT2(data_N2 ,fps ,dx)
% Purpose: perform an FFT of a real-valued input signal , and generate the
% single-sided output , in amplitude and phase , scaled to the same units as
%the input. Edits: AL (5/4/2016) allowing for an FFT2 looking both at
%frequency and wavenumber

% Assume that fps is literally frames/second
ScanRate = fps*2*pi;

% Assume dx is meters/pixel , needs to be transformed to rads/meter)
x_res = 1/(dx/(2*pi));

% Find the size of the data set. n corresponds to time and number of frames
% while m corresponds to number of horizontal points (pixels)
[n,m] = size(data_N2);
%generate the vector of frequencies
halfn = round(n / 2);
deltaf = 1 / ( n / ScanRate);
frq = (0:(halfn-1)) * deltax;

```

```

halfm = floor(m/2);
deltak = 1 / ( m / x_res);
k = (0:(halfm-1))*deltak;

% Perform the FFT2
fft2_t_x = abs(fft2(data_N2)/(m*n));
fft2_t_x(2:length(freq),2:length(k)) = fft2_t_x(2:length(freq),2:length(k))*2;
amp = fft2_t_x(1:length(freq),1:length(k));
end

function [E_sum, E_range] = IW_Evan_Energy(freq, k, N,dN2_dz,amp,omega,k_wave)
% This function calculates energy of a line in an evanescent region

time_size = length(freq);
x_size = length(k);
Evan_E2 = zeros(time_size, x_size);
q = -sqrt((k.^2)'*(1-N^2./freq.^2))';
for ii = 1:time_size
%Evan_E2(ii,:) = (abs(-(1-N^2./freq(ii)^2)^.5*freq(ii)*amp(ii,:)/(dN2_dz-k(1,:))
    *(1-N^2./freq(ii)^2)^.5*N^2)).^2+(abs(1i*freq(ii)*amp(ii,:)/(dN2_dz-k(1,:))
    *(1-N^2./freq(ii)^2)^.5*N^2)).^2;
Evan_E2(ii,:) = (abs(-q(ii,:).*freq(ii).*amp(ii,:)/(k(1,:).(dN2_dz+q(ii,:).*N
    ^2))).^2+(abs(1i*freq(ii)*amp(ii,:)/(dN2_dz+q(ii,:).*N^2))).^2;

end

% We only want the energy near the peak of k_wave and omega
[~,index_k] = min(abs(k-k_wave));
[~,index_omega] = min(abs(freq-omega));
E_select = Evan_E2(index_omega-1:index_omega+1,index_k:index_k+1);
% Sum the energy near the peak
E_sum = sum(sum(E_select));
E_range = Evan_E2(index_omega-1:index_omega+1,:);
end

function [E_sum, E_range ] = IW_Prop_Energy( freq, k, N,dN2_dz,amp,omega,k_wave
)

time_size = length(freq);
x_size = length(k);
E = zeros(time_size, x_size);
for ii = 1:length(freq)
    E(ii,:) = (freq(ii).^2*N.^2)/(k(1,:).^2*abs(N.^2-freq(ii).^2)+(freq(ii)*
        dN2_dz./N.^2).^2).*(abs(amp(ii,:)/N^2)).^2;
end

% We only want the energy near the peak of k_wave and omega
[~,index_k] = min(abs(k-k_wave));
index_omega = find(freq<omega);
index_omega_end = index_omega(end);
E_select = E(index_omega_end-1:index_omega_end+1,index_k-1:index_k+1);

% Sum the energy near the peak
E_sum = sum(sum(E_select));

```

```
E_range = E(index_omega_end-1:index_omega_end+1,:);
end
```

B.1.5 PIV calculations

```
%% Creating time series PIV
% Annie Wesolek
% 10/31/18

clear
%% %%%%%%%%%%%%%%%%%%%%%%%%%%%%%%%%%%%%%%%%%%%%%%%%%%%%%%%%%%%%%%%%%%%%%%%%%% Variables that change with every test
%% %%%%%%%%%%%%%%%%%%%%%%%%%%%%%%%%%%%%%%%%%%%%%%%%%%%%%%%%%%%%%%%%%%%%%%%%%%
%% Specific setup for 9-27-18-Test_b

% File location of dat files
location = 'I:\Allison_Research\PIV\9-27-18-Test_b\';
% File location to save the files
mat_fil_name = strcat(location, 'timeseries_PIV_9_27_18_test_b.mat');

%Test Specific information needed to analyze energy
timeseries_info.omega = 1.410;
timeseries_info.f = 4.5; % Frequency
timeseries_info.dt = .09; % Time between pairs of images
timeseries_info.num_images = 1000; % Total number of images

% Type of topography
timeseries_info.top = 'Medium'; % Options are 'Medium' 'Steep' 'Complex' 'Sine
,
timeseries_info.L= .048*2; % distance topography moves during an ENTIRE period
(left+right)
timeseries_info.u_top = timeseries_info.L/(2*pi/timeseries_info.omega);

% timeseries_info.k_wave = 2*pi/(timeseries_info.L/2+.0495); % Steep,
calculated wavenumber (depends upon the shape of the topography)
timeseries_info.k_wave = 2*pi/(timeseries_info.L/2+.2); % Medium, calculated
wavenumber (depends upon the shape of the topography)
% timeseries_info.k_wave = 2*pi/(timeseries_info.L/2+.235); % Complex,
calculated wavenumber (depends upon the shape of the topography)
% timeseries_info.k_wave = 2*pi/(.11); % Sinusoidal, calculated wavenumber (
depends upon the shape of the topography)

% Calculated variables
g = 9.81;
rho_o = 1000;

% Use the correlation picture to match the SS data locations to the PIV
% pictures
%SS location in Real World coordinates
timeseries_info.dx_SS = (.361 +.239)/1359; % m/pixel from digiflow
timeseries_info.dz_SS = (.442+.022)/1029; % m/pixel from digiflow
timeseries_info.x_left_SS = 0;
```

```

timeseries_info.x_right_SS = timeseries_info.x_left_SS + timeseries_info.dx_SS
    *1359;
timeseries_info.z_end_SS = .5 + 170*timeseries_info.dz_SS +(0.695-0.660); %Top
    of camera height +(Density-withstick)
timeseries_info.z_start_SS =timeseries_info.z_end_SS-timeseries_info.dz_SS
    *1029;%bottom of camera
timeseries_info.z_SS = timeseries_info.z_start_SS:timeseries_info.dz_SS:
    timeseries_info.z_end_SS; %real world locations of SS
timeseries_info.x_SS = timeseries_info.x_left_SS:timeseries_info.dx_SS:
    timeseries_info.x_right_SS; %real world locations of SS

%PIV locations in Real World coordinates
timeseries_info.dx_PIV = (0.0613+0.17699)/(344-1);
timeseries_info.dz_PIV = (0.01667+0.16049)/(256-1);
timeseries_info.j_end_PIV = 712; %SS location of top of PIV camera
timeseries_info.j_start_PIV = 351; %SS location of bottom of PIV camera
timeseries_info.i_left_PIV = 513 - (0.0616621 + 0.000694)/timeseries_info.dx_SS;
    %SS location of left of PIV camera
timeseries_info.i_right_PIV = 513 +(0.176996 - 0.000694)/timeseries_info.dx_SS;
    %SS location of right of PIV camera

%real world locations of start and finish based on SS conversion
timeseries_info.z_start_PIV = timeseries_info.z_start_SS + timeseries_info.
    dz_SS*timeseries_info.j_start_PIV ;
timeseries_info.z_end_PIV = timeseries_info.z_start_PIV + timeseries_info.
    dz_PIV*255;
timeseries_info.x_left_PIV = timeseries_info.x_left_SS + timeseries_info.dx_SS
    *timeseries_info.i_left_PIV ;
timeseries_info.x_right_PIV = timeseries_info.x_left_PIV + timeseries_info.
    dx_PIV*343;
%real world coordinates
timeseries_info.x_PIV = timeseries_info.x_left_PIV:timeseries_info.dx_PIV:
    timeseries_info.x_right_PIV ;
timeseries_info.z_PIV = timeseries_info.z_start_PIV:timeseries_info.dz_PIV:
    timeseries_info.z_end_PIV ;

% The location of the turning depth
timeseries_info.ztd = .3;
%% Finding N
% Use the following if statements to create the correct N and dN2/dz
% profile

% Choose one of the following profile options , then adjust the a,b,c and/or
% d values in the appropriate section of the if statement
% profile = 1; % Two Layer
% profile = 2; % Exponential
% profile = 3; % Parabolic
% profile = 4; % Quadratic
profile = 5; % One Layer

timeseries_info.profile_type = profile;

```

```

if profile == 1
    % for 2 Layer N
    % Two layer profile
    timeseries_info.a = 113.7929;    % Evanescent Region
    timeseries_info.b = -2.4107;    % Evanescent Region
    timeseries_info.c = 1.0025E3;    % Propagating region
    timeseries_info.d = 0;          % Propagating region

    for ii = 1:length(timeseries_info.z_PIV)
        if timeseries_info.z_PIV(ii)<timeseries_info.ztd
            % Prop region
            timeseries_info.N(ii) = sqrt(-g/rho_o*timeseries_info.c);
            timeseries_info.dN2_dz(ii) = 0;
        else
            % Evan region
            timeseries_info.N(ii) = sqrt(-g/rho_o*timeseries_info.a);
            timeseries_info.dN2_dz(ii) = 0;
        end
    end
end
elseif profile == 2
    % rho = a*exp(b*z)+c (b is negative)
    timeseries_info.a = 113.7747;
    timeseries_info.b = -2.3823;
    timeseries_info.c = 1.0046E3;
    timeseries_info.N = sqrt(-g/rho_o*(timeseries_info.a*timeseries_info.b*exp(
        timeseries_info.b*timeseries_info.z_PIV)));
    timeseries_info.dN2_dz = -g/rho_o*timeseries_info.a*timeseries_info.b^2*
        exp(timeseries_info.b*timeseries_info.z_PIV);

elseif profile == 3
    % rho = az^3 + bz^2 + cz + d
    timeseries_info.a = 277.4272;
    timeseries_info.b = -331.0401;
    timeseries_info.c = 1.1244E3;
    timeseries_info.d = 0;
    timeseries_info.N = sqrt(-g/rho_o*(3*timeseries_info.a*timeseries_info.z_PIV.^2+2*timeseries_info.b*timeseries_info.z_PIV+timeseries_info.c))
        ;
    timeseries_info.dN2_dz = -g/rho_o*(6*timeseries_info.a*timeseries_info.z_PIV+2*timeseries_info.b);

elseif profile == 4
    % rho = az^2 + bz + c
    timeseries_info.a = 115.0451;
    timeseries_info.b = -229.5245;
    timeseries_info.c = 1129.3;
    timeseries_info.N = sqrt(-g/rho_o*(2*timeseries_info.a*timeseries_info.z_PIV+timeseries_info.b));
    timeseries_info.dN2_dz = zeros(1,length(timeseries_info.z_PIV))+(-g/rho_o*(2*timeseries_info.a));

elseif profile == 5
    % rho = az+b;
    timeseries_info.a = -145.5148;
    timeseries_info.b = 1.1174E3;

```

```

timeseries_info.N = sqrt(-g/rho_o*timeseries_info.a)+zeros(length(
    timeseries_info.z_PIV));
timeseries_info.dN2_dz = zeros(length(timeseries_info.z_PIV));
end
%%% Values that (generally) don't need to be changed
%%%
% Sometimes an extra zero gets added or removed from y_gradient0000000.dat.
% Sometimes the number of rows, columns, or times might change
%%% Read in large time file
end_time = timeseries_info.num_images;

tic
for i = 1:end_time
    if i<10
        formatspec = 'B0000%d.dat';
        filename = sprintf(formatspec,i);
    elseif i<100
        formatspec = 'B000%d.dat';
        filename = sprintf(formatspec,i);
    elseif i<1000
        formatspec = 'B00%d.dat';
        filename = sprintf(formatspec,i);
    end
    full_filename = strcat(location,filename);
    [x_values,z_values,Vx_matrix,Vz_matrix] = importfile_PIV_process(
        full_filename);
    x(:,i) = x_values;
    z(:,i) = z_values;
    Vx(:, :, i) = Vx_matrix;
    Vz(:, :, i) = Vz_matrix;
end
toc

tic
for i = 1:length(z(:,1))
    formatspec1 = 'Vx_row-%d';
    formatspec2 = 'Vz_row-%d';
    series1 = sprintf(formatspec1,i);
    series2 = sprintf(formatspec2,i);
    full_matrix1 = Vx(i, :, :);
    full_matrix2 = Vz(i, :, :);
    timeseries_info.(series1) = squeeze(full_matrix1).';
    timeseries_info.(series2) = squeeze(full_matrix2).';
end

timeseries_info.z = z(:,1)/1000;
timeseries_info.x = x(:,1)/1000;
timeseries_info.dx = abs(timeseries_info.x(end)-timeseries_info.x(1))/length(
    timeseries_info.x);
timeseries_info.dz = abs(timeseries_info.z(end)-timeseries_info.z(1))/length(
    timeseries_info.z);
timeseries_info.num_rows = length(z(:,1));
save(mat_fil_name, '-struct', 'timeseries_info')
toc

```



```

function [x_values , y_values , Vx_matrix , Vy_matrix] = importfile_PIV_process (
    filename)
%%IMPORTFILE2 Import numeric data from a text file as column vectors.
%   [VARIABLES,VARNAME2,POSITION,VARNAME4] = IMPORTFILE2(FILENAME) Reads
%   data from text file FILENAME for the default selection.
%
%   [VARIABLES,VARNAME2,POSITION,VARNAME4] = IMPORTFILE2(FILENAME,
%   STARTROW, ENDROW) Reads data from rows STARTROW through ENDROW of text
%   file FILENAME.
%
% Example:
%   [VARIABLES,VarName2,position,VarName4] = importfile2('B00011.dat',4, 1379)
%   ;
%   See also TEXTSCAN.

% Auto-generated by MATLAB on 2017/06/27 16:36:26

%% Initialize variables.
delimiter = {' ','\n'};
if nargin <= 2
    startRow = 4;
    endRow = inf;
end

%% Format string for each line of text:
%   column1: double (%f)
%   column2: double (%f)
%   column3: double (%f)
%   column4: double (%f)
% For more information, see the TEXTSCAN documentation.
formatSpec = '%f%f%f%f%*s%*s%*s%*s%*s%[^\\n\\r]';

%% Open the text file.
fileID = fopen(filename, 'r');

%% Read columns of data according to format string.
% This call is based on the structure of the file used to generate this
% code. If an error occurs for a different file, try regenerating the code
% from the Import Tool.
dataArray = textscan(fileID, formatSpec, endRow(1)-startRow(1)+1, 'Delimiter',
    delimiter, 'HeaderLines', startRow(1)-1, 'ReturnOnError', false);
for block=2:length(startRow)
    frewind(fileID);
    dataArrayBlock = textscan(fileID, formatSpec, endRow(block)-startRow(block)
        )+1, 'Delimiter', delimiter, 'HeaderLines', startRow(block)-1, '
        ReturnOnError', false);
    for col=1:length(dataArray)
        dataArray{col} = [dataArray{col}; dataArrayBlock{col}];
    end
end

%% Close the text file.
fclose(fileID);

```

```

%% Post processing for unimportable data.
% No unimportable data rules were applied during the import, so no post
% processing code is included. To generate code which works for
% unimportable data, select unimportable cells in a file and regenerate the
% script.

%% Allocate imported array to column variable names
x_pos = dataArray{:, 1};
y_pos = dataArray{:, 2};
Vx = dataArray{:, 3};
Vy = dataArray{:, 4};

tmp = y_pos(1)-y_pos;
value = 0;
ctr = 0;
while value == 0
    [value, index_loc] = min(tmp);
    tmp(1) = [];
    ctr = 1 +ctr;
end
% Create x and y vectors in length units
length_y = length(x_pos)/(ctr-1);
y_values = y_pos(1:(ctr-1):end);
x_values = x_pos(1:ctr-1);

% Create the Velocity matrices
Vx_matrix = zeros(length_y, ctr-1);
Vy_matrix = Vx_matrix;

for ii = 1:length_y
%     Vx_matrix(ii, :) = Vx((ii*(ctr-1)+1):(ii+1)*ctr-1);
    Vx_matrix(ii, :) = Vx(1:ctr-1);
    Vy_matrix(ii, :) = Vy(1:ctr-1);
    Vx(1:ctr-1) = [];
    Vy(1:ctr-1) = [];
end

clear;
% data_PIV = load('J:\groups\intwaves3\PIV matlab files\PIV Energy\timeseries\
    timeseries_PIV_12_6_18_test_d.mat');
data_PIV = load('J:\groups\intwaves3\PIV_Paper\timeseries\
    timeseries_PIV_8_14_18_test_c.mat');

x = data_PIV.x_PIV;
z = sort(data_PIV.z_PIV, 'descend');
tic
for ii = 1:1:data_PIV.num_rows
    name_x = sprintf('Vx_row-%d', ii);
    Vx = data_PIV.(name_x);
%     [frq, k, signal, vx_amp] = filtered_fft_PIV(Vx, data_PIV.f, 1/data_PIV.
    dx_PIV, omega, k_wave);
%     filtered_signal_x(ii, :, :) = signal.';

```

```

    Vx_raw(ii ,: ,:) = Vx.';
%     Vx_amp(ii ,:) = vx_amp;

    name_z = sprintf('Vz_row_%d',ii);
    Vz = data_PIV.(name_z);
%     [frq , k , signal_z , vz_amp] = filtered_fft_PIV( Vz , data_PIV.f , 1/
data_PIV.dz_PIV , omega , k_wave );
    Vz_raw(ii ,: ,:) = Vz.';
%     filtered_signal_z(ii ,: ,:) = signal_z.';
%     Vz_amp(ii ,:) = vz_amp;

end

Energy_PIV.x = data_PIV.x_PIV;
Energy_PIV.z = data_PIV.z_PIV;
Energy_PIV.Vz_amp = Vz_amp;
Energy_PIV.Vx_amp = Vx_amp;
Energy_PIV.KE_amp = Vx_amp.^2+Vz_amp.^2;
save('J:\groups\intwaves2\Energy-timeseries.info_PIV_12_6_18_d.mat' , '-struct' ,
'Energy_PIV');

% function [frq , amp , phase] = simpleFFT2( signal , ScanRate , x_res )
% Purpose: perform an FFT of a real-valued input signal , and generate the
%         single-sided
% output , in amplitude and phase , scaled to the same units as the input.
% Edits: AL (5/4/2016) allowing for an FFT2 looking both at frequency and
% wavenumber

%inputs:
%   signal: the signal to transform
%   ScanRate: the sampling frequency (in Hertz)
%   x_res (cycles/length) wavenumber version of Hertz

% outputs:
%   frq: a vector of frequency points (in Hertz)
%   amp: a vector of amplitudes (same units as the input signal)
%   phase: a vector of phases (in radians)

function [frq , k , signal_clean , Velocity_Peak] = filtered_fft_PIV( signal ,
    ScanRate , x_res , omega , k_wave )

ScanRate = ScanRate*2*pi;
x_res = x_res*(2*pi); % use this one for PIV

fft_signal = fft2(signal);
[n,m] = size(fft_signal);

%generate the vector of frequencies
halfn = round(n / 2);
deltaf = 1 / ( n / ScanRate);
frq = (0:(halfn-1)) * deltax;
halfm = floor(m/2);
deltak = 1 / ( m / x_res);

```

```

k = (0:(halfm-1))*deltak;
[~,f_index] = min(abs(omega-frq));
[~,k_index] = min(abs(k_wave-k));
amp_no_filter= abs(fft_signal/(n*m));
amp_full = abs(amp_no_filter);

%% Create Filtered signal (for imaging)
filter = fft_signal;
filter(1:f_index-5,:) = 0;
filter(f_index+5:n-f_index-5,:) = 0;
filter(n-f_index-5:end,:) = 0;

filter(:,1:k_index-2) = 0;
filter(:,k_index+2:m-k_index-2) = 0;
filter(:,m-k_index-2:end) = 0;
signal_ifft= ifft(fft(filter)).';
signal_clean = real(signal_ifft);
%% Find peak velocity
amp(1,:) = amp_full(1,1:halfm);
amp(2:halfn,2:halfm) = 2*amp_full(2:halfn,2:halfm);

Velocity_Peak = sum(sum(amp(f_index-1:f_index+1,k_index-1:k_index+1)));

% making spectrum figure
% figure;
% contour(k, frq , abs(amp(1: halfn ,1: halfm)));
% xlim([0 100]); ylim([0 3]);
% colorbar
% xlabel('k (m-1)'); ylabel('Frequency (s-1)');
end

% clear

SS_location = 'J:\groups\intwaves3\PIV_Paper\SS_KE\KE_wrange\
Energy_timeseries_info_y_';
PIV_location = 'J:\groups\intwaves3\PIV_Paper\PIV_KE\Energy_PIV_range_of_k\
Energy_timeseries_info_PIV_';
Total_energy_save_location = 'J:\groups\intwaves3\PIV_Paper\Combined_KE\
KE_range_k\total_energy_';
addpath('J:\groups\intwaves3\PIV_Paper')
tic
for ii = 18:18%1:19
    if ii ==1 %9-19-18-a          9-19-18-b
        num_SS = 1;
        num_PIV = 1;
        test_date_PIV{1} = paper_3_tests_PIV_4_9_19(4,23);
        test_date_SS{1} = paper_3_tests_SS_4_9_19(1,18);

    elseif ii ==2 %9-20-18-a      9-20-18-b
        num_SS = 1;
        num_PIV = 1;

```

```

test_date_PIV{1} = paper_3_tests_PIV_4_9_19(4,24);
test_date_SS{1} = paper_3_tests_SS_4_9_19(1,19);

elseif ii ==3 %9-25-18-a    9-25-18-b
num_SS = 1;
num_PIV = 1;
test_date_PIV{1} = paper_3_tests_PIV_4_9_19(4,25);
test_date_SS{1} = paper_3_tests_SS_4_9_19(1,20);

elseif ii ==4 %9-27-18-a    9-27-18-b
num_SS = 1;
num_PIV = 1;
test_date_PIV{1} = paper_3_tests_PIV_4_9_19(4,26);
test_date_SS{1} = paper_3_tests_SS_4_9_19(1,21);

elseif ii ==5 %9-12-18-a    9-12-18-b
num_SS = 1;
num_PIV = 1;
test_date_PIV{1} = paper_3_tests_PIV_4_9_19(4,21);
test_date_SS{1} = paper_3_tests_SS_4_9_19(1,16);

elseif ii ==6 %9-13-18-a    9-13-18-b
num_SS = 1;
num_PIV = 1;
test_date_PIV{1} = paper_3_tests_PIV_4_9_19(4,22);
test_date_SS{1} = paper_3_tests_SS_4_9_19(1,17);

elseif ii ==7 %10-16-18-a    10-16-18-c
num_SS = 1;
num_PIV = 1;
test_date_PIV{1} = paper_3_tests_PIV_4_9_19(4,27);
test_date_SS{1} = paper_3_tests_SS_4_9_19(1,22);

elseif ii == 8 % 12-12-18-a/12-12-18-b    12-12-18-c|12-12-18-d
num_SS = 2;
num_PIV = 2;
test_date_PIV{1} = paper_3_tests_PIV_4_9_19(4,12);
test_date_PIV{2} = paper_3_tests_PIV_4_9_19(4,13);
test_date_SS{1} = paper_3_tests_SS_4_9_19(1,10);
test_date_SS{2} = paper_3_tests_SS_4_9_19(1,11);

elseif ii == 9 %12-13-18-a    12-13-18-c
num_SS = 1;
num_PIV = 1;
test_date_PIV{1} = paper_3_tests_PIV_4_9_19(4,14);
test_date_SS{1} = paper_3_tests_SS_4_9_19(1,12);

elseif ii == 10 % 12-11-18-a/12-11-18-b    12-11-18-c|12-11-18-d
num_SS = 2;
num_PIV = 2;
test_date_PIV{1} = paper_3_tests_PIV_4_9_19(4,5);
test_date_PIV{2} = paper_3_tests_PIV_4_9_19(4,6);
test_date_SS{1} = paper_3_tests_SS_4_9_19(1,8);

```

```

test_date_SS {2} = paper_3_tests_SS_4_9_19(1,9);

elseif ii ==11 %8-14-18-a 8-14-18-b|8-14-18-c
num_SS = 1;
num_PIV = 2;
test_date_PIV {1} = paper_3_tests_PIV_4_9_19(4,17);
test_date_PIV {2} = paper_3_tests_PIV_4_9_19(4,18);
test_date_SS {1} = paper_3_tests_SS_4_9_19(1,14);

elseif ii ==12 %8-15-18-a 8-15-18-b|8-15-18-c
num_SS = 1;
num_PIV = 2;
test_date_PIV {1} = paper_3_tests_PIV_4_9_19(4,19);
test_date_PIV {2} = paper_3_tests_PIV_4_9_19(4,20);
test_date_SS {1} = paper_3_tests_SS_4_9_19(1,15);

elseif ii ==13 %8-8-18-a 8-8-18-b|8-8-18-c
num_SS = 1;
num_PIV = 2;
test_date_PIV {1} = paper_3_tests_PIV_4_9_19(4,15);
test_date_PIV {2} = paper_3_tests_PIV_4_9_19(4,16);
test_date_SS {1} = paper_3_tests_SS_4_9_19(1,13);
elseif ii == 14 % 3-6-19-a 3-6-19-b
num_SS = 1;
num_PIV = 1;
test_date_PIV {1} = paper_3_tests_PIV_4_9_19(4,6);
test_date_SS {1} = paper_3_tests_SS_4_9_19(1,4);

elseif ii == 15 %3-7-19-a 3-7-19-b
num_SS = 1;
num_PIV = 1;
test_date_PIV {1} = paper_3_tests_PIV_4_9_19(4,7);
test_date_SS {1} = paper_3_tests_SS_4_9_19(1,5);

elseif ii == 16 %3-1-19-a 3-1-19-b
num_SS = 1;
num_PIV = 1;
test_date_PIV {1} = paper_3_tests_PIV_4_9_19(4,1);
test_date_SS {1} = paper_3_tests_SS_4_9_19(1,1);

elseif ii == 17 % 12-6-18-a/12-6-18-b 12-6-18-c|12-6-18-d
num_SS = 2;
num_PIV = 2;
test_date_PIV {1} = paper_3_tests_PIV_4_9_19(4,8);
test_date_PIV {2} = paper_3_tests_PIV_4_9_19(4,9);
test_date_SS {1} = paper_3_tests_SS_4_9_19(1,6);
test_date_SS {2} = paper_3_tests_SS_4_9_19(1,7);

elseif ii == 18 % 3-1-19-d 3-1-19-e|3-2-19-a
num_SS = 1;
num_PIV = 2;
test_date_PIV {1} = paper_3_tests_PIV_4_9_19(4,2);
test_date_PIV {2} = paper_3_tests_PIV_4_9_19(4,3);
test_date_SS {1} = paper_3_tests_SS_4_9_19(1,2);

```

```

elseif ii == 19 % 3-2-19-b 3-2-19-c|3-2-19-d
    num_SS = 1;
    num_PIV = 2;
    test_date_PIV{1} = paper_3_tests_PIV_4_9_19(4,4);
    test_date_PIV{2} = paper_3_tests_PIV_4_9_19(4,5);
    test_date_SS{1} = paper_3_tests_SS_4_9_19(1,3);
end
make_energy_file(num_SS,num_PIV,test_date_SS,test_date_PIV,SS_location,
    PIV_location,Total_energy_save_location)
clear test_date_SS test_date_PIV
end
toc
function [] = make_energy_file(num_SS,num_PIV,test_date_SS,test_date_PIV,
    SS_location,PIV_location,Total_energy_save_location)

% Load Experiment
SS_date_info_1=test_date_SS{1};
SS_info_1 = load(strcat(SS_location,SS_date_info_1));

if strcmp(SS_info_1.date,'9_13_18_a')==1
    SS_info_1.z_total_height =0.63;
end

% Find averages of experiment KE over the three frequencies
for ii = 1:1030
    name = sprintf('row-%d',ii-1);
    SS_info_1.KE_ave_f_1(ii,:) = mean(SS_info_1.KE_exp_range.(name));
    SS_info_1.KE_f_1(ii,:) = SS_info_1.KE_exp_range.(name)(2,:);
end

if num_SS ==2
    SS_date_info_2=test_date_SS{2};
    SS_info_2 = load(strcat(SS_location,SS_date_info_2));
    for ii = 1:1030
        name = sprintf('row-%d',ii-1);
        SS_info_2.KE_ave_f_1(ii,:) = mean(SS_info_2.KE_exp_range.(name));
        SS_info_2.KE_f_1(ii,:) = SS_info_2.KE_exp_range.(name)(2,:);
    end
end

check_topo_med = strcmp('Medium',SS_info_1.top);
check_topo_steep = strcmp('Steep',SS_info_1.top);
check_topo_sine = strcmp('Sine',SS_info_1.top);
check_topo_complex = strcmp('Complex',SS_info_1.top);

if check_topo_med ==1
    topo_case = 1;
elseif check_topo_steep ==1
    topo_case = 2;
elseif check_topo_sine ==1
    topo_case = 3;
elseif check_topo_complex ==1

```

```

    topo_case = 4;
%     SS_info_1.H = 0.07;
%     H = 0.07;
end

%% Topography Specific Information
if topo_case == 1 % Medium Topography
    SS_info_1.H = 0.1; % Set H
    H = 0.1;
    L = SS_info_1.L/2; % Distance topography moves in 1/2 period
    width = 0.18+L; % Apparent width
    WH = width/H; % Apparent W/H

    for ii = 1:1030 % Average KE over three frequencies
        name = sprintf('row_%d',ii-1);
        SS_info_1.KE_ave_f_1(ii,:) = mean(SS_info_1.KE_exp_range.(name));
    end

    b_gaus = sqrt(2*(WH/6*0.1)^2); % apparent b_gaus
    k_dx = 2*pi/(SS_info_1.dx*1360)*(0:(1360/2-1)); % Range of k based on
    dx
    k_range = k_dx*b_gaus; % Normalized k by b_gaus
    % index overwhich Energy will be averaged for all methods (SS,PIV,
    Theory)

% info specific to theory
syms x_top t_top
h = SS_info_1.H*exp(-(x_top-L/2*sin(SS_info_1.omega*t_top))^2/b_gaus^2);
k_max_limit = 5/b_gaus;
k_min_limit = floor(k_dx(2));
k = k_min_limit:1:k_max_limit;
kmax = sqrt(2)/b_gaus;
kmax_index = find(k>kmax);
k(kmax_index(1)-1) = kmax;
amp_func_value = k*b_gaus.*exp(-(k*b_gaus/2).^2);
amp_func_limit = find(amp_func_value<0.05);
k(amp_func_limit) = [];
[~,mean_index_max] = min(abs(k_dx-k(end)));
mean_index = 2:mean_index_max;
elseif topo_case ==2 % Steep Topography
    SS_info_1.H = 0.1; % Set H
    H = 0.1;
    L = SS_info_1.L/2; % Distance topography moves in 1/2 period
    width = 0.0495+L; % Apparent width
    WH = width/H; % Apparent W/H

    for ii = 1:1030 % Average KE over three frequencies
        name = sprintf('row_%d',ii-1);
        SS_info_1.KE_ave_f_1(ii,:) = mean(SS_info_1.KE_exp_range.(name));
    end

    b_gaus = sqrt(2*(WH/6*0.1)^2); % apparent b_gaus
    k_dx = 2*pi/(SS_info_1.dx*1360)*(0:(1360/2-1)); % Range of k based on
    dx

```



```

k_range = k_dx*b_gaus;    % Normalized k by b_gaus
    % index overwhich Energy will be averaged for all methods (SS,PIV,
    Theory)

% info specific to theory
syms x_top t_top
h = SS_info_1.H*exp(-(x_top-L/2*sin(SS_info_1.omega*t_top))^2/b_gaus^2);
k_max_limit = 5/b_gaus;
k_min_limit = floor(k_dx(2));
k = k_min_limit:1:k_max_limit;
kmax = sqrt(2)/b_gaus;
kmax_index = find(k>kmax);
k(kmax_index(1)-1) = kmax;
amp_func_value = k*b_gaus.*exp(-(k*b_gaus/2).^2);
amp_func_limit = find(amp_func_value<0.05);
k(amp_func_limit) = [];
[~,mean_index_max] = min(abs(k_dx-k(end)));
mean_index = 2:mean_index_max;

elseif topo_case ==3 % sinusoidal topography
    SS_info_1.H = 0.071; % Set H
    H = SS_info_1.H;
    k_wave = SS_info_1.k_wave;
    L = SS_info_1.L/2; % Distance topography moves in 1/2 period
    % width = 0.0495+L; % Apparent width
    % WH = width/H; % Apparent W/H
    %
    for ii = 1:1030 % Average KE over three frequencies
        name = sprintf('row-%d',ii-1);
        SS_info_1.KE_ave_f_1(ii,:) = mean(SS_info_1.KE_exp_range.(name));
    end

    k_dx = 2*pi/(SS_info_1.dx*1360)*(0:(1360/2-1)); % Range of k based on
    dx
    k_range = k_dx/k_wave; % Normalized k by b_gaus
    % index overwhich Energy will be averaged for all methods (SS,PIV,
    Theory)

% info specific to theory
syms x_top t_top
x_new = x_top-L*sin(SS_info_1.omega*t_top);
h = H*sin(x_new*2*pi/.110)+.0355;
% k_max_limit = 5/b_gaus;
k_min_limit = floor(k_dx(2));
% k = k_min_limit:1:k_max_limit;
% kmax = sqrt(2)/b_gaus;
% kmax_index = find(k>kmax);
% k(kmax_index(1)-1) = kmax;
% amp_func_value = k*b_gaus.*exp(-(k*b_gaus/2).^2);
% amp_func_limit = find(amp_func_value<0.05);
% k(amp_func_limit) = [];
% [~,mean_index_max] = min(abs(k_dx-k(end)));
[~,mean_index_max] = min(abs(k_range-3));

```

```

    mean_index = 2:mean_index_max;
    k = k_min_limit:1:2.2*k_wave;
elseif topo_case ==4 % complex topography
    L = SS_info_1.L/2; % Distance topography moves in 1/2 period
    H = 0.2; % Height of the topography
    SS_info_1.H = H;
    syms x_top t_top
    x_new = x_top-L*sin(SS_info_1.omega*t_top);
    h=H*exp(-(x_new.^2)/0.0032).*abs(0.25*sin(x_new*520)+cos(x_new*115));
    width = .2428;
    b_gaus = sqrt(-((width+L)/2)^2/log(0.01));
    k_max_limit = 5/b_gaus;
    k_dx = 2*pi/(SS_info_1.dx*1360)*(0:(1360/2-1)); % Range of k based on
        dx
    k_min_limit = floor(k_dx(2));
    k = k_min_limit:1:k_max_limit;
    kmax = sqrt(2)/b_gaus;
    kmax_index = find(k>kmax);
    k(kmax_index(1)-1) = kmax;
    amp_func_value = k*b_gaus.*exp(-(k*b_gaus/2).^2);
    amp_func_limit = find(amp_func_value <0.05);
    k(amp_func_limit) = [];
    [~, mean_index_max] = min(abs(k_dx-k(end)));
    mean_index = 2:mean_index_max;
end

%% Density specific information
profile_coef = [SS_info_1.a SS_info_1.b SS_info_1.c SS_info_1.d];

if SS_info_1.profile_type==1
    profile_coef(end+1) = SS_info_1.ztd;
end

%% Experiments
SS_info_1.KE_k_mean_1 = mean(SS_info_1.KE_ave_f_1(:, mean_index), 2)';

if num_SS ==2
    SS_info_1.KE_k_mean_2 = mean(SS_info_2.KE_ave_f_1(:, mean_index), 2)';
end

%% Theory
if topo_case ~ = 3
    x_match = b_gaus;
    t_match = 0;

    amp_func_max = sqrt(2).*exp(-(sqrt(2)/2).^2);
    A0_ratio = amp_func_value ./ amp_func_max;

    % Set up extra variables needed for linear theory
    A0_info = 0;
    A0_actual = 0;
    % Run linear Theory

```

```

[SS_info_1.z_theory , SS_info_1.KE_evan , SS_info_1.KE_airy , SS_info_1.KE_prop
~, ...
SS_info_1.prop_start_value , SS_info_1.N_theory , SS_info_1.evan_end_value
, SS_info_1.ztd , A0_actual ]...
= linear_theory_4_18_19(SS_info_1.profile_type , profile_coef , h , ...
SS_info_1.omega , SS_info_1.k_wave , SS_info_1.u_top , SS_info_1.z_exp ,
x_match , t_match , ...
SS_info_1.z_total_height , SS_info_1.H , A0_info , A0_actual);
KE = zeros(1030, length(k));

for ii =1:length(k)-1

    A0_info = A0_ratio(ii);
    % Run linear Theory
    [~,~,~,~,KE_theory,~,~,~,~, ~]...
    = linear_theory_4_18_19(SS_info_1.profile_type , profile_coef , h , ...
SS_info_1.omega , k(ii) , SS_info_1.u_top , SS_info_1.z_exp , x_match , t_match
, ...
SS_info_1.z_total_height , SS_info_1.H , A0_info , A0_actual);
    KE(:, ii) = KE_theory';
end

SS_info_1.KE_theory_k = KE;
SS_info_1.KE_theory_k_ave = mean(KE,2);

else
x_match = 0;
t_match = 0;
A0_info = 0;
A0_actual = 0;
amp_func_max = sqrt(2).*exp(-(sqrt(2)/2).^2);
% A0_ratio = amp_func_value ./ amp_func_max;

% Set up extra variables needed for linear theory
A0_info = 0;
A0_actual = 0;
% Run linear Theory
[SS_info_1.z_theory , SS_info_1.KE_evan , SS_info_1.KE_airy , SS_info_1.KE_prop ,
KE_theory , ...
SS_info_1.prop_start_value , SS_info_1.N_theory , SS_info_1.evan_end_value
, SS_info_1.ztd , A0_actual ]...
= linear_theory_4_18_19(SS_info_1.profile_type , profile_coef , h , ...
SS_info_1.omega , SS_info_1.k_wave , SS_info_1.u_top , SS_info_1.z_exp ,
x_match , t_match , ...
SS_info_1.z_total_height , SS_info_1.H , A0_info , A0_actual);
SS_info_1.KE_theory_k = KE_theory;
SS_info_1.KE_theory_k_ave = KE_theory;
end
%% PIV
% PIV_date_1 = '9_19_18_test_b.mat';
PIV_date_1=test_date_PIV{1};
PIV_info_1 = load(strcat(PIV_location , PIV_date_1));

```

```

k_PIV = PIV_info_1.Energy_PIV.k_PIV;
[~,mean_index_max_PIV] = min(abs(k_PIV-k(end)));
mean_index_PIV = 2:mean_index_max_PIV;
PIV_info_1.KE_amp = mean(PIV_info_1.Energy_PIV.Vx_amp(:,mean_index_PIV),2).^2+
    mean(PIV_info_1.Energy_PIV.Vz_amp(:,mean_index_PIV),2).^2;

if num_PIV ==2
    PIV_date_2=test_date_PIV{2};
    PIV_info_2 = load(strcat(PIV_location,PIV_date_2));
    PIV_info_2.KE_amp = mean(PIV_info_2.Energy_PIV.Vx_amp(:,mean_index_PIV),2)
        .^2+mean(PIV_info_2.Energy_PIV.Vz_amp(:,mean_index_PIV),2).^2;
end

SS_info_1.x_PIV_1 = PIV_info_1.Energy_PIV.x;
SS_info_1.z_PIV_1 = PIV_info_1.Energy_PIV.z;

% SS_info_1.Vx_PIV_1 = PIV_info_1.Energy_PIV.Vx_amp;
% SS_info_1.Vz_PIV_1 = PIV_info_1.Energy_PIV.Vz_amp;
SS_info_1.KE_PIV_1 = PIV_info_1.KE_amp;
SS_info_1.k_PIV_1 = PIV_info_1.Energy_PIV.k_PIV;

if num_PIV ==2
    SS_info_1.x_PIV_2 = PIV_info_2.Energy_PIV.x;
    SS_info_1.z_PIV_2 = PIV_info_2.Energy_PIV.z;
%     SS_info_1.Vx_PIV_2 = PIV_info_2.Energy_PIV.Vx_amp;
%     SS_info_1.Vz_PIV_2 = PIV_info_2.Energy_PIV.Vz_amp;
%     SS_info_1.KE_PIV_2 = PIV_info_2.Energy_PIV.KE_amp;
    SS_info_1.KE_PIV_2 = PIV_info_2.KE_amp;
end

%%
SS_info_1.num_PIV = num_PIV;
SS_info_1.num_SS = num_SS;
field = 'KE_exp_range';
SS_info_1 = rmfield(SS_info_1,field);
save(strcat(Total_energy_save_location,SS_date_info_1),'-struct','SS_info_1')
end

```

B.1.6 Linear theory calculations

```

%% Linear Theory Analysis of Evanescent to Propagating Waves
% Allison Lee
% 5/9/17
% This program will use an assumed amplitude for the evanescent waves
% (based on the topography movement), allow that to move through the

```

```

% evanescent region , and then use an Airy Patch to move from the evansecnt
% region to the propagating region .
%
% It is assumed that the natural Frequency (N) is not constant. Equations
% of motion for the waves in both regions come from Lighthill (1978) and
% from Pedlosky (2003). The topographies used are Gaussian in nature , with
% defining characteristics labeled with _gauss .
% clc

% Updated 8/18/17
% Updated 11/11/17
% Updated 1/24/18
% Updated 2/14/18
% Updated 3/13/18– Now takes different N and H profiles

function [z,KE_egan,KE_airy,KE_prop,KE_total,prop_start_value,N,egan_end_value
,ztd,A0_egan] =...
    linear_theory_4_18_19(profile,profile_coef,h,omega,k_wave,u_top,z,x_match,
        t_match,water_height,H,A0_info,A0_actual)
percent_wavelength = 0.01;
z = sort(z,'descend');
zmax = max(z);
g = 9.81;
rho_o = 1000;
%% Two layer Liner profile
if profile == 1
    a = profile_coef(1);
    c = profile_coef(3);
    N_egan_ave = (c*-g/rho_o)^.5;
    N_prop_ave = (a*-g/rho_o)^.5;
    ztd = profile_coef(5);
    z_egan = z(z>=ztd);
    z_prop = z(z<=ztd);
    N_egan = zeros(1,length(z_egan))+sqrt(-g/rho_o*c);
    N_prop = zeros(1,length(z_prop))+sqrt(-g/rho_o*a);
    N_ave = [];
    N = [N_egan,N_prop];
    q = k_wave*(1-N_egan.^2/omega^2).^5;
    m_prop= sqrt(N_prop.^2*k_wave^2/omega^2-k_wave^2);
    h_match = subs(h,x_match);
    h_match=double(subs(h_match,t_match));
%% Evanescent Region
    q_match = q(1);
    theta_egan = q.*(-zmax+z_egan);
    [dh_dt_evaluate_xt] = topography_matching(h,x_match,t_match,u_top);
    A0_egan = dh_dt_evaluate_xt/real(exp(1i*k_wave*x_match-omega*t_match)*exp(
        q_match*h_match));
    A_egan = A0_egan./(q./q_match).^5;
    KE_egan = A_egan.^2.*exp(2*theta_egan).*(q.^2/k_wave^2+1);
%% Airy Patch is not necessary for a two layer , constant N
% The matching condition here is rho_o*w_egan = rho_o*w_prop from Nappo
% A0_prop_match = A_egan(end)*exp(q(end)*z_egan(end))/exp(m_prop(1)*z_prop
(1));
    A0_prop_match = A_egan(end)*exp(q(end)*(ztd-zmax));

```

```

%% Propagating Waves

% Now use an amplitude from the airy patch to calculate the first needed
% amplitude for the propagating waves. Then continue with the standard,
% varying N propagating wave equations.
%   N_prop_match = sqrt(-g/rho_o*(a*b*exp(b*z_prop_match)));
A0_prop = A0_prop_match;
KE_prop = A0_prop.^2.*(1+m_prop.^2/k_wave^2);
%% Find KE_total
KE_total = cat(2,KE_evan,KE_prop(1:end));
z_airy_patch = [];
KE_airy = [];
prop_start_value = ztd;

KE_ave_prop = trapz(z_prop,KE_prop)/(z_prop(end)-z_prop(1));
%% Exponential Profile
elseif profile == 2
    % set up variables
    a = profile_coef(1);
    b = profile_coef(2);
    N_prop_ave = [];
    N_ave = [];
    syms z_td
    ztd =double(vpasolve(-omega+sqrt(-g/rho_o*(a*b*exp(b*z_td)))));
    syms z_func
    N_func = sqrt(-g/rho_o*(a*b*exp(b*z_func)));
    N_evan_ave = 1/(zmax-ztd-H)*double(int(N_func,[ztd zmax-H]));

    z_evan = z(z>ztd);
    z_prop = z(z<ztd);
    N = sqrt(-g/rho_o*(a*b*exp(b*z)));
    N_evan = sqrt(-g/rho_o*(a*b*exp(b*z_evan)));
    N_prop = sqrt(-g/rho_o*(a*b*exp(b*z_prop)));
    q = -k_wave*(1-N_evan.^2/omega^2).^5;
    m_prop= sqrt(N_prop.^2*k_wave^2/omega^2-k_wave^2);
    m2 =(N.^2*k_wave^2/omega^2-k_wave^2);
    h_match = subs(h,x_match);
    h_match=double(subs(h_match,t_match));
    z_match = water_height-h_match;
    %% Evan region values
    N_match = sqrt(-g/rho_o*(a*b*exp(b*(z_match))));
    q_match = -k_wave*(1-N_match.^2/omega^2).^5;
    theta_evan = -2/b*(q-q_match-k_wave*atanh(q/k_wave)+...
        k_wave*atanh(q_match/k_wave));
    if A0_info ==0
    [dh_dt_evaluate_xt] = topography_matching(h,x_match,t_match,u_top);
    A0_evan = dh_dt_evaluate_xt/real(exp(1i*k_wave*x_match-omega*t_match)*exp(
        q_match*h_match));
    else
        A0_evan = A0_info*A0_actual;
    end
    A_evan = A0_evan./(q./q_match).^5;
    KE_evan = A_evan.^2.*exp(2*theta_evan).*(q.^2/k_wave^2+1);

```

```

%% Airy Patch
% Both the evanescent and propagating energy go to infinity as they
% approach
% the turning depth. We will use the Airy function (based on Lighthill's
% work) to move from one region to the next. This is usually done when
% approaching a turning depth from the rpropagating region and allows for
% reflection of the wave. We start in the evanescent region and move into
% the propagating region.

% Beta is used as a linear approximation of m (vertical wavenumber) where
%  $m^2 = k^2 * (N^2 / \omega^2 - 1)$ . Beta is only accurate near the turning
% depth, especially since m for our case is exponentially varying (due to
% N)
tic
beta1 = k_wave^2 ./ (ztd - z) .* (N.^2 / omega^2 - 1);

% Beta should be a constant value, not a changing value. We need only one
% value for the approximation. So we find beta near the turning depth and
% then average those values. Beta needs to be positive.
tmp = abs(z - ztd);
[~, index_loc] = min(tmp); % Find where in the z matrix ztd is located.
% Pull out beta's close to td
beta1_short = beta1((index_loc - 2):(index_loc + 2));
beta1_airy = mean(beta1_short); % Average betas near td
mean_q = mean(q);
% Finding the average m in the propagating region to define average
% vertical length scale
% Find location "close to" turning depth (TD)
z_airy = round((ztd + abs(percent_wavelength * (2 * pi / mean_q))) * 1000) / 1000;
% Let the amplitude start opposite to where the evanescent wave amplitude
% was taken for the airy patch. Symmetry is nice. Set up all needed
% variables to calculate w_prop and u_prop. (very similar to variables
% needed for airy patch amplitude calculation)
z_evan_distance = max(z_evan) - min(z_evan);
prop_ave_location = z_prop(1) - z_evan_distance;
[~, index_prop_ave] = min(abs(prop_ave_location - z_prop));
mean_m = mean(m_prop(1:index_prop_ave));
% Find location "close to" turning depth (TD)
z_prop_match = round(((ztd - percent_wavelength * (2 * pi / mean_m)) * 1000) / 1000);
up_bound_z_airy = z_airy;
low_bound_z_airy = z_prop_match;
[~, index_up_bound] = min(abs(z - up_bound_z_airy));
[~, index_low_bound] = min(abs(z - low_bound_z_airy));
z_airy = z(index_up_bound);
% Finding N at location close to TD
N_airy = sqrt(-g / rho_o * (a * b * exp(b * z_airy)));
q_airy = -sqrt(1 - N_airy^2 / omega^2) * k_wave; % Finding m near TD
theta_airy = -2 / b * (q_airy - q_match - k_wave * atanh(q_airy / k_wave) + ...
    k_wave * atanh(q_match / k_wave));
A0_airy = A0_evan / (q_airy / q_match)^.5;

% The airy patch needs to move from the evan to the prop region. It's not
% necessary to calculate it over the whole field. We will set up bounds

```

```

% based on a percentage of the vertical wavenumber and use that to set up
% a z vector around the turning depth.

z_airy_patch = z(index_up_bound:index_low_bound);
% Calculate the amplitude of the Airy Patch

Q1_w = A0_airy*exp(theta_airy)./(airy(beta1_airy^(1/3)*(z_airy-ztd)));
Q1_u = q_airy*A0_airy*exp(theta_airy)./(beta1_airy^(1/3)*airy(1,beta1_airy
^(1/3)*(z_airy-ztd)));

KE_airy = Q1_w^2*(airy(beta1_airy^(1/3)*(z_airy_patch-ztd)).^2)+Q1_u^2*(
beta1_airy^(2/3)/k_wave^2*(airy(1,(beta1_airy^(1/3)*(z_airy_patch-ztd)))
.^2);
%% Propagating Waves
% Now use an amplitude from the airy patch to calculate the first needed
% amplitude for the propagating waves. Then continue with the standard,
% varying N propagating wave equations.
N_prop_match = sqrt(-g/rho_o*(a*b*exp(b*z_prop_match)));
m_prop_match = sqrt(N_prop_match^2*k_wave^2/omega^2-k_wave^2);
theta_prop_match = 0;
theta_prop = 2/b*(m_prop-m_prop_match+k_wave.*(atan(m_prop_match/k_wave)
...
-atan(m_prop/k_wave)));
A0_prop_match = Q1_w*airy(beta1_airy^(1/3)*(z_prop_match-ztd))...
/exp(1i*theta_prop_match);

A0_prop = A0_prop_match./(m_prop./m_prop_match).^0.5;

KE_prop = A0_prop.^2.*(1+m_prop.^2/k_wave^2);
%% Find KE_total
evan_end = find(z_evan == z_airy_patch(1))-1;
evan_end_value = z_evan(evan_end);
prop_start = find(z_prop == z_airy_patch(end))+1;
prop_start_value = z_prop(prop_start);
KE_total = cat(2,KE_evan(1:index_up_bound-1),KE_airy,KE_prop(prop_start:
end));
KE_ave_prop = trapz(z_prop(prop_start:end),KE_prop(prop_start:end))/(
z_prop(end)-z_prop(prop_start));

%% Parabolic Profile
elseif profile == 3
% Set up variables
a = profile_coef(1);
b = profile_coef(2);
c = profile_coef(3);
N = sqrt(-g/rho_o*(3*a*z.^2+2*b*z+c));
syms z_func
N_func = sqrt(-g/rho_o*(3*a*z_func.^2+2*b*z_func+c));
dN_dz = diff(N_func, z_func);
syms z_td
ztd = double(vpasolve(-omega + sqrt(-g/rho_o*(3*a*z_td^2+2*b*z_td+c)), z_td
,[0 Inf]));
z_evan = z(z>ztd);
z_prop = z(z<ztd);

```



```

N_evan = sqrt(-g/rho_o*(3*a*z_evan.^2+2*b*z_evan+c));
N_prop = sqrt(-g/rho_o*(3*a*z_prop.^2+2*b*z_prop+c));
q = k_wave*(1-N_evan.^2/omega^2).^5;
m_prop= sqrt(N_prop.^2*k_wave^2/omega^2-k_wave^2);
h_match = subs(h, x_match);
h_match=double(subs(h_match, t_match));
z_match = water_height-h_match;
N_evan_ave = 1/(zmax-ztd-H)*double(int(N_func,[ztd zmax-H]));
N_prop_ave = 1/(ztd-min(z))*double(int(N_func,[min(z) ztd]));
N_ave = 1/(zmax-min(z))*double(int(N_func,[min(z) zmax]));
%% Evan region values
N_match = sqrt(-g/rho_o*(3*a*z_match.^2+2*b*z_match+c));
q_match = k_wave*(1-N_match.^2/omega^2).^5;
theta_evan = zeros(1, length(z_evan));
int_theta = int(k_wave*(1-N_func^2/omega^2)^.5);
int_lower = double(subs(int_theta, z_match));
for jj= 1:length(z_evan)
    theta_evan(jj) = double(subs(int_theta, z_evan(jj)))-int_lower;
end
if A0_info ==0
[dh_dt_evaluate_xt] = topography_matching(h, x_match, t_match, u_top);
A0_evan = dh_dt_evaluate_xt/real(exp(1i*k_wave*x_match-omega*t_match)*exp(
    q_match*h_match));
else
    A0_evan = A0_info*A0_actual;
end

A_evan = A0_evan./(q./q_match).^5;
KE_evan = A_evan.^2.*exp(2*theta_evan).*(q.^2/k_wave^2+1);
%% Airy Patch
% Both the evanescent and propagating energy go to infinity as they
    approach
% the turning depth. We will use the Airy function (based on Lighthill's
% work) to move from one region to the next. This is usually done when
% approaching a turning depth from the rpropagating region and allows for
% reflection of the wave. We start in the evanescent region and move into
% the propagating region.

% Beta is used as a linear approximation of m (vertical wavenumber) where
% m^2 = k^2*(N^2/omega^2 - 1). Beta is only accurate near the turning
% depth, especially since m for our case is exponentially varying (due to
    N)
tic
beta1 = k_wave^2./(ztd-z).*(N.^2/omega^2-1);

% Beta should be a constant value, not a changing value. We need only one
% value for the approximation. So we find beta near the turning depth and
% then average those values. Beta needs to be positive.
tmp = abs(z-ztd);
[~, index_loc] = min(tmp); % Find where in the z matrix ztd is located.
% Pull out beta's close to td
beta1_short = beta1((index_loc-2):(index_loc+2));
beta1_airy = mean(beta1_short); % Average betas near td
mean_q = mean(q);

```

```

% Finding the average m in the propagating region to define average
% vertical length scale
% Find location "close to" turning depth (TD)
z_airy = round((ztd+percent_wavelength*(2*pi/mean_q))*1000)/1000;
% Let the amplitude start opposite to where the evanescent wave amplitude
% was taken for the airy patch. Symmetry is nice. Set up all needed
% variables to calculate w_prop and u_prop. (very similar to variables
% needed for airy patch amplitude calculation)
mean_m = mean(m_prop);
% Find location "close to" turning depth (TD)
z_prop_match = round(ztd-percent_wavelength*(2*pi/mean_m),3);
up_bound_z_airy = z_airy;
low_bound_z_airy = z_prop_match;
[~,index_up_bound] = min(abs(z-up_bound_z_airy));
% [~,index_z_evan_to_airy] = min(abs(z_evan-up_bound_z_airy));
% [~,index_low_bound] = min(abs(z-low_bound_z_airy));
z_airy = z(index_up_bound);
% z_prop_match = z(index_low_bound);
% Finding N at location close to TD
N_airy = sqrt(-g/rho_o*(3*a*z_airy.^2+2*b*z_airy+c));
q_airy = sqrt(1-N_airy^2/omega^2)*k_wave; % Finding m near TD
theta_airy = double(subs(int_theta , z_airy))-int_lower;
A0_airy = A0_evan/(q_airy/q_match).^5;

% The airy patch needs to move from the evan to the prop region. It's not
% necessary to calculate it over the whole field. We will set up bounds
% based on a percentage of the vertical wavenumber and use that to set up
% a z vector around the turning depth.

z_airy_patch = z(index_up_bound:index_low_bound);

Q1_w = A0_airy*exp(theta_airy)./(airy(beta1_airy^(1/3)*(z_airy-ztd)));
Q1_u = q_airy*A0_airy*exp(theta_airy)./(beta1_airy^(1/3)*airy(1,beta1_airy
^(1/3)*(z_airy-ztd)));

KE_airy = Q1_w^2*(airy(beta1_airy^(1/3)*(z_airy_patch-ztd)).^2)+0.5*Q1_u^2*(
beta1_airy^(2/3)/k_wave^2*(airy(1,(beta1_airy^(1/3)*(z_airy_patch-ztd)))
.^2);
%% Propagating Waves
% Now use an amplitude from the airy patch to calculate the first needed
% amplitude for the propagating waves. Then continue with the standard,
% varying N propagating wave equations.
N_prop_match = sqrt(-g/rho_o*(3*a*z_prop_match.^2+2*b*z_prop_match+c));
m_prop_match = sqrt(N_prop_match^2*k_wave^2/omega^2-k_wave^2);
theta_prop_match = 0;

A0_prop_match = Q1_w*airy(beta1_airy^(1/3)*(z_prop_match-ztd))...
/exp(1i*theta_prop_match);

A0_prop = A0_prop_match./(m_prop./m_prop_match).^0.5;

% theta_prop = 2/b*(m_prop-m_prop_match+k_wave.*(atan(m_prop_match/k_wave)
...
% -atan(m_prop/k_wave)));

```

```

    KE_prop = A0_prop.^2.*(1+m_prop.^2/k_wave^2);
    %% Find KE_total
    prop_start = find(z_prop == z_airy_patch(end))+1;
    prop_start_value = z_prop(prop_start);
    KE_total = cat(2,KE_evan(1:index_up_bound-1),KE_airy,KE_prop(prop_start :
        end));
    KE_ave_prop = trapz(z_prop(prop_start:end),KE_prop(prop_start:end))/(
        z_prop(end)-z_prop(prop_start));
end

end
%%
function [dh_dt_evaluate_xt] = topography_matching(h,x_match,t_match,velocity)
% h = H*exp(-(x_top-L/2*sin(omega*t_top))^2/b_gaus^2);

syms x_top t_top
% h = H*sin((x_top-L/2*sin(omega*t_top))*k);
dh_dx = diff(h,x_top);
dh_dt = diff(h,t_top);
dh_dt_total = dh_dt+dh_dx*velocity;
dh_dt_evaluate_x = subs(dh_dt_total,x_top,x_match);
dh_dt_evaluate_xt = double(subs(dh_dt_evaluate_x,t_top,t_match));

end

```

B.2 Arduino

```

#include <Wire.h>
#include <Adafruit_MotorShield.h>
#include "utility/Adafruit_PWMServoDriver.h"

Adafruit_MotorShield AFMS = Adafruit_MotorShield();
Adafruit_StepperMotor *motor = AFMS.getStepper(200, 2);
const int buttonPin = 2;
int buttonState = 0;
float e;

void setup() {
    float d,V,T,w,L,s;

    //V=.3; // Enter speed in cm/sec

    T=(2*3.1415)/.775-1.35; // Enter time period in sec. -1.7 adjusts for error
    L = 5; // Excursion length in cm
    V = 2*L/T;
    d=.8125; // Spool diameter in inches
    //L=(T*V)/2; // Excursion length in cm
    s=(V*60)/(3.1415*2.54*d); // motor speed in rev/min
    e=(L*200)/(d*3.1415*2.54); // number of steps in each direction

    Serial.begin(9600); // set up Serial library at 9600 bps
    Serial.println("Internal_Waves_Test");
}

```

```

AFMS.begin();
motor->setSpeed(s); // 50 rpm
pinMode(buttonPin, INPUT);
// motor.step(200, FORWARD, DOUBLE);
motor->release();
}

```

B.3 Supercomputer files

B.3.1 Setup data for SS kinetic energy processing

Supercomputer bash file to used to run MATLAB files of individual tests such as Test_3_6_19_a.m:

```

#!/bin/bash
#SBATCH -C rhel7
#SBATCH --time=0:20:00 # walltime
#SBATCH --ntasks=12 # number of processor cores (i.e. tasks)
#SBATCH --nodes=1 # number of nodes
#SBATCH --mem-per-cpu=7G # memory per CPU core
#SBATCH -J "Test_3_6_19_a" # job name
#SBATCH --mail-user=allisonlee8@gmail.com # email address
#SBATCH --mail-type=END
module load matlab
matlab -nodisplay -nosplash -r Test_3_6_19_a

```

B.3.2 Create experimental energy

Supercomputer bash file used to calculate kinetic energy by running the MATLAB file SC_Experiment_Energy_AL_04_29_19.m:

```

#!/bin/bash
#SBATCH -C rhel7
#SBATCH --time=02:00:00 # walltime
#SBATCH --ntasks=3 # number of processor cores (i.e. tasks)
#SBATCH --nodes=1 # number of nodes
#SBATCH --mem-per-cpu=60G # memory per CPU core
#SBATCH -J "exp_energy" # job name
#SBATCH --mail-user=allisonlee8@gmail.com # email address
#SBATCH --mail-type=END
module load matlab/r2017b
matlab -nodisplay -nosplash -r SC_Experiment_Energy_AL_04_29_19

```

APPENDIX C. UNCERTAINTY ANALYSIS

Each measurement of the experimental process has an uncertainty associated with it, and that uncertainty is propagated into the calculation of dependent variables. While different methods can be used to quantify the uncertainty of an experimental calculation, here sequential perturbation will be used. Following the methods outlined by Manteufel [114], the various measured independent variables (x_i) of an equation are perturbed by their respective uncertainty values, and a new solution for the dependent variable (R_i) is found. By comparing the perturbed solutions to the original solution, total relative uncertainty can be estimated, along with importance factors for each independent variable. Sequential perturbation will be used for three equations in this section. First, the calculation of the density perturbation or $\partial\rho'/\partial z$ from Sec. 1.5.2, and then the two kinetic energy calculations of KE_1 and KE_2 from Sec. 2.3.2. Each equation is listed here for convenience.

C.1 Density perturbation

To estimate the density perturbation (ρ') based on the variation in pixel movement and lengths associated with the experimental setup (See Fig. 1.6), the following equation is solved using the commercial software Digiflow [94]:

$$\Delta z = -\frac{1}{2} \left[\frac{L - B - \left(1 - \frac{n_{\text{air}}}{2n_0}\right)W - 2\left(1 - \frac{n_{\text{air}}}{2n_{\text{wall}}}\right)T}{L - \left(1 - \frac{n_{\text{air}}}{n_0}\right)W - 2\left(1 - \frac{n_{\text{air}}}{n_{\text{wall}}}\right)T} \right] W \left(W + 2\frac{n_0}{n_{\text{air}}}B + 2\frac{n_0}{n_{\text{wall}}}T \right) \frac{\beta}{\rho_0} \frac{\partial\rho'}{\partial z} \quad (\text{C.1})$$

In this equations, L is the distance between the camera and the light mask, T is the thickness of one side of the tank, B is the distance from the outside of the tank to the light mask, and W is the interior width of the tank as shown in Fig. 1.6. Here, density has been defined as $\rho = \rho_0 + \bar{\rho} + \rho'$, where ρ_0 is the background or reference density of the fluid, $\bar{\rho}$ is the stratification profile, and

Table C.1: Inputs and output of Eq. C.1 with a sequential perturbation analysis. The labels on the right half of the table indicate which variable was perturbed. $\partial\rho'/\partial z$ for each scenario, along with the uncertainty (based on the perturbed solution) are listed in the bottom row. All inputs have units of meters, with $\partial\rho'/\partial z$ in units of kg/m^4 .

Input	Value	Uncertainty	Relative Uncertainty	L	B	W	T	Δz
L	3.2258	0.0016	0.050%	3.2274	3.2258	3.2258	3.2258	3.2258
B	0.93	0.0005	0.054%	0.93	0.9305	0.93	0.93	0.93
W	0.12	0.0005	0.417%	0.12	0.12	0.1205	0.12	0.12
T	0.018	0.0005	2.778%	0.018	0.018	0.018	0.0185	0.018
$\Delta z (10^{-5})$	-4.46	-1.19	26.584%	-4.46	-4.46	-4.46	-4.46	-5.65
Output:								
$\partial\rho'/\partial z$	2.23	0.59	26.59%	2.23	2.23	2.22	2.23	2.82

ρ' is the perturbation density. The index of refraction for air and the wall of the experimental tank are represented with η_{air} and η_{wall} , respectively, and are assumed to be constants. η_0 is the reference index of refraction for the experimental fluid and is also needed for the definition of β , where $\beta = (\rho_0/n_0)(\partial n/\partial\rho)$. Although the index of refraction of the fluid will vary with the density, the actual derivative of $\partial n/\partial\rho$ can be considered constant for water. Thus, with $\rho_0 = 1000 \text{ kg/m}^3$ and $n_0 = 1.3332$ [115] as the reference density and index of refraction for water, $\beta \approx 0.184$. This equation assumes that the experiment is two dimensional so the variation in the y direction is negligible. A PIV cross-correlation algorithm is used to estimate Δz . Although Eq. (C.1) is for Δz , the actual value of interest is $\partial\rho'/\partial z$ as kinetic energy density is estimated by $\Delta N^2 = -g/\rho_0(\partial\rho'/\partial z)$. Thus, it is important to understand the uncertainty of $\partial\rho'/\partial z$.

Based on Eq. C.1, sequential perturbation is performed by perturbing the variables L , B , W , T , and Δz . Values for the index of refraction are all held constant in this analysis because of the consistency of the values based on the literature. For example, $n_{\text{air}} = 1.0$ and varies less than 0.01% with temperatures and pressures measured between $-40 - 40 \text{ }^\circ\text{C}$ and $60 - 110 \text{ kPa}$ [116]. Along with n_{air} , other values include $n_0 = 1.3332$ [115], and $n_{\text{wall}} = 1.491$ [117]. β is also assumed constant [58]. For the analysis, B , W , and T , were each measured with a standard measuring tape in centimeters, with an error of $\pm 0.5 \text{ mm}$. L was regularly measured in inches, with a resolution of

$\pm 1/16''$, or 1.58 mm. Dalziel et al. [58] indicate that the algorithm used to compare SS test images and calculate Δz has a resolution of 0.02 pixels, which translates to 0.012 mm for the scenario presented here.

Each variable was individually perturbed and then Eq. C.1 was solved for $\partial\rho'/\partial z$. Table C.1 indicates the input values and the associated uncertainty, along with the calculated values of $\partial\rho'/\partial z$ given the perturbation of each individual variable. As indicated by the table, the original independent variables provide a solution of $\partial\rho'/\partial z = 2.23 \text{ kg/m}^4$, which varies only slightly for each variation of the measured lengths. However, this variation increases for the calculated value of Δz due its associated uncertainty. Comparing the differences between each output for the different inputs, the calculated value of Δz has a 99.97% impact on $\partial\rho'/\partial z$, with each other independent variable causing less than 0.03% variation. The total uncertainty is calculated by

$$\text{Uncertainty} = \sqrt{\sum [(\partial\rho'/\partial z)_{\text{org}} - (\partial\rho'/\partial z)_{\text{pert}}]^2} \quad (\text{C.2})$$

where $(\partial\rho'/\partial z)_{\text{org}}$ is the original solution and $(\partial\rho'/\partial z)_{\text{pert}}$ is the solution with one variable perturbed. Although each of the lengths listed in Tab. C.1 are important, the overall calculation is highly dependent upon the Digiflow calculation of Δz . It is recommended that synthetic schlieren process be run at the highest fidelity possible (relative to needed processing time) to decrease the error associated with this variable. In addition, this analysis does not indicate a specific bias error that consistently increases or decreases $\partial\rho'/\partial z$.

C.2 Kinetic energy

After solving for $\partial\rho'/\partial z$ and calculating ΔN^2 with $\Delta N^2 = -g/\rho_0(\partial\rho'/\partial z)$, kinetic energy density can then be estimated using either Eq. (C.3) or (C.4) for the evanescent and propagating regions, respectively:

$$KE_1 = \left| \frac{-q\omega\Delta\tilde{N}^2}{k(\partial_z N^2 + qN^2)} \right|^2 + \left| \frac{i\omega\Delta\tilde{N}^2}{\partial_z N^2 + qN^2} \right|^2 \quad (\text{C.3})$$

Table C.2: Uncertainty analysis of KE_1 based on Eq. (C.3).

Input	Value	Uncertainty	Relative Uncertainty	ω (s ⁻¹)	N (s ⁻¹)	k (m ⁻¹)	ΔN^2 (s ⁻²)	$\partial_z N^2$ (m ⁻¹ s ⁻²)
ω	1.00	0.016	1.60%	1.01	1.00	1.00	1.00	1.00
N	0.8	0.04	5.00%	0.8	0.84	0.8	0.8	0.8
k	27.925	0.005	0.02%	27.925	27.925	27.930	27.925	27.925
ΔN^2	0.022	0.006	26.59%	0.022	0.022	0.022	0.028	0.022
$\partial_z N^2$	-5.6	0.280	5.00%	-5.60	-5.60	-5.60	-5.60	-5.32
Output:								
KE_1 (J/kg 10 ⁻⁵)	1.74	1.07	61.47%	1.81	1.74	1.74	2.79	1.95

$$KE_2 = \frac{\omega^2 N^2}{k^2(N^2 - \omega^2) + (\omega \partial_z N^2 / N^2)^2} \left| \frac{\Delta \tilde{N}^2}{N^2} \right|^2 \quad (C.4)$$

Each equation contains similar independent variables. $\Delta \tilde{N}^2$ refers to the Fourier amplitude of ΔN^2 and the total uncertainty for this variable is 26.59%, as indicated by Tab. C.1. ω is the excitation frequency, which is measured by timing the period of the topography oscillation (T_T) using a stopwatch with a resolution of 0.1 seconds and then $\omega = 2\pi/T_T$. This translates into a 1.6% relative uncertainty. N , the natural frequency, is calculated from the measured density in the experimental tank. Density is measured every 3 cm using an Anton Paar DMA 4100M density meter with an accuracy of ± 0.0001 g/cm³, or ± 1.000 kg/m³. Density measurement locations were set using a standard meter stick with 1 mm increments, giving an uncertainty of ± 0.0005 m. Combining the relative uncertainty of these two measurements provides an overall uncertainty of 5% for N . k is calculated from the width of the topography (18 cm for the 3D printed medium Gaussian topography) and the excursion length which is measured before an experiment is performed with a resolution of ± 0.001 m. Thus the relative uncertainty of $k = 2\pi/(W + L)$ is 0.02%. Note that W and L here refer to the topography width and excursion length, not the SS lengths in Eq. (C.1). In Eq. (C.3), the variable q is listed, but $q = \sqrt{1 - N^2/\omega^2}$, and thus is not an independent variable used in this uncertainty analysis. The final variable in both equations is the z -derivative of N^2 , which is assumed to have the same uncertainty as N .

Table C.3: Uncertainty analysis of KE_2 based on Eq. (C.4).

Input	Value	Uncertainty	Relative Uncertainty	ω (s ⁻¹)	N (s ⁻¹)	k (m ⁻¹)	ΔN^2 (s ⁻²)	$\partial_z N^2$ (m ⁻¹ s ⁻²)
ω	1.00	0.016	1.60%	1.01	1.00	1.00	1.00	1.00
N	1.1	0.055	5.00%	1.1	1.155	1.1	1.1	1.1
k	27.925	0.005	0.02%	27.925	27.925	27.930	27.925	27.925
ΔN^2	0.022	0.006	26.59%	0.022	0.022	0.022	0.028	0.022
$\partial_z N^2$	-0.35	-0.018	5.00%	-0.35	-0.35	-0.35	-0.35	-0.37
Output:								
KE_2 (J/kg 10 ⁻⁸)	1.39	1.36	97.45%	1.99	0.51	1.39	2.24	1.40

Tables C.2 and C.3 contain the uncertainty analysis for KE_1 and KE_2 and each is set in the same format as Tab. C.1. Between the two tables, ω , k , and ΔN^2 are the same, but N and $\partial_z N^2$ are varied based on the respective values of the evanescent and propagating regions. Units for each variable are listed in the top row. For the evanescent region, the total relative uncertainty, calculated using Eq. (C.2) with KE_1 in place of $\partial \rho' / \partial z$, is 61.47%, and ΔN^2 has the largest percent impact on the solution, followed by $\partial_z N^2$ and ω . Variations in N and k have a negligible effect on the solution. By decreasing the uncertainty of ΔN^2 , the overall uncertainty estimate of KE_1 could be greatly improved.

For KE_2 in the propagating region, the overall uncertainty is larger than KE_1 at 97.45%. Unlike KE_1 , only the impact of k and $\partial_z N^2$ are negligible, while ω , N , and ΔN^2 each have an important percent impact on KE_2 . In addition, the variable with the highest impact is N , followed closely by ΔN^2 .

Although the uncertainty of four of the five variables is 5% or less for Tab. C.2 and Tab. C.3, the combined uncertainty for both kinetic energy calculations is very high. To improve on the total relative uncertainty, it is recommended that the highest resolution possible be used for calculating ΔN^2 when using the software Digiflow. Also the resolution of the measurements for the heights needed to calculate N and $\partial_z N^2$ could be increased by using a better ruler. Improving

the measurement of ω by using a better stopwatch or by using image processing software to track the period of the topography would also improve the total uncertainty.